Tip vortex modelling for cavitation noise applications: A verification and validation study in ReFRESCO

Master of Science Thesis

Rens *Henricus Adrianus Arnoldus* Liebrand

July 2019

Delft University of Technology

TU Delft Delft University of Technology

Challenge the future

TIP VORTEX MODELLING FOR CAVITATION NOISE APPLICATIONS: A VERIFICATION AND VALIDATION STUDY IN REFRESCO

MASTER OF SCIENCE THESIS

by

RENS *Henricus Adrianus Arnoldus* LIEBRAND

born in Eindhoven, The Netherlands

in partial fulfillment of the requirements for the degree of

Master of Science
in Aerospace Engineering

at the Delft University of Technology.
This thesis is to be defended publicly on Friday July 12, 2019 at 2:00 PM.

Supervisors:	Ir. M. D. Klapwijk,	Delft University of Technology
	Dr. Ir. G. N. V. B. Vaz,	Maritime Research Institute Netherlands
Thesis committee:	Dr. Ir. M. I. Gerritsma,	Delft University of Technology
	Dr. Ir. A. H. van Zuijlen,	Delft University of Technology
	Prof. Dr. Ir. T. J. C. van Terwisga,	Delft University of Technology

Keywords: Cavitating tip vortex noise, elliptical wing, ReFRESCO, verification and validation.

TU Delft Delft University of Technology

MARIN

SUMMARY

Cavitating tip vortices of marine propellers are the main contributors to underwater radiated ship noise due to their dynamic behaviour and broadband sound spectrum. Experimentally, it is challenging to get a detailed insight into the vortex structure which makes it difficult to understand the noise generating mechanisms. Although Computational Fluid Dynamics (CFD) could offer a solution to this, knowledge regarding the modelling of the inception and dynamics of tip vortex cavitation is insufficient to obtain reliable numerical results in relation to noise predictions.

To this end, an extensive verification and validation study in the context of transition and turbulence modelling of an elliptical planform with NACA66$_2$ − 415 cross-section (known as the 'Arndt' wing) is carried out. The finite length of the lifting surface causes the generation of a tip vortex without the additional complexity of secondary motion (propeller rotation). The effect of transition and turbulence modelling on the structure of the vortex is first assessed in wetted (non-cavitating) conditions. Thereafter it is checked whether the observations in wetted flow conditions also apply to cavitating conditions and what the effect of the cavitation model on other flow variables is. CFD simulations are carried out using the community based open-usage code ReFRESCO.

The 'Arndt' wing is considered at 5 and 9 degrees Angle(s) of Attack (AoA) with a root-chord based Reynolds number of 8.95×10^5. The computational domain matches the geometry of the cavitation tunnel of Delft University of Technology to allow for validation using the stereographic-particle image velocimetry measurements by Pennings et al. (2015b). For all calculations, multi-block hexahedral structured grids are used. The grids are locally refined in the vortex and wake regions to minimise numerical diffusion. Convergence criteria are set based on a trade-off between the computational efficiency and iterative uncertainty plus the requirement that the iterative error should be at least one order of magnitude lower compared to the discretisation error.

Transition modelling

While prior researchers explained early decay of vorticity and therefore an underpredicted cavity size by (i) numerical diffusion, and (ii) overprediction of eddy-viscosity, it is argued that the assumption of a fully turbulent Boundary Layer (BL) in CFD simulations also contributes. This statement is made based on combining (i) experimental observations that the vortex of the 'Arndt' wing mainly interacts with the BL on the suction side through the vortex roll-up process, (ii) the 'McCormick' hypothesis, and (iii) an analytical expression for a cavitating Lamb-Oseen vortex.

In order to prove this statement, the SST turbulence model is supplemented with the $\gamma - \tilde{R}e_{\theta_t}$ transition model to take laminar-to-turbulent transition into account and change the state of the BL. Steady state simulations are performed and the spatial discretisation uncertainty is determined by means of systematic grid refinement. Literature showed that the behaviour of the transition model is sensitive to the turbulent inflow conditions (eddy-viscosity and turbulence intensity). A 2D sensitivity analysis of the wing at half-span is carried out to acquire a set of turbulent inflow conditions to vary the BL thickness. These inflow conditions are used in 3D simulations of the full wing. The resulting BL thickness is decreased by a factor of three for an almost completely laminar BL relative to a fully turbulent BL for the wing at 5 degrees AoA. The effect this has on the viscous core radius and consequently the pressure reduction in the vortex is found to be 20%. Not controlling (or measuring) the transition location in the experiments can therefore result in a large input uncertainty in the vortex measurements for the wing at 5 degrees AoA. The vortex at 9 degrees AoA is not affected by the state of the BL since transition on the suction side is triggered at the leading edge regardless of the turbulent inflow conditions. This minimises the input uncertainty and therefore the wing at 9 degrees AoA is considered for validation purposes.

Furthermore, a well-known property of the $\gamma - \tilde{R}e_{\theta_t}$ model, namely the stagnation of the iterative solution procedure, is addressed. It is argued and mathematically substantiated that local grid refinement in streamwise direction at the transition location should avoid this. Local priori grid refinement by means of adaptive refinement boxes is used to increase the streamwise (and spanwise, for 3D calculations) resolution of the grid at the transition location. For the 2D calculations, this avoids stagnation. However, the 3D calculations do not reach iterative convergence, even though these calculations use the same grid resolution as used in the 2D calculations.

Nevertheless, the root-mean-square of the residual vectors of the (dominant) transition variables are decreased by half an order of magnitude and the forces are observed to be converged.

Turbulence modelling
Previous research has shown that overprediction of eddy-viscosity yields excessive turbulent diffusion of the vortex. A literature study showed that, theoretically, the KSKL, EARSM, DDES, and IDDES models should suffer less from turbulent diffusion, or be able to capture the anisotropic character of the turbulent structures in the vortex. All turbulence models are assessed for the wing at 9 degrees AoA. The spatial and temporal discretisation errors (estimated using a systematic grid and timestep refinement study), and the statistical errors (calculated by means of the transient scanning technique) are determined for all calculations. Results are compared against the experimental measurements by Pennings et al. (2015b).

The lift coefficient predicted by all models is within the uncertainty bounds, except for the EARSM simulation, which underpredicts the lift due to early flow separation. The eddy-viscosity near the vortex centre of the EARSM simulation is found to be low compared to the other RANS models. This was expected to benefit the axial velocity in the vortex but the opposite is observed. By analysing the anisotropic normal and shear Reynolds stresses, it is observed that the Reynolds stresses in axial direction are responsible for this. The EARSM is the only model which is able to reproduce some of the anisotropic character of the turbulence near the viscous core radius.

Even though promising theory, the KSKL model still suffers from excessive production of turbulent kinetic energy and thus turbulent diffusion of the vortex. Despite the well matching lift coefficient, this still yields large modelling errors of the flow quantities in the vortex region.

The viscous core radius and consequently the pressure in the vortex centre for the hybrid models (DDES and IDDES) matches well with the experiments. This also applies to the axial and azimuthal velocity profiles which are within the uncertainty bounded over almost the entire vortex radius. However, the outcome contains a large modelling error because the resolved Reynolds stress components are found to be negligible compared to the unresolved stresses.

Cavitation modelling
The previous conclusions are all drawn based on wetted flow simulations. For cavitating flow conditions, vapour in the tip vortex is modelled by employing the Schnerr-Sauer cavitation model. The effect of transition modelling is assessed by analysing the cavity (defined as the region where the vapour volume fraction is larger than 0.1) both qualitatively and quantitatively. The length of the cavity is found to be sensitive to the state of the BL. Similar numbers as for the sensitivity of the pressure in wetted conditions are observed, i.e. the cavity length and maximum cavity radius are increased by about 20% for the most laminar BL relative to a fully turbulent BL. Growth of the cavity radius is predominantly found in the positive lift direction (at the suction side), which supports the experimental observation that the vortex mainly interacts with the BL on the suction side of the wing.

The length of the actual cavity for the different turbulence models is compared to the isocontour of the vapour pressure in wetted flow conditions. It is found that for the SST and EARSM simulations the actual cavity extends 81% and 111% further downstream, which is because the turbulent diffusion is reduced by the vapour region within the vortex.

Furthermore, the effect of the cavitation model on the other flow variables is assessed by comparing spatially averaged profiles of the pressure, velocities, turbulence quantities and Reynold stresses along the vortex radius for wetted and cavitating conditions. The formulation of the cavitation model yields a constant pressure in the entire cavity and no velocity gradients in any direction. The absence of velocity gradients causes (i) constant axial and azimuthal velocities in the cavity, (ii) almost no eddy-viscosity since the production term of the turbulent kinetic energy vanishes while the destruction term remains, and (iii) much lower Reynolds normal stresses in the cavity due to the Boussinesq hypothesis. This yields the vapour flow in the cavity to have the same characteristics as a potential flow. Whether the constant pressure is physically plausible is questionable. However, no pressure (nor velocity) measurements of the flow within a cavity in a tip vortex are found in literature.

PREFACE

I want to thank my supervisors, Dr. Marc Gerritsma, Dr. Sander van Zuijlen, Dr. Guilherme Vaz, and Dr. Thomas Lloyd for their guidance and enriching discussions along the past nine months. Their vast knowledge regarding cavitation, computational fluid dynamics, verification and validation, and professional writing were key in this work and my personal development. Special words to Ir. Maarten Klapwijk who has been my daily supervisor for this period. Thank you for the freedom you gave me, answering my numerous questions, and enhancing the quality of my work. Prof. Tom van Terwisga is thanked for being part of my thesis committee as well. I would like to thank Maurits van den Boogaard for being the best office partner, both from a professional as well as personal perspective. The support of all colleagues at MARIN was also much appreciated. Special gratitude to Ir. Rui Lopes for his contribution to one of the publications that came out of this research, and to Dr. Serge Toxopeus for providing me with a validation dataset.

Mom and dad, you are the best parents I can imagine. Thank you for the endless support, indescribable trust, but most importantly the work ethic you have taught me since I was young. My beautiful little sister, Maartje, thank you for everything as well I am very proud of you! The respect I received from the rest of my entire family is also much appreciated. My love, Jessica, your patience during my studies was unbelievable, your support endless, I am much looking forward to travelling the world together. My friends since I was little, Kay, Bert, Rik, Sjors, Giel, Jippe, Jouri, Mats, and Nick thank you guys for all the memories we share and freedom you provided me with when I moved to Delft for my studies. Martin, thanks a lot for being my soul-mate through the last years of our studies, the enormous amount of challenges we encountered, and just for being an amazing friend. Max and Robin, thank you for all the laughter and the good times we have spent and will spend together in the future. My cousins, Nino and Sjors, your support during my studies was much appreciated.

Rens Henricus Adrianus Arnoldus Liebrand
Wageningen, July 2019

CONTENTS

LIST OF FIGURES

LIST OF TABLES

ABBREVIATIONS

2D	Two-Dimensional	xi, 7, 9, 37, 48, 52, 54, 56, 63, 80, 115
3D	Three-Dimensional	vi, 8, 32, 33, 37, 48, 52, 54, 55, 67, 115
AoA	Angle(s) of Attack	ii, 11, 12, 33–37, 42, 48, 50, 51, 54, 57–65, 67, 68, 84, 87, 89, 94, 98, 99
AR	Aspect Ratio	32, 35
ARSM	Algebraic Reynold Stress Model(s)	22
BC	Boundary Condition(s)	32, 37, 48
BL	Boundary Layer	ii, iii, ix, 2, 4, 6, 11, 13–18, 20, 24, 25, 27, 32, 35, 41, 43, 44, 47, 48, 50–61, 63–66, 71, 79, 82, 84–87, 89, 98, 99, 114
CC	Curvature Correction(s)	66
CFD	Computational Fluid Dynamics	ii, viii, 1, 2, 4–6, 13, 15, 16, 20, 25, 27, 28, 31, 33, 38–40, 45, 47, 58, 61–63, 68, 80, 83, 85, 97, 98
CFL	Courant-Friedrichs-Lewy	32, 67
CG	Conjugate Gradient	30
DDES	Delayed Detached-Eddy Simulation(s)	xi, 2, 24, 25, 27, 67, 69, 71, 73–76, 78, 79, 81, 82, 88, 93, 115, 116
DES	Detached Eddy Simulation(s)	2, 22–24, 66, 68, 79, 83, 116
DNS	Direct Numerical Simulation(s)	18, 23
EARSM	Explicit Algebraic Reynolds Stress Model(s)	ii, iii, xi, 22, 27, 66, 68–71, 74–79, 81, 82, 88, 93, 99, 115
FOU	First-Order Upwind	29, 48–50, 54
GIS	Grid Induced Separation	2, 24, 40, 66, 67
GMRES	Generalized Minimal Residual	30
HIT	Homogenous Isotropic Turbulence	22
IDDES	Improved Delayed Detached-Eddy Simulation(s)	xi, 2, 24, 25, 27, 67–69, 71, 73–76, 78, 79, 81, 82, 116
ILES	Implicit Large Eddy Simulation(s)	2, 66
KSKL	$k-\sqrt{k}L$	xi, 21, 22, 27, 66, 68, 71, 72, 74–78, 81, 82, 114
LDKM	Localized Dynamic Kinematic subgrid stress Model	2, 66
LE	Leading Edge	ix, 12, 48–50, 52, 54, 57, 59, 60, 63, 64, 85
LES	Large Eddy Simulation(s)	23–25, 66, 67, 78, 79, 81, 83, 116
LSB	Laminar Separation Bubble	6, 11, 12, 16, 44, 50, 51, 54, 55, 57, 58, 61

MARIN	Maritime Research Institute Netherlands	1, 28, 42
MSD	Modelled Stress Depletion	67, 78, 79
N-S	Navier-Stokes	10, 19, 23, 28, 32, 39, 49
NWO	Nederlandse Organisatie voor Wetenschappelijk Onderzoek	6, 13
PANS	Partially-Averaged Navier Stokes	23
PDF	Probability Density Function	viii, 38
PIV	Particle Image Velocimetry	9
QUICK	Quadratic Upstream Interpolation for Convective Kinematics	29, 49, 50, 54, 63
RANS	Reynolds Averaged Navier Stokes	ii, 2, 16–19, 21, 23–25, 28, 32, 42, 66, 71–80, 82, 83, 99, 116
ReFRESCO	Reliable & Fast Rans Equations (solver for) Ships, Construction (and) Offshore	1
RHS	Right Hand Side	5, 26, 31
RMS	Root Mean Square	39, 55, 73
R-P	Rayleigh-Plesset	xi, 7, 26, 27, 116, 118
RSM	Reynolds Stress Model(s)	22, 73
SA	Spalart-Allmaras	2, 24
SAS	Scale Adaptive Simulation(s)	21
SIMPLE	Semi-Implicit Method for Pressure Linked Equations	30, 31
S-PIV	Stereographic-Particle Image Velocimetry	xi, 1, 2, 11, 32, 43, 44, 46, 58, 60, 61, 63, 64, 70, 81, 83, 99
SRS	Scale Resolved Simulation(s)	2, 17, 18, 21–24, 32, 66
SST	Shear Stress Transport	xi, 16, 19, 20, 22–24, 27, 33–35, 37, 48, 50, 52, 53, 55, 56, 58–63, 66–71, 73–78, 80–82, 84, 88, 93, 98, 114, 115
TE	Trailing Edge	35, 51, 55, 61, 70
TST	Transient Scanning Technique	viii, 41, 45, 67–69, 79
URN	Underwater Radiated Noise	5, 6, 8, 13
V&V	Verification and Validation	38, 45
VoF	Volume of Fluid	25, 26, 28, 90, 95

1

INTRODUCTION

1.1. BACKGROUND

In marine applications, cavitation, especially on ship propeller blades, is responsible for undesired effects such as noise generation (Baudin and Mumm, 2015; Bosschers, 2018) and erosion (Thiruvengadam, 1974; Li, 2012). Cavitation is the explosive evaporation of a liquid in low pressure regions and the subsequent implosion when the pressure increases (Brennen, 2005). In the past decades, the maritime world has been searching for more efficient propeller designs to reduce fuel emissions (Ligtelijn, 2010). For most modern propellers, more propulsive efficiency results in more cavitation in almost the entire spectrum of operating conditions (Kuiper, 1997). The associated erosion and noise is often not dealt with since their respective impact is hard to assess during the design process (Carlton, 2018). The ability to predict various forms of cavitation and its tendency to emit sound or cause erosion is therefore desired. This research focusses on noise emission because of the increased awareness of the harmful environmental impacts of underwater radiated noise generated by marine traffic (Hildebrand, 2009; Frisk, 2012) as well as increasing care for on-board comfort (Veritas, 2003; De Lorenzo and Biot, 2006).

To reduce noise emission, there is a need to better understand the noise-generating mechanisms. Experimentally, it was concluded that cavitating tip vortices are the main contributors to ship noise due to their dynamic behaviour and distinct broadband sound spectrum (van Wijngaarden et al., 2005). However, it was also found that it is hard to acquire a detailed insight into the cavitating structures through flow measurements (Higuchi et al., 1989; Dacles-Mariani et al., 1995; Pennings et al., 2015b). Computational Fluid Dynamics (CFD) is supposed to offer a solution to this. While the numerical prediction of developed sheet cavitation is relatively well-understood (Foeth, 2008), knowledge regarding the modelling of the inception and dynamics of tip vortex cavitation is still insufficient to obtain reliable numerical results in relation to noise predictions (Schot, 2014; Asnaghi, 2018; Paskin, 2018). For this reason, the Netherlands Organisation for Scientific Research (Nederlandse Organisatie voor Wetenschappelijk Onderzoek, `www.nwo.nl`) funded the research project called 'NOISOURCE - Experimental and Computational Techniques to quantify noise sources from cavitating ship propellers'. This project is a collaboration between experimental work performed at Delft University of Technology and numerical work (predominantly) done at Maritime Research Institute Netherlands (MARIN). On the numerical side, particular attention is paid to the correct representation of cavity volume dynamics. Calculations are performed using Reliable & Fast Rans Equations (solver for) Ships, Construction (and) Offshore (ReFRESCO). ReFRESCO is a community-based open-usage CFD solver developed by MARIN in cooperation with i.a. Delft University of Technology, Instituto Superior Técnico (Lisbon), and University of Southampton.

A popular approach for studying cavitating vortices is to consider a tip-loaded finite span lifting surface that induces a tip vortex while avoiding rotational motion (Higuchi et al., 1987). In this research the elliptical 'Arndt' wing (Arndt et al., 1991) is considered since Stereographic-Particle Image Velocimetry (S-PIV) measurements of the vortex (in wetted and cavitating flow conditions) are available (Pennings et al., 2015b). Furthermore, this wing is currently also being tested in an experimental campaign at Delft University of Technology, within the NOISOURCE project.

1

1.2. RESEARCH OBJECTIVES

Previous numerical studies did not have access to local flow measurements of the cavitating tip vortex of the 'Arndt' wing (Schot et al., 2014; Asnaghi, 2018; Paskin, 2018). For this reason, validation was mainly done by comparing force measurements or qualitative velocity fields of the vortex. Local quantitive comparison would increase the credibility of the numerical results. Numerous approaches are taken to validate tip vortices (e.g. by Frank et al. (2007) and Dacles-Mariani et al. (1995)). However, extensive validation of local measurements of cavitating tip vortices is rarely found.

Arndt et al. (1991) observed that "the vortex mainly interacts with the boundary layer on the suction side of the wing; boundary layer fluid is entrained in the vortex which affects the core radius" for the 'Arndt' wing. Interestingly enough, transition is rarely controlled in most simulations or experiments while it is responsible for the state of the Boundary Layer (BL) and therefore likely affects the structure of the vortex. To account for this, Schot et al. (2014) applied BL tripping to the Spalart-Allmaras (SA) turbulence model by including a source of turbulent viscosity at a specified chord-wise location of the wing. This resulted in more accurate lift and more particularly drag results. However, the effect on the vortex is not elaborated on.

The current literature reports the use of a wide variety of turbulence models for the 'Arndt' wing. Schot (2014) concluded that the use of Reynolds Averaged Navier Stokes (RANS) in combination with a one or two equation closure based on the Boussinesq hypothesis is not able to reproduce the anisotropic turbulence in the vortex core and overpredicts the eddy-viscosity in this region, since it is insensitive to streamline curvature (Bradshaw, 1973). This results in excessive turbulent diffusion in the vortex and therefore an underpredicted cavity length. Curvature corrections are found to improve results but still insufficient. As a result, more comprehensive turbulence models were advised.

Asnaghi (2018) and Paskin (2018) followed this recommendation and continued by simulating the flow around the same geometry using Scale Resolved Simulation(s) (SRS). The former performed Implicit Large Eddy Simulation(s) (ILES) and Localized Dynamic Kinematic subgrid stress Model (LDKM) simulations of the cavitating vortex. The integral quantities agreed arguably well (within 5%), and the models prevent the early decay of the vortex. It is questionable whether all relevant physics are captured in the vortex, since it is not certain that all turbulent velocity fluctuations in the BL are properly developed whereby it could be that the model resolves a too laminar vortex. Paskin (2018) performed Detached Eddy Simulation(s) (DES). Although the lift coefficient not matches the experiments well, the work showed the ability of DES to capture velocity fluctuations in the vortex. The discrepancy in the lift coefficient is due to premature BL detachment. This is a well-known property of the model, known as Grid Induced Separation (GIS) (Menter et al., 2003b). Adapted DES models such as Delayed Detached-Eddy Simulation(s) (DDES) (by Spalart et al. (2006)) and Improved Delayed Detached-Eddy Simulation(s) (IDDES) (by Gritskevich et al. (2012)) are designed to overcome this problem, yet their application to cavitating vortices is not found in literature for this test case.

Based on these observations, the following research questions are formulated:

I) What technique should be used to validate the CFD results of the vortex structure based on S-PIV measurements, and which numerical errors should be assessed?

II) What is the effect of transition modelling on the structure of the vortex?

III) What turbulence model performs best in capturing the anisotropy character of the turbulent structures in the vortex core region and avoids excessive turbulent diffusion?

IV) Do the observations regarding transition and turbulence modelling hold for wetted as well as cavitating conditions, and what is the effect of the cavity on the other flow variables in the vortex?

1.3. THESIS OUTLINE

Chapter 2 introduces the problem at hand by defining cavitation, identifying and theoretically supporting the key features of vortex cavitation, and describing the 'Arndt' wing in more detail. The next chapter presents the theories of the required physical models to accomplish objectives II-IV but also substantiates why these specific models are chosen. Chapter 4 describes the numerical implementation of the problem in the CFD solver. Chapter 5, concerning Verification & Validation, provides the answer to the first research question and analyses which numerical errors should be assessed. The three successive chapters present the numerical results to answer research questions II-IV respectively. Finally, Chapter 9 summarises the conclusions and recommendations for future work.

2

PROBLEM STATEMENT

This chapter provides a description of the problem at hand. Because this thesis is written for a broad audience (for whom cavitation might be a new subject), the first section gives a general introduction to the subject and presents some basic aspects concerning cavitation. The second section describes the different types of cavitation. These two sections might be skipped by readers with thorough background knowledge regarding cavitation. The third section pays attention to tip vortex cavitation in particular, followed by a description of the test case.

2.1. CAVITATION

First, a general introduction to cavitation is given, and the mechanism behind the emergence of cavitation is explained. After that, the three most important side effects are shortly named.

2.1.1. FUNDAMENTALS OF CAVITATION

Cavitation is the process of a liquid which changes from a liquid to vapour state by de-pressurisation under (almost) constant temperature (Brennen, 2005). While *cavitation* is sometimes confused with *vaporisation*, classical thermodynamics provides a clear distinction: a liquid changing phase by depositing energy in it is referred to as vaporisation while changing phase by setting up tension is called cavitation. Figure 2.1 visualises this distinction through a phase diagram. In this project, only the latter is of interest and is considered to be a purely isothermal process. The most common form of applying tension on a fluid is due to pressure. In regions where the static pressure drops below a certain threshold, the liquid starts to cavitate. In water, this pressure drop can either be achieved hydrodynamically due to gradients in the fluid flow or acoustically by sound waves. On a micro-fluid level, this can be seen as the breakdown of a liquid medium resulting in vapour regions within the fluid. The pressure threshold would ideally be determined based on considerations on a microscopic scale. However, taking the actual state of scientific knowledge as well as the need for a practical solution into account, it is most appropriate to only rely on macroscopic fluid properties (Franc and Michel, 2006). The time-scales involved in this process are very small, such that cavitation develops almost spontaneously. The phenomenon of cavitation was already observed by pioneers such as Reynolds (1873) and has been a topic of interest in many research fields ever since.

Despite the pronounced cohesion of water that yields the liquid to be stable under tension for a long time ($\mathcal{O}(10^2)\ MPa$ according to Zheng et al. (1991)), a lot of modern systems suffer from the negative side effects of cavitation which are named in Section 2.1.3. Examples are (i) internal combustion systems (Chaves et al., 1995), (ii) pumps (Moore and Ruggeri, 1969), (iii) biomedical applications (Apfel, 1982), and (iv) maritime system (Kuiper, 1997). In this project, the focus lies on maritime systems and in particular propellers.

2.1.2. CAVITATION INCEPTION

The start of a cavitation process is known as cavitation inception. Typical situations in which cavities emerge are regions of low pressure, shear flows, rough walls, vibrating structures, and shock waves (Franc and Michel, 2006). In propeller application, hydrodynamic inception (i.e. inception by local low-pressure regions) is most often observed (Bosschers, 2018). In this thesis, inception refers to hydrodynamic inception, and the influence of other factors is neglected.

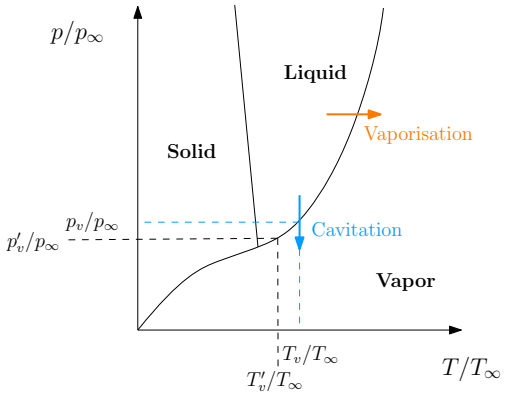

Figure 2.1: Phase diagram with indication for vaporisation and cavitation.

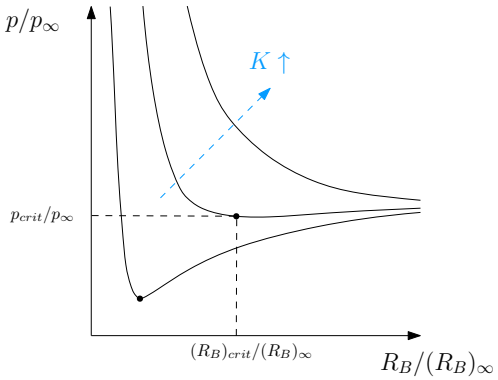

Figure 2.2: Illustration of the relation between bubble radius and outside pressure for increasing gas content (K).

The most used non-dimensional parameter to match experimental and numerical studies in the context of cavitation is the cavitation number (σ) defined as,

$$\sigma = \frac{p_\infty - p_v}{\frac{1}{2}\rho U_\infty^2}, \tag{2.1}$$

where p_v is the saturated (vapour) pressure of the fluid, p_∞ the freestream pressure, ρ the fluid density, and U_∞ the freestream velocity. The cavitation number can be interpreted as a kind of pressure ratio which represents the sensitivity of the fluid to cavitation: the higher the pressure difference in the numerator (increasing σ), the more tension needs to be applied to the fluid in order to start inception. When researching cavitation processes on a model scale, it is necessary to match the cavitation number with full scale. This ensures that one operates at properly scaled conditions. Incorrect scaling results in an advanced or delayed inception point whereby the development and effects of the cavity do not correspond to the full-scale situation. To do so, the ambient pressure can often be adjusted in experimental campaigns by de-pressurising the entire test facility.

The actual value at which inception takes place is called the inception cavitation number, σ_i. Inception occurs at the 'weakest' spots in the liquid. In water, these spots are predominantly the presence of nuclei, which are microscopic air bubbles trapped in the liquid.

In practice, inception is rarely triggered exactly at the vapour pressure for several reasons. Firstly, the diffusion of heat from the liquid phase into the vapour region which results in a thermal Boundary Layer (BL) near the cavity. This local temperature decrease ($T/T_\infty - T'/T_\infty$ in Figure 2.1) causes the inception pressure to be slightly lower than the vapour pressure and is referred to as thermal delay (Franc and Michel, 2006). This effect can safely be neglected for the considered flow conditions as the fluid's critical point temperature is much higher relative to the freestream temperature (Osterman et al., 2010). Secondly, contamination of the fluid causes the fluid to withstand a higher/lower tensile force, as discussed by Billet (1985). Prior research often refers to 'strong' and 'weak' water as an indication for the amount of contamination of the water (e.g., Arndt and Keller (1992)). Thirdly, a finite residence time to evolve to an observable bubble size is required for the cavitation nuclei (Brennen, 2005). The difference between the theoretical vapour pressure and the actual local pressure triggering inception ($p_v/p_\infty - p'_v/p_\infty$ in Figure 2.1) is named the tensile strength of the liquid. In modern Computational Fluid Dynamics (CFD), the previous points are rarely taken into account, however they are explicitly discussed here to provide the reader with a complete view of the inception process.

Not accounting for (i) the thermal BL, (ii) fluid contamination, and (iii) residence times implies that inception is triggered *at* the vapour pressure. The magnitude of the vapour pressure can be derived as follows. To start the inception process, nuclei are required. For a bubble (or nucleus) with a radius R_B to be stable in a given pressure field, the inside pressure (p_{in}) should be equal to the outside pressure (p) plus the surface tension at the bubble radius,

$$p_{in} = p + \frac{2Q}{R_B}, \tag{2.2}$$

where Q is the surface tension along the interface. The pressure inside the bubble is equal to the sum of the

vapour pressure and partial gas pressure which yields,

$$p_v + \frac{K}{R_B^3} = p + \frac{2Q}{R_B}. \tag{2.3a}$$

$$p_v = p + \frac{2Q}{R_B} - \frac{K}{R_B^3}. \tag{2.3b}$$

In these equations, K represents the nucleus' gas content. In the formulation of the partial pressure, isothermal conditions are assumed. Furthermore, no mass transfer between the bubble and the liquid is assumed, whereby K is constant. The function is schematically illustrated in Figure 2.2. By differentiating Equation (2.3) with respect to R_B, one can determine the minimum bubble radius $(R_B)_{crit} = \sqrt{\frac{3K}{2Q}}$. The corresponding pressure is referred to as the critical pressure which is also indicated in the figure. This pressure is often considered to be the vapour pressure of the liquid. Substituting the critical bubble radius into the same equation results in,

$$p + \frac{2Q}{\sqrt{\frac{3K}{2Q}}} - \frac{K}{\frac{3K}{2Q}\sqrt{\frac{3K}{2Q}}} = p_v, \tag{2.4a}$$

$$p_i = p_v - \frac{4Q}{3\sqrt{\frac{3K}{2Q}}}. \tag{2.4b}$$

This implies that the difference between vapour and inception pressure (p_i) is positively correlated with the surface tension and negatively with the initial gas content of the nucleus. Therefore, mainly the largest nuclei (and thus weakest points) in the fluid determine the inception pressure of the fluid. Most state-of-the-art CFD codes (including ReFRESCO), do not account for this. To minimise the comparison error with experiments, measurements with the lowest amount of nuclei should be used in the validation process as will be described in Chapter 5.

2.1.3. CAVITATION SIDE EFFECTS

Cavitation is known mostly for its noise generation, the damage it does to nearby surfaces, and the adverse effect on the performance of systems. Noise is of particular interest in this thesis, however the others are also briefly touched upon in the following paragraphs. Although cavitation is brought forward as a highly undesired side-effect in this section, there exist some examples of applications which benefit from the harsh impact of cavitation. Examples are biomedical applications by humans (Brennen, 2015), and as a defence/strike mechanisms by certain animals (Patek et al., 2004).

NOISE

Cavitation is a highly dynamic process which causes pressure fluctuations (p') and thus sound waves. Noise is mainly generated when cavitating structures collapse as is it directly related to the second derivative of the volume ($\mathcal{V}$) in time (t), i.e. $p' \sim d^2\mathcal{V}/dt^2$ (Wang and Brennen, 1995). The magnitude of p' is therefore large for bubbles during a collapse due to the (very) short time-scales involved. Rayleigh (1917) published the following expression to estimate the collapse time (t_c) of bubbles (neglecting surface tension and gas content),

$$t_c = 0.915\sqrt{\frac{\rho R_B^2}{p_\infty - p_v}}. \tag{2.5}$$

To get an idea of the time-scales involved, a bubble with $R_B = 2\mu m^1$ in water with a density of $\rho = 998 kg^1 m^{-3}$ and cavitation number of 2.0 results in a collapse time in the order of 0.5 μs. According to Brennen (2005) this would yield pressure pulses up to $10^{10} Bar$. Note that this number does not take gas diffusion and compressibility into account and, therefore, will be a couple of orders of magnitude lower in reality. However, it still shows the potential of noise formation by collapsing cavities.

The dynamic behaviour of cavities on, or in the vicinity of, ship propeller blades causes pressure fluctuations which excite the hull structure above the propeller. These pressure fluctuations are observed to be mainly in phase at the ships surface, which makes cavitation a very efficient inboard noise and vibration generator (Bosschers, 2017). Nowadays, people that board ships care more about their comfort which drives up requirements with regard to noise in modern ship design and bounds the amount of cavitation that is acceptable (Veritas, 2003).

Besides, the collapse, interaction, and shedding of cavitating structures generates Underwater Radiated Noise (URN). For military purposes, URN means easier detection by enemy sonars, and it could interfere with onboard equipment which requires low self-noise.

Last, the awareness of the harmful environmental noise effects by the ever-growing amount of marine traffic has increased in the last decade (Hildebrand, 2009; Frisk, 2012). Recently, this has led to the development of several guidelines within the maritime industry for noise generation (see e.g. Baudin and Mumm (2015)). The prediction of URN originating from cavities remains a challenging topic. This is the primary motivation of the Netherlands Organisation for Scientific Research (Nederlandse Organisatie voor Wetenschappelijk Onderzoek (NWO)) to fund the NOISOURCE[1] project of which this research is part.

EROSION

Erosion occurs when cavitating structures interact with material surfaces. Interaction in this context often means a collapse of the cavities during which the accumulated energy in the cavity is released and causes damage. The released energy is mainly in the form of shock waves and the formation of micro-jets during the collapse. They can be so violent that surface material is knocked off. This subject has extensively been researched in the second part of the last century (Knapp, 1970; Thiruvengadam, 1974), but remains a challenging topic due to the unsteadiness of the problem in combination with the material reaction at the liquid-solid interface (Brennen, 2005).

In modern CFD codes, it remains a challenge to take all the relevant physics of cavitation erosion into account (Li, 2012). Most of the present erosion models (e.g. by Kato et al. (1996) and Bark et al. (2004)) are only applicable to specific flow problems.

PROPELLER PERFORMANCE

Cavitation regions affect the flow field and thus the performance of the force generating surfaces. Although cavitation does not drastically affect the integral forces in normal operation conditions (Sampson, 2010), it introduces additional uncertainty. If cavitation occurs, it is reliable to say that its dynamic behaviour influences the forces over time. In maximum power settings, cavitation at the propeller surface can also yield a breakdown of trust.

In modern engineering, the main effect of cavitation on propeller performance is implicit. Engineers have aimed for high propulsive efficiencies at the expense of more cavitation and thus noise emission and erosion (Kuiper, 1997). In other words, a tip loaded propeller is more efficient but more sensitive to tip vortex cavitation (as will be described in Section 2.2.3). This means that such a propeller thus generates more URN and erosion. Ligtelijn (2010) estimated the losses in efficiency to be 5-10% in his paper with the suitable name 'The pay-off between cavitation and efficiency'.

2.2. TYPES OF CAVITATION

On marine propellers, cavitation is, despite its negative side effects, an often accepted phenomenon due to high thrust requirements and to benefit the propeller efficiency. The low-pressure regions on the propeller yield different forms of cavitation, which are described next.

2.2.1. SHEET CAVITATION

The best-understood form of cavitation on marine propellers is sheet cavitation (Foeth, 2008). Physically this can be seen as a region of separated flow which is filled with vapour and reattaches at a certain length downstream. Figure 2.3 displays a photograph, including a schematic visualisation of the process. In the pressure distribution over the foil, it can typically be recognised by a region of constant pressure like a Laminar Separation Bubble (LSB). However, the detachment mechanism is not identical. BL separation is observed to occur a certain distance upstream of the cavity (Brennen, 1969). A (small) recirculation zone is present as can be seen in the figure. The length of this region is dependent on the Reynolds number rather than the cavitation number (Arakeri, 1975).

Sheet cavitation often forms a problem when its behaviour gets dynamic. For certain flow conditions, (part of) the cavity can detach and convect with the flow. The breakdown of the detached cavity yields smaller independent cavitating structures in the flow. Knapp (1955) was among the first to describe this process and named it cloud cavitation. He described it as a 're-entrant' jet, which causes an upstream flow which rapidly detaches the cavity. Figure 2.3 visualises this process, including the stagnation point which is formed just downstream of the cavity, and the corresponding re-entrant jet. Although the term re-entrant jet was widely accepted in the past, current

[1] https://www.nwo.nl/actueel/nieuws/2016/alw/negen-projecten-in-topsector-water-call.html

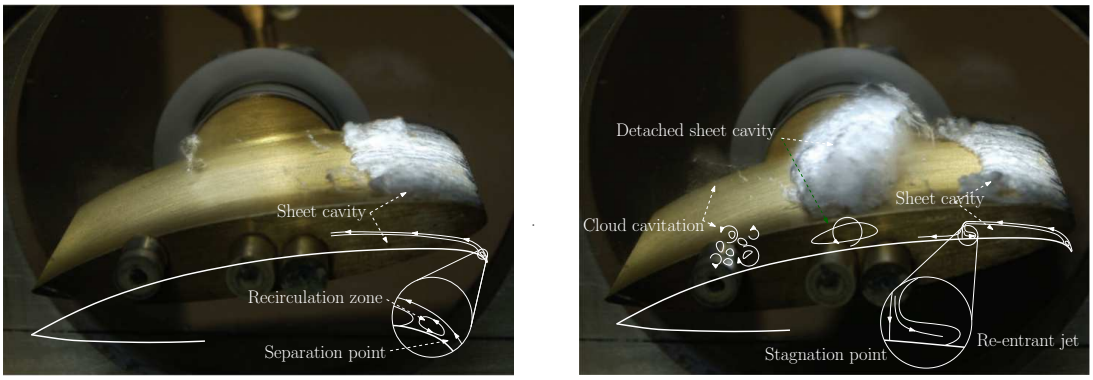

Figure 2.3: Schematic visualisation of sheet (left) and cloud (right) cavitation. Photographs taken by Foeth (2008). Note that the flow direction is from right to left.

researchers doubt the formulation (Franc and Michel, 2006) and describe it as a 'recirculation zone under the tail' (Hoekstra and Vaz, 2009). This is, especially for Two-Dimensional (2D) cases, a more adequate description when considering conservation of mass.

2.2.2. BUBBLE CAVITATION

Bubble cavitation is an unpredictable form of cavitation. It essentially is the growth of nuclei to observable size in lower pressure regions, as shown in Figure 2.4. A number of reasons why this is so unpredictable exist: (i) low-pressure regions are formed at various places. Dependent on the magnitude of the static pressure in these regions and the radius of a passing nucleus, bubble cavitation can be triggered. In experiments, one has to ensure the right amount of nuclei and corresponding radius, while in numerical simulations nuclei trajectories and nuclei expansions and contractions must be calculated. In practice this is difficult to obtain, which makes it challenging to research this kind of cavitation both experimentally (Akhatov et al., 2001) as well as numerically (Song and Qin, 2001). Furthermore, (ii) bubbles are often assumed to be spherical, such that the growth can be described by the analytical Rayleigh-Plesset (R-P) equation (Rayleigh, 1917). In reality however, bubbles are rarely perfect spheres due to the influence of pressure gradients and the presence of other flow features (shear regions, boundary layers, etc.) which cause bubbles to deform (Ceccio and Brennen, 1991). This makes it hard to determine their expansion or contraction. Lastly, (iii) bubbles interact. The expansion of the bubbles will be affected by their interaction and will therefore depend on the concentration of bubbles in the flow.

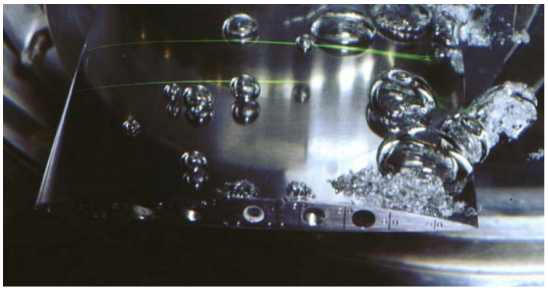

Figure 2.4: High-speed photograph of bubble cavitation (Franc and Michel, 2006).

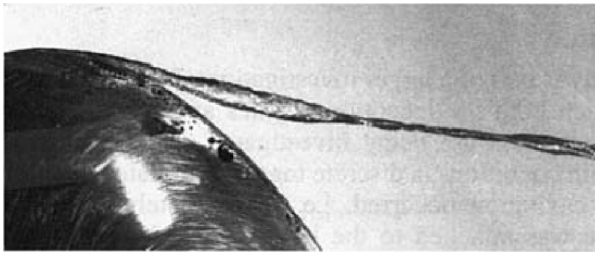

Figure 2.5: High-speed photograph of tip vortex cavitation (Maines and Arndt, 1997a).

2.2.3. VORTEX CAVITATION

Several kinds of vortices are present on propellers such as leading edge vortices, hub vortices, and tip vortices (Van Terwisga et al., 1999). In this study, the tip vortex is of particular interest. The velocities in vortices cause the static pressure to drop whereby inception is triggered and part of the core is 'filled' with vapour. This yields a vapour column with radius η_c inside the vortex as shown in Figure 2.5. This region is often seen as a solid body with a circulating flow around it. The cavity is present as long as the pressure in the core remains below the vapour

pressure.

Although research on cavitating vortices was already carried out by pioneers such as McCormick (1962), its appearance and behaviour are still not well understood (Arndt, 2012). Experimental (Higuchi et al., 1987; Dacles-Mariani et al., 1995; Pennings et al., 2015b) as well as numerical (Schot, 2014; Asnaghi, 2018; Paskin, 2018) studies exposed the difficulties in analysing this kind of flow. Furthermore, this kind of cavitation is the main mechanism responsible for the unwanted URN and vibration effects (Van Wijngaarden, 2011). For these reasons, this research project focusses on cavitating tip vortices in particular.

2.3. KEY FEATURE OF TIP VORTEX CAVITATION

From now on, the focus will be on tip vortex cavitation. The most comprehensive reference concerning wet vortices would probably be the work by (Green, 2012). The first part of this section reviews the tip vortex as part of the lifting line system. After that, the structure of the vortex is discussed and analytical expressions to describe the velocity profile in a (non)-cavitating vortex are presented.

2.3.1. LIFTING LINE THEORY

Some researchers explain the formation of a tip vortex from the fact that a finite lifting surface (referred to as wing from now) in a freestream generates a pressure and suction side which have to merge in the tip region (e.g. Devenport et al. (1996)). The swirling flow is the result of the flow moving from the high to the low-pressure region; its convection downstream forms a vortex. Although this definition is widely accepted and describes the local flow phenomenon, it does not serve as a complete description of the lifting system.

A more global way of looking at a vortex is the Kutta-Joukowski theorem, independently formulated by Kutta, and Joukowski in 1902, and 1906 respectively. This theorem states that to generate lift (L), a certain amount of circulation (Γ) over the wing is required,

$$L/b = \rho U_\infty \Gamma, \tag{2.6}$$

with b the wingspan, U_∞ the freestream velocity, and ρ the fluid density. From this equatio, it can be concluded that in the case of a steady incompressible inflow, the lift only varies due to the circulation. Circulation is defined as, $\Gamma \equiv -\oint_C \vec{U}\cdot \mathrm{d}\vec{s}$, and can be interpreted as the integral of the velocity vector ($\vec{U}$) along an arbitrary *closed* curve C as illustrated in Figure 2.6. This relates to vorticity through Stokes theorem which results in (Saffman, 1992),

$$\Gamma = -\oint_C \vec{U}\cdot \mathrm{d}\vec{s} = \int\int_A (\nabla \times \vec{U})\cdot \vec{n}_A \mathrm{d}A = \int\int_A \vec{\omega}\cdot \vec{n}_A \mathrm{d}A, \tag{2.7}$$

where $\vec{\omega}$ is the vorticity vector, mathematically formulated as the curl of the velocity vector ($\vec{\omega} = \nabla \times \vec{U}$). By taking the dot product of the vorticity with the surface normal $\vec{n}_A$, only the normal component with respect to the surface A is integrated. Another way of looking at circulation is thus the amount of rotation in the flow normal to a given area. According to Helmholtz (1858), this principle can be extended into the third dimension which yields the following thought experiment. Consider the Three-Dimensional (3D) curve C in as shown in Figure 2.7, with on either side an attached surface, in this case A_1 and A_2. According to Equation (2.7) the following must hold,

$$\Gamma = -\int\int_{A_1} \vec{\omega}_1 \cdot \vec{n}_{A_1} \mathrm{d}A_1 = \int\int_{A_2} \vec{\omega}_2 \cdot \vec{n}_{A_2} \mathrm{d}A_2 . \tag{2.8}$$

Under the condition of equal surface areas, which is always possible since they are arbitrarily chosen, the vorticity on these areas must be equal. Now imagine the vortex tube T_1 with constant vorticity (with magnitude ω) coming into a volume bounded by A_1 and C. When this tube would end in the bounded region, it would increase the total vorticity on that side with magnitude ω, violating Equation (2.8). Would this tube be closed (T_2 in Figure 2.7) in space though, it would result in a net increase of zero ($+\omega - \omega = 0$). This principle should hold for the entire domain. Therefore, Helmholtz (1858) concluded in his second theorem that 'vortex tubes must appear as closed loops, extend to infinity, or start/end at solid boundaries'. Lord Kelvin extended this idea of vorticity conservation in 1869 by proving that the circulation along a closed curve is also constant in time, i.e. $\frac{D\Gamma_c}{Dt} = 0$. His insight led to most of the vortex line approaches still used in many applications nowadays. The most complete and well-explained work concerning vorticity conservation is probably by Katz and Plotkin (2001).

The first to apply this on a wing was Ludwig Prandtl in 1914 (Anderson Jr, 2010). The application is known as Prandtl lifting-line theory and can be explained based on the graphical display in Figure 2.8. For a given lift

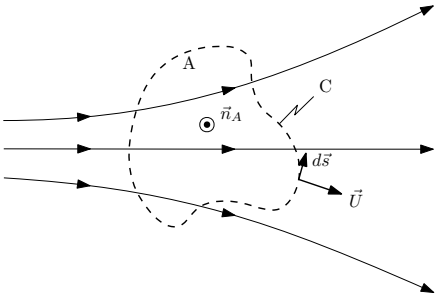

Figure 2.6: Visualisation of the definition of circulation in surface A which is bounded by closed curve C.

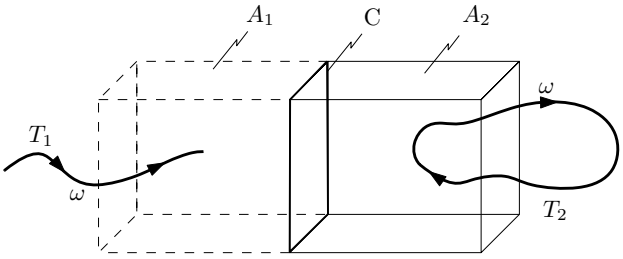

Figure 2.7: Visualisation of Helmholtz second theorem. T_1 and T_2 represent open en closed tubes of constant circulation with magnitude ω.

distribution over a wing, at each point where the circulation changes ($\frac{d\Gamma}{dz} \neq 0$), a trailing vortex is shed to conserve circulation. According to Helmholtz second theorem, the so-called 'horseshoe' vortices (a combination of trailing and lifting vortices) must be closed. The bound (or starting) vortex accounts for this and closes the lifting system. This bound vortex is generated when the lifting line starts generating lift, and can thus be assumed being at infinity in practical application. In Figure 2.8, the rotational direction of the vortices is indicated according to the so-called 'right-hand-rule', a double arrow stands for a vortex with strength Γ and triple for 2Γ.

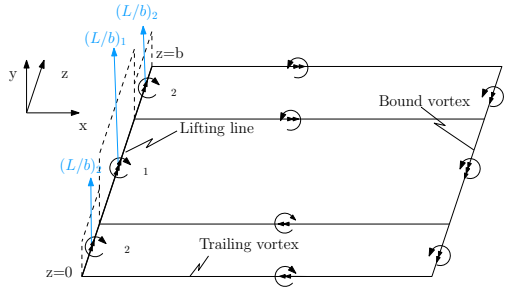

Figure 2.8: Visualisation of lifting line theory. Arrows indicate magnitude and direction of circulation.

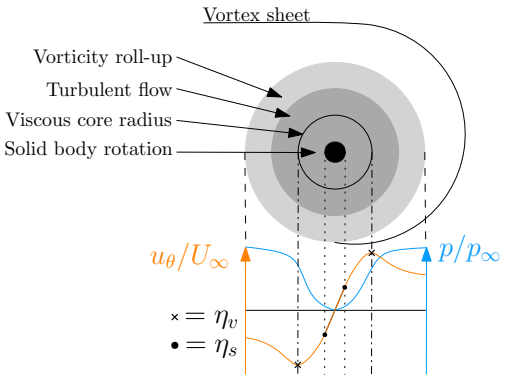

Figure 2.9: Illustration of vortex structure including azimuthal velocity and pressure distributions.

Considering the tip vortex as part of the lifting line system rather than a local phenomenon provides a broader insight into the existence and influence of the vortex on the rest of the flow field. One can conclude that the vortex is inherently coupled to the circulation over the wing. Furthermore, the roll-up of the vortex sheet in the wake of the wing transports the low momentum BL fluid into the vortex. This makes the circulation and BL characteristics crucial parameters in this study.

2.3.2. VORTEX FLOW FIELD

Phillips (1981) provides a clear explanation of the 2D flow surrounding the vortex core, which is illustrated in Figure 2.9. Generally speaking, the core of a vortex is seen as a solid body rotation which results in a laminar flow within the core (η_s). Figure 2.9 illustrates this by means of the linear part in the azimuthal velocity distribution (Rankine vortex model). Just outside the vortex core, the flow is dominated by turbulent activity and decays under the influence of viscosity. The core radius, defined as the location where the azimuthal velocity is largest, lies within this turbulent region. The velocity distribution around it is described according the Lamb-Oseen vortex (the definition will follow in Equation (2.9)). The rolled-up vorticity often indicates the outer layer of the vortex. This region of high vorticity is also the main focus of the most popular vortex identification methods like the Q-(Hunt et al., 1988) and λ_2-criteria (Jeong and Hussain, 1995).

Particle Image Velocimetry (PIV) measurements by Dreyer et al. (2014) and Pennings et al. (2015a) have shown that the azimuthal velocity distribution for cavitating vortices is identical to non-cavitating vortices far away from

the cavity. Near the cavity interface, however, the velocity decreases relative to the wet case. The velocity distribution for the wet vortex which decays under the influence of the kinematic viscosity (ν) can be described by the classical Lamb-Oseen vortex (Lamb, 1932),

$$u_\theta(\eta) = \frac{\Gamma_\infty}{2\pi\eta}\left(1 - e^{-\frac{\eta^2}{\eta_\nu^2}}\right), \tag{2.9}$$

where u_θ is the azimuthal velocity, η the vortex radius, η_ν the viscous core radius of the vortex, and Γ_∞ the freestream vorticity in the plane of the vortex. Figure 2.10 visualises the velocity distributions for different values of the kinematic viscosity. The graph shows that increasing ν yields a less intense vortex with a larger viscous radius for equal values of the freestream circulation. Bosschers (2009) presented a similar approach to come up with an equation for a 'cavitating Lamb-Oseen vortex'. The main idea is to write the Navier-Stokes (N-S) equations in cylindrical coordinates and cross out some terms based on assumptions valid in a vortical flow. These assumptions read (i) the flow is considered axisymmetric, which yields the derivatives in azimuthal direction to zero (note that this assumption forces the cavity to be spherical), (ii) the velocity component in the axial direction is constant, and (iii) the derivatives in the same direction are also considered zero. The most important aspect is the cavity interface for which jump relations are used that require the shear stress at the cavity to be zero. The resulting azimuthal velocity distribution reads,

$$u_\theta(\eta) = \frac{\Gamma_\infty}{2\pi\eta}\left(1 - \frac{\eta_\nu^2}{\eta_\nu^2 + \zeta\eta_c^2} e^{-\zeta\frac{\eta^2-\eta_c^2}{\eta_\nu^2}}\right). \tag{2.10}$$

Here η_c is the cavity radius, and the constant $\zeta = 1.2564$ yields the azimuthal velocity to be maximal at the vortex core radius. Figure 2.10 displays the velocity distribution for different cavity sizes given a constant vortex core radius. The velocity distribution further away from the cavity nicely matches the non-cavitating Lamb-Oseen vortex, the velocity decreases substantially towards the cavity what is also observed in experiments. In Bosschers (2018), the analytical expression (including a term to account for vortex roll-up) is validated against a cavitating tip vortex. It shows that the implied boundary condition is appropriate and realistic.

Although this analysis is purely two-dimensional, it forms the basis of many vortex studies and will also be a key aspect in Chapters 6 and 7.

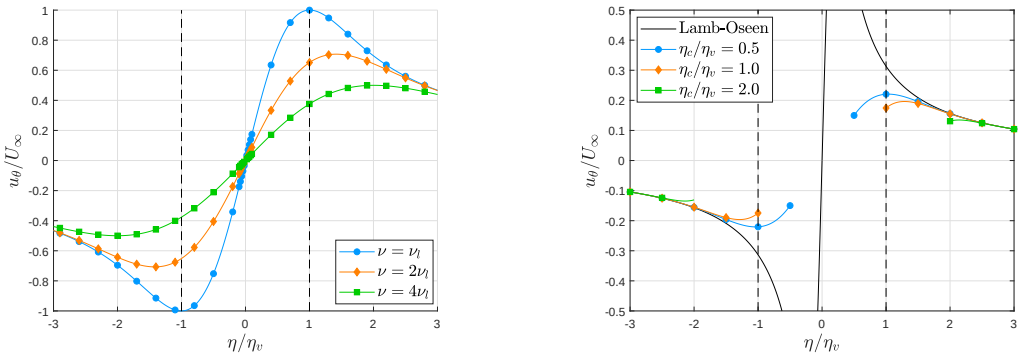

Figure 2.10: Effect of viscosity (left) and cavity radius (right) on velocity distributions of (non)-cavitating Lamb-Oseen vortex. The y-axis in the right graph is scaled with a factor 1/2 compared to the left graph.

2.4. TEST CASE SELECTION

To investigate tip vortex cavitation, stationary wings are often considered. The first paragraph of this section provides the motivation for the selected test case. The second part concerns the actual geometry and flow pattern.

2.4.1. MOTIVATION FOR SELECTION

The direct investigation of cavitating structures on propellers is complex due to the rotational motion (Morgut, 2012). Often used benchmarks in current research are stationary (elliptical) planforms under cavitating condi-

tions. The finite length of the lifting surface causes the generation of a tip vortex as described in Section 2.3, while avoiding any unwanted secondary motion.

In the past years, a substantial amount of research regarding the tip vortices of elliptical wings was done both experimentally as well as numerically. A close collaboration between both research fields is required as it is experimentally hard to get a detailed insight into the flow characteristics within the vortex (Higuchi et al., 1987; Arndt et al., 1991; Pennings et al., 2015b), while numerical simulations are capable to extract all flow variables within the core, but require extensive validation is required. The most frequently assessed test cases are the rectangular NACA0015 planform with rounded tips (Dacles-Mariani et al., 1995; Ahmad, 2013; Pereira, 2018) and the elliptical NACA66$_2$ – 415 planform (Schot, 2014; Klapwijk, 2018; Asnaghi, 2018; Paskin, 2018). Validation data for both cases in (non)-cavitating flow conditions at different Reynolds numbers is available in Dacles-Mariani et al. (1995), and Arndt and Keller (1992) and Pennings et al. (2015b) respectively.

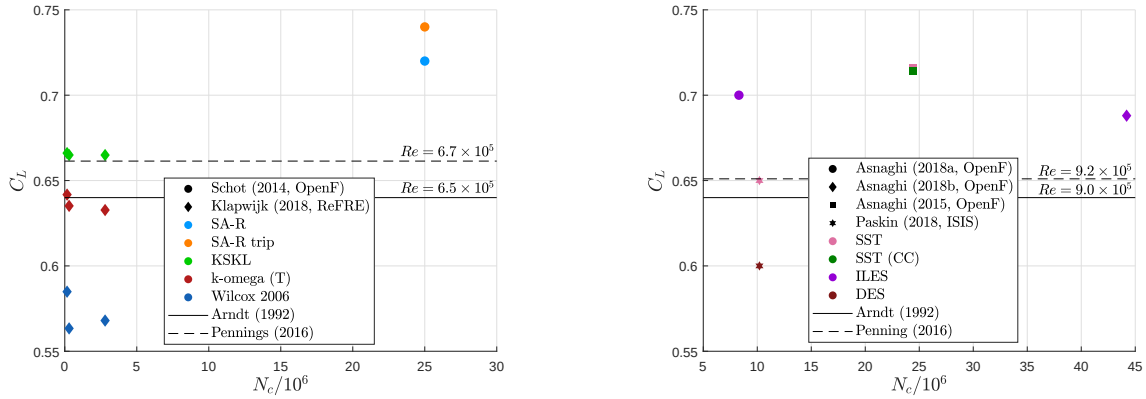

Figure 2.11: Published lift coefficient data of the 'Arndt' wing at $\alpha = 9°$ for $Re = 6.8 \times 10^5$ (left) and $Re = 8.95 \times 10^5$ (right). The shape of the data points indicates the reference; the colour stands for the employed turbulence models; the lines represent experimental results.

Based on a trade-off, a case study concerning the elliptical NACA66$_2$ – 415 planform (referred to as the 'Arndt' wing) is considered to be the most feasible. The main reason for this is that Stereographic-Particle Image Velocimetry (S-PIV) measurements of the tip vortex are currently carried out by Ph.D. candidate at the faculty of Marine Technology of Delft University of Technology, Ir. S. Nanda. This experimental research is also part of the NOISOURCE project. Chapter 5 elaborates on this in more detail. The major drawback of the 'Arndt' wing is the presence of a LSB for some of the test conditions (Arndt et al., 1991). Due to the reduction of chordwise Reynolds number towards the tip, the bubble length increases and consequently changes the lift distribution over the wing. The variation in circulation causes trailing vortices to emerge and interact with the main tip vortex (Arndt et al., 1991). Figure 2.11 presents an overview of the amount of work done regarding the 'Arndt' wing in the form of the published lift coefficients for the following most frequently assessed test conditions: Angle(s) of Attack (AoA) of 9 degrees and Reynolds numbers of $Re = 6.8 \times 10^5$ and $Re = 8.95 \times 10^5$ respectively. The results are obtained using different solvers, namely OpenFOAM, ReFRESCO and ISIS-CFD and different experimental facilities. The uncertainty of the measurements is not visualised because it is unknown for the most experimental and numerical results.

2.4.2. CASE DESCRIPTION

The 'Arndt' wing is an elliptical planform with NACA66$_2$ – 415 modified mean line 0.8 cross section. Figure 2.12 visualises the cross-section shape (referred to as foil from now) at zero and nine degrees AoA. The nomenclature of the foil indicates (i) a NACA 6 series (thus laminar) foil design, (ii) location of minimum pressure at $x_{LE}/c = 0.6$, (iii) the BL remains laminar for a lift coefficient of ±0.2 of the (iv) design lift coefficient of 0.4, (v) a maximum thickness of 15% of the chord, and (vi) the BL remains laminar until $x_{LE}/c \approx 0.8$. The approach for adapting the mean line is presented by Abbott and Von Doenhoff (1959).

The actual geometry is a scaled version of the original wing used by Arndt et al. (1991). The motivation why they used this wing shape is not explicitly mentioned, but it is believed that this geometry was selected due to the use in propeller design during that time. Pennings et al. (2015b) modified the lengths such that it matched

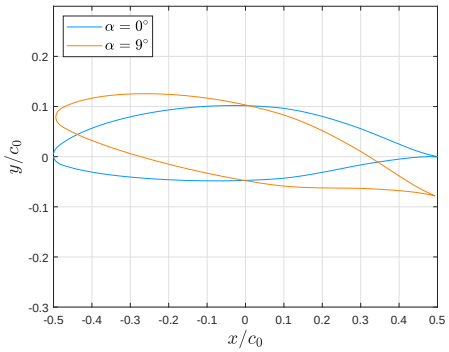

Figure 2.12: Visualisation of the NACA66$_2$ – 415 foil for $\alpha = 0°$ and $\alpha = 9°$.

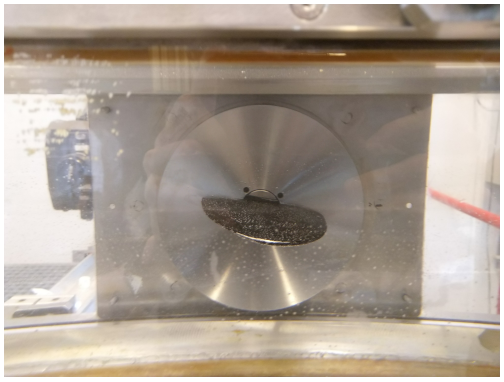

Figure 2.13: Photograph of the 'Arndt' wing mounted in the cavitation tunnel at Delft University of Technology. Picture taken without flow by Ir. M.D. Klapwijk at 01/05/2019.

the most relevant flow characteristics such as the Reynolds number. Figure 2.13 shows a picture of wing mounted in the cavitation tunnel of Delft University of Technology (the technical drawing is present in Appendix A). The root chord of the wing (c_0) is 0.1256m and the wingspan b is 0.15m. In this work, the wingspan is defined as the distance between the root and the wing tip, contrary to tip-tip distance like in many aeronautical applications. The surface area (S) of the suction side of the wing is 0.01465m^2, and this is used as the reference area in this study.

The circulation distribution over the (elliptical) wing at moderate AoA is supposed to be (Katz and Plotkin, 2001),

$$\Gamma(z) = \Gamma_0 \sqrt{1 - \left(\frac{z}{b}\right)^2} \quad \text{for} \quad z \geq 0.0, \tag{2.11}$$

where $\Gamma(z)$ denotes the local circulation at spanwise location z (see Figure 2.8), Γ_0 the total circulation over the wing, and b the wingspan. The original equation in Katz and Plotkin (2001) is based on the different definition of b (see previous paragraph). Equation (2.11) is a slightly modified version of this to match the definition of the wingspan in this report. The total wing circulation can be determined by substituting this equation in the Kutta-Joukowski theorem (Equation (2.6)) which yields,

$$\Gamma_0 = \rho U_\infty \int_{-\frac{b}{2}}^{\frac{b}{2}} \Gamma_0 \sqrt{1 - \left(\frac{2z}{b}\right)} dz = \rho U_\infty \left[\frac{1}{2} z \sqrt{1 - \left(\frac{z}{b}\right)^2} + b \sin\left(\frac{z}{b}\right) \right]_{-\frac{b}{2}}^{\frac{b}{2}} = \frac{4L}{\rho U_\infty \pi b}. \tag{2.12}$$

To obtain insight into the flow pattern over the wing, Arndt et al. (1991) carried out surface oil-flow visualisation in a wind tunnel for a somewhat lower Reynolds number. Figure 2.14 shows the visualised streamlines for an AoA of 5 and 10 degrees. Note that in the report of Arndt and colleagues, this corresponds to an AoA of 7.5 and 12.5 degrees respectively, which is the geometrical AoA plus the angle of zero-lift, which is $\alpha_0 = 2.5°$. For $\alpha = 5°$, a LSB can clearly be observed. The transition location is approximately at the position of this bubble and thus at about 60% of the chord. Increasing the AoA moves the transition location forwards to just downstream of the Leading Edge (LE) of the wing.

Furthermore, an investigation by Higuchi et al. (1989) exposed a remarkable characteristic of this test case. They observed a 'very strong, low pitch tone' for certain test conditions. Building on this work, Maines and Arndt (1997b) described this tonal noise as 'singing'. They concluded that the phenomenon is sensitive to the cavitation number, and the dominant frequency is inversely proportional to the hydrofoil size. It only occurs for a small range of cavitation numbers for a given lift coefficient. The exact mechanism behind this phenomenon is not known, one possibility could be that a standing wave travelling over the vortex cavity is in phase with the oscillation of a sheet cavity at the tip.

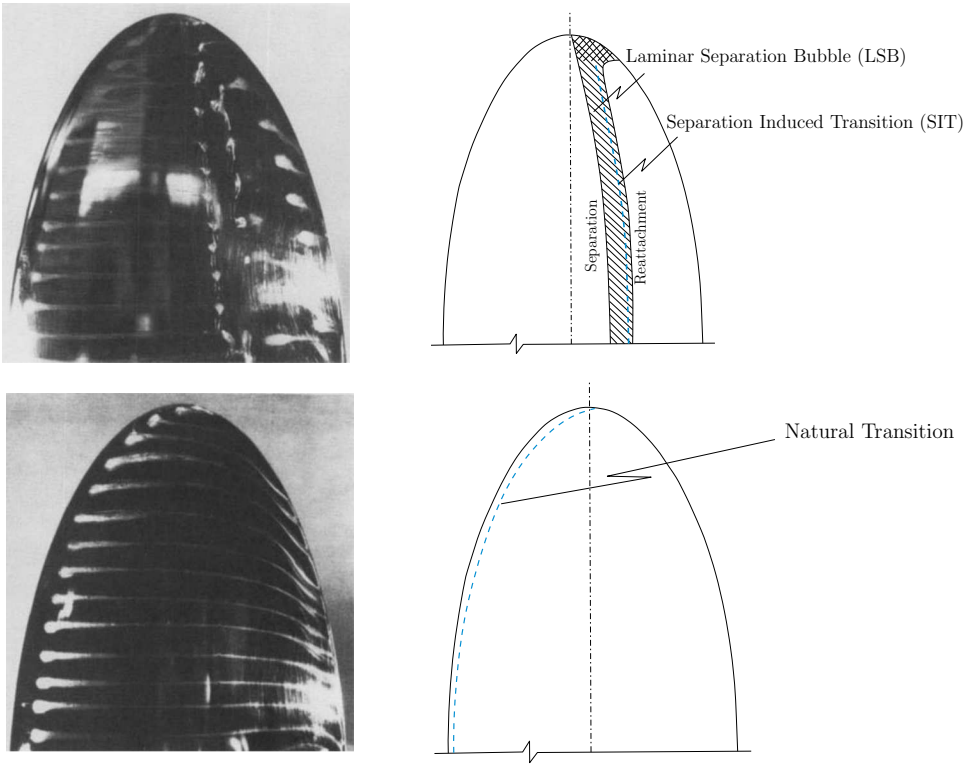

Figure 2.14: Flow visualisation (left) over 'Arndt' wing at $\alpha = 5^\circ$ (top) and $\alpha = 10^\circ$ (bottom). Estimated transition locations indicated by the dashed lines in the schematic figures (right). Flow at $Re = 5.4 \times 10^5$.

2.5. CONCLUSIONS

Cavitation occurs in numerous engineering applications and is known for its harsh and dynamic behaviour. In maritime applications and in particular propellers, cavitation causes i.a. erosion and URN. Due to the increased environmental (Hildebrand, 2009) and inboard noise (Veritas, 2003) requirements, this project focusses on the most effective cavitation noise source: cavitating tip vortices (Van Wijngaarden, 2011). This thesis is part of a broader research into marine noise sources funded by the NWO called the NOISOURCE project.

A popular approach to study this subject is by means of numerical simulations (Schot et al., 2014; Asnaghi, 2018; Paskin, 2018) or experiments (Higuchi et al., 1989; Arndt et al., 1991; Pennings et al., 2015b) of the elliptical 'Arndt' wing. The finite length of the lifting surface allows research into the cavitating vortex but avoids any additional rotational motion.

If the static pressure in a tip vortex drops below a certain threshold (the vapour pressure), cavitation is triggered. This process is called inception and is mainly determined by the (non-dimensional) cavitation number σ. It was concluded that the difference between the actual inception pressure and vapour pressure is positively correlated with the surface tension and negatively with the gas content of the nuclei. Therefore, mainly large nuclei trigger inception. It is not possible to track all these larger bubbles in CFD simulations and therefore validation based on experiments with small bubbles is preferred to minimise input errors as much as possible.

Approaching the tip vortex from a lifting line perspective provides more insight into the problem: First, the vortex strength is directly proportional to the circulation over the wing and therefore, the lift distribution. Second, the vortex roll-up process implies that the vortex core radius should be proportional to certain BL characteristics. For these reasons, the lift distribution as well as the BL quantities are additional parameters of interest when analysing a tip vortex flow.

Several 2D analytical (non)-cavitating vortex models are published in the past. Bosschers (2009) revised the well-known Lamb-Oseen vortex to come up with a cavitating formulation of the expression. The equation provides insight into the effect of viscosity as well as viscous core and cavity radii on the flow pattern.

3

PHYSICAL MODELS

This chapter presents the theory of the physical models which are used in the Computational Fluid Dynamics (CFD) simulations. Moreover, this chapter motivates why these specific models are chosen. The reader is supposed to have a general understanding of classical fluid mechanics, therefore little attention will be paid to general concepts as e.g. conservation laws and boundary layer theory. For the theory concerning these aspects, the author would like to point to fundamental references used: White and Corfield (2006) and Anderson Jr (2010). The most important (physical) aspects of all models are present in the sections below, Appendix B presents further mathematical details.

All sections are built up similarly: First, a short introduction on the topic is given together with the assumptions involved. After that, the theory of the different models is discussed. The first topic is transition-, the second turbulence-, and the third cavitation models.

3.1. TRANSITION MODEL

The phenomenon of transition is known to be responsible for many key flow features (Mack, 1984). However, the majority of the presently used turbulence models fail to predict transition since they are not built to capture this physical process (Rumsey, 2007; Walters and Cokljat, 2008). In this section the $\gamma - \tilde{R}e_{\theta_t}$ transition model is described in detail since this model is considered to be the most comprehensive model available nowadays (Coder, 2017; Baltazar et al., 2018; Lopes et al., 2018)

3.1.1. INTRODUCTION AND ASSUMPTIONS

Laminar-to-turbulent transition is the process which a fluid flow undergoes when transforming from a steady and ordered (laminar) state to an unsteady and chaotic (turbulent) state, predominantly due to viscous forces. The location where this process starts is determined by the critical Reynolds number (Re_c), which reflects the ability of the flow to damp (or amplify) flow perturbations. Re_c depends on the exposed pressure gradient, wall roughness, Mach number, wall suction/blow, wall heating/cooling, and turbulence intensity (White and Corfield, 2006). A quantitative way of looking at the process is the shape factor of the Boundary Layer (BL) defined as the ratio of the displacement- (δ^*) and momentum thickness (θ), i.e. $H = \delta^*/\theta$. This quantity indicates the 'fullness' of the BL as indicated in Figure 3.1. The more turbulent the BL, the more it deviates from the laminar Blasius solution and the lower the shape factor is. During the transition process, the shape factor thus decreases, as shown in Figure 3.1. The length over which the BL develops from laminar to fully turbulent is called the transition length, L_{tr}. Figure 3.2 illustrates typical skin-friction distributions for laminar, transitional and turbulent flows. The profiles can easily be understood from the definition of the wall shear stress (τ_w), $\tau_w = \mu(\frac{\partial u}{\partial y})_{y=0}$. Turbulent BL profiles result in larger velocity gradients near the wall and thus more wall shear stress.

Transition was first reported by Osborn Reynolds in 1883 using his famous dye-injected pipe flow experiment, but even the most used turbulence models still lack the ability of modelling this process correctly for a number of reasons. First, the fact that transition can be triggered through different mechanisms namely:

I) *Natural transition*, caused by low amplitude perturbations. These flow instabilities (also known as Tollmein-Schlichting waves) exponentially grow into two-dimensional waves and breakdown into turbulent structures (Schlichting and Gersten, 2016).

II) *Bypass transition* is triggered by large disturbances like acoustic waves, surface vibrations and a noisy free-stream. This yields direct vortex breakdown resulting in turbulent structures, the early stages of natural transition are skipped (Morkovin, 1969). This kind of transition is not expected to occur for the 'Arndt' wing.

III) *Separated flow transition* occurs when a laminar BL separates due to a pressure gradient and undergoes natural transition in the separated shear layer which may, or may not, reattach (Walker, 1992). If it reattaches, a Laminar Separation Bubble (LSB) is formed.

Second, a wide range of scales is involved in the transitional process. Momentum and energy transfer is affected by the non-linear interaction between them. By Reynolds averaging the governing equations (as will be described in Section 3.2.2), the ability of the system to capture this non-linear synergy between eddies is eliminated. Methods based on stability equations, e.g. the e^n method by (Van Ingen, 1956) avoid this problem but are hard to incorporate in modern CFD codes, and in principle can only handle natural transition (Drela and Giles, 1987).

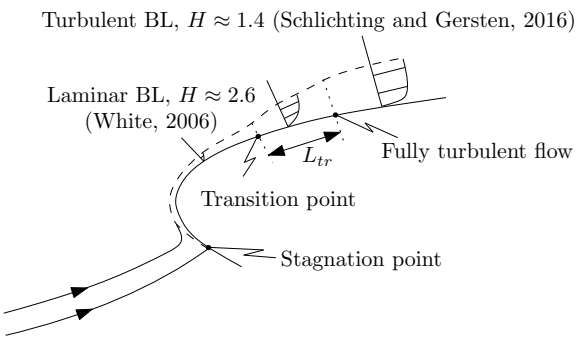

Figure 3.1: Schematic visualisation of transition. BL profiles are also drawn with corresponding shape factors (H).

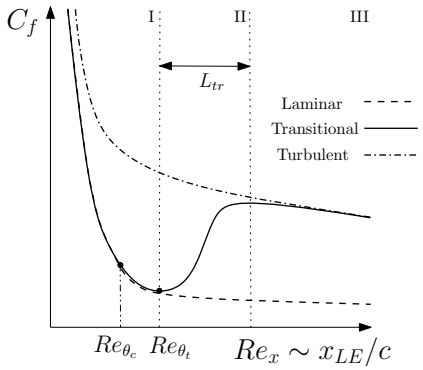

Figure 3.2: Typical skin-friction distributions for laminar, transitional and turbulent flows.

Most of the general assumptions which will be stated in Section 3.2 about turbulence, also hold for transition modelling since the two phenomena are inherently coupled. Furthermore, since the $\gamma - \tilde{R}e_{\theta_t}$ transition model is a supplementary on Reynolds Averaged Navier Stokes (RANS) models, most of the assumptions of a RANS formulation also hold for this model as well.

3.1.2. $\gamma - \tilde{R}e_{\theta_t}$ MODEL

Langtry (2006) first introduced the transition model in his Ph.D. thesis and the final version was published in Langtry and Menter (2009). According to Coder (2017), this was a 'water-shedding moment in CFD transition modelling'. The idea is to solve two additional transport equations to trigger transition locally. Main requirements for the model were: (i) compatible with modern CFD codes (i.e. strictly built on local variables), (ii) the inclusion of the different transition mechanisms, and (iii) not affecting the behaviour of the turbulence model. Both transport equations are discussed below.

INTERMITTENCY TRANSPORT EQUATION

The intermittency (γ) is used to modify the turbulent kinetic energy production (P_k) and destruction (D_k) terms of the Shear Stress Transport (SST) model presented in Section 3.2.2,

$$\tilde{P}_k = \gamma_{eff} P_k; \qquad \tilde{D}_k = \min[\max(\gamma_{eff}, 0.1), 1.0] D_k\,, \tag{3.1}$$

where $\gamma_{eff} = \max(\gamma, \gamma_{sep})$. Here γ_{sep} is a modification to the intermittency for predicting separation induced transition. Using the intermittency to adapt the production and dissipation terms instead of modifying the eddy-viscosity increases the robustness of the model. In this way, γ does not enter the momentum equation directly and therefore does not have to be linearised (which is difficult because of the empirical relations in the source term shown later).

The intermittency equation in this model is an adaptation of the one formulated by Menter et al. (2002) to avoid early transition in the region of the stagnation point and reads,

$$\frac{\partial \gamma}{\partial t} + \frac{\partial \left(u_j \gamma\right)}{\partial x_j} = P_\gamma - E_\gamma + \frac{\partial}{\partial x_j}\left[\left(\nu + \nu_t\right)\frac{\partial \gamma}{\partial x_j}\right]. \tag{3.2}$$

In the freestream, RANS formulations inherently result in a turbulent flow where the intermittency is one. At the start of the BL, $\gamma = 0$ indicates a completely laminar flow. When the BL develops, the intermittency is mainly increased by the production term,

$$P_\gamma = F_{length} c_{a1} |\overline{S}_{ij}| \left[\gamma F_{onset}\right]^{0.5} \left(1 - c_{e1}\gamma\right), \tag{3.3}$$

where c_{a1} and c_{e1} are constants given later, and $|\overline{S}_{ij}| = \sqrt{2\overline{S}_{ij}\overline{S}_{ij}}$ is the magnitude of the strain-rate tensor (where $(\cdot)_{ij}$ stands for the Einstein convention). P_γ acts as a source and is designed to be zero upstream of the transition point and to be activated when the transition starts. This is achieved by the limiter F_{onset}, further elaborated on in Appendix B. The intensity of the production (i.e. controlling the transition length L_{tr} as shown in Figure 3.2) is determined by F_{length} based on an empirical correlation.

The formulation of the relaminariation term (E_γ) is moved to Appendix B. Mathematically the model recognises transition if the local vorticity Reynolds number ($Re_\omega = y^2|\overline{S}_{ij}|/\nu$) exceeds the critical momentum-thickness Reynolds number, Re_{θ_c}. The onset criterion is determined by a second transport equation (for $\tilde{Re}_{\theta_t}$) since $F_{onset} \sim F_{onset2} \sim F_{onset1} \sim Re_{\theta_c} \sim \tilde{Re}_{\theta_t}$. For the definition of these parameters the reader is referred to Appendix B.1.

TRANSPORT EQUATION FOR TRANSITION MOMENTUM THICKNESS

Before discussing the actual transport equation, a clear distinction must be made between the critical Reynolds number $Re_{\theta c}$ and transition Reynolds number $Re_{\theta t}$ as indicated in Figure 3.2. When the critical Reynolds number is reached, intermittency starts to increase in the BL. Turbulence first has to build up before it affects the velocity profile, whereby the point of transition lies further downstream. This is physically plausible since instabilities first have to develop before breaking down. The correlation between the two Reynolds numbers, as well as the relation for the transition length, is determined experimentally. These empirical relations are presented in Appendix B.1.

The transport equation for $\tilde{Re}_{\theta t}$ is shown in Equation (3.4). The rationale behind this transport equation is completely different with respect to intermittency equation. By definition, the transition Reynolds number in the freestream is known and depends on a number of flow conditions like turbulence intensity and pressure gradient, i.e. $Re_{\theta_t} = f(I, \partial p/\partial x_i)$. The quantity Re_{θ_t} is translated into a *local* quantity $\tilde{Re}_{\theta_t}$ in the BL by means of the transport equation,

$$\frac{\partial \tilde{Re}_{\theta t}}{\partial t} + \frac{\partial \left(u_j \tilde{Re}_{\theta t}\right)}{\partial x_j} = P_{\theta t} + \frac{\partial}{\partial x_j}\left[\sigma_{\theta t}\left(\nu + \nu_t\right)\frac{\partial \tilde{Re}_{\theta t}}{\partial x_j}\right]. \tag{3.4}$$

Information from the freestream is passed into the BL by means of the diffusion term. In order to match the local and global variables in the freestream, the production term is employed,

$$P_{\theta t} = \frac{c_{\theta_t}}{J}\left(Re_{\theta t} - \tilde{Re}_{\theta t}\right)\left(1.0 - F_{\theta t}\right), \tag{3.5}$$

where J is discussed in Appendix B, and c_{θ_t} is a constant. The blending factor F_{θ_t} is responsible for deactivating the production inside the BL and activating the term in the freestream. In this blending factor, a function F_{wake} ensures that the blending function is *not* active in the wake regions.

The last missing piece is the value of Re_{θ_t} in the freestream. As indicated earlier, this quantity mainly depends on the turbulence intensity and pressure gradients in the outer flow. Menter et al. (2002) published an empirical relation for this quantity. The one present in this transition model are improvements of the original proposal by Menter and colleagues. The full equations are given in the Appendix B.1.

3.2. TURBULENCE MODELS

Turbulence modelling can generally be dived into two classes, (i) RANS models and (ii) Scale Resolved Simulation(s) (SRS). Several RANS models are introduced first, after that SRS models are discussed. A common approach is to blend the RANS and SRS closures, named hybrid or bridging methods. These type of methods are included in the section concerning SRS.

3.2.1. INTRODUCTION AND ASSUMPTIONS

It is surprising how the underlying mathematics of RANS and SRS diverge significantly while they have the same goal: describing a large range of length and time scales in a flow which are inherently three-dimensional, chaotic, random, and time-dependent (Goldstein et al., 1938). One of the most comprehensive references concerning the fundamentals of turbulent flow (e.g. statistical description, correlations, and turbulent scale motion) are the first seven chapters by Pope (2000).

Most (if not all) models are developed for homogeneous flows, the effect of a liquid-vapour medium is therefore rarely taken into account. The effects of a multiphase flow formulation on the behaviour of turbulent structures are considered to be out of the scope of this research. Despite, it is of major importance to be aware of, and understand them:

- Although the speed of sounds in water $\mathcal{O}(1.5 \times 10^3) m^1 s^{-1}$ and water vapour $\mathcal{O}(3 \times 10^2) m^1 s^{-1}$ easily fulfil the requirement of incompressibility in this application, a mixture does *not*. Several experimental studies showed that the sonic speed in a mixture drops with 2-3 orders of magnitude (Karplus, 1958). For certain values of the vapour fraction the sonic speed can drop down to 20-50$m^1 s^{-1}$ resulting in a maximum Mach number of about 0.5 for this test case.

  This would violate some of the fundamental assumptions in the formulation of incompressible turbulence models. However, the discussion above holds for (very) 'bubbly' flows like cloud cavitation (Brennen, 2005). The vortex cavity for this test case is observed to be a solid structure rather than a region full of heavily dispersed small cavitating structures. This makes it more resistant to the drop in sonic speed (since there are just two individual media separated by an interface), which results in a less compressible medium.

- A clear liquid-vapour interface is present within the vortex. This interface more or less acts like a solid wall in the sense that it blocks the turbulent momentum transfer in the direction perpendicular to the cavity. This results in a BL-like profile near the interface which should in principle be resolved. Furthermore, Celik and Rodi (1988) showed that the hydrodynamic pressure and surface tension at the interface affect the behaviour of eddies. Especially the normal components of the velocity fluctuations and length scales are affected, resulting in anisotropic turbulence.

- The energy spectrum of turbulent flows can be affected by bubble motion, the influence depends on the bubble size and turbulence intensity. Lance and Bataille (1991) published an experimental study using relatively large bubbles in an uniform inflow with turbulence inducing grids upstream of the bubble injection. They concluded that for a vapour volume fraction of 0.025 and 0.04 ($\phi_v = 0.025, 0.04$), the slope in the turbulent spectrum becomes -8/3 (see Section 3.2.3). This implies a larger drain of energy through the turbulence energy cascade. They hypothesised that this is due to energy dissipation in the wake of the bubbles whereby the turbulence intensity decreases. This effect will also be minimised by using validation data with as little nuclei as possible.

- Clustering of bubbles can cause non-homogeneous turbulence. Due to pressure gradients in the flow, the resulting lift and drag forces on the individual bubbles differ. As a result of this, bubbles cluster in certain areas which increases the vapour volume fraction in these regions and thus influences the turbulence *locally*. This also occurs in vortical structures where the bubbles are 'sucked' into the vortex. Mazzitelli et al. (2003) performed Direct Numerical Simulation(s) (DNS) of a Lagrangian (two-way) coupled bubble flow and showed that the bubbles accumulate on the side of the vortex with downward velocity. This effect cannot be assessed in this work due to the enormous computation costs of DNS.

- Assumptions for the different models are elaborated on in the following sections since they are specific for RANS and SRS methods.

3.2.2. REYNOLDS AVERAGED FORMULATIONS

Due to the well-balanced ratio of computational costs and accuracy, RANS formulations are widely used in many engineering applications. In RANS, the effect of the turbulent structures (referred to as eddies from now) is *completely* modelled by either using algebraic constitutive relations in combination with a number of additional transport equations, or by transport equations of the individual Reynolds stresses. Before actually moving towards the models themselves, first the mathematical foundation introduced by Reynolds (1895) is explained.

The flow field is described as a mean quantity $\overline{(\cdot)}_i$ with a fluctuation $(\cdot)'_i$ superimposed,

$$u_i(\vec{x},t) = \overline{u}_i(\vec{x},t) + u'_i(\vec{x},t), \quad p(\vec{x},t) = \overline{p}(\vec{x},t) + p'(\vec{x},t)\,, \tag{3.6}$$

here u_i is any velocity component, p pressure, $\vec{x}$ the vector with spatial coordinates, and t the temporal coordinate. The bars indicate the time averaged value, formally written as $\overline{(\cdot)} = \lim_{T\to\infty} \frac{1}{T}\int_{t_0}^{t_0+T}(\cdot)\mathrm{d}t$. Substituting this into the *incompressible* viscous Navier-Stokes (N-S) equations and applying averaging rules results in,

$$\frac{\partial \overline{u}_i}{\partial x_i} = 0\,, \tag{3.7a}$$

$$\frac{\partial \overline{u}_i}{\partial t} + \overline{u}_j\frac{\partial \overline{u}_i}{\partial x_j} = -\frac{\partial \overline{p}}{\partial x_i} + \nu\frac{\partial^2 \overline{u}_i}{\partial x_j \partial x_j} - \frac{\partial \tau_{ij}}{\partial x_j}\,, \tag{3.7b}$$

where $\tau_{ij} \equiv \overline{u'_i u'_j}$ represents the Reynolds stress tensor. By definition, all averages of fluctuation-included terms vanish except of the one originating from the non-linear convective term (since this is a product of fluctuations) what results in the Reynolds stresses. To close the set of equations, the eddy-viscosity (or Boussinesq) hypothesis is used often (Boussinesq, 1877). In this analogy, the momentum transfer caused by turbulent eddies is modelled by an eddy-viscosity ν_t,

$$\tau_{ij} \equiv \overline{u'_i u'_j} \cong \nu_t\left(2\overline{S}_{ij} - \frac{2}{3}\frac{\partial \overline{u}_k}{\partial x_k}\delta_{ij}\right) - \frac{2}{3}k\delta_{ij} \overset{\text{incomp.}}{=} 2\nu_t\overline{S}_{ij} - \frac{2}{3}k\delta_{ij}\,, \tag{3.8}$$

where $\overline{S}_{ij}$ is the mean strain-rate tensor, k the turbulent kinetic energy and δ_{ij} the Kronecker delta.

This approach is similar to the transfer of momentum caused by molecular diffusion (i.e. friction) which is accounted for by the molecular viscosity ν. The Reynolds stress term reflects the influence of the turbulent scales on the mean stresses. This can easily be understood from the first term on the Right Hand Side (RHS) since the strain-rate tensor $\left(S_{ij} = \frac{1}{2}\left[\frac{\partial u_i}{\partial x_j} + \frac{\partial u_j}{\partial x_i}\right]\right)$ includes all velocity gradients and is multiplied by a kinematic viscosity-like term. The Reynolds stress tensor consists of six additional unknowns (three normal and three shear components) composed of a combination of the velocity fluctuations in all three directions. This is the origin of the problem in the closure of the system of equations, which originates from the non-linear convective term.

Most RANS models aim to model the Reynolds stress. A popular approach is representing turbulent structures in terms of turbulent length (l_0) and time (τ_0) scales, so $\tau_{ij}(\vec{x},t) = f(\overline{u_i}, l_0, \tau_0, \vec{x}, t)$. A vast number of models are formulated in the past, which can generally be classified in: (i) zero-equation models, (ii) one-equation models, (iii) two-equation models, and (iv) Reynolds stress-equation models (Alfonsi, 2009). Zero and one-equation models are not found to be sufficiently accurate for the 'Arndt' wing as stated earlier, so all attention will be paid to the two-equation and Reynolds stress models in the next paragraphs. Most original models are applicable for compressible flows, but for consistency rewritten to incompressible form in this thesis.

Most theories presented in the following paragraphs are based on the book by Wilcox et al. (1998).

$k-\omega$ SHEAR STRESS TRANSPORT

Most two-equation models are based on solving the modelled transport equation for the turbulent kinetic energy $\left(k \equiv \overline{u'_i u'_i}/2\right)$ in combination with either turbulence dissipation rate ($\varepsilon \equiv \nu\overline{\frac{\partial u'_i}{\partial x_j}\frac{\partial u'_i}{\partial x_j}}$) or specific turbulence dissipation rate ($\omega \equiv \varepsilon/k$). By definition, the turbulence length and time scales can be related to these,

$$l_0 \propto k\sqrt{k}/\varepsilon = \sqrt{k}/\omega, \quad \tau_0 \propto k/\varepsilon = 1/\omega\,. \tag{3.9}$$

Probably the most popular two-equation closure is the proposal by Menter (1994) known as the SST model. This strategy blends the $k-\omega$ and $k-\varepsilon$ models such that their two main advantages are combined: First, ω is

singular at the wall boundaries whereby it requires less empirical damping and is, therefore, more robust and accurate in that region. Second, ε is independent of the freestream. Therefore the $k-\omega$ model is employed in near-wall regions and the $k-\varepsilon$ model in the outer flow regions. The two additional modelled closure equations read,

$$\frac{\partial(k)}{\partial t}+\frac{\partial(\overline{u}_j k)}{\partial x_j}=\tau_{ij}\frac{\partial \overline{u}_i}{\partial x_j}-\beta^*\omega k+\frac{\partial}{\partial x_j}\left[(\nu+\sigma_k\nu_t)\frac{\partial k}{\partial x_j}\right], \tag{3.10a}$$

$$\frac{\partial(\omega)}{\partial t}+\frac{\partial(\overline{u}_j \omega)}{\partial x_j}=\frac{\gamma}{\nu_t}\tau_{ij}\frac{\partial \overline{u}_i}{\partial x_j}-\beta\omega^2+\frac{\partial}{\partial x_j}\left[(\nu+\sigma_\omega\nu_t)\frac{\partial \omega}{\partial x_j}\right]+2(1-F_1)\frac{\sigma_{\omega 2}}{\omega}\frac{\partial k}{\partial x_j}\frac{\partial \omega}{\partial x_j}. \tag{3.10b}$$

All the variables are named earlier; all coefficients can be determined as, $\Phi=\Phi_1 F_1=\Phi_2(1.0-F_1)$, where Φ_1 and Φ_2 are the coefficients presented in Table 3.1. The so called cross-diffusion term, the last term in the ω transport equation, allows the model to alter between a $k-\omega$ and $k-\varepsilon$ type by means of the blending function F_1,

$$F_1=\tanh\left[\min\left\{\max\left(\frac{\sqrt{k}}{\beta^*\omega d},\frac{500\nu}{d^2\omega}\right),\frac{4\rho\sigma_{\omega 2}k}{\max\left(2\rho\sigma_{\omega 2}\frac{1}{\omega}\frac{\partial k}{\partial x_j}\frac{\partial \omega}{\partial x_j},10^{-10}\right)d^2}\right\}^4\right], \tag{3.11}$$

with d being the distance to the closest wall.

Table 3.1: Coefficients of the SST turbulence model.

a_1	γ_1	γ_2	β_1	β_2	β^*	σ_{k_1}	σ_{k_2}	σ_{ω_1}	σ_{ω_2}
0.310	5/9	0.440	0.075	0.0828	0.090	0.850	1.000	0.500	0.856

In this work, the version proposed by Menter et al. (2003b) is used. In this formulation, the turbulence shear stresses are limited in the BL to bound the production of turbulence in regions of an adverse pressure gradient. This is incorporated by the definition of the eddy-viscosity,

$$\nu_t=\frac{a_1 k}{\max(a_1\omega,\sqrt{2\overline{S}_{ij}\overline{S}_{ij}}F_2)},\quad \text{with}\quad F_2=\tanh\left(\max\left\{\frac{2\sqrt{k}}{\beta^*\omega d},\frac{500\nu}{d^2\omega}\right\}^2\right), \tag{3.12}$$

here the second blending function F_2 can be recognised. Another adaptation is the change of the production term in the turbulent kinetic energy equation to account for overprediction of turbulence due to the high gradients in the vicinity of the stagnation point,

$$P_k=\min\left(\nu_t\tau_{ij}\frac{\partial \overline{u}_i}{\partial x_j},10\beta^* k\omega\right). \tag{3.13}$$

KSKL MODEL

Although the k equation can be derived with relatively few assumptions as shown for the SST model, and is mainly dependent on the large energy containing eddies in the flow, transport equations for ω and ε are highly dependent on the behaviour of the small eddies. They thereby require numerous assumptions and can hardly be tackled by a term-by-term modelling approach, so that often dimensionality arguments are used instead (Launder and Spalding, 1972).

One of the few exceptions is the approach by Rotta (1951). He proposed a transport equation dependent on the turbulent length scale, L. Higher order derivatives are included in the source term of this equation. Physically this is plausible since it can be argued that the size of (turbulent) eddies cannot only be proportional to the first velocity derivatives but requires more information. The transport equation is based on the turbulent kinetic energy and length scale defined (in y-dominated shear flows, where y is defined as the coordinate perpendicular to the freestream) as,

$$kL=\frac{3}{16}\int_{-\infty}^{\infty}R_{ii}(\vec{x},s_y)ds_y,\quad \text{with}\quad R_{ii}=\overline{\overline{u}_i(\vec{x})\overline{u}_i(\vec{x}+s_y)}, \tag{3.14}$$

where R_{ii} introduces the two-point correlation tensor which can be interpreted as a kind of measure for eddy size, and s_y the distance between the two points. This allows to perform a term-by-term modelling approach as further elaborated on in Appendix B.2. Rotta (1951) analysed homogenous turbulence causing the second velocity derivatives to vanish since the product of the symmetric R_{12} and anti-symmetric s_y terms is integrated (integral of a symmetric times an anti-symmetric term is by definition zero). Mathematically, $\partial^2\overline{u}(\vec{x})/\partial y^2 \int_{-\infty}^{\infty} R_{12} s_y ds_y = 0$. This leaves $\partial^3\overline{u}/\partial^3 y$ as the leading in the production term. However, this is hardly ever implemented in modern CFD codes because (i) there is no physical argument why the length scale should be determined by a third derivative rather than a second, and (ii) it is a tedious variable to determine in most codes. Due to the omission of this derivative, the main distinction of the model compared to other two-equation models is lost.

Menter and Egorov (2006) revised the model and made some interesting remarks. Based on their findings, they reformulated the model into the $k-\sqrt{k}L$ (KSKL) model and termed it Scale Adaptive Simulation(s) (SAS). The KSKL model solves a transport equation for $\sqrt{k}L$ instead of kL (as originally proposed by Rotta (1951)). Theoretically, it is a full RANS method, it allows however to capture part of the turbulent spectrum according to the theory. Menter and his group do not agree with Rotta's argument to cancel the second derivative of the velocity. The assumption of homogeneous turbulence would require the second derivative to be zero anyway, which yields Rotta's argument to be too restrictive. By its nature, the term is thus inhomogeneous and has to be evaluated for non-homogeneous flows. Mathematically, varying length scales in the flow yield R_{12} to become anti-symmetric and therefore the previously mentioned integral to become non-zero. This can be interpreted as illustrated in Figure 3.3. In constant shear conditions, i.e. homogeneous flow, the turnover frequencies of eddies are spatially independent and are therefore able to merge into one. Eddies will grow to an infinite size which yields the spatial correlation and thus the entire second derivative term to be zero. In a non-homogeneous flow, the turnover frequencies differ as shown. As a result, a velocity difference exists at the interface of two eddies whereby they cannot merge but move around each other. In other words, correlations remain whereby $\int_{-\infty}^{\infty} R_{12} s_y ds_y \neq 0$.

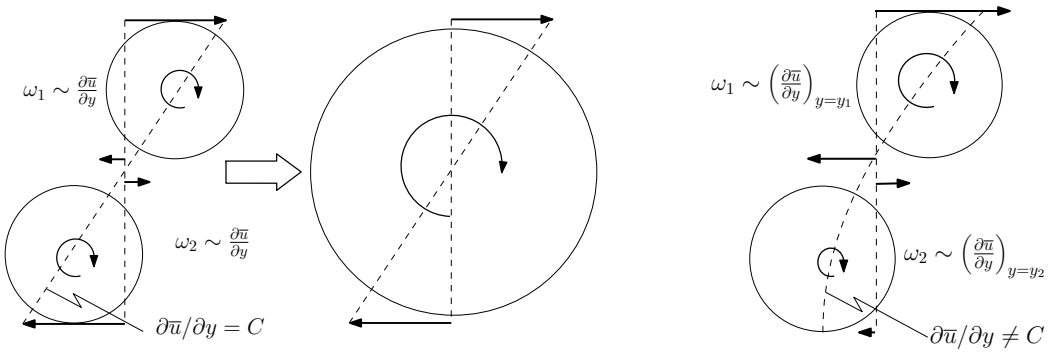

Figure 3.3: Behaviour of eddies in homogeneous (left), and non-homogeneous (right) turbulence. Idea of illustration stems from Menter et al. (2003a). Arrows indicate directions and magnitudes of the velocity vector.

Menter et al. (2006) proposed to model this term in a similar way as Rotta did for the third derivative. However, they included the ratio of the turbulent and Von Kármán length scale (L_{vK}/L) which is a non-dimensional indication for non-homogeneity. The modelled term reads,

$$\int_{-\infty}^{\infty} R_{12} s_y ds_y = c_{2,skL} \nu_t L \left(\frac{L}{L_{vK}}\right)^2, \tag{3.15}$$

where $c_{2,skl}$ is a constant shown in Table 3.2. In homogeneous shear flows, the ratio of L/L_{vK} tends to zero which yields the entire term to vanish (i.e. exactly what is desired). All other terms are modelled like Rotta (1951) did as presented in Appendix B.2.1. The final transport equations read,

$$\frac{\partial k}{\partial t} + \overline{u}_j \frac{\partial k}{\partial x_j} = P_k - c_\mu^{3/4} \frac{k^{3/2}}{L} + \frac{\partial}{\partial x_j}\left(\frac{\nu_t}{\sigma_k}\frac{\partial k}{\partial x_j}\right), \quad \text{with} \quad \nu_t = c_\mu^{1/4}\frac{kL}{\sqrt{k}}, \tag{3.16a}$$

$$\frac{\partial(\sqrt{k}L)}{\partial t} + \overline{u}_j \frac{\partial(\sqrt{k}L)}{\partial x_j} = \frac{\sqrt{k}L}{k}\nu_t |\overline{S}_{ij}| \left(c_{kL,1} - c_{2,kskl}\left(\frac{L}{L_{vk}}\right)^2\right) - c_{kskl,3} k + \frac{\partial}{\partial x_j}\left[\frac{\nu_t}{\sigma_{kskl}}\frac{\partial(\sqrt{k}L)}{\partial x_j}\right]. \tag{3.16b}$$

The main advantage of the model compared to other two-equation models is its behaviour in unsteady simulations. Classical eddy-viscosity models applied in time-dependent simulation often result in (unphysical) single-mode vortex shedding, see e.g. Bosch and Rodi (1998). This was long believed to be a consequence of Reynolds averaging but Menter et al. (2006) proved that the turbulence closure is responsible for this instead. The ability of the Von Kármán length scale to dynamically adjust itself to turbulent flow structures yields the model to have a kind of SRS behaviour. The important difference is that SAS should achieve SRS characteristics without explicitly depending on the grid resolution (Δ_c).

Table 3.2: Coefficients of the KSKL turbulence model.

$c_{kskl,1}$	$c_{kskl,2}$	$c_{kskl,3}$	c_μ	σ_k	σ_{kskl}
0.8	1.47	0.0288	0.09	2/3	2/3

The model has extensively been tested by its developer on i.a. separated and attached airfoil flows, but more interesting is its application on the decay of Homogenous Isotropic Turbulence (HIT) which is often used to calibrate classical SRS models. It is observed that the KSKL model allows a turbulent spectrum to build up, however, it does not provide enough damping at the (dissipative) high wave numbers. Menter et al. (2006) argued that this is not surprising since the Von Kármán length scale adapts to the smallest scales and therefore produces an eddy-viscosity high enough to allow for the formation of even smaller ones. This goes on until the grid resolution is met, but the KSKL equations do not have any information concerning a cut-off frequency. This yields energy to accumulate at the smallest resolved scales. So, although the grid spacing is not explicitly incorporated in the equations, it does enter implicitly. An example of a further validation study performed by independent authors is Zheng et al. (2016) who concluded that the mean flow features and normal Reynolds stresses predicted by the KSKL model agree well with Detached Eddy Simulation(s) (DES) results. However, the time-averaged Reynolds shear stresses are higher in magnitude which causes a larger turbulent kinetic energy. For this reason it is questionable whether KSKL improves the results within the for the 'Arndt' wing, this will be determined in Chapter 7.

EXPLICIT ALGEBRAIC REYNOLDS STRESS MODEL

Both the SST and KSKL closures are based on the Boussinesq hypothesis and therefore a linear relation between the unresolved Reynolds stress and the mean strain-rate tensor ($\overline{u_i' u_j'} \sim \overline{S}_{ij}$) exists. However, this assumption is typically too restrictive in free turbulent shear flows like vortices since it removes any dependence on the anti-symmetric (rotational) part of the mean velocity gradient tensor (Green, 2012). To surpass this, Chou (1945) proposed a more general class of turbulence models known as the Reynolds Stress Model(s) (RSM). In this approach, a transport equation for each of the components of the Reynolds stress tensor is solved whereby the model is able to account for correlations and directional effects in the flow and thus anisotropic turbulence. Although this approach is promising for the considered test case (Pereira and Vaz, 2018), it is not yet been implemented in the current release of ReFRESCO.

An interesting subset of this kind of models are the Algebraic Reynold Stress Model(s) (ARSM). Instead of solving all individual equations, a modelled Reynolds stress transport equation is derived by Rodi (1976). He expressed the 'advection minus the diffusion of the individual Reynolds stresses as the product of the corresponding quantity for the kinetic energy, k and the individual Reynolds stresses normalised by k'. For details, one is referred to the previous reference. In principle, the model implicitly calculates the (local) Reynolds stresses using k, ω and the mean velocity gradients. Hence, the Reynolds stress anisotropy tensor (a_{ij}) can be included in Equation (3.8), this yields the following *non-linear* constitutive relation,

$$\tau_{ij} = 2\nu_t \overline{S}_{ij} - \frac{2}{3} k \delta_{ij} - a_{ij} k \,. \tag{3.17}$$

Not only the normal components of the Reynolds stress tensor (which are included in $k \sim \overline{u_i' u_i'}$) are subtracted from the strain-rate tensor but also the shear components $\overline{u_i' u_j'}$ which are modelled by means of a_{ij}.

The implicit dependency of a_{ij} on the local flow variables is found to be numerically cumbersome in most applications. For this reason, Wallin and Johansson (2000) developed a method to determine the Reynolds stress anisotropy tensor explicitly, named the Explicit Algebraic Reynolds Stress Model(s) (EARSM). They expressed the

anisotropy tensor using a tensor polynomial,

$$a_{ij} = \beta_3(\overline{\Omega}^*_{ik}\overline{\Omega}^*_{kj} - II_{\overline{\Omega}}\delta_{ij}/3) + \beta_4\left(\overline{S}^*_{ik}\overline{\Omega}^*_{kj} - \overline{\Omega}^*_{ik}\overline{S}^*_{kj}\right) + \beta_6(\overline{S}^*_{ik}\overline{\Omega}^*_{kl}\overline{\Omega}^*_{lj} + \overline{\Omega}^*_{ik}\overline{\Omega}^*_{kl}\overline{S}^*_{lj} - II_{\overline{\Omega}}\overline{S}^*_{ij} - 2II_{\overline{S}\,\overline{\Omega}}\delta_{ij}/3) + \beta_9(\overline{\Omega}^*_{ik}\overline{S}^*_{kl}\overline{\Omega}^*_{lm}\overline{\Omega}^*_{mj} - \overline{\Omega}^*_{ik}\overline{\Omega}^*_{kl}\overline{S}^*_{lm}\overline{\Omega}^*_{mj}), \quad (3.18)$$

here the mean strain-rate and vorticity tensors are included in non-dimensional form. In the model, non-dimensionalisation of these quantities is accomplished by using a (empirically) scaled version of the specific dissipation rate (τ),

$$\overline{S}^*_{ij} = \frac{\tau}{2}\left(\frac{\partial u_i}{\partial x_j} + \frac{\partial u_j}{\partial x_i}\right), \quad \overline{\Omega}^*_{ij} = \frac{\tau}{2}\left(\frac{\partial u_i}{\partial x_j} - \frac{\partial u_j}{\partial x_i}\right). \text{ Where } \tau = \frac{1}{\beta^*}\omega. \quad (3.19)$$

The definition for all β-coefficients can be found in Appendix B.2.2. These coefficients are a function of the three independent invariants of the mean strain-rate and vorticity tensors ($\overline{S}_{ij}$ and $\overline{\Omega}_{ij}$ respectively),

$$II_{\overline{\Omega}} = \overline{\Omega}^*_{kl}\overline{\Omega}^*_{lk}, \quad II_{\overline{S}\,\overline{\Omega}} = \overline{S}^*_{kl}\overline{\Omega}^*_{lm}\overline{\Omega}^*_{mk}, \quad II_{\overline{S}} = \overline{S}^*_{kl}\overline{S}^*_{lk}. \quad (3.20)$$

Furthermore, the eddy viscosity is computed from,

$$\nu_t = \frac{C_\mu}{\beta^*}\frac{k}{\omega}, \text{ with } C_\mu = -\frac{1}{2}(\beta_1 + II_{\overline{\Omega}}\beta_6). \quad (3.21)$$

Besides the original proposal, other proposals for tuning the model constants have been published by Dol et al. (2002), Hellsten (2005), and Menter et al. (2012). For the 'Arndt' wing, the proposal by Hellsten (2005) is expected to be best since tuning was done for aerodynamic high-lift devices. They applied the explicit formulation on the SST model and calibrated the result using free shear-, mixing- and boundary layers. The authors claim that the resulting model behaves quite much like the original model of Wallin and Johansson (2000) in simple shear flows, but it has better potential to predict the effects of swirl, rotation and streamline curvature. This promise would therefore be ideal for this test case.

3.2.3. SCALE RESOLVING SIMULATIONS

Numerically solving the N-S equations for a turbulent flow requires resolving a wide range of coherent structures. One could see these as vortical structures in the flow which break down into smaller and smaller structures forming the turbulence energy cascade (large eddies break down into smaller high frequent structures and finally dissipate). The largest eddies in the flow (with a low frequency f and high wavenumber ξ) are of the same length scale as the characteristic length of the problem, say the root-chord for a wing. The smallest eddies are called the Kolmogorov scales with characteristic length, time, and velocity of $(\nu^3/\varepsilon)^{1/4}$, $(\nu/\varepsilon)^{1/2}$, and $(\nu\varepsilon)^{1/4}$ respectively (Pope, 2000).

In RANS *none* of the scales is resolved, while DNS solves the equations using a grid which is sufficiently fine to resolve the entire spectrum. This makes DNS too expensive for flows with industrial applications. SRS aim to resolve part of the spectrum in order to find a balance between accuracy and computational costs. SRS can be divided into two classes namely, bridging methods like Partially-Averaged Navier Stokes (PANS) and hybrid methods like DES and Extra-Large Eddy Simulations.

This work focusses on hybrid methods since they are shown to be promising for the 'Arndt' wing (Paskin, 2018). Hybrid methods apply RANS and Large Eddy Simulation(s) (LES) in a zonal matter. The LES framework works as follows: by means of low-pass filtering (which acts like a spatial filter instead of temporal filter like in RANS) the N-S equations, the scales are separated into a filtered/resolved $\langle\xi\rangle$ part and a modelled/unresolved ξ^* part,

$$\xi = \langle\xi\rangle + \xi^*. \quad (3.22)$$

The details of the averaging process can be found in e.g. Germano (1992). In summary, the filtering should be (i) constant conserving $\langle\xi\rangle = \xi$, (ii) linear $\langle\xi_i + \xi_j\rangle = \langle\xi_i\rangle + \langle\xi_j\rangle$, and (iii) commutative with derivatives $\overline{\frac{\partial\xi}{\partial x_i}} = \frac{\partial\overline{\xi}}{\partial x_i}$. Ideally, commutation errors would not exists however this is hardly achieved, see the discussion by Geurts and Holm (2006).

The filtered system of equations and Reynolds stress tensor is identical to the the RANS formulation, shown in

Equation (3.7) and Equation (3.8) respectively. However, instead of a temporal filter ($\bar{\cdot}$), a spatial filter ($\langle\cdot\rangle$) applies to all variables. The Reynolds tensor accounts for the effect of the unresolved (and thus modelled) scales on the resolved velocity field. It aims to drain energy from the largest scales to mimic the dissipation of turbulent kinetic energy by the smallest (unresolved) scales.

In the LES framework, the spatial resolution is incorporated in the momentum equations by means of the eddy-viscosity. One of the most popular approaches to model the eddy-viscosity is proposed by Smagorinsky (1963),

$$\nu_t = (C_s \Delta_c)^2 |\langle S_{ij} \rangle| , \tag{3.23}$$

where C_s is the Smagorinsky model constant, $|\langle S_{ij} \rangle| = \sqrt{2\langle S_{ij} \rangle \langle S_{ij} \rangle}$ the magnitude of the filtered strain-rate tensor, and $\Delta_c = \max(\Delta_x, \Delta_y, \Delta_z)$ the maximum edge length of a grid cell. This length determines what range of scales can be resolved ($\xi \leq \xi_c$) and which require modelling ($\xi > \xi_c$). This threshold is called the cut-off wavenumber, ξ_c. To resolve a certain wavenumber, half the wavelength must be captured in a single grid cell and the cut-off wave number is thus defined as $\xi_c \equiv \frac{\pi}{\Delta_c}$ (Nyquist principle). Figure 3.4 shows a typical turbulent energy spectrum. For high Reynolds numbers, Kolmogorov's third hypothesis states that 'the statistics of scales in the turbulent spectrum are universally and uniquely determined by the wave number and energy dissipation'. A dimensional analysis therefore requires, $E(\xi) \sim \varepsilon^{2/3} \xi^{-5/3}$. Plotting this function on log-scale yields the typical 'linear' range as shown.

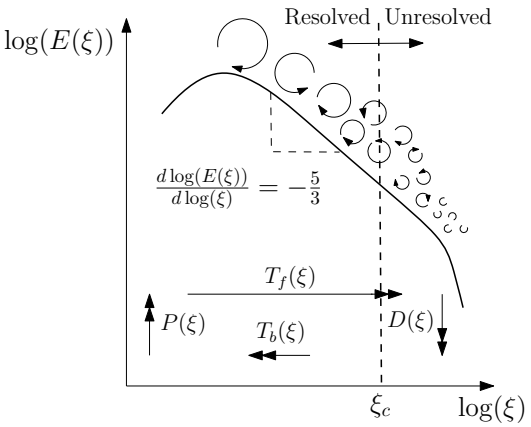

Figure 3.4: Energy spectrum in turbulent flow conditions. Arrows represent the energy cascade.

To model part of the spectrum, it is essential to realise what happens in the energy cascade. The large energy containing length scales (low ξ) obtain their kinetic energy ($P(\xi)$) from the mean flow and the interaction between each other. The larger scales break down into smaller ones and transfer energy ($T_f(\xi)$) to larger wavenumbers. Theoretically, it is possible that some of the small scales merge into larger ones which results in backscatter ($T_b(\xi)$). However, this rate is much smaller than the forward energy cascade (Hickel and Hulshoff, 2017). Most of the dissipation ($D(\xi)$) occurs at the lowest energy containing scales. The main modelling aim in SRS is therefore to provide the correct amount of energy drain at the cut-off wave number.

DETACHED-EDDY SIMULATIONS

In this work, the DES framework is considered which applies RANS (the earlier presented SST model) in the attached BL, and LES in the detached and outer regions. The reason for this choice is that Paskin (2018) concluded that 'velocity profiles indicate that the DES-SST model is the only one to accurately predict the velocity field in the vortex core with negligible modelling errors.'

All forms of DES more or less find their roots in the ideas of Spalart (1997) to couple RANS and LES. This is achieved by adapting the dissipation term of the turbulent kinetic energy equation of the SST model,

$$\frac{\partial(k)}{\partial t} + \frac{\partial(\overline{u}_j k)}{\partial x_j} = \tau_{ij} \frac{\partial \overline{u}_i}{\partial x_j} - \frac{\sqrt{k^3}}{l_t} + \frac{\partial}{\partial x_j} \left[(\nu + \sigma_k \nu_t) \frac{\partial k}{\partial x_j} \right] . \tag{3.24}$$

The introduction of the turbulent length scale, l_t, allows the model to alter between the two frameworks,

$$l_t^{DES} = \tilde{f}_d (l_t^{RANS}, l_t^{LES}) , \tag{3.25}$$

here $\tilde{f}_d$ is a generic auxiliary function, known as the shielding or blending function (Pereira et al., 2018). The RANS length scale is an estimate of the integral length scale ($l_t^{RANS} \sim \sqrt{k}/\omega$) while the LES length scale is the characteristic length of the smallest resolved scales, $l_t^{LES} \sim \Delta_c$.

Coupling, or matching these length scales and thus the RANS and LES regions (done by $\tilde{f}_d$) appears to be the main challenge of the method. This results in Grid Induced Separation (GIS) problems. Spalart et al. (2006) adapted the shielding function to overcome this and named it Delayed Detached-Eddy Simulation(s) (DDES).

This approach was taken one step further by Shur et al. (2008) who improved the wall-modelling capability of DDES by adapting the model such that it also applies LES in the upper part of the BL. Both DDES and Improved Delayed Detached-Eddy Simulation(s) (IDDES) were originally formulated in combination with the Spalart-Allmaras (SA) turbulence model. Gritskevich et al. (2012) revised and recalibrated both models in combination with the SST closure. Feder et al. (2018) compared the two models for a wing tip vortex and concluded that DDES would be preferred. However, they only consider the vortex after 1.5 chords behind the wing tip while this thesis is primarily concerned about the vortex upstream of that position. Furthermore, they applied the vorticity confinement method (Steinhoff et al., 1992) to avoid problems with vortex diffusion. This method 'adds' the diffused energy as a source term in the momentum equations which stabilises the vortex. For these reasons, it is questionable whether Feder's results can be generalised to the 'Arndt' wing. Furthermore, it could be argued that better resolving the BL improves the results in the vortex as well. For these reasons, it is decided that both the DDES and IDDES models should be tested. The differences are discussed shortly in the following paragraphs.

The DDES length scale is determined as,

$$l_t^{DDES} = l_{RANS} - \tilde{f}_d \max(0, l_{RANS} - l_{LES}). \tag{3.26}$$

Here $\tilde{f}_d$ functions as the shielding function: it ranges from 0 to 1 and results in a quick switch from the RANS part of the BL ($\tilde{f}_d = 1.0$) to the LES region ($\tilde{f}_d = 0.0$). Appendix B.2.3 presents the mathematical definitions of l_{RANS} and l_{LES}.

The formulation of the turbulent length scale in the IDDES approach reads,

$$l_t^{IDDES} = \tilde{f}_d(1 + f_e) l_t^{RANS} + (1 - \tilde{f}_d) l_t^{LES}. \tag{3.27}$$

The empirical function f_e aims to prevent the excessive reduction of the Reynolds stresses at the RANS-LES interface. This function is the main difference between DDES and IDDES and should improve the accuracy in the upper part of the BL. Appendix B.2.4 elaborates on further mathematical details of the model.

Grid refinement is only applied within the vortex region and therefore the IDDES model is supposed to apply RANS outside and LES inside the vortex. However, if the grid spacing is increased, i.e. the limit of $\Delta_c \to \infty$, $\tilde{f}_d$ does not yield the turbulent length scale to converge to l_t^{RANS} (Pereira, 2018). In other words, this model does not recover towards a RANS solution in detached and outer regions where the spatial resolution is not sufficient to activate the LES framework. This is not the case for DDES and should be taken into account when comparing the IDDES results outside the vortex to the other turbulence models.

3.3. CAVITATION MODEL

A detailed description of the most important physical processes involved during cavitation, such as inception and the effect of nuclei, was already given in Chapter 2. This section describes the details of the cavitation model used in this thesis.

3.3.1. INTRODUCTION AND ASSUMPTIONS

In reality, inception is triggered by the growth of nuclei in a low-pressure region (Brennen, 2005). To capture this in simulations, the trajectory and size of all nuclei would be required in either a one or two-way coupling way. The nuclei distribution is often unknown (the concentration, however, is often measurable) and calculating all the paths is expensive (the nuclei content of most cavitation tunnels is in the order of 0.1-10 nuclei per cm^3 (Rijsbergen, 2016) and would thus be $1.8 \times 10^4 - 10^6$ nuclei for the considered domain). For these reasons, more basic cavitation models are used in most CFD packages. It is remarkable that in modern engineering, comprehensive models for physical process such as turbulence and transition exist. However, the models concerning cavitation are limited which already shows the complexity of this process.

Most models are based on the idea of solving an additional transport equation for the phase volume fraction for each cell, $\phi_{i_p} = \frac{\mathcal{V}_{i_p}}{\sum_{i_p=1}^{n_p} \mathcal{V}_{i_p}}$. Here $\mathcal{V}_{i_p}$ is the volume for phase i_p, and the sum of ϕ_{i_p} must be 1. To satisfy continuity, the inter-phase mass transfer must be modelled by the cavitation model. This approach of 'separating' the continuity equations by means of the volume fraction is known as the Volume of Fluid (VoF) approach (Hirt and Nichols, 1981). The VoF method introduces a source/sink term in the continuity equation(s) which are therefore not divergence-free any more,

$$\frac{\partial(\phi_{i_p}\rho_{i_p})}{\partial t}+\frac{\partial(\phi_{i_p}\rho_{i_p}u_{j_{ip}})}{\partial x_j}=S_{i_p}\,. \tag{3.28}$$

The goal of the cavitation models is to estimate the source term (S_{i_p}). The density and viscosity of the mixture are defined as,

$$\rho=\sum_{i_p=1}^{n_p}\rho_{i_p}\phi_{i_p} \quad \xrightarrow{\textit{Liquid-vapour mixture}} \quad \rho=\rho_l\phi_l+\rho_v\phi_v\,, \tag{3.29a}$$

$$\mu=\sum_{i_p=1}^{n_p}\mu_{i_p}\phi_{i_p} \quad \xrightarrow{\textit{Liquid-vapour mixture}} \quad \mu=\mu_l\phi_l+\mu_v\phi_v\,. \tag{3.29b}$$

The majority of the models is based on a number of assumptions; the most important ones are listed below.

- The phase(s) are assumed to be homogenous however each cell contains both phases. This does not yield a sharp (it is rather diffused) interface between the liquid and vapour in the simulations. In reality however, a clear interface between the different phases exists, i.e. no intermediate-phases or mixed-states are present. This is a known limitation of the VoF method but no other methods (i.e. the level set method by Sussman et al. (1994)) are available in ReFRESCO yet.
- If a model takes bubble behaviour into account, a uniform bubble distribution is assumed unless specified otherwise. Furthermore, bubble-bubble interactions, as well as bubble coalescence, are neglected.
- As motivated earlier, only *hydrodynamic* inception is considered.
- In most model derivations, bubble surface tension is neglected. Note that for other models, surface tension is implicitly taken into account by the definition of the vapour pressure (see Equation (2.4)).

Cavitation models used in most engineering applications can be classified into two categories, (i) models based on the technique presented by Merkle (1998), and (ii) models based on the theory of Schnerr and Sauer (2001). All these models are found to be quite basic and either depend linearly on the difference between the hydrostatic pressure (p) and vapour pressure (p_v), or depend on $\sqrt{|p_v-p|}$. To show the similarity of the different models, Appendix B.3 provides a comparison of the ones available in ReFRESCO. Within this thesis the model by Schnerr and Sauer (2001) is used since this is by many considered as the most complete (e.g. by Senocak and Shyy (2002) and Morgut (2012)).

3.3.2. SCHNERR AND SAUER MODEL

The model by Schnerr and Sauer (2001) finds it roots in the Rayleigh-Plesset (R-P) equation for bubble dynamics (Plesset, 1949). The idea is to rewrite the VoF formulation for a multi-phase flow in dispersed form as displayed in Figure 3.5. Assuming N_b spherical bubbles, and a liquid vapour mixture, the vapour volume fraction can be written as,

$$\phi_v=\frac{\mathcal{V}_v}{\mathcal{V}_{cell}}=\frac{\frac{4}{3}N_B\pi R_B^3}{\mathcal{V}_v+\mathcal{V}_l}=\frac{\frac{4}{3}n_B\mathcal{V}_l\pi R_B^3}{\frac{4}{3}n_B\mathcal{V}_l\pi R_B^3+\mathcal{V}_l}=\frac{\frac{4}{3}n_B\pi R_B^3}{1+\frac{4}{3}n_B\pi R_B^3}\,, \tag{3.30}$$

where R_B is the bubble radius, and n_B the bubble concentration defined as, $n_B=N_B/\mathcal{V}_l$. Here subscripts l and v indicate liquid and vapour respectively. As a consequence of the expanding/contracting bubbles, the velocity field is not divergence free any more. The non-conservative form of continuity, neglecting the spatial variation of the density within each phase reads,

$$\frac{\partial u_j}{\partial x_j}=-\frac{1}{\rho}\left(\frac{\partial\overline{\rho}}{\partial t}+u_j\cancel{\frac{\partial\overline{\rho}}{\partial x_j}}\right)\approx 0 \approx -\frac{\rho_v-\rho_l}{\phi_v\rho_v+(1-\phi_v)\rho_l}\frac{d\phi_v}{dt}\,. \tag{3.31}$$

The transport equation for the vapour volume fraction for this family of models is present in Equation (3.32). Although the original paper terms the RHS as a production term, calling it a phase changing term would be more appropriate. This is because it can act like a source (when cavitating) but also like a sink (when condensating).

This term represents the number of bubbles per cell times the change in bubble volume. In this form, it guarantees the conservation of the number of bubbles (if a bubble expands, ϕ_v increases, ϕ_l decreases and the number of bubbles in that cell goes down).

$$\frac{\partial \phi_v}{\partial t} + \frac{\partial (\phi_v u_j)}{\partial x_j} = \left(\frac{n_b}{1 + \frac{4}{3} n_b \pi R_B^3} \right) \frac{d}{dt} \left(\frac{4}{3} \pi R_B^3 \right). \tag{3.32}$$

To complete the derivation, the change in bubble radius must be evaluated. To so do, the R-P equation is considered,

$$\frac{d^2 R_B}{dt^2} + \frac{3}{2} \left(\frac{dR_B}{dt} \right)^2 = \frac{p(R_B) - p_\infty}{\rho_l} - \frac{2Q}{\rho_l R_B} - 4 \frac{\nu_l}{R_B} \frac{dR_B}{dt}, \tag{3.33}$$

where Q is the surface tension. The small time scales involved cause the second derivative to vanish. Neglecting viscosity and surface tension yields an estimate for the bubble growth, $dR_B/dt \approx \sqrt{\frac{2}{3} \frac{p(R_B) - p_\infty}{\rho_l}}$. This closes the system, the only parameters which need to be specified are the bubble radius and concentration. According to the developers, this formulation lends itself for unsteady cavities and cloud-like cavitation. Moreover, the R-P equation cannot predict bubble collapse whereby this family of models would be less suitable to capture bubble collapse. However this is irrelevant for this test case since bubble cavitation is not expected to occur. The actual formulation in ReFRESCO is slightly modified compared to the original proposal, as shown in the Appendix B.3.

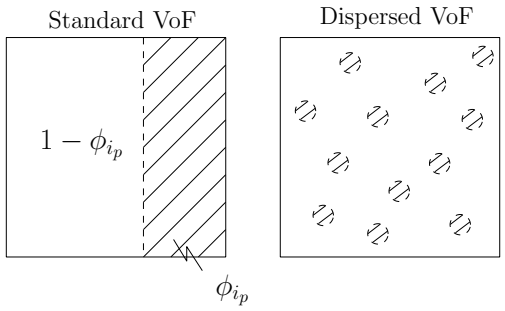

Figure 3.5: Phase distribution in a computational cell for the standard VoF model (left) and dispersed VoF model (right).

3.4. CONCLUSIONS

This chapter elaborated on the three most important modelling aspects in cavitating vortex simulations: (i) transition-, (ii) turbulence-, and (iii) cavitation models. The $\gamma - \tilde{R}e_{\theta_t}$ transition model is by many considered as the most complete model since it is able to capture the three different transition mechanisms, and it is formulated using *local* variables which makes it compatible with modern CFD codes.

It is concluded that cavitating structures can highly influence the turbulent behaviour of the flow by (i) changing the speed of sound, (ii) a BL-like velocity profile near the vapour-liquid interfaces, (iii) turbulent dissipation/production in the wake of the bubbles and (iv) clustering of bubbles which yields anisotropic turbulence. The following turbulence models are found to be promising to consider for the 'Arndt' wing to prevent excessive turbulent diffusion or to capture the anisotropic character of the turbulent structures: First, the SST model because it is the only model which is compatible with the $\gamma - \tilde{R}e_{\theta_t}$ transition model. Second, the KSKL model since (in theory) it should be able to 'resolve' part of the turbulent scales in unsteady simulations. Third, the EARSM since it avoids a linear relation between the eddy-viscosity and the strain-rate. Fourth, DDES because it resolves part of the spectrum within the refined vortex region. Fifth, IDDES since it should increase the accuracy in the BL with reference to DDES.

Cavitation models are found to be very basic. They are either based on the R-P equation or the equation of state. The former yields the source terms to be dependent on $\sqrt{|p - p_v|}$, the latter results in a linear dependency. They only take pressure into account while cavitation inception also depends on i.a. the amount of nuclei, surface tension, water quality, and surface roughness. The Schnerr-Sauer cavitation model is found to be the most comprehensive and mostly used model in literature and will therefore be used in this thesis.

4

NUMERICAL IMPLEMENTATION AND SET-UP

This chapter aims to highlight the, for this study, most important aspects of the Computational Fluid Dynamics (CFD) code as well as presenting the computational set-up. The first section gives a short introduction to ReFRESCO and identifies the most important assumptions. The subsequent sections zoom in on relevant subjects like numerical discretisation and the solution procedures. These sections aim to clarify all the input choices made during the simulations which will be presented in the Chapter 6, 7 and 8. The last section presents the development of the computational grids used in this thesis.

4.1. INTRODUCTION TO REFRESCO

ReFRESCO is community based open-usage/open-source CFD code that solves the viscous multiphase (un)steady incompressible Navier-Stokes (N-S) equations. The code originates from 2005 and was a collaboration between Maritime Research Institute Netherlands (MARIN), Technische Universität Hamburg-Harburg, and Hamburgische Schiffbau-Versuchsanstalt. The original name of the code was FreSCO (Free Surface COde) which separated into FreSCO$^+$ and ReFRESCO in 2009. Currently, ReFRESCO is being developed at MARIN in collaboration with i.a. Instituto Superior Técnico (Lisbon), Delft University of Technology, USP-TPN (São Paulo), University of Twente and Chalmers University (Göteborg). ReFRESCO resembles a generally applicable CFD package in several aspects, but it is optimised, verified and validated for maritime applications in particular. Further information can be found on the community website (ReFRESCO, 2017).

Originally, ReFRESCO was a full Reynolds Averaged Navier Stokes (RANS) solver. This was expanded by i.a. Pereira (2018) with more comprehensive turbulence models as presented in the Chapter 3. ReFRESCO describes a multiphase flow by means of a Volume of Fluid (VoF) approach. The equations are discretised using a finite-volumes with cell-centred (i.e. staggered) collocated variables in strong-conservation form (Section 4.2 will present this). The equations are linearised using Picard's method and consequently solved by applying a pressure-correction equation based on the SIMPLE algorithm to ensure mass conservation. Section 4.3 briefly touches on this topic.

4.2. NUMERICAL DISCRETISATION

ReFRESCO numerically solves the non-linear N-S equations (as shown in Equation (3.7)), by means of a finite-volume approach with cell-centred (staggered) variables. It thus divides the computational domain into a finite number of control-volumes (called cells from now on), and solves the governing equations in each of them to satisfy the balance of any quantity globally. The most convenient way to write any conservation equation in this context reads,

$$\underbrace{\frac{\partial}{\partial t}\iiint_{\mathcal{V}} \phi \mathrm{d}\mathcal{V}}_{\text{unsteady}} + \underbrace{\iint_{\mathcal{S}} \phi(\vec{U}\cdot\vec{n})\mathrm{d}\mathcal{S}}_{\text{convection}} = \underbrace{\iint_{\mathcal{S}} q\nabla\phi\cdot\vec{n}\mathrm{d}\mathcal{S}}_{\text{diffusion}} + \underbrace{\iiint_{\mathcal{V}} S_\phi \mathrm{d}\mathcal{V}}_{\text{source}}, \tag{4.1}$$

where ϕ represents any flow variable, $\vec{U}$ the velocity vector, S_ϕ any source term, q the diffusivity of ϕ (ν for the momentum equations), $\vec{n}$ the surface normal of the cell face, $\mathcal{V}$ a volume and $\mathcal{S}$ a surface. Note that the diver-

gence theorem is applied for the convective and diffusive terms to write the volume integral as a surface integral. The flow variables are defined in the centre of each cell (ϕ_c), the volume and surface integrals are determines as,

$$\iiint_{\mathcal{V}} \phi \mathrm{d}\mathcal{V} \approx \phi_c \Delta\mathcal{V}\,, \quad \text{and} \quad \iint_{\mathscr{S}} \phi \mathrm{d}\mathscr{S} \approx \sum_{i=1}^{N_f} \phi_{f_i} \mathscr{S}_{f_i}\,, \tag{4.2}$$

where $\Delta\mathcal{V}$ is the cell volume, $\mathscr{S}_{f_i}$ is the surface area of each face, N_f the number of faces per control volume, and ϕ_{f_i} the variable ϕ at each face. The source term can be directly computed by this formulation.

4.2.1. UNSTEADY TERM

The time-dependent term (equal to zero in steady computations) is discretised by means of an implicit three time level (second-order backward, see Süli and Mayers (2003)) approach,

$$\frac{\partial}{\partial t} \iiint_{\mathcal{V}} \phi \mathrm{d}\mathcal{V} = \iiint_{\mathcal{V}} \frac{\partial \phi_c}{\partial t} \mathrm{d}\mathcal{V} \approx \frac{3\phi_c^n - 4\phi_c^{n-1} + \phi_c^{n-2}}{2\Delta t} \Delta\mathcal{V}\,, \tag{4.3}$$

in which n denotes the n^{th} timestep, and Δt the magnitude of each timestep. This is called a three time level method because a parabolic interpolation of the last three timesteps is performed to come up with the above equation.

4.2.2. CONVECTION TERM

The surface integral of the convective term can be written in discretised form as,

$$\iint_{\mathscr{S}} \phi(\vec{U}\cdot\vec{n})\mathrm{d}\mathscr{S} \approx \sum_{i=1}^{N_f} \phi_{f_i} (\vec{U}\cdot\vec{n})_{f_i} \mathscr{S}_{f_i}\,, \tag{4.4}$$

where $\phi_{f_i}(\vec{U}\cdot\vec{n})_{f_i}$ is the flux at each cell face. To determine this flux, the cell centered variables must be related to the variables at the faces. Different types of interpolation methods are available in ReFRESCO. In all calculations the second-order accurate Quadratic Upstream Interpolation for Convective Kinematics (QUICK) scheme is desired to determine the face quantities, if for any robustness reasons a first-order accurate scheme is required, the First-Order Upwind (FOU) scheme is used.

QUICK SCHEME

Consider a cell with centre C, a neighbour cell to the west with centre W and face w, a neighbour cell to the east with centre E and face e, and the east neighbour of cell E with centre EE and face ee. The QUICK scheme determines the east face value (ϕ_e) using a parabolic expression. The third point used in the expression depends on whether the flow enters ($(\vec{U}\cdot\vec{n})_e > 0$) or leaves ($(\vec{U}\cdot\vec{n})_e < 0$) the cell,

$$\phi_e = \begin{cases} \phi_P + \frac{(x_e - x_P)(x_e - x_W)}{(x_E - x_P)(x_E - x_W)}(\phi_E - \phi_P) + \frac{(x_e - x_P)(x_E - x_e)}{(x_P - x_W)(x_E - x_W)}(\phi_P - \phi_W), & \text{if} \quad (\vec{U}\cdot\vec{n})_e > 0\,; \\ \phi_E + \frac{(x_e - x_E)(x_e - x_{EE})}{(x_P - x_E)(x_P - x_{EE})}(\phi_P - \phi_E) + \frac{(x_e - x_E)(x_P - x_e)}{(x_E - x_{EE})(x_P - x_{EE})}(\phi_E - \phi_{EE}), & \text{if} \quad (\vec{U}\cdot\vec{n})_e < 0\,. \end{cases} \tag{4.5}$$

This method is third-order accurate for the face value, however only a second-order approximation for the entire cell (Waterson and Deconinck, 2007). The exact formulation implemented in ReFRESCO also stems from this reference.

FOU SCHEME

A more robust but less accurate scheme, is the first-order accurate FOU approach. The value at each face is directly linked to either of the bounded cells, again depending on the direction of the inflow,

$$\phi_e = \begin{cases} \phi_E, & \text{if} \quad (\vec{U}\cdot\vec{n})_e > 0\,; \\ \phi_P, & \text{if} \quad (\vec{U}\cdot\vec{n})_e < 0\,. \end{cases} \tag{4.6}$$

4.2.3. DIFFUSION TERM

Like the convective term, the surface integral of the diffusive term can also be expressed in a discrete form,

$$\iint_{\mathscr{S}} q\nabla\phi\cdot\vec{n}\mathrm{d}\mathscr{S} \approx \sum_{i=1}^{N_f} q_{f_i}(\nabla\phi\cdot\vec{n})_{f_i}\mathscr{S}_{f_i}\,. \tag{4.7}$$

In ReFRESCO, the gradients of all variables ($\nabla\phi$) are determined according to Green-Gauss' theorem (Sozer et al., 2014) which is second-order accurate. To interpolate the gradients calculated in the cell centres to the cell faces, the Central Differencing Scheme (CDS) is used which make the discretisation of the diffusion term second-order accurate.

CDS SCHEME

Central differencing comes down to assuming that the value at the face is the average of the two bounded cells. Mathematically this can be written as,

$$\phi_e = \frac{\phi_P + \phi_E}{2}\,, \tag{4.8}$$

which can be proven to be second-order accurate (Waterson and Deconinck, 2007).

4.3. SOLUTION PROCEDURE

ReFRESCO solves the system of equations through a segregated solution procedure. This means that all equations are solved separately (and sequentially) assuming that the other variables are known. An iterative solution procedure is used to solve every transport equation (inner loop), this new variable is then used to solve the next equation (first momentum in combination with continuity is solved, then additional equations such as turbulence, transition, and cavitation). All equations are coupled in each outer loop. Convergence of both the inner and outer loops is checked by either a convergence criterion (a particular norm of the residual vector of each equation) or the solver progresses if a specified maximum number of iterations is reached. To ensure mass conservation in each outer loop, ReFRESCO employees the Semi-Implicit Method for Pressure Linked Equations (SIMPLE) algorithm (Patankar and Spalding, 1983). If the computation is unsteady, a time loop is active which updates the time after every convergenced outer loop. Time is updated by a user specified timestep and for a user defined number of timesteps.

Figure 4.1 visualises this process schematically. The following sections discuss the most important parts of the solution procedure. The reader is referred to Ferziger and Peric (2012) for a detailed description of the numerical methods. The actual implementation of the algorithms in the code can be found in ReFRESCO (2017).

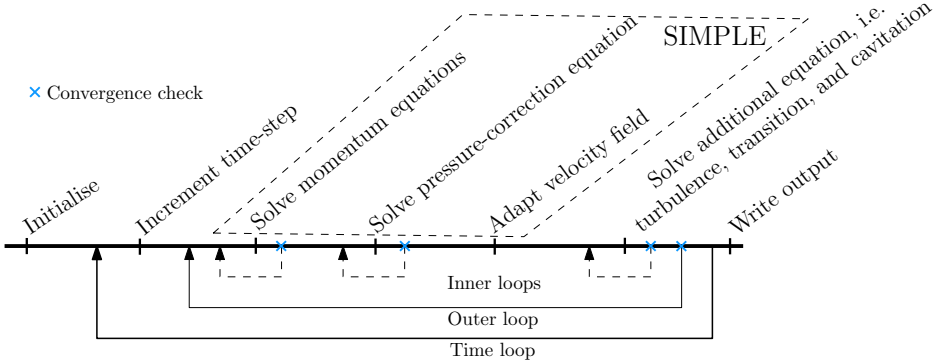

Figure 4.1: Schematic illustration of segregated solver, figure also indicates inner, outer and time loops.

4.3.1. ITERATIVE SOLVERS

For every equation, a linear system of equations ($A\vec{\phi} = \vec{b}$) must be solved. Here A is the coefficient matrix with size $N_c \times N_c$. Directly inverting this matrix would computationally be too expensive since the matrix size will be

be proportional to the number of grids cells. For this reason, iterative methods are developed. In this thesis, the Generalized Minimal Residual (GMRES) and Conjugate Gradient (CG) methods are used. Both methods are Krylov subspace methods. The GMRES method was used since this method is known to be one of the most efficient approaches to solve a large linear system (Vuik and Lahaye, 2015). The GMRES method for the pressure equation was changed to the CG method since this equations was harder to converge and CG was found to be more robust.

For both solution procedures, a Jacobi preconditioner is used to increase computational efficiency. This choice was based on advice in ReFRESCO (2017). 'The term preconditioning refers to replacing the linear system to solve by another one that it easier to solve while keeping the same solution' (Vuik and Lahaye, 2015). I.e. the preconditioner (P) modifies the system as $AP^{-1}\vec{\varphi} = \vec{b}$, $\vec{\phi} = P^{-1}\vec{\varphi}$.

Convergence of each inner and outer loop is checked by means of the maximum of the residual (i.e. the infinity norm, L_∞) vector of each equation. The residual in each cell (R_i) for any variable ϕ is defined as,

$$R_i = A_{ij}\phi_i - b_i\,, \tag{4.9}$$

where A_{ij} contains all coefficients of the linear system, and b_i the Right Hand Side (RHS) of the equations. Normalisation of the residuals is done by means of the diagonal of the coefficient matrix to ensure that the residual in every cell is normalised by the actual value of the same variable in that cell (Pereira and Vaz, 2018). Equation (4.10) describes this mathematically. The normalised residual ($\hat{R}_i$) is still dimension-full though, the code uses a user-specified reference value ϕ_{ref} to determine the non-dimensional normalised residual $\hat{R}^*_i$,

$$\hat{R}_i = \frac{A_{ij}\phi_i - b_i}{A_{ii}}\,, \quad \text{and} \quad \hat{R}^*_i = \frac{1}{\phi_{ref}}\frac{A_{ij}\phi_i - b_i}{A_{ii}}\,. \tag{4.10}$$

In this thesis, convergence is checked by means of the infinity norm of the normalised residual vectors of all transport variables. The actual convergence criteria are problem dependent and are given in every results chapter (Chapters 6, 7, and 8).

4.3.2. MASS-MOMENTUM COUPLING

In the segregated approach, the mass and momentum equations are solved separately. The problem is also considered to be incompressible, therefore there is no direct coupling between the pressure and the density of the fluid. Mass-conservation is ensured by means of a pressure correction using the SIMPLE algorithm (Patankar and Spalding, 1983). In this algorithm, the velocities (u^*_i) are first estimated by solving all momentum equations (all other variables from the previous iteration are used). Picard's method $(\phi^2)^{t+1} \approx \phi^t\phi^{t+1}$ is employed to linearise the convective terms to be able to solve the momentum equations (Ortega and Rheinboldt, 1970). Next, u^*_i, which does not satisfy continuity yet, is coupled to the pressure using a pressure correction method. The SIMPLE algorithm uses the divergence of the momentum equations to acquire this coupling. The new pressure field is subsequently used to update the velocity field such that it ensures mass-conservation.

4.3.3. RELAXATION PROCEDURES

An iterative process is required to account for the Picard's linearisation. This is achieved by means of the outer loops. In each outer loop, first the mass-momentum coupling is performed. The resulting velocity and pressure (which are computed using the turbulence, transition, and cavitation quantities of the previous iteration) are then used to determine the new turbulence, transition , and cavitation quantities. This procedure is repeated until the solution is converged.

To increase stability of CFD computations, relaxation factors are often implemented (Ferziger and Peric, 2012). After each outer loop, all variables need to be updated. To ensure that the differences between subsequent iterations do not become too large and cause numerical instabilities, explicit relaxation is utilised,

$$\phi^n = \phi^{n-1} + \kappa((\phi^n)^* - \phi^{n-1})\,, \tag{4.11}$$

where ϕ can be any variable, ϕ^{n-1} is the solution of the previous iteration, $(\phi^n)^*$ the solution of the outer loop, ϕ^n the variable of the outer loop after relaxation is applied, and κ the explicit relaxation factor. In other words, the updated variable is a weighted average of the new and old values. Setting κ is thus a trade-off between computational efficiency and stability. Increasing κ decreases the required time to converge, however increases the

chance of diverging.

A second robustness factor is used in the form of implicit relaxation. The idea behind implicit relaxation is to increase the diagonal dominance of the linear system, which makes it easier to solve. Note that this is supplementary and does not replace explicit relaxation. Explicit relaxation is applied between all outer loops. Implicit relaxation however, is only applied at the first N_{imp} outer loops in this thesis as advised in section 5.4.3. of Ferziger and Peric (2012).

4.3.4. TIMESTEPPING

After each converged outer loop, the physical time is updated by Δt. For steady calculations this parameter goes towards infinity which yields all unsteady terms to be zero, i.e. $\lim_{\Delta t \to \infty} \Delta\phi/\Delta t = 0$, and therefore one does not have to advance in time. For unsteady simulations, this is not the case, and the non-linear systems must be solved every timestep. The choice of the timestep is based on the Courant-Friedrichs-Lewy (CFL) number.

ReFRESCO only features implicit timestepping schemes, whereby the solver is less sensitive to numerical instabilities and therefore the choice of the CFL number (van Buuren, 1999). The choice of CFL number does, therefore, impact the stability of the calculations less. The definition of this non-dimensional number reads,

$$CFL = \max\left(\frac{u\Delta t}{\Delta x}, \frac{v\Delta t}{\Delta y}, \frac{w\Delta t}{\Delta z}\right), \tag{4.12}$$

and reflects 'how many cell lengths information travels within one timestep' (Anderson Jr, 2010). In this definition $\Delta(\cdot)$ implies the maximum cell size each direction. Ideally, one would like to set the timestep such that the CFL number is below one through the entire domain to avoid any errors due to incorrect propagation of information through the domain. However, this is found not to be feasible for this problem because the cross-flow just above the Boundary Layer (BL) at the tip of wing results in a CFL number which is a factor 15 higher compared to the rest of the domain. The large CFL number is because the near-BL cells have a high Aspect Ratio (AR) and their edge length in spanwise direction is therefore small. The small edge length in combination with the cross-flow components, which is in the order of 10% of the freestream velocity, drives up the CFL number.

The actual timestep is chosen such that the CFL number is smaller than one in regions where Scale Resolved Simulation(s) (SRS) is applied to resolve the time fluctuations of the flow quantities. This choice is made since RANS is applied near the tip for all simulations. RANS solves for time-averaged equations whereby the CFL number is less important and the higher CFL number in that region is therefore not expected to affect the results.

4.4. COMPUTATIONAL GRIDS

To solve the N-S equations with the described methods, computational grids are made. The following sections present the grids used for the computations in Chapters 6, 7, and 8.

4.4.1. 3D GRIDS

Measurements by Pennings et al. (2015b) were performed in the cavitation tunnel of Delft University of Technology. Figure 4.2 shows a photograph of the tunnel, where the flow is coming from the right and the suction side of the wing is pointing downwards. In the Stereographic-Particle Image Velocimetry (S-PIV) measurements, the laser was placed underneath the tunnel. Figure 4.3 visualises the tunnel geometry schematically. This domain is used for the computations. The inlet is located $5c_0$ upstream of wing; the outlet $10c_0$ downstream. The wing is placed exactly in the middle of the domain, i.e. the tunnel height is twice the wingspan and the distance between the wing's surface and the top/bottom wall is also equal to the wingspan b ($b = 1.2c_0$). The x-axis is aligned with the flow, y-axis is in positive lift direction, and z-axis is along the span. The origin of this Cartesian reference system is located at the wing tip.

To simulate the experimental conditions, the Boundary Condition(s) (BC) are mimicked as accurate as possible. Table 4.1 provides an overview and gives a short description of the imposed BC. These are the same BC as Schot (2014) used. Asnaghi (2018) and Paskin (2018) also applied a non-slip BC on the wall at which the wing in mounted. Asnaghi (2018) resolved this wall in his computations, Paskin (2018) designed the grid to fit in to a wall function law ($y^+ \approx 30$) in that region. The effect this could have on the vortex itself (input error) will be discussed in Section 5.1.2. Note that the computational domain is the same as all other researchers.

The researchers mentioned in the previous paragraph used unstructured (hexahedral dominated) grids for their calculations. In general, these type of grids are easier to produce, but their cell quality is often worse. More-

Table 4.1: Boundary conditions and their description for the different planes indicated in Figure 4.3.

BC	Description
INLET	Three components of velocity and other scalars (Dirichlet), pressure extrapoled from interior.
PRESSURE	Dirichlet for pressure (constant over the plane). Velocities and other scalar are extrapolated from interior.
NOSLIP-WALL	Dirichlet for velocity components (all zero), Neumann for pressure and all other scalars.
SLIP-WALL	Normal velocity at wall is zero, tangential velocity is arbitrary. The other variables are defined as for a no-slip wall.

over, a larger amount of cells is generally required to obtain the same accuracy compared to structured grids. Section 3.1 already mentioned that the $\gamma - \tilde{R}e_{\theta_t}$ transition model is hard to converge. Grid quality in, and around, the BL is a requirement to improve convergence. For these reasons, multi-block hexahedral structured grids were made using GridPro (`www.gridpro.com`). An elliptical block is made around the wing. To accurately mesh the edges of the wing, additional blocks are used in these regions. Grids are made for two different Angle(s) of Attack (AoA): $\alpha = 5°$ and $\alpha = 9°$. Table 4.2 presents the grid details.

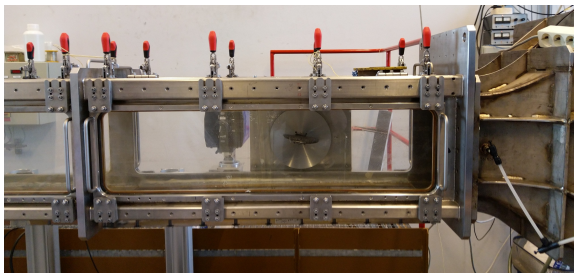

Figure 4.2: Photograph of the cavitation tunnel of Delft University of Technology. The 'Arndt' wing in mounted in the tunnel wall, picture taken on 01/05/2019 by Ir. M.D. Klapwijk.

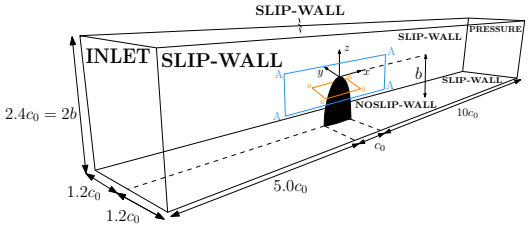

Figure 4.3: Schematic visualisation of the 3D (computational) domain including geometrical parameters expressed in c_0. Boundary conditions are shown as well.

One drawback of the structured grids is the diffusion of the grid cells downstream of the wing. To capture the gradients in the roll-up process as well as in the vortex itself, the resolution in these regions must be increased. ReFRESCO features two types of adaptive grid refinement, (i) a priori grid refinement in pre-specified regions, or (ii) online grid refinement during the simulation based on certain parameters. The drawback of the second option is that this approach is hard to control and perturbs the grid similarity required for the analysis of the discretisation error (see Section 5.1.1). The drawback of a priori grid refinement is that the 'to-be-refined' regions must be known beforehand (these regions will differ for different numerical settings in most test cases). Fortunately, the vortex trajectory and wake regions can be well-established beforehand. Arndt et al. (1991) showed that the vortex trajectory is independent of most relevant parameters such as the Reynolds number, cavitation number, and AoA. Asnaghi et al. (2017a) confirmed this through CFD simulations. For this reason, it was decided to apply a priori grid refinement, the following paragraphs show the results for the vortex and wake refinement respectively.

Table 4.2: Grid details of structured 3D grids for $\alpha = 5°$ (left) and $\alpha = 9°$ (right). Surface averaged $\overline{(\cdot)}$ and maximum $(\cdot)_m$ non-dimensional normal (n), tangential (t) and spanwise (s) wall cell sizes are obtained by steady Shear Stress Transport (SST) simulations for $Re = 8.95 \times 10^5$.

Grid	$N_c'/10^6$	$\overline{x_n^+} \times 10^1$	$\overline{x_t^+}/10^2$	$\overline{x_s^+}/10^3$	$(x_n^+)_m \times 10^1$	$(x_t^+)_m/10^3$	$(x_s^+)_m/10^3$
$G_{1,5}^{3D'}$	2.82	1.17	2.65	0.53	3.42	1.24	2.84
$G_{2,5}^{3D'}$	1.32	1.47	3.43	0.69	4.23	1.61	3.67
$G_{3,5}^{3D'}$	0.67	1.85	4.26	0.86	4.99	2.00	4.57
$G_{4,5}^{3D'}$	0.30	2.39	5.67	1.14	6.57	2.61	6.10

Grid	$N_c'/10^6$	$\overline{x_n^+} \times 10^1$	$\overline{x_t^+}/10^2$	$\overline{x_s^+}/10^3$	$(x_n^+)_m \times 10^1$	$(x_t^+)_m/10^3$	$(x_s^+)_m/10^3$
$G_{1,9}^{3D'}$	2.77	1.25	2.71	0.61	4.71	1.17	3.22
$G_{2,9}^{3D'}$	1.30	1.55	3.51	0.79	5.47	1.49	4.12
$G_{3,9}^{3D'}$	0.66	1.96	4.36	0.98	6.74	1.83	5.09
$G_{4,9}^{3D'}$	0.29	2.53	5.82	1.30	7.97	2.42	6.47

4.4.2. ADAPTIVE GRID REFINEMENT

VORTEX REFINEMENT

For the same case, Asnaghi et al. (2017b) investigated the effect of the grid resolution in the vortex on the trajectory, axial velocity in the vortex centre, and the lift coefficient. They found that 'the mesh resolution requirement in the plane of the vortex is higher than the streamwise direction, due to having higher flow gradients in the in-plane directions. They advised an in-plane and streamwise resolution of $1/8\eta_v$ and $1/4\eta_v$ respectively. Here η_v is the viscous core radius of the vortex.

To meet these requirements (for the finest grid), adaptive grid refinement in the vortex region is applied by

means of refinement boxes (h-refinement) along the vortex trajectory. This refinement is performed from the tip until two root-chord lengths ($2c_0$) downstream of the tip. ReFRESCO marks all cells located in the specified boxes and splits them (for Three-Dimensional (3D) grids) in $2^3 = 8$ cells per refinement level. Boxes are positioned along the vortex trajectory, the streamwise distance between each box is set as $0.04c_0$ to ensure smooth diffusion of the grid. The vortex trajectory is the line through the vortex centres (minimum pressure) at all streamwise locations. The in-plane lengths (Δy and Δz) of the boxes are set equal to the viscous core radius of the vortex (η_ν).

To determine η_ν, at every spanwise location, the slice of the vortex is transformed from a cartesian (x, y, z) to a polar $(x, r = \sqrt{y^2 + z^2}, \theta = \arctan 2(z/y))$ coordinate system with point of minimum pressure (vortex centre) as the origin. The azimuthal velocity in this plane reads,

$$u_\theta = -v\sin(\theta) + w\cos(\theta)\,, \tag{4.13}$$

where v and w are the in-plane velocity components. The viscous core radius is defined as the radius where the azimuthal velocity is maximum and is not constant over θ due to the roll-up process, i.e. the vortex is asymmetric. To determine the viscous core radius, the azimuthal velocity is determined over lines of constant θ. Figure 4.4 shows the velocity profiles for four different angles. The viscous core radius is determined by taking the average of η_ν for all angles. Note that Figure 4.4 only shows four angles, however in the post-processing the viscous core radius is determined for every degree so 360 samples.

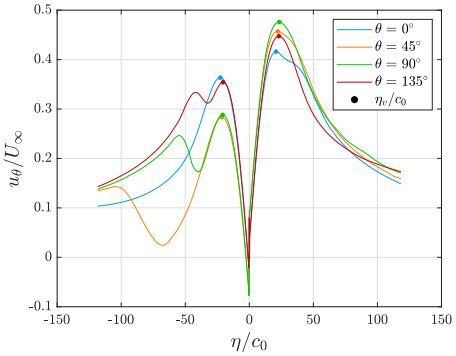

Figure 4.4: Azimuthal velocity profiles over lines of constant θ. Dots indicate the viscous core radii. The velocity profiles are obtained by an SST simulation for the wing at 9 degrees AoA, the streamwise location is $x/c_0 = 0.50$.

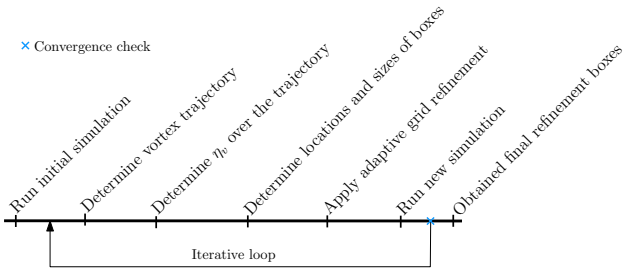

Figure 4.5: Iterative adaptive grid refinement approach of the vortex region.

The initial multi-block structured grid is not refined in the vortex region, whereby the initial estimates for the vortex core size and trajectory are not reliable. An iterative approach is used to perform the grid refinement as accurately as possible and to minimise computational costs (to avoid refining in regions where no refinement is needed). Figure 4.5 provides an overview of this process. The iterative process is considered to be converged when the difference of the viscous core radius over the entire trajectory between two subsequent iterations is on average less than 1%. Figure 4.6 displays the viscous core radius over the trajectory for different iterations (four iterations (N_{adapt}) were required to converge). Since the structured grids are relatively fine near the tip, the viscous core radius was estimated quite well in the simulation without grid refinement. Further downstream of the tip, the change between the iterative steps is much larger since the initial cells in that region can be up to 20 times larger compared to the cells just downstream of the tip.

Figure 4.7 displays the resulting boxes around the vortex trajectory. A maximum refinement level of three in the vortex, $(R_{x,y,z})_\nu = 3$, is needed to obtain the required grid resolution in the region $x/c_0 < 0.5$. Further downstream of that location, the requirement of $1/4\eta_\nu$ for the streamwise cell length was not met due to the large AR cells in that region. An extra refinement level in streamwise direction was applied ($(R_x)_\nu = 4$) to overcome this. For the region $x/c_0 > 1.00$, the grids is on average 10% coarser than the suggested values. However it was decided to not apply another refinement step since (i) previous searchers showed that due to turbulent diffusion the vortex is diffused anyway downstream of that location and (ii) it would increase the computational costs by 30%.

Around the tip, an extra refinement box is placed to merge the refined vortex region with the BL. To control

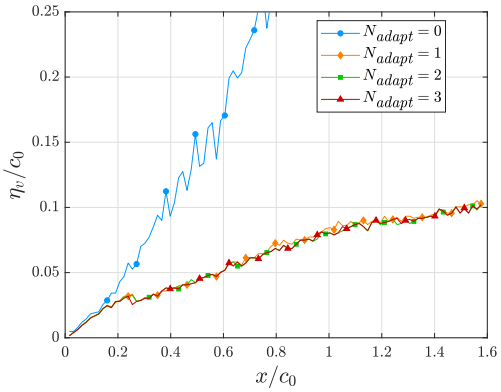

Figure 4.6: Viscous core radius along the trajectory during the iterative adaptive grid refinement process.

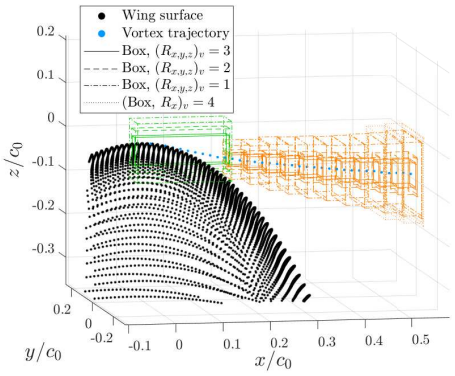

Figure 4.7: Adaptive grid refinement boxes around the vortex trajectory, green box uses $AR = 4$ while $AR = 10$ is used for the orange boxes.

the refinement into the BL (refinement until the wall is not desired since this would result in very high AR cells near the wall), a refinement criterion based on the AR is set (see colour of boxes in Figure 4.7). If the AR of a cell is above this value, the cell is treated as a BL cell which means that the shortest side in the cell is not split. The maximum AR for the box near the tip (green box) is set to 4. For the orange boxes, an AR of 10 is set to make sure that all marked cells are actually refined.

WAKE REFINEMENT

To account for the gradients in the wake during the roll-up process, adaptive grid refinement is also applied in the wake region. Asnaghi et al. (2017b) published clear requirements for the grid resolution of the vortex, however for the wake region no requirements were found in literature. In this thesis, the wake region is defined as the region downstream the Trailing Edge (TE) of the wing where the magnitude of the velocity in the axial direction is less than 95% of the freestream velocity, i.e. $u < 0.95U_\infty$. Based on this, the locations and sizes of the adaptive grid refinement boxes were calculated. Figure 4.8 displays the refinement boxes in the wake for the wing at 9 degrees AoA. To determine how many refinement levels are required in the wake, two parameters which are important in the context of vortex roll-up are considered. These parameters are (i) the circulation contained in the vortex core Γ_{η_v}, and (ii) the pressure in the vortex centre $(C_p)_c$ (Saffman, 1992).

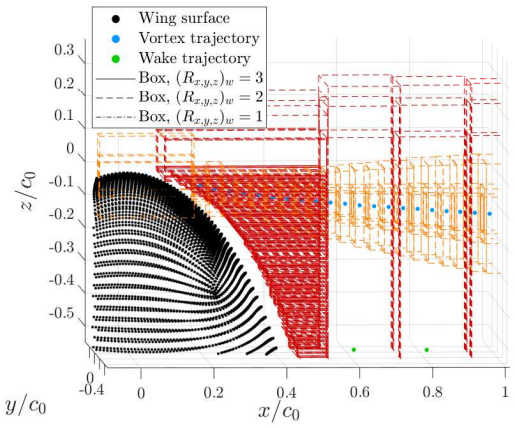

Figure 4.8: Adaptive grid refinement boxes around the wake trajectory (red). Vortex refinement boxes of Figure 4.7 are also included (orange).

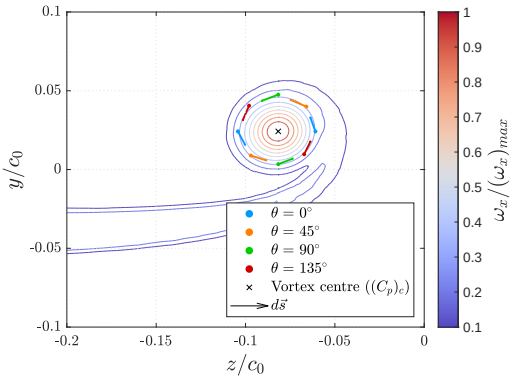

Figure 4.9: Contour plot of the x-component of the vorticity vector at $x/c_0 = 0.50$ and $\alpha = 9°$. Dots indicate the viscous core radius, the arrows show the path along which the velocity vector is integrated to obtain the circulation.

The circulation contained in the vortex core is determined using Equation (2.7), i.e. the velocity vector parallel to the viscous core is integrated. Note that in this way it is assumed that the plane is perfectly perpendicular to the vortex (only the x-component of the vorticity vector is integrated). This is plausible in the region where the vortex

trajectory is parallel to the freestream, $x/c_0 > 0.35$. The viscous core radii for the different angles (as determined in Figure 4.4) are visualised in the contour plot of the x-component of the vorticity in Figure 4.9. The arrows indicate the vectors along which the in-plane velocity vector is integrated. Figure 4.10 presents Γ_{η_v}/Γ_0 and $(C_p)_c$

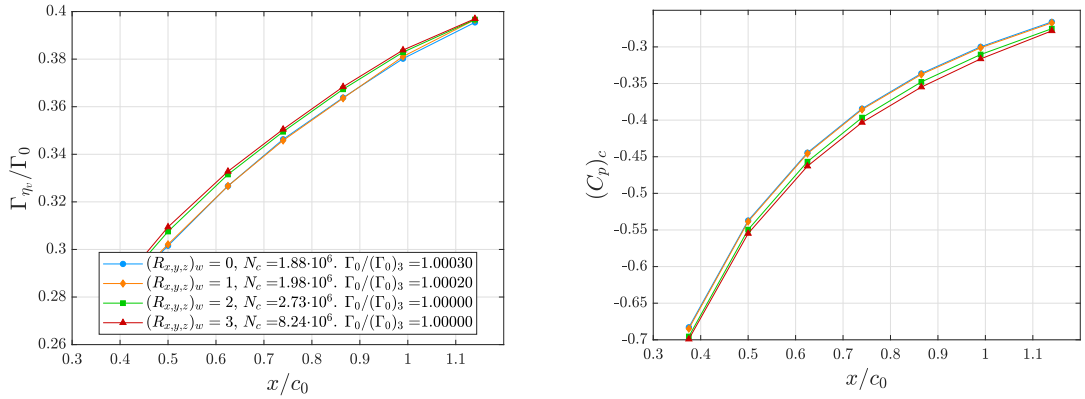

Figure 4.10: Circulation contained in the vortex core (left) and pressure coefficient in the vortex centre (right) along the trajectory for different wake refinement levels $(R_{x,y,z})_w$. Results for $\alpha = 9°$.

over the vortex trajectory for $\alpha = 9°$. The legend in the graph indicates the refinement level applied in the wake $(R_{x,y,z})_w$, the total number of grids cells (N_c) and wing circulation relative to the finest grid $(\Gamma_0/(\Gamma_0)_3)$. This study was performed using grids $G^{3D}_{2,9}$ and the SST model in steady state. It was observed that the wing's circulation is not affected. The circulation contained in the viscous core increases and the pressure drops as the wake is refined. This is because less energy is numerically diffused in the wake region for higher refinement levels. One

Table 4.3: The resulting amount of grids cells after wake and vortex refinement for $\alpha = 5°$ (left) and $\alpha = 9°$ (right).

Grid	$N'_c/10^6$	$(\Delta N_c)_v/10^6$	$(\Delta N_c)_w/10^6$	$N_c/10^6$	h_i/h_1
$G^{3D}_{1,5}$	2.82	1.13	1.77	5.72	1.00
$G^{3D}_{2,5}$	1.32	0.54	0.83	2.69	1.28
$G^{3D}_{3,5}$	0.67	0.29	0.44	1.40	1.59
$G^{3D}_{4,5}$	0.30	0.13	0.20	0.63	2.08

Grid	$N'_c/10^6$	$(\Delta N_c)_v/10^6$	$(\Delta N_c)_w/10^6$	$N_c/10^6$	h_i/h_1
$G^{3D}_{1,9}$	2.77	1.73	2.09	6.59	1.00
$G^{3D}_{2,9}$	1.30	0.83	0.98	3.11	1.28
$G^{3D}_{3,9}$	0.66	0.42	0.53	1.61	1.59
$G^{3D}_{4,9}$	0.29	0.21	0.23	0.73	2.08

refinement level improves the results slightly, increasing the refinement level to two results in a large change, and the difference between refinement level two and three is relatively small. The decrease of spatial discretisation error between refinement levels two and three is not considered to outweigh the additional computational costs (about 300%, i.e. 5.5×10^6 computational cells). The same conclusions were drawn for the 5 degrees AoA case. It was therefore decided to use two refinement levels in the wake region.

Table 4.3 displays the total number of grid cell of the original grids N'_c, the additional grid cells for the vortex and wake refinements, $(\Delta N_c)_v$ and $(\Delta N_c)_w$ respectively, and the total number of grid cells (N_c). Note that the non-dimensional cell sizes at the wall in all directions remain the same as shown in Table 4.2 (assuming that the vortex and wake refinements do not influence the wall-bounded flow) since no refinement at the wing's surface is applied. Figures 4.12 and 4.13 visualise $G^{3D}_{3,9}$.

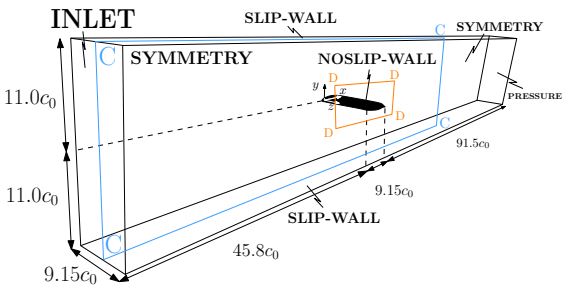

Figure 4.11: Schematic visualisation of the 2D (computational) domain including geometrical expressed in c_0.

4.4.3. 2D GRIDS

For the 2D analysis, the wing at half-span $(z/b = 0.5)$ is considered. At this location, the chord c of the wing is $0.87c_0$. The grid generator requires the chord of the foil to be unity. To match the domain size with the cavitation tunnel, all lengths were scaled with the same factor. Figure 4.11 shows the geometry of the domain, the edge lengths, and the imposed BC.

For the Two-Dimensional (2D) calculations, almost the same set of BC as for the 3D simulations is used. The only difference is the BC for the symmetry planes. For the 2D calculations a symmetry BC is used. In ReFRESCO,

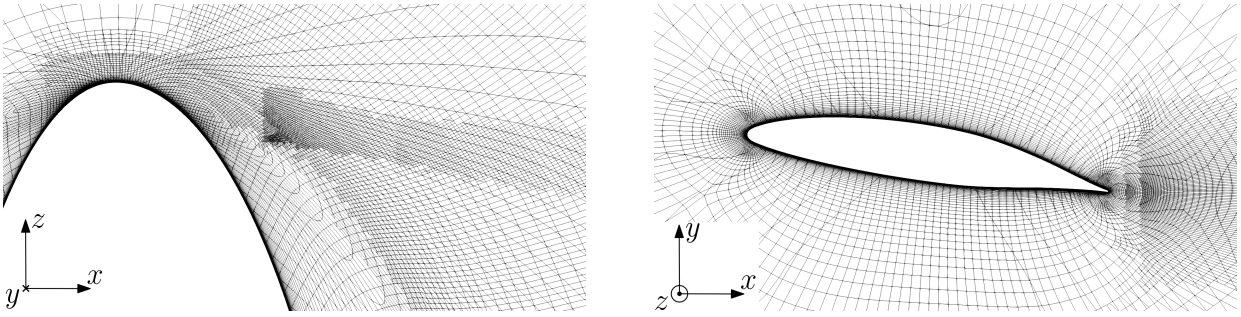

Figure 4.12: Visualisation of $G^{3D}_{3,9}$ at cross sections A-A-A-A (left) and B-B-B-B (right). Locations of the cross-sections are indicated in Figure 4.3.

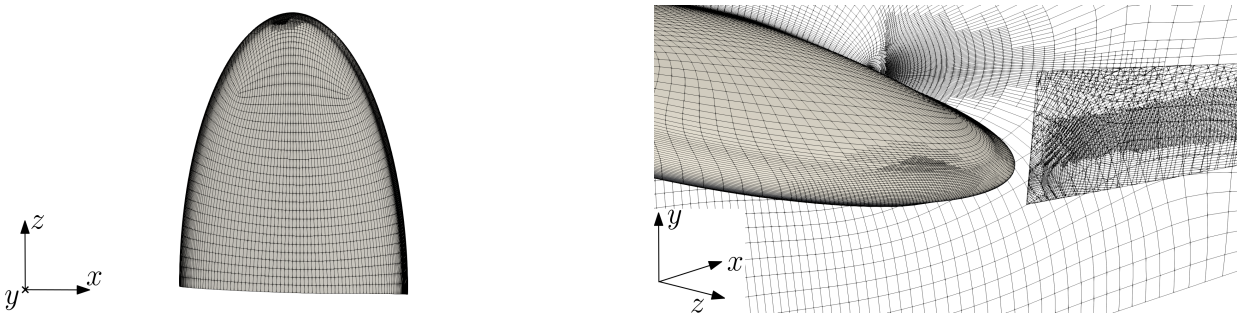

Figure 4.13: Visualisation of $G^{3D}_{3,9}$ on the wing surface (left) and wing surface including vortex and wake refinements (right).

this BC has the same specifications as a slip-wall. Multi-block structured hexahedral grids were generated using the foil grid generator of IST Lisbon. A total number of nine blocks were used. One O-block shaped like an ellipsis around the foil, hyperbolic grid generation is used for that region. The grids in the other eight H blocks (three above the foil, three on the bottom, one upstream of the foil, and another downstream) were generated by an elliptical grid generator. Table 4.4 presents the grid details for both AoA. Figure 4.14 visualises $G^{2D}_{3,9}$.

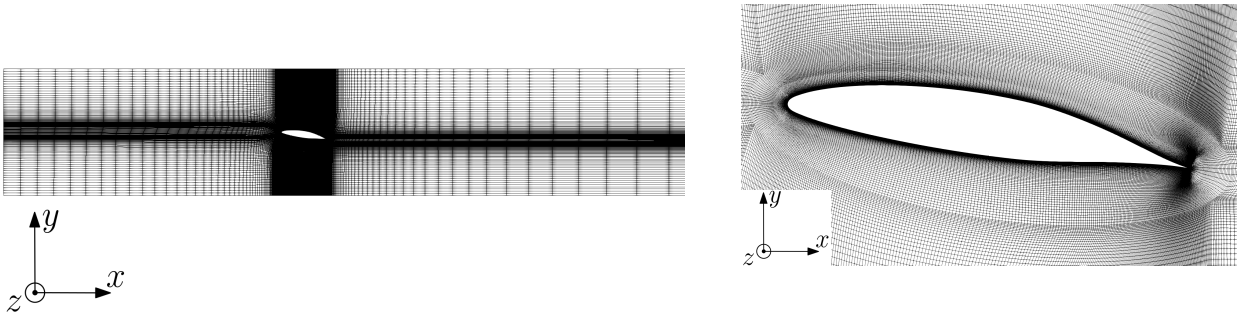

Figure 4.14: Visualisation of $G^{2D}_{2,9}$ at cross sections C-C-C-C (left) and D-D-D-D (right). Locations of the cross-sections are indicated in Figure 4.11

Table 4.4: Grid details of structured 2D grids for $\alpha = 5°$ (left) and $\alpha = 9°$ (right). Surface averaged $\overline{(\cdot)}$ and maximum $(\cdot)_m$ non-dimensional normal (n), tangential (t) wall cell sizes are obtained by steady SST simulations for $Re = 8.95 \times 10^5$.

Grid	$N_c/10^5$	h_i/h_1	$\overline{x_n^+} \times 10^2$	$\overline{x_t^+}/10^2$	$(x_n^+)_m \times 10^1$	$(x_t^+)_m/10^2$
$G^{2D}_{1,5}$	2.56	1.00	5.69	0.88	1.37	2.47
$G^{2D}_{2,5}$	1.96	1.14	6.52	1.00	1.57	2.82
$G^{2D}_{3,5}$	1.44	1.33	7.65	1.17	1.85	3.29
$G^{2D}_{4,5}$	1.00	1.60	9.25	1.40	2.24	3.95

Grid	$N_c/10^5$	h_i/h_1	$\overline{x_n^+} \times 10^2$	$\overline{x_t^+}/10^2$	$(x_n^+)_m \times 10^1$	$(x_t^+)_m/10^2$
$G^{2D}_{1,9}$	2.56	1.00	6.03	0.86	1.79	2.42
$G^{2D}_{2,9}$	1.96	1.14	6.92	0.98	2.05	2.76
$G^{2D}_{3,9}$	1.44	1.33	8.12	1.14	2.40	3.22
$G^{2D}_{4,9}$	1.00	1.60	9.81	1.36	2.90	3.86

5

VERIFICATION & VALIDATION

Performing Computational Fluid Dynamics (CFD) calculations of complex turbulent flows comes with the need to determine the credibility of the output. This is done by means of a Verification and Validation (V&V) process. Within this thesis the definition of V&V by Roache (2009) is followed: 'Verification is a purely mathematical exercise that intends to show that we are "solving the equations right", whereas validation is a scientific/engineering activity that intends to show that we are "solving the right equations'. This implies that verification is concerned with numerical errors/uncertainties, while validation deals with modelling errors/uncertainties.

The first part of this chapter is mainly devoted to the term verification, which consists of two activities: Code verification and solution verification. A significant amount of effort has already been put into the code verification of ReFRESCO (see i.a. Eça et al. (2010), Rijpkema and Vaz (2011) and Eça et al. (2014)). For this reason, not a lot of attention will be paid to actual code verification of ReFRESCO. The verification process of the solver output is therefore mainly solution verification. The second part of this chapter deals with the validation process. Since the two terms verification and validation are inherently linked, there is some overlap in the two parts.

5.1. ERROR QUANTIFICATION

Errors in numerical simulations depend on (i) the accuracy of the governing equations to represent the intended physical process (modelling error, $E_m(\phi)$), (ii) the boundary and initial conditions (input error, $E_i(\phi)$), and (iii) the ability of the mathematical procedures to solve the governing equations (numerical errors, $E_n(\phi)$). This is schematically visualised in Figure 5.1.

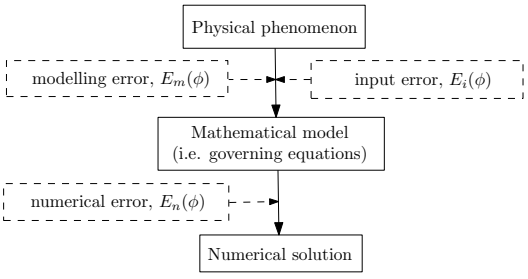

Figure 5.1: Decomposition of the errors in a CFD simulation.

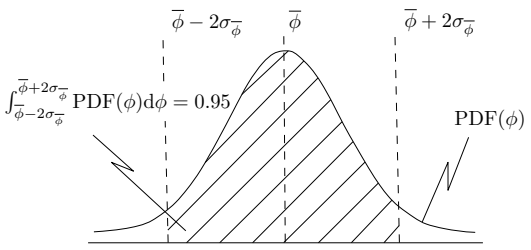

Figure 5.2: Illustration of normal distributed Probability Density Function (PDF) of ϕ including 95% confidence interval.

The total error is defined as the difference between the simulation output (ϕ) and the experimental value (ϕ_e),

$$E(\phi) \equiv \phi - \phi_e = E_n(\phi) + E_i(\phi) + E_m(\phi)\,. \tag{5.1}$$

The following sections discuss the individual components of this expression.

5.1.1. NUMERICAL ERROR

An exact solution for the non-linear Navier-Stokes (N-S) is not always proven to exist nor proven not to exist. A number of numerical techniques have to be applied to end up with a 'solution', which in fact is an estimate for most practical flows. The process of numerically solving the differential equations gives rise to a number of numerical errors,

$$E_n(\phi) \equiv \phi - \phi_0 = E_r(\phi) + E_{it}(\phi) + E_d(\phi) + E_s(\phi)\,, \tag{5.2}$$

here ϕ_0 denotes the exact solution, $E_r(\phi)$ the round-off error, $E_{it}(\phi)$ the iterative error, $E_d(\phi)$ the discretisation error and $E_s(\phi)$ the statistical error.

Before treating the different errors and their sources, it is important to distinguish between errors $E(\phi)$ and uncertainties $U(\phi)$. Note that the exact solution is *not* a validation dataset (measurements), the exact solution for the given set of equations with the given input parameters. For this reason, the exact solution is often unknown, and therefore it is not possible to determine the errors. In these cases, the uncertainty, which establishes an interval where the solution is contained in with a certain degree of confidence, is determined. In this thesis, this interval is defined such that the interval contains the solution with 95% coverage, as visible in Figure 5.2. The 95% confidence interval is the region bounded by $\overline{\phi} \pm 2\sigma_{\overline{\phi}}$, the uncertainty does therefore not possess a sign (i.e. $U(\phi) = \pm U(\phi)$) (Dekking et al., 2005). Here $\sigma_{\overline{\phi}}$ is the standard deviation of the mean of ϕ.

ROUND-OFF ERROR

Round-off errors occur because computers have a limited precision to execute mathematical operations. This error is not addressed in this thesis. The reason for this is that all computations are run on double-precision. This guarantees the round-off error to be negligible relative to the others (Stern et al., 2006). Note that the importance of this error will increase as grids become finer, however is not of importance still.

ITERATIVE ERROR

The iterative solution procedures as described in Section 4.3 introduce iterative errors in CFD simulations (Roache, 1997). In theory, the iterative errors should decrease to machine precision, however this level of convergence is often not achievable or is computationally too expensive for complex turbulent flows.

According to Eça and Hoekstra (2006), the most appropriate technique to map the iterative error during CFD simulations is by using the maximum value ($L_\infty = \|\phi\|_\infty$) and Root Mean Square (RMS) ($L_2 = \|\phi\|_2$) of the normalised residual vectors. Eça and Hoekstra (2006) and Pereira et al. (2015) performed a study concerning iterative errors using ReFRESCO with the same residual normalisation as described in Section 4.3.1. They performed calculations for different specified convergence tolerances of the L_∞ norm of all flow variables. In both studies, a requirement of $L_\infty \leq 10^{-5}$ is found to be sufficient to ensure that the iterative error is at least one order of magnitude smaller compared to the discretisation error. This conclusion was drawn for different flow problems, i.a. a 3D cylinder, a finite flat plate, and a KVLCC2M tanker. This number obviously is case dependent, however still gives an indication as to which orders of magnitude to consider. It is expected that this requirement can be generalised to the 'Arndt' wing, however this will be checked by altering the convergence criterion and checking the flow variables for these different settings.

DISCRETISATION ERROR

Spatial and temporal discretisation is often named as the main contributor to the numerical error (Stern et al., 2006; Roache, 2009). In literature, two perspectives to determine this error are taken: (i) by executing systematic spatial and temporal refinement studies (Celik et al., 2008; Eça and Hoekstra, 2014) and (ii) by determining the error from an additional error transport equation (Celik and Hu, 2004; Phillips and Roy, 2011). The first method requires a substantial amount of computational resources, however this is unavoidable since the second method can only be applied when using at least a third order discretisation scheme. This would not be achievable for this test case and the transition model (Asnaghi, 2018; Lopes et al., 2018).

In this thesis, the approach by Eça and Hoekstra (2014) is followed. The goal of this method is to determine the 95% confidence interval by,

$$\phi - U_d(\phi) \leq \phi_0 \leq \phi + U_d(\phi)\,, \tag{5.3}$$

where $U_d(\phi)$ is the discretisation uncertiainty. Prior to calculating this uncertainty, first the actual discretisation error is estimated. The method to do this relies on a (truncated) power series expansions (Roache, 1997),

$$E_d(\phi) \equiv \phi - \phi_o \approx \beta_s \Delta h_i^{p_s} + \beta_t \Delta t_i^{p_t}, \tag{5.4}$$

here the indices s and t indicate the spatial and temporal components, Δh and Δt the spatial (grid) and temporal (timestep) resolutions respectively, β the constants to be determined, and p the observed orders of grid convergence.

For simplicity, let's assume a steady simulation, this reduces the error to,

$$E_d(\phi) \equiv \phi - \phi_o \approx \beta_s \Delta h_i^{p_s}. \tag{5.5}$$

To determine the three unknowns ϕ_0, β_s, and p_s, a set of three geometrically similar structured grids is required. Flux limiters, damping functions and switches in the turbulence model result in noise in the CFD output (Eça and Hoekstra, 2014). This sometimes yields the proposed estimation in Equation 5.5 to be unreliable since p_s is sensitive to a noisy dataset.

In order to account for this, two redundancy factors are present in the model. First, the order of error function is adjusted,

$$E_d(\phi) = \begin{cases} \beta_s \Delta h_i, & \text{if } p_s \leq 1; \\ \beta_s \Delta h_i^2, & \text{if } p_s \geq 2; \\ \beta_{s1} \Delta h_i + \beta_{s_2} \Delta h_i^2, & \text{if non-monotonic}. \end{cases} \tag{5.6}$$

These formulations are used when the observed order of grid convergence is either too low, too high or non-monotonic respectively. The second redundancy factor is the use of a least-square approach to determine the constant. Instead of three grids, a minimum number of grids (N_g) of four is required to determine the fit. This significantly increases the reliability of the method according to the Eça and Hoekstra (2014). The mathematically details for the least-square minimisation are presented in Appendix C.

The resulting uncertainty $U_d(\phi)$ is determined according to the Grid Induced Separation (GIS) procedure by Roache (1997),

$$U_d(\phi) = \begin{cases} 1.25 E_d(\phi) + \sigma + |\phi - \phi_{fit}|, & \text{for } 0.5 \leq p_s < 2.1 \text{ and } \sigma < \Delta_\phi; \\ 3.00 E_d(\phi) + \sigma + |\phi - \phi_{fit}|, & \text{for } 0.5 \leq p_s < 2.1 \text{ and } \sigma \geq \Delta_\phi; \\ 3.00 \frac{\sigma}{\Delta_\phi} (E_d(\phi) + \sigma + |\phi - \phi_{fit}|), & \text{otherwise}. \end{cases} \tag{5.7}$$

In the calculation of the 95% confidence interval for $U_d(\phi)$, a safety factor of 1.25 or 3 depending on the quality of the fit is used. The 'quality' of the fit is determined by comparing the standard deviation of the fit (σ) to the so called range parameter Δ_ϕ,

$$\Delta_\phi = \frac{\phi_{max} - \phi_{min}}{N_g - 1}, \tag{5.8}$$

which is a measure for the spread of data points. Appendix C also presents the calculation of the standard deviation.

STATISTICAL ERROR

In transient calculations, unsteadiness in the time signal due to (i) the initial conditions, and (ii) random flow statistics, gives rise to a statistical error (also known as random or aleatory error). To estimate this uncertainty, many different approaches are taken (see e.g. Lin et al. (1990) and Molloy (2006)). The approach by Brouwer et al. (2015) is used in this work because the effect of the initial conditions (start-up effect) and randomness in the signal can be assessed simultaneously. The main idea is to compare the standard deviation of the time signal to the theoretically expected trend for a stochastic stationary process.

The theoretical expression of the standard deviation (σ_ϕ) reads,

$$\sigma_\phi^2 = \frac{1}{T} \int_0^T \left(1 - \frac{dt}{T}\right) C_{\phi\phi}(dt) \mathrm{d}(dt), \tag{5.9}$$

where T is the total simulation time and $C_{\phi\phi}$ the autocovariance function. Both the derivation of Equation (C.19) and the definition of the autocovariance function can be found in Appendix C. This expression should hold for a process which is stochastically stationary and the standard deviation of the mean should thus decay with T^{-1}. In

other words, a plot of the standard deviation versus time (or versus the amount of timesteps) on logarithmic scale should be parallel to a line with slope -1 if the process is statistically converged.

Figure 5.3 shows a schematic visualisation of what the method is expected to do. The time signal clearly shows a start-up effect. Since uniform initial conditions are used, this start-up effect is expected to be present for all calculations. After the start-up period, the signal becomes statistically steady around the mean $\overline{\phi}$. The analysis of the time signal according to the mathematics presented above, is also shown in Figure 5.3. Note that time in the right graph is inversely plotted, i.e. the signal is analysed from the end to the start. At the first timesteps (region I) the standard deviation is high due to the start-up effect. When $t > t_{start}$ the statistically converged state of the process can be recognised since $\log(\sigma_{\overline{\phi}})$ has a slope equal to -1 (region II). Towards the end of the signal (region III) the uncertainty is high again, this is because the standard deviation at this position is determined only based on the first couple of analysed timesteps.

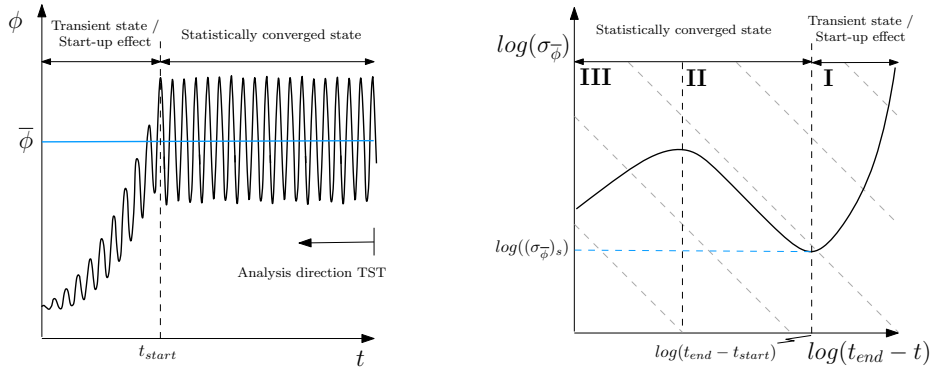

Figure 5.3: Schematic illustration of Transient Scanning Technique (TST): Time signal (left), standard deviation of $\overline{\phi}$ (right).

.

The statistical uncertainty of the statistically converged region can directly be obtain from the standard deviation plot as indicted by $(\sigma_{\overline{\phi}})_s$. This value for the combined uncertainty can be translated to the statistical uncertainty bound as follows,

$$U_s(\phi) = k(\sigma_{\overline{\phi}})_s \quad \text{with} \quad k = 1.96 \text{ for a 95\% uncertainty bound.} \tag{5.10}$$

Note that this variable still has a dimension. To non-dimensionalise this quantity, it should be divided by $\overline{\phi}$.

5.1.2. INPUT ERROR

Input errors originate from the fact that the experimental and numerical set-ups can never be matched exactly. Most discrepancies come from i.a. (i) insufficient transparency of the experimental campaign (documentation is insufficient), and (ii) excessive numerical requirements (resolving walls or extremely big geometries). ASME (2009) defined the term *input error* as 'the uncertainty in the simulation result due to errors in the simulation input parameters', and can therefore be interpreted very broadly. In the next paragraphs, the expected input errors are discussed.

The geometry of the cavitation tunnel is known precisely and is therefore duplicated. However, resolving all tunnel walls would be too computationally expensive Schot (2014) and Asnaghi et al. (2015). The developing Boundary Layer (BL) on the walls decreases the effective area of the tunnel and therefore the flow experiences a contraction which accelerates the flow. An increased velocity yields, for instance, a higher lift force and therefore a stronger vortex compared to the simulations.

One of the main points of concern is the quality of the inflow in the experimental set-up. Although the 'quality/strength' of the water (i.e. the amount of dissolved oxygen) is measured and reported, the turbulence intensity (I) is not. This parameter is of major importance when considering transition since the $\gamma - \tilde{R}e_{\theta_t}$ transition model is known to be sensitive to this quantity (Langtry, 2006; Lopes et al., 2018; Salahudeen and Baeder, 2018). To quantify this uncertainty, a sensitivity analysis has to be carried out ASME (2009). The input error can be approximated by,

$$E_i(\phi) = \phi - \phi_{ref}, \tag{5.11}$$

in which ϕ_{ref} is the simulation output with settings which match the experimental results best (Pereira, 2018). In theory, a linear Taylor expansion in parameter space could be used to determine the corresponding input uncertainty,

$$U_i(\phi) = \sum_{i=1}^{N_v} \frac{\partial \phi}{\partial N_i} U(N_i)\,, \tag{5.12}$$

where N_v is the total amount of variables, and N_i could be any variable (ASME, 2009). In this formulation, the variables are assumed to be uncorrelated. However, this is certainly not the case for the two parameters of interest (the turbulence intensity and eddy-viscosity). According to Spalart and Rumsey (2007), the user specified eddy-viscosity at the inlet determines the decay of turbulent kinetic energy (k) and therefore turbulence intensity throughout the domain. The mathematical argumentation behind this relies on the k-transport equation in a uniform inflow where only the destruction term is active. For the full derivation one is referred to Spalart (1997), the eventual relation for the decay reads,

$$k = k_{in}\left[1 + \frac{\omega_{in} x_{inlet}}{U_\infty}(C_{\varepsilon 2} - 1)\right]^{-\frac{1}{C_{\varepsilon 2}-1}}, \tag{5.13}$$

where k_{in} and ω_{in} are the turbulence quantities at the inlet, and x_{inlet} the streamwise distance to the inlet.

This correlation makes the quantification of the input uncertainty for this problem much harder. This is currently being tackled at Maritime Research Institute Netherlands (MARIN) by other researchers and is considered not to be part of this thesis. Pure Reynolds Averaged Navier Stokes (RANS) formulations without a transition model appear to be much less sensitive to the turbulent inflow conditions (see e.g. Rumsey and Spalart (2009) and Han et al. (2012)) and will probably suffer less from the input uncertainty of the turbulence intensity.

5.1.3. MODELLING ERROR

The modelling error $E_m(\phi)$ reflects how accurate the model predicts the real physics. Naturally, this error is thus determined by the validation process. The interval which contains the modelling error can be expressed as (Coleman and Stern, 1997),

$$E(\phi) - U_v(\phi) \leq E_m(\phi) \leq E(\phi) + U_v(\phi)\,, \tag{5.14}$$

here $E(\phi)$ is the total error, as defined in Equation (5.1), and $U_v(\phi)$ the validation uncertainty. $U_v(\phi)$ is the sum of the numerical $U_n(\phi)$ (Section 5.1.1), input $U_i(\phi)$ (Section 5.1.2), and the experimental uncertainties $U_e(\phi)$,

$$U_v(\phi) \equiv U_n(\phi) + U_i(\phi) + U_e(\phi)\,. \tag{5.15}$$

The experimental uncertainty originates from, for example, the accuracy of measurement sensors or the accuracy of some experimental settings (e.g. Angle(s) of Attack (AoA) or the inflow velocity). Figure 5.4 presents a schematic visualisation of a model which is considered as not valid and one which is considered valid. The valid case has a modelling error equal to $|\phi_e - \phi| + U_v(\phi)$, whether or not this error is acceptable depends on the application.

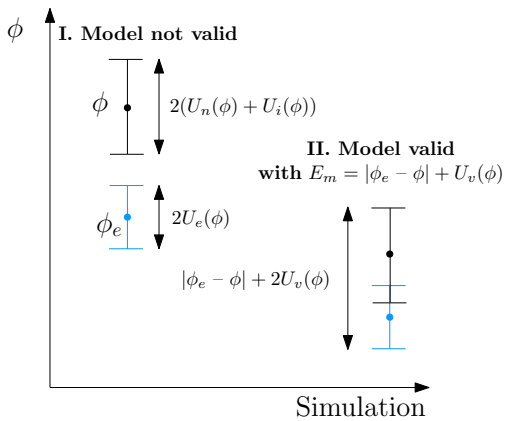

Figure 5.4: Graphical visualisation of modelling error. Non-valid model (left) and valid model (right) are compared.

5.2. VALIDATION

For the assessment of the modelling error, one needs a set of experimental measurements. The first section discusses the availability of validation data. After that, the validation strategy will be presented.

5.2.1. EXPERIMENTAL DATA

The main region of interest is the vortex. However, objective II is regarding transition modelling and therefore the flow pattern over the wing itself is also of major importance. First, the availability of data regarding the vortex itself (which is mainly important for the validation process of objectives III and IV) is discussed. Second, the availability of the transition-related validation data is discussed.

VORTEX MEASUREMENTS

Higuchi et al. (1987) and Arndt et al. (1991) were among the first who performed measurements for this test case. Higuchi et al. (1987) focussed more on the wake of the wing; Arndt et al. (1991) more on the vortex itself. Both performed LDA measurements at some locations downstream of the wing. Furthermore, they measured the viscous core radius (η_v) along the vortex trajectory and the coordinates of the trajectory itself. Pennings et al. (2015b) reconsidered the test case and performed Stereographic-Particle Image Velocimetry (S-PIV) measurements of the vortex in combination with force measurements.

Pennings et al. (2015b) considered the wing at different angles of attack ($\alpha = 5°, 7°, 9°$), Reynolds numbers ($Re \approx 6.8 \times 10^5, 9.0 \times 10^5$), cavitation numbers ($\sigma \approx 8.0, 4.0, 2.0, 1.3, 1.0$), and dissolved oxygen content ($\gamma \approx 2.5, 4.6 mg^1 l^{-1}$). The temperature of the fluid during the experiments was $T \approx 296K$, the kinematic viscosity $\nu \approx 9.3 \times 10^{-4} kg^1 m^{-1} s^{-1}$, and vapour pressure $p_v \approx 2.8 \times 10^3 Pa$. In this measurement campaign, the forces were obtained by performing balance measurements. However, the reported uncertainty of the lift force is 5% while 'the drag force was an order of magnitude smaller than the lift force. Since this is not accurately resolved by the force sensor and was irrelevant for the present study, it is not discussed further' (Pennings et al., 2015b). More interesting are the S-PIV measurements of the vortex itself. Table 5.1 shows the details of the measurement planes for different downstream locations of the tip.

Table 5.1: Details of S-PIV planes for different locations downstream of the tip.

x/c_0	0.50	0.74	1.14	1.75	5.50
Interrogation area [pixels]	6×6	8×8	12×12	24×24	48×48
Vector spacing [μm]	42	55	83	165	332
Number of points	1357×1707	1024×1279	674×845	347×429	136×186

It can be seen that small interrogation windows were used to resolve the high velocity gradients in the vortex. This results in planes which consist of more than 2.3×10^6 points. Unfortunately, no experimental uncertainties of the S-PIV measurements were reported. Figure 5.5 visualises an example of one of the measurement planes. The velocity distribution clearly shows the tip vortex, the region where the BL rolls-up, and the cavity within the vortex. One would expect a circular region in the vortex core as the cavity, however, the reflection of light on the water-vapour interface blurs the entire region at $z/c_0 \approx 3 \times 10^{-3}$.

Figure 5.6 shows an illustration of the experimental set-up. The computational domain as described in Section 4.4.1 matches this geometry.

ATTACHED FLOW MEASUREMENTS

The S-PIV measurements of the vortex itself lend themselves as excellent validation material from objectives III and IV, however, not for objective II. The best reference material of the flow along the wing surface is flow visualisation of the suction side by means of oil film visualisations by Higuchi et al. (1987) and Arndt and Keller (1992). These qualitative measurements show natural transition, but for some test conditions also a Laminar Separation Bubble (LSB) as shown in Figure 2.14. However, these results cannot function as validation material to determine the modelling error for the transitional flow over the wing's surface. No quantitative measurements are found in literature.

Fortunately, there is a collaboration with an experimental study concerning the same test case in the NOISOURCE project. As already shortly pointed out in Section 2.4.1, Ir. S. Nanda is currently carrying out S-PIV measurements. In one of the first meetings, it was agreed that he will take S-PIV measurements of the flow around the wing. To tackle both validation of the wall-bounded flow and the input uncertainty introduced by the turbulent inflow conditions (see Section 5.1.2), the measurement plane will be placed such that it covers both. This is shown in Figure 5.7 which is cross-section A-A of Figure 5.6. The wing is considered at half-span ($z/b = 0.5$), region I covers the entire cross-section while the turbulence intensity can be calculated using region II.

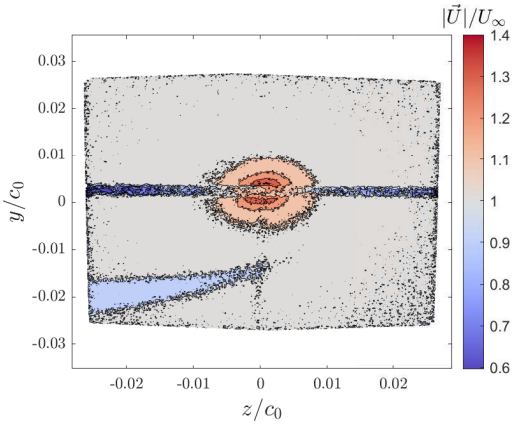

Figure 5.5: Experimentally obtained magnitude of the normalised velocity vector, by Pennings et al. (2015b). Conditions: $\alpha = 9°$, $Re = 9.07 \times 10^5$, $\sigma = 2.13$, $\gamma = 2.5$, and $x/c_0 = 1.14$.

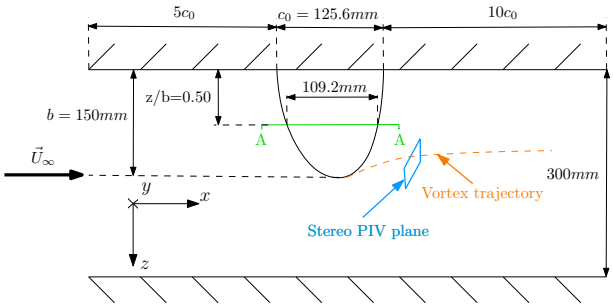

Figure 5.6: Illustration of the top view of the cavitation tunnel including S-PIV measurement plane which Pennings et al. (2015b) used.

5

Due to unforeseen problems with the cavitation tunnel, the measurement campaign was delayed. Measurements will become available in the near future but no longer in the timespan of this thesis. These measurement would function as validation data for the transition simulations in Chapter 6 and it is recommended to validate these results at a later time.

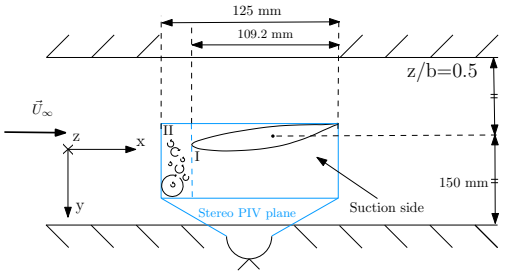

Figure 5.7: Illustration of side view of cavitation tunnel (section A-A in Figure 5.6) including S-PIV measurement plane around the wing.

5.2.2. STRATEGY

During the validation process, different parameters should be considered. Figure 5.8 visualises the strategy, and the successive paragraphs discuss the different parameters. Because the data for the attached (transitional) flow is not yet available, only the strategy to process the vortex measurements is considered. However, the approach for transition will be similar.

INTEGRAL QUANTITIES

The integral quantities, and in particular the lift coefficient, are considered first. This because the strength of the tip vortex is directly proportional to the lift (see Section 2.3.1). For the transitional BL, the skin friction drag coefficient C_{df} is also important since this quantity provides an indication of the state of the BL. This value cannot be validated since only the total (equal to the sum of pressure and friction drag) drag is measured.

VORTEX TRAJECTORY

Next are the vortex trajectory and the quantities along it. The coordinates (x/c_0, y/c_0, z/c_0) of the vortex centre give an indication of the vortex roll-up process. Moreover, important parameters along this path are the pressure coefficient in the vortex centre, viscous core radius, and vorticity contained in the viscous core (Saffman, 1992). By plotting them over the vortex trajectory, it provides a global insight into the decay of vorticity.

LOCAL VELOCITY PROFILES

Local velocity profiles, in particular the azimuthal and axial velocity distributions in the vortex itself, provide insight into its structure. Bosschers (2018) used a similar approach to validate his analytical expressions. He averaged the axial and azimuthal velocity over 1/4th of the vortex in positive lift direction (indicated by Sector I in Figure 5.8).

VORTEX FIELD

Last is the entire velocity field of the vortex as Pennings et al. (2015b) measured. Based on the work by Hills (2006), the ASME (2009) proposed a method to quantify the modelling error for an arbitrary set of points. For N_p points,

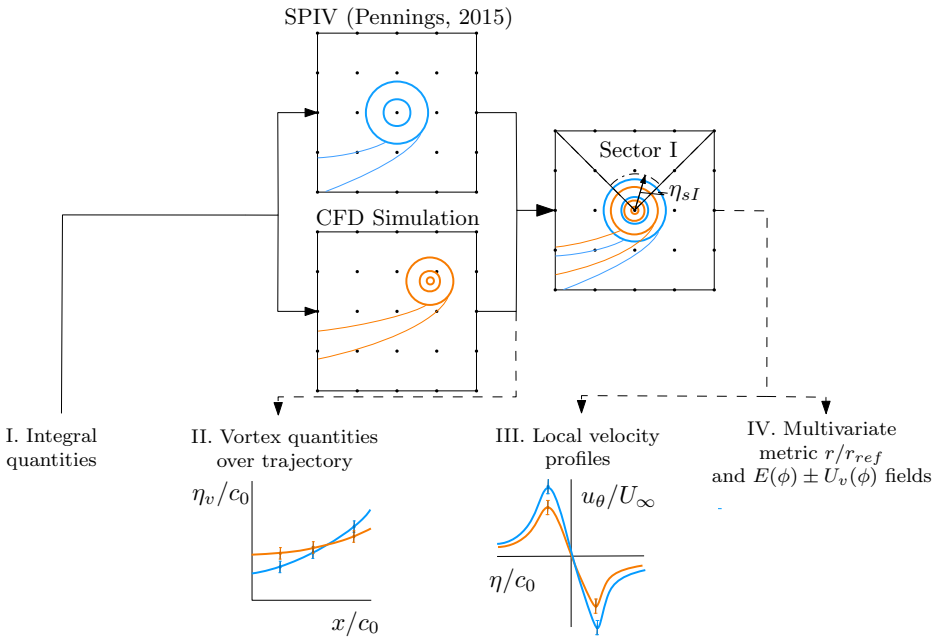

Figure 5.8: Schematic illustration of proposed validation process based on methods found in literature.

the metric r of $E_m(\phi)$ and $U_v(\phi)$ reads,

$$r = \sqrt{\vec{E}_m^T \vec{U}_v^{-1} \vec{E}_m}, \tag{5.16}$$

where $\vec{E}_m = [E_{m,N_1}, E_{m,N_2}, ..., E_{m,N_p}]^T$ and $\vec{U}_v = \text{diag}([U_{v,N_1}, U_{v,N_2}, ..., U_{v,N_p}])$. If the uncertainties in the N_p points are represented by a normal distribution, the expected value of r is represented by a χ^2 distribution. This means that the reference value r_{ref} is the sum of the expected value and the standard uncertainty (Hills, 2006),

$$r_{ref} = \sqrt{N_p + \sqrt{2N_p}}. \tag{5.17}$$

The value of r/r_{ref} is thus a measure whether 'the model is globally valid'. This quantity is a weighted 2-norm of the error vector, the weighting is done by the uncertainty of each individual point. When r/r_{ref} exceeds one, it is evident that the simulations are *not* consistent with the measurements. If $r/r_{ref} \leq 1$, the difference between experimental data and numerical results is *globally* within the level of $U_v(\phi)$ which indicates that the model is valid.

A way to increase insight in which regions the model is valid is to plot the $E(\phi) \pm U_v(\phi)$ field. In this way, one can directly see where to model is 'valid' and in which regions there are large discrepancies.

5.3. CONCLUSIONS

In this chapter, the V&V process is addressed. First, a clear distinction is made between errors and uncertainties. The total error in CFD simulations is the sum of:

- **Numerical errors**, composed of:
  - *Round-off errors*, which are considered to be negligible for this test case.
  - *Iterative errors*, are expected to be at least one order of magnitude lower than the discretisation error in ReFRESCO when the maximum of the normalised residual vector for all variables is below $L_\infty < 10^{-5}$. To verify this, simulations with different convergence criteria should be carried out.
  - *Discretisation errors*, are found to be the dominant error source of the numerical error. Systematic grid and timestep refinement should be used to assess the uncertainty.
  - *Statistical errors*, can be determined by the TST technique. By means of this approach, the start-up effect can be excluded and the statistical uncertainties can be determined.

- **Input errors**, is found to be a broad definition. For this particular test case, the main contributor to the input errors is the uncertainty in the turbulent inflow conditions. Especially the transition model is sensitive to the turbulence intensity in the freestream, which is not measured.
- **The modelling errors**, which are assessed during the validation process. The validation process should be concerning (i) integral quantities (if uncertainties allow), (ii) vortex quantities over its trajectory, (iii) local velocity profiles, and (iv) full velocity planes based on the multivariate metric r/r_{ref}.

Validation data consist of S-PIV measurements of the vortex at several locations downstream of the wing. Also, force measurements are taken, however the experimental uncertainty of these is in the order of 5%. For the validation of the transitional flow, only flow field visualisation of the suction side of the wing is available yet. It was agreed to take S-PIV measurements around the wing at half-span to determine (i) the turbulence intensity of the inflow, and (ii) the transition/separation location. Due to unforeseen problems this validation data-set was not available within the time frame of this thesis. The modelling error of the transition modelled is advised to be assessed later.

6

TRANSITION MODELLING RESULTS

In this chapter, the effect of transition modelling on the structure of the vortex is addressed. With this knowledge, it can be determined whether not controlling transition in experimental measurements (not controlling the transition in this thesis means not tripping the Boundary Layer (BL) or not measuring the transition location) affects the vortex measurements. The main questions reads: can vortex measurements in which transition is not controlled be used for validation purposes, or is more information about the flow field over the wing required? The majority of this chapter has previously been published in Liebrand et al. (2019).

The chapter is structured as follows: first, theoretical arguments regarding the effect of the BL on the vortex are given from which a hypothesis is formulated. After that, two sections with results are presented. The last section presents the conclusion and a discussion concerning the hypothesis.

6.1. INTRODUCTION AND HYPOTHESIS

In Computational Fluid Dynamics (CFD) calculations, difficulties in the prediction of the transition location cause errors in the prediction of the BL profile over the wing. Since the BL rolls up in the wake of a lifting surface, it is evident that the structure of the vortex is related to its characteristics. Maines and Arndt (1997b) observed that "*the vortex mainly interacts with the boundary layer on the suction side of the wing, boundary layer fluid is entrained in the vortex which affects the core radius*". The McCormick (1962) hypothesis relates the BL thickness to the state of the BL. If these observation are combined, the following proportionality is found,

$$\eta_v \sim \delta_s \sim Re_c^{-h}, \tag{6.1}$$

with η_v the viscous core radius, δ_s the BL thickness on the suction side of the wing, and $Re_c = U_\infty c/\nu$ the chord-based Reynolds number. In this equation, U_∞ is the freestream velocity, c the local chord length, and ν the kinematic viscosity. The constant h reflects the state of the BL and is typically about 0.2 for a turbulent BL and 0.4 for a transitional BL (McCormick, 1962).

The flow characteristics within the vortex core play a crucial role in the cavitation inception process as well as the dynamics of the cavity. Bosschers (2018) derived a two-dimensional analytical expression for the velocity and pressure distributions within a cavitating vortex. The derivation is based on the Lamb-Oseen vortex (Lamb, 1932) which is supplemented with jump relations for the mass transfer and shear stress as boundary conditions at the vapour-liquid interface. The resulting analytical expression for the velocity profile in the vortex was already presented in Section 2.3.2. The pressure is supposed to be at its minimum (p_{min}) in the centre of the vortex core ($\eta = 0$). This yields the relation,

$$p(\eta = 0) - p_\infty = p_{min} - p_\infty = -\frac{\rho \Gamma_\infty^2}{(2\pi\eta_v)^2}\zeta \ln(2), \tag{6.2}$$

where the pressure is denoted by p, the freestream pressure by p_∞, fluid density by ρ (which is constant for the wetted flow conditions), and the freestream circulation of the vortex by Γ_∞. The latter is related to the circulation over the wing (Γ_0) through the roll-up process. Analytical expressions to relate the freestream circulation to the Γ_0 exist (e.g. by Kaden (1931) and Moore (1974)) but are found to not always agree experimental results (Phillips,

1981; Staufenbiel, 1984). Incorpreting such a relationship would introduce too much complexity and therefore is was decided to assume $\Gamma_\infty = \Gamma_0$ to test the hypothesis. Furthermore, Schot et al. (2014) observed that the roll-up process is finished between $1.0 < x/c_0 < 2.0$ whereby $\Gamma_\infty \approx \Gamma_0$ is valid after that point anyway. The constant $\zeta = 1.2564$ is introduced to ensure that the azimuthal velocity is maximum at the viscous core radius. Combining Equation (6.1) and Equation (6.2) yields the following proportionality,

$$p(\eta = 0) \sim (\Gamma_\infty/\eta_v)^2 \sim (\Gamma_0/\delta_s)^2 \sim (\Gamma_0/Re_c^{-h})^2, \tag{6.3}$$

which implies that the pressure in the core of the vortex is related to the state of the BL on the suction side of the wing. A transition model delays the mixing properties of the BL which yields a laminar profile over a longer distance compared to a fully turbulent BL assumption. This means that the resulting BL is thinner and thus the viscous core radius smaller, this should result in a lower minimum pressure and therefore more cavitation. While in prior research (Schot, 2014; Asnaghi, 2018) the underpredicted vortex cavity length is explained by (i) overprediction of the eddy-viscosity in the vortex core, and (ii) numerical diffusion, it could be that the assumption of a fully turbulent BL also contributes.

Prior to considering the vortex itself to test this hypothesis, it is important to understand the transitional behaviour of the flow over the foil section under different flow conditions. To this end, a Two-Dimensional (2D) sensitivity analysis of the foil at half-span to the turbulent inflow conditions is performed to acquire a suitable set of inflow conditions to control the BL thickness. This is presented in Section 6.2. Based on these findings, a set of Three-Dimensional (3D) calculations is performed to investigate the effect of the BL on the structure of the the tip vortex in Section 6.3.

6.2. NACA66$_2$ − 415 FOIL (2D ANALYSIS)

The aim of the 2D simulations is to establish a proper set of inflow conditions to eventually test the hypothesis of Equation (6.3) by means of 3D calculations. First, the numerical settings and iterative convergence are discussed. After that, the 2D results are presented.

6.2.1. NUMERICAL SETTINGS

The hypothesis relates the pressure in the vortex to $(\Gamma_0/\delta_s)^2$. To investigate the effect of both quantities, the foil is considered at two Angle(s) of Attack (AoA): 5° and 9°. This is because transition on the suction side for $\alpha = 5°$ is expected to be sensitive to the turbulent inflow conditions (therefore δ_s is expected to vary) while this is not the case for $\alpha = 9°$ (δ_s is constant). This was visualised already in Figure 2.14.

2D steady-state simulations of the wing at half-span ($z/b = 0.5$) are carried out. The $k-\omega$ Shear Stress Transport (SST) turbulence model is supplemented with the $\gamma - \tilde{R}e_{\theta_t}$ transition model. To investigate the effect of the inflow conditions, both the turbulence intensity and eddy-viscosity ratio are varied, i.e. $I = [1,2,3]$% and $\nu_t/\nu = [1,2,3]$. This results in a set of nine different inflow conditions. Furthermore, the transport equations for k and ω are solved without destruction term until $0.1c_0$ upstream of the foil. In the remainder of this thesis this is called 'freezing' and is applied to control turbulence decay in the freestream upstream of the Leading Edge (LE) (Spalart and Rumsey, 2007) which could affect the transition location.

Details of the computational grids and Boundary Condition(s) (BC) can be found in Section 4.4.3. Note that the chord length is unity which was required for the grid generation. The inflow velocity is adapted such that it matches the Reynolds number of the 3D wing at half-span. Further details with regard to the numerical settings, e.g. numerical solvers, convergence criteria, and discretisation schemes, can be found Appendix D.

6.2.2. ITERATIVE CONVERGENCE

ITERATIVE ERROR

To ensure effective use of computational resources, a trade-off between computational cost and iterative error was made. For each AoA, six calculations with different convergence criteria for the maximum residual (L_∞) were performed. The residuals for the transition equations are excluded from these criteria since it was not possible to reach $L_\infty = 10^{-7}$ and $L_\infty = 10^{-8}$ using a First-Order Upwind (FOU) scheme for the convective flux discretisation of γ and $\tilde{R}e_{\theta_t}$. Calculations were performed on the finest grids (i.e. $G^{2D}_{1,5}$ and $G^{2D}_{1,9}$) to minimise the influence of the spatial discretisation error. The turbulent inflow conditions are not varied for this analysis and set to $[I, \nu_t/\nu] = 1$.

Figure 6.1 displays the most relevant quantity for transition, C_{df}, versus the convergence criteria. The right axis shows the computational costs to reach the specified L_∞. By making a trade-off between computational

costs and iterative accuracy, a convergence criterion of $(L_\infty)_{\notin \gamma,\, \tilde{R}e_{\theta_t}} = 10^{-5}$ is considered to be sufficient for both cases. At this level, the iterative errors relative to the 10^{-8} simulation are 0.40% and 0.31% for $\alpha = 5°$ and $\alpha = 9°$ respectively. In order to reduce this error to 0.14% and 0.07% at $(L_\infty)_{\notin \gamma,\, \tilde{R}e_{\theta_t}} = 10^{-6}$, the computational costs increase by 132% and 111% respectively.

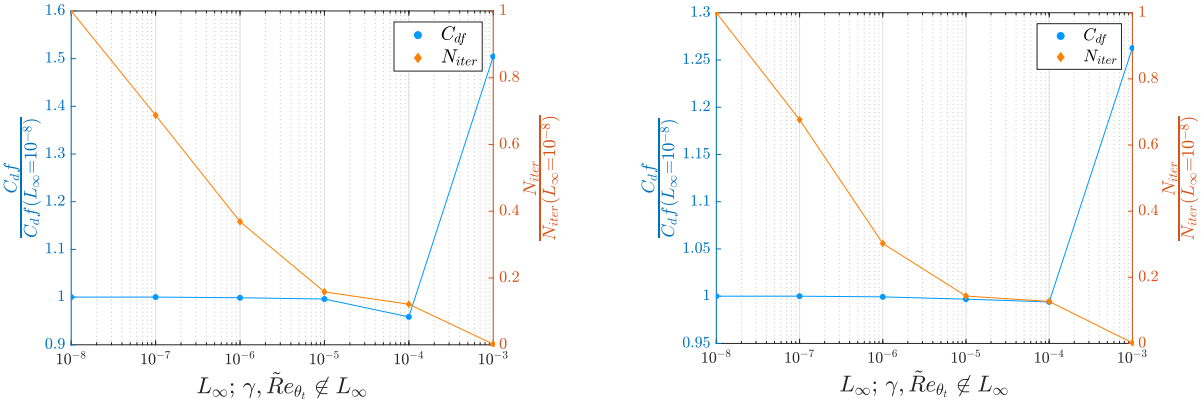

Figure 6.1: Iterative error analysis for $G^{2D}_{1,5}$ (left) and $G^{2D}_{1,9}$ (right), showing the trade-off between numerical accuracy and computational cost.

LOCAL GRID REFINEMENT

A well-known problem of the $\gamma - \tilde{R}e_{\theta_t}$ model is stagnation of the outer loops, see e.g. Baltazar et al. (2018). If a FOU scheme for the discretisation of the convection term in the transport equations of the transition variables is employed, the simulations converge to the residual criterion ($L_\infty = 10^{-5}$). However, when using the Quadratic Upstream Interpolation for Convective Kinematics (QUICK) scheme in all equations the calculations typically stagnate. Although the residuals are not converged, the forces are observed to be constant over the stagnated outer loops.

The stagnating behaviour is related to the transition location continuously switching between two streamwise cells. If the location moves to the neighbouring cell, the flow-field adapts itself accordingly whereafter the transition location moves back to the original location. This can be explained by the fact that the γ-production is triggered by the limiter $F_{onset} = \max(F_{onset2} - F_{onset3}, 0)$, see Section 3.1. In the γ-production term, the magnitude of F_{length} is typically large whereby the production increases drastically when F_{onset2} exceeds F_{onset3}. F_{onset3} is relatively constant throughout the simulation since it only depends on the turbulent kinetic energy (k) and the specific dissipation rate (ω). The main term responsible for triggering the onset of production is thus F_{onset2}. This term is implicitly related to the strain-rate tensor (S_{ij}) in the flow by $F_{onset2} \sim F_{onset1} \sim Re_V \sim S_{ij}$. This causes the observed behaviour: When production of γ starts, P_k, and thus k and ν_t, increase. The resulting higher eddy-viscosity smooths the solution which reduces the magnitude of the gradients. This results in a lower strain-rate causing $Re_V \sim F_{onset1} \sim F_{onset2}$ to drop. If this drop is sufficient, the magnitude of F_{onset2} ends up lower than F_{onset3} whereby the limiter cancels the production term again. Although F_{onset3} is introduced to avoid this sort of behaviour Langtry (2006), it fails to do so in this case. Increasing the streamwise resolution of the grid is therefore supposed to avoid stagnation.

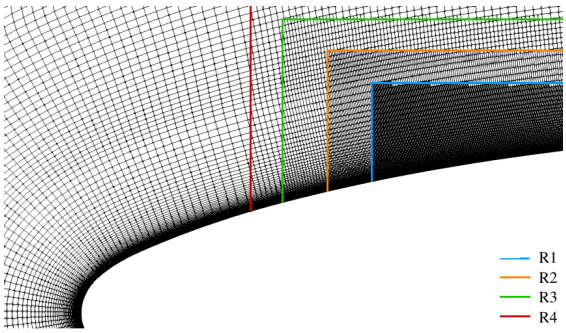

Figure 6.2: Grid of the suction side at the LE, $G^{2D}_{4,5}$. Colours indicate refinement levels.

This reasoning is tested by means of local grid refinement (h-refinement) at the transition location (x_{tr}). The transition location is defined as the point where the derivative of the skin friction changes from negative to positive. If the grid is sufficiently fine in the tangential direction (x_t^+), the iterative stagnating behaviour should be absent. The four different refinement levels applied at the suction side (R1-4) are shown in Figure 6.2. All refinement levels are applied on $G^{2D}_{4,5}$

The largest residuals in the original simulation were located at the point of transition on the suction side of the foil. Only refining at that location does not yield convergence but shifts the maximum residual towards the transition location at the pressure side. Convergence is obtained when the grid around both transition locations is sufficiently refined while controlling the grid diffusion. The diffusion of the grid is controlled by using several boxes around each other such that the grid resolution is gradually increased. Table 6.1 presents all relevant quantities of the refined grids.

Table 6.1: Results for locally refined grids on the suction side (left) and pressure side (right) of the foil. Values for x_t^+ at the transition location and x_{tr} given for the corresponding side. x_t^+ on opposite side was 9.1 for simulations a-d, and 11.8 for simulations e-h.

Sim.	$N_c/10^5$	x_t^+	$\frac{C_l}{(C_l)_{d,h}}$	$\frac{C_{df}}{(C_{df})_{d,h}}$	$\frac{x_{tr}}{(x_{tr})_{d,h}}$
a	1.35	99.1	1.0012	0.9950	1.0308
b	1.43	47.3	1.0006	0.9973	1.0301
c	1.58	23.7	1.0005	0.9989	1.0240
d	1.89	11.8	1.0000	1.0000	1.0000

Sim.	$N_c/10^5$	x_t^+	$\frac{C_l}{(C_l)_{d,h}}$	$\frac{C_{df}}{(C_{df})_{d,h}}$	$\frac{x_{tr}}{(x_{tr})_{d,h}}$
e	1.59	71.8	1.0008	1.0006	0.9997
f	1.63	36.2	1.0003	0.9986	1.0006
g	1.72	18.2	1.0003	0.9987	1.0002
h	1.89	9.1	1.0000	1.0000	1.0000

When a QUICK scheme is used to determine the convective fluxes of the transition variables without local grid refinement, the computation typically stagnates with the γ-residual being the largest as shown in Figure 6.3. Figure 6.4 displays the residuals of the γ-equation for all refinement levels. In order to obtain convergence, a maximum x_t^+ of ~ 24 and ~ 36 is required on the suction and pressure side respectively. These values are expected to be case specific. Table 6.1 also includes the lift coefficient, skin friction drag coefficient, and transition location on the suction side with respect to the results of the d,h simulation (finest grid on both sides of the foil). The quantities appear to be within 0.12%, 0.5%, and 3.08% respectively. This shows that the actual flow fields obtained by a stagnated solution (e.g. simulation a or e) do not deviate much with respect to a converged simulation (simulation d,h).

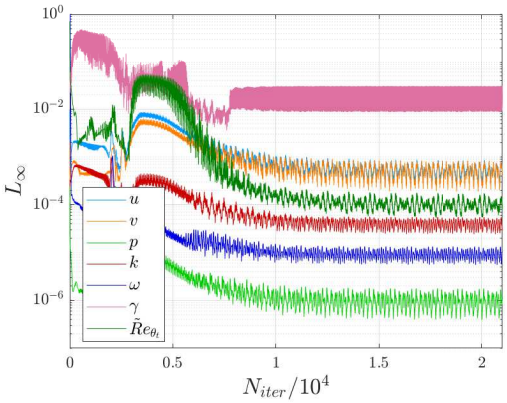

Figure 6.3: Convergence plot for $\gamma - \tilde{R}e_{\theta_t}$ simulations on $G^{2D}_{4,5}$. QUICK is employed for all flux discretisations.

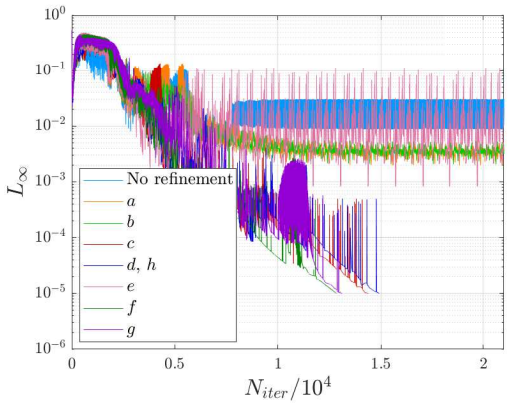

Figure 6.4: Convergence of γ-residual for all simulations of in Table 6.1. Stagnated QUICK simulation is also included.

6.2.3. SENSITIVITY TO INFLOW CONDITIONS

A final simulation was performed using the minimum required x_t^+ values. This converged QUICK simulation only differs 0.65% for C_l, 0.25% for C_{df}, and 0.96% for x_{tr} with respect to a converged FOU simulation without refinement. Considering the increase of computational cost of local grid refinement to obtain convergence if a QUICK scheme is employed in all equations, it was decided to use the FOU scheme for the transition variables in this sensitivity analysis.

Figure 6.5 presents the sensitivity of the integral forces to the turbulent inflow conditions. The SST result for $I = 1\%$ and $\nu_t/\nu = 1$ is also given in blue. All results are normalised by the $\gamma - \tilde{R}e_{\theta_t}$ simulation with $I = 1\%$ and $\nu_t/\nu = 1$ ($[I, \nu_t/\nu] = 1.0$). I.e., if the turbulence intensity and eddy-viscosity ratio are both increased to 2, the skin friction increases with about 10% for $\alpha = 5°$. Transition predominantly affects the C_{df} since it changes the shape of the BL and thus the velocity derivative at the wall, $C_{df} \sim \tau_w \equiv \mu(\partial u/\partial y)_{y=0}$. Furthermore, the transition model influences the pressure distribution and thus the lift coefficient by its ability to capture an Laminar Separation Bubble (LSB) or predicting laminar and turbulent separation more accurately.

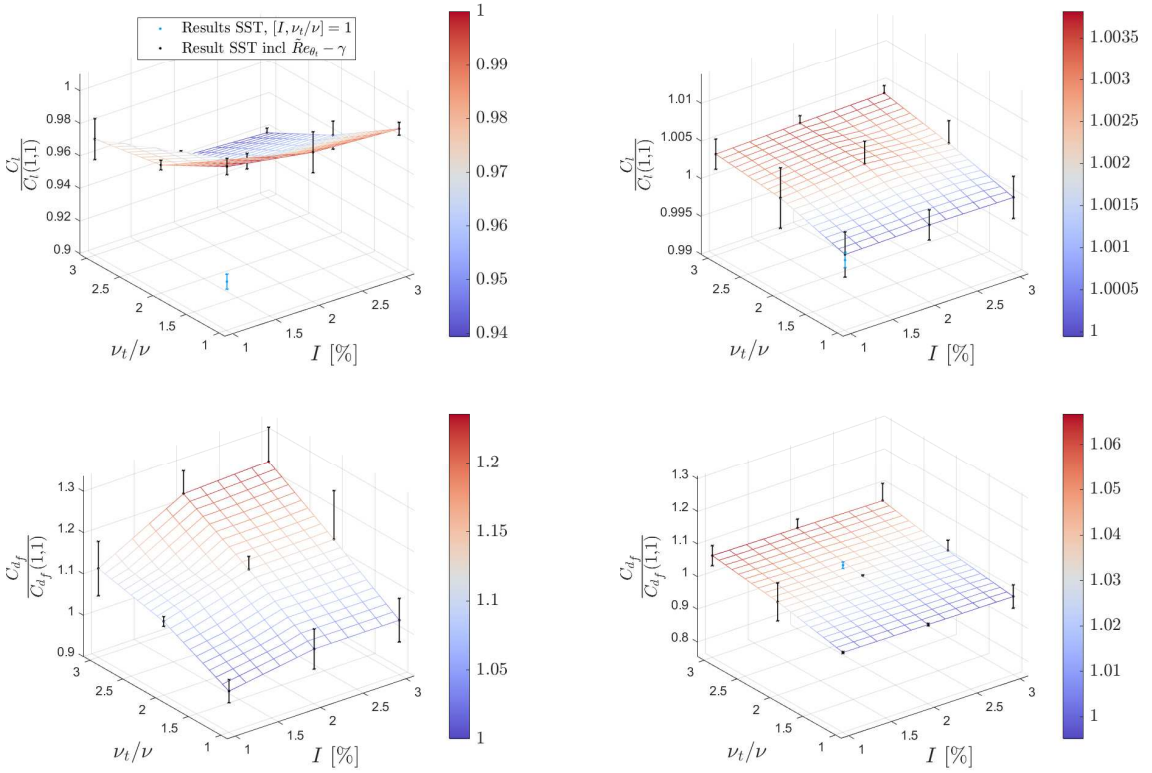

Figure 6.5: Sensitivity of the normalised lift (top) and skin friction drag (bottom) coefficients to the turbulent inflow conditions for $\alpha = 5°$ (left) and $\alpha = 9°$ (right), results for G_1^{2D}. The error bars indicate the discretisation uncertainty for the same grid.

The skin friction drag for both AoA is significantly affected by the change of turbulent inflow conditions; it increases about 25% for $\alpha = 5°$ and 6% for $\alpha = 9°$. This is due to the up- or downstream movement of the transition location on the suction and pressure side of the foil. It can be observed that C_{df} for $\alpha = 9°$ is less sensitive to the turbulent inflow conditions. This is due to the high LE curvature at a higher AoA, which forces transition independently of the turbulent state of the inflow. This is confirmed by the skin friction distributions shown in Figure 6.6 where the high curvature of the LE causes the magnitude of the skin friction to be large for $x_{LE}/c_0 < 0.1$ and therefore triggers transition. For $\alpha = 5°$, transition on the suction side occurs at $x/c \simeq 0.2$ resulting in a completely different distribution.

As expected, the lift coefficient is less sensitive to the turbulent inflow quantities. For $\alpha = 5°$, the change in lift coefficient is at maximum 6%, for $\alpha = 9°$ this reduces to only 0.4%. The fact that the 5 degrees AoA case is influenced more, is again due to the shift in transition location on the suction side. The location where the flow undergoes transition determines its sensitivity to turbulent separation at the aft of the foil. This can be recognised in the friction and pressure distributions in Figure 6.6 as C_f is smaller than zero near the Trailing Edge (TE) for the $\alpha = 5°$, $\gamma - \tilde{R}e_{\theta_t}$ simulation. For both AoA, the lift coefficients predicted by the SST simulations are lower compared to the $\gamma - \tilde{R}e_{\theta_t}$ simulations. The LSB on the pressure side, captured by the $\gamma - \tilde{R}e_{\theta_t}$ model, is partly responsible for this. For both AoA, the bubble is located at $x_{LE}/c_0 \approx 0.75$ of the foil, Figure 6.6 shows that this causes an increased pressure (the curves shift downwards in the pressure distribution since the vertical axis is plotted inversely) on the pressure side and therefore a slightly higher lift coefficient. The lift coefficient for the $\alpha = 5°$ case is also more sensitive due to the change in BL thickness. The change in BL thickness affects the effective chamber and thickness of the foil. This could increase or decrease the lift coefficient compared to a fully turbulent BL depending on the curvature of the foil, transition location on both sides of the foil, and AoA.

To further clarify the sensitivities of the integral quantities, Figure 6.7 presents the sensitivity of the transition locations. All results are reported with respect to the transition location for $[I, \nu_t/\nu] = 1.0$ again. I.e., if turbulence intensity and eddy-viscosity ratios are both increased to a value of 2, the transition location at the suction side for $\alpha = 5°$ shifts about 0.08 chords upstream.

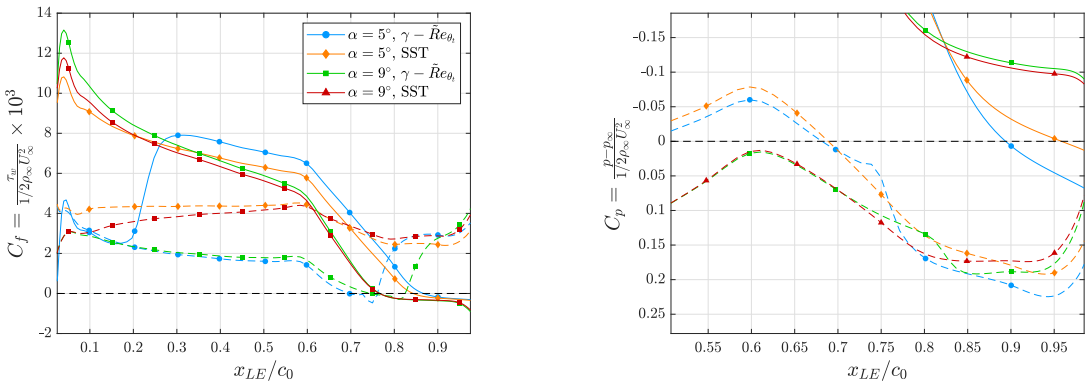

Figure 6.6: Skin friction (left) and pressure (right) distributions for both AoA. Both SST and $\gamma - \tilde{Re}_{\theta_t}$ ($[I, \nu_t/\nu] = 1$) results are shown. Solid lines indicate distributions over the suction side of the foil, dashed lines over the pressure side.

The transition location on the suction side for $\alpha = 5°$ moves 15% upstream if both quantities are tripled. This is intuitive since more energetic turbulence upstream should yield earlier transition. In the model, this is incorporated by the empirical relation between I and the global Re_{θ_t}: an increased I yields the global Re_{θ_t} to be lower whereby this value is more 'diffused' into the BL which encourages production of γ and thus triggers transition. It is interesting to note that the results are much less sensitive when either of the two turbulence quantities is varied. This is due to the decay of turbulence in the region just upstream of the wing (the quantites are frozen in the inflow). Increasing the eddy-viscosity ratio accordingly avoids this since a higher ν_t/ν reduces the damping (Spalart and Rumsey, 2007). For $\alpha = 9°$, the transition location on the suction side is barely changed, a maximum shift of 0.3% is observed. This is due to the reason given earlier: the curvature of the foil triggering transition just downstream of the LE regardless of the turbulent inflow conditions.

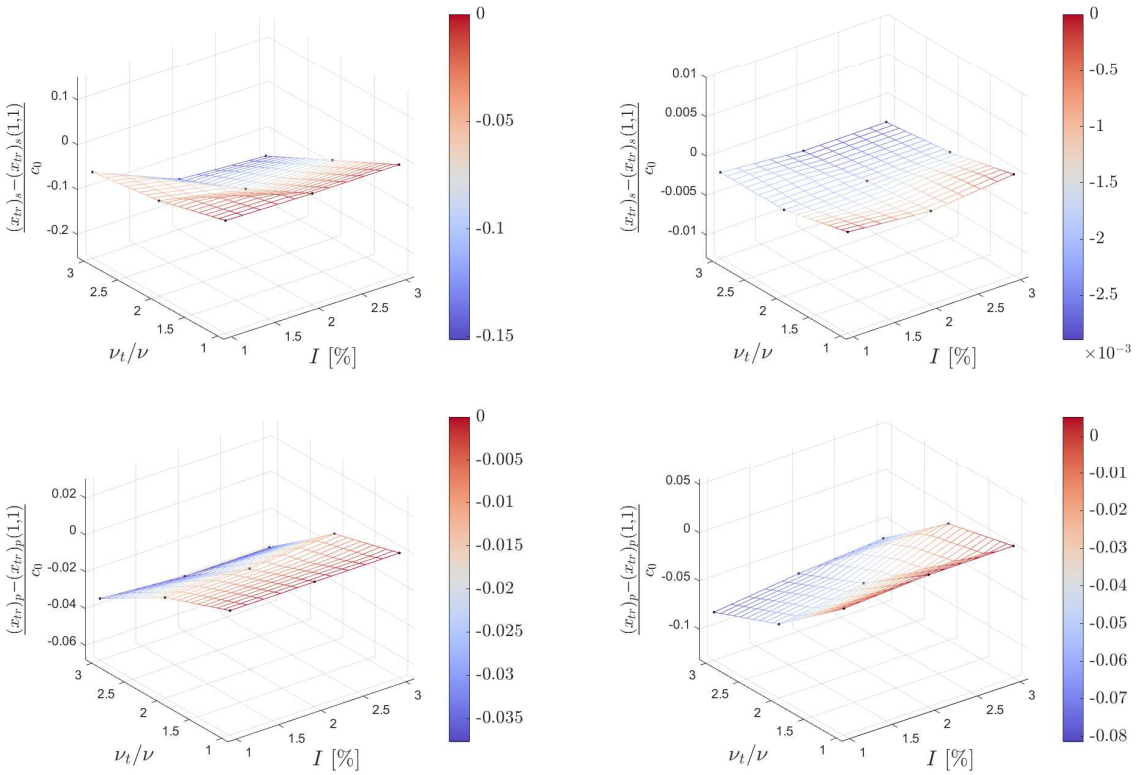

Figure 6.7: Sensitivity of the transition location on the suction (top) and pressure (bottom) sides to the turbulent inflow conditions for $\alpha = 5°$ (left) and $\alpha = 9°$ (right), results for G_1^{2D}.

Transition on the pressure side is triggered at almost the same location for both cases. This location varies more for $\alpha = 9°$ (maximum of $\sim 0.08c$) than for $\alpha = 5°$ (maximum of $\sim 0.035c$). The transition location of the pressure side is much less sensitive to the turbulent inflow conditions compared the the transition location on the suction side for $\alpha = 5°$. This is because the flow is 'pushed' against the inclined wing which makes the BL more stable. For both cases, it moves upstream for the reasons previously given. This causes the BL to become turbulent sooner.

So the increase in C_{df} is predominantly explained by the changing transition location on the suction side of the wing. This is exactly what is desired in 3D simulations to actually test the hypothesis: varying the turbulent inflow conditions causes the transition location on the suction side for $\alpha = 5°$ to shift while it is fixed for $\alpha = 9°$. This set of turbulent inflow conditions is therefore advised for the 3D simulations as well, however, to amplify the effect it is advised to increase the range slightly: from 0.5 to 4.0 instead of 1.0 to 3.0. Also, it is observed that the transition location is only sensitive to the varied inflow conditions if (i) the quantities are changed simultaneously, and (ii) the turbulence quantities are frozen until $0.1c_0$ upstream of the wing's LE.

6.2.4. BOUNDARY LAYER CHARACTERISTICS

The effect of the changed transition location on the suction side for $\alpha = 5°$ is investigated by analysing the BL profiles at different locations. The BL profiles are obtained by using line monitors in ReFRESCO. The surface normals ($\vec{n}_s$) are used to extract all three components of the velocity ($w = 0$ for the 2D computations). For $\alpha = 5°$ and $[I, \nu_t/\nu] = 1$, transition occurs at $x_{LE}/c_0 \approx 0.25$ as shown in the skin friction distribution of Figure 6.6. The corresponding BL profiles for $0.15 \leq x_{LE}/c_0 \leq 0.35$ for the transitional BL ($\gamma - \tilde{R}e_{\theta_t}$), as well as, the fully turbulent BL (SST) are shown in Figure 6.8. Here x_{LE} denotes the streamwise distance with respect to the LE. The BL for the SST simulation is indeed fully turbulent over the considered region. Clearly, the flow undergoes laminar-to-turbulent transition for the $\gamma - \tilde{R}e_{\theta_t}$ model as the profiles become 'fuller'. This is also recognisable in the shape factors (H): for the SST simulation $H \approx 1.6$, for the transition BL it decreases from about 2.7 to 1.7 (the definition of the shape factor was addressed in Section 3.1).

These values are consistently higher compared to the values for a turbulent BL ($H \approx 1.4$) and a Blasius solution ($H = 2.6$). This implies that the BL profiles are 'emptier' compared to a fully developed turbulent or laminar BL on a flat plate. Intuitively this makes sense since at the considered region, $0.15 \leq x_{LE}/c_0 \leq 0.35$, the foil's geometry yields an adverse pressure gradient which 'pushes' the flow back. This pressure gradient locally decreases the production of turbulence (Pope, 2000). Mathematically, this can substantiated by considering the x-momentum equation at the wall ($y = 0$). Both velocity components have to be zero at that location which results in,

$$\left.\frac{\partial^2 u}{\partial y^2}\right|_{y=0} = \frac{1}{\nu}\frac{dp}{dx}, \tag{6.4}$$

which implies that a negative pressure gradient yields the second derivative of the velocity with respect to y to be negative as well. This yields the BL-profiles to be emptier with consequently a higher value for its shape factor.

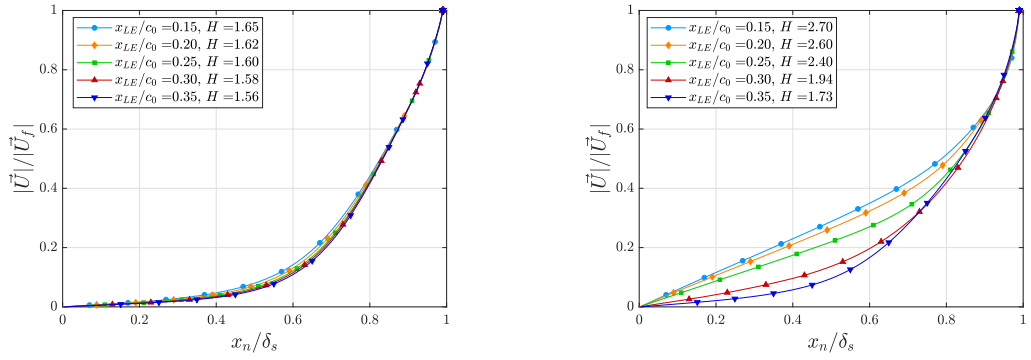

Figure 6.8: BL profiles for different locations along the chord, pure SST simulation (left); $\gamma - \tilde{R}e_{\theta_t}$ model applied (right). $[I, \nu_t/\nu] = 1$ for both computations. $\vec{U}_f$ represents the velocity vector in the freestream above the considered chord-wise location and x_n the normal distance to the wall.

The corresponding BL thickness over the same chordwise positions ($0.15 \leq x_{LE}/c_0 \leq 0.35$) is shown in Figure 6.9. It is clear that applying the $\gamma - \tilde{R}e_{\theta_t}$ transition model decreases the BL thickness. Laminar to turbulent transition can be recognised since the slope ($d\delta_s/dx_{LE}$) increases so the BL thickness start growing quicker. At the end, $x_{LE}/c_0 \approx 0.35$, this slope almost matches the slope for the fully turbulent BL implying that transition is almost finished. So the transition model causes changes on the the shape factor and the thickness of the BL. The difference in BL thickness is almost a factor 2 at this chordwise position.

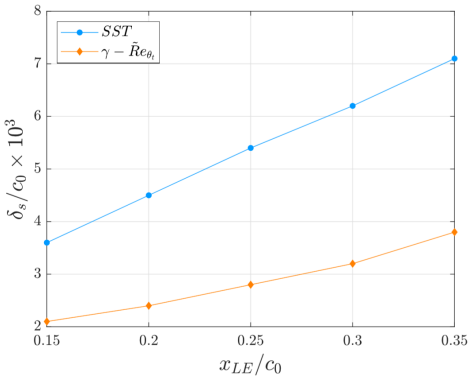

Figure 6.9: BL thickness on the suction side for $0.15 \leq x_{LE}/c_0 \leq 0.35$ at $\alpha = 5°$ for the SST simulation and $\gamma - \tilde{R}e_{\theta_t}$ model. For both simulations the turbulent inflow conditions are $[I, \nu_t/\nu] = 1$, and $G^{2D}_{1,5}$ is used.

6.2.5. 2D CONCLUSIONS

Local grid refinement around the transition location was found to improve convergence when a QUICK scheme for the convective flux discretisation in the transport equations of γ and $\tilde{R}e_{\theta_t}$ is used. Results for C_l, C_{df} and x_{tr} obtained using the QUICK scheme and the FOU scheme are found to be within 1%. Based on a trade-off between the discrepancy of the forces and the additional computational costs to perform local grid refinement, it was decided to use the FOU scheme during the sensitivity analysis. Whether this is also true for the 3D simulations has still to be addressed.

It was observed that C_{df} is much more sensitive to the turbulent inflow conditions for $\alpha = 5°$ than for $\alpha = 9°$. The lift coefficient is found to be relatively constant for both AoA. Accounting for transition results in an LSB on the pressure side of the foil for both AoA. Varying the inflow conditions from 1.0 to 3.0 caused the transition location on the suction side to move $0.15c$ upstream. The effect was also observed in the BL profiles and the corresponding BL thickness. For this reason a similar range for the turbulent inflow quantities is advised for the 3D simulations, however somewhat extended ($[I, \nu_t/\nu] = [0.5, 1.0, 2.0, 4.0]$) to acquire a larger sensitivity. To obtain this sensitivity it is required to (i) vary the turbulence quantities simultaneously, and (ii) freeze the turbulence quantities until $0.1c$ upstream of the LE to avoid problems with decay.

6.3. BL-VORTEX INTERACTION (3D ANALYSIS)

The 2D sensitivity analysis provided a valuable set of inflow conditions and insight into the behaviour of the $\gamma - \tilde{R}e_{\theta_t}$ model for this test case. In this section, the actual hypothesis is tested. The effect of the BL on the vortex itself is examined in this section by means of 3D calculations.

6.3.1. NUMERICAL SETTINGS

The wing is considered at $\alpha = 5°$ and $\alpha = 9°$ for the reasons given earlier. The simulations are still steady state since experimentally (e.g. by Higuchi et al. (1987) and Arndt et al. (1991)) as well as numerically (e.g. by Schot (2014) and Asnaghi (2018)) no large separation regions are observed nor is there any evidence for shedding of trailing vortices. The inflow conditions as found in the 2D study are used.

Multi-block hexahedral structured grids with adaptive grid refinement in the wake and vortex regions are used. Details of the grids and the adaptive grid refinement process are described in Section 4.4.1. Further numerical settings are similar to the 2D simulation, they can also be found in Appendix D.

6.3.2. ITERATIVE CONVERGENCE

To improve iterative convergence, again local grid refinement at the transition location is applied. Both the suction and pressure side are locally refined until the requirements ($x_t^+ < 24$ and $x_t^+ < 36$ for suction and pressure side respectively) are met. Not only the tangential cell size is reduced but also the cell size in spanwise direction to account for cross-flow. Table 6.2 presents the details of the refined grids.

Despite the increased resolution at the transition location in both directions, the solution still stagnates as can be seen in the convergence plots of γ in Figure 6.10 (the residual of the γ-equation is dominant in all simulations). The magnitude of the maximum residual (L_∞) is not changed by the local grid refinement, however, the Root Mean Square (RMS) of the residual vector (L_2) drops half an order of magnitude.

Table 6.2: Grid details of locally refined grids. N_c denotes the number of grids cell, x_t^+ the non-dimensional cell-size in tangential direction, and x_s^+ in spanwise direction. The cell-sizes are determined at the transition location and averaged over the span of the wing indicated by $\overline{(\cdot)}_{tr,suc/pres}$.

Sim.	$N_c/10^6$	$\overline{(x_t^+)}_{tr,suc}$	$\overline{(x_s^+)}_{tr,suc}$	$\overline{(x_t^+)}_{tr,pres}$	$\overline{(x_s^+)}_{tr,pres}$	$C_l/(C_l)_m$	$C_{df}/(C_{df})_m$
i	2.69	161	434	289	273	0.9978	0.9852
j	2.78	109	297	178	198	0.9992	0.9870
k	3.13	64.9	172	94.9	109	0.9995	0.9956
l	4.44	34.0	91.3	50.6	63.2	1.0003	0.9920
m	9.51	26.3	88.5	26.7	33.2	1.0000	1.0000

To get more insight into the stagnation problem, isocontour plots of the maximum γ-residuals are shown in Figure 6.11. The maximum residuals are observed to be located at the transition location (just above the LSB) on the pressure side of the wing. It is clear that the region of $(L_\infty)_\gamma = 1.5 \times 10^{-1}$ decreases as the grid is refined around the transition location. For the finest grids, still small regions where $(L_\infty)_\gamma = 1.5 \times 10^{-1}$ remain. These regions are just before the tip and near the root and lie within the refined region. No maximum residuals are found to be outside of the refinement region.

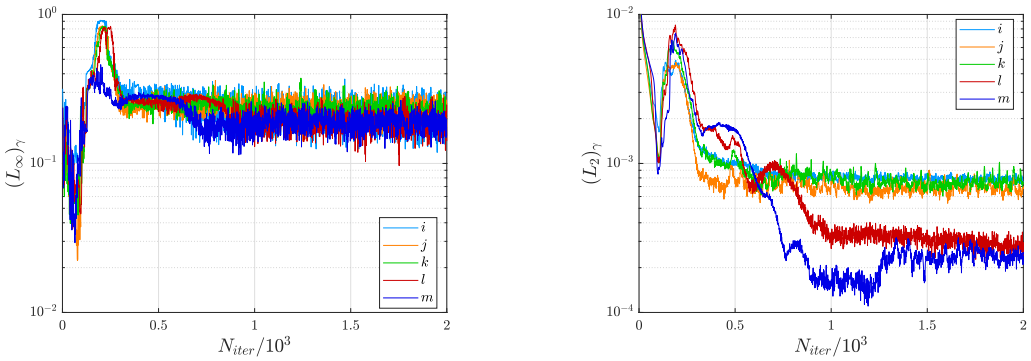

Figure 6.10: Convergence plot of γ transport equation, maximum of the residual vector (left) and RMS of the residual vector (right).

For the remainder of the 3D calculations it is decided to proceed without local grid refinement. This because (i) no convergence is obtained despite the increased resolution in both tangential and spanwise directions, (ii) the lift coefficient is within 0.3% compared to the finest grid (see Table 6.2), (iii) skin friction drag coefficient is within 1.5% of the finest grid (see Table 6.2), (iv) forces are observed to be totally constant over the stagnated region (the standard deviation of the time signal of both forces over the last 100 iterations is less than 1×10^{-6}), and (v) computational costs would almost triple.

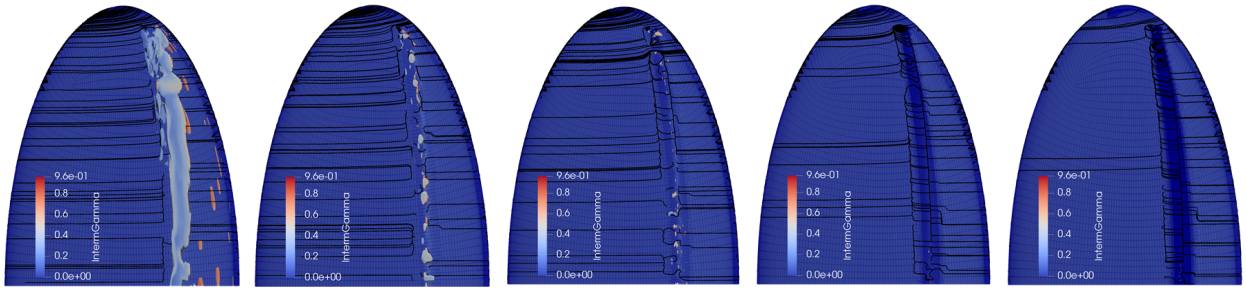

Figure 6.11: Isocontour plots of $(L_\infty)_\gamma = 1.5 \times 10^{-1}$ at the pressure side of the wing at $\alpha = 5°$. Isocontour is coloured by the intermittency, limiting streamlines are also shown. From left to right: simulation i, j, k, l, and m.

6.3.3. BOUNDARY LAYER CHARACTERISTICS

$\alpha = 5°$

To visualise transitional flows on 3D bodies, either contour plots of the magnitude of the shear stress or limiting streamlines are used in literature (see e.g. Reverberi et al. (2016) and Langtry and Menter (2005)). Limiting streamlines provide more details into the flow direction and are therefore used here. Limiting streamlines are the paths parallel to the shear stress vector at the wall, i.e. $\vec{ds} \times \vec{\tau}_w = 0$. Here $\vec{ds}$ is the limiting streamline and $\vec{\tau}_w$ the shear stress vector at the wall. In ReFRESCO, the latter is determined according to the definition which, for a horizontal flat plate reads, $\tau_w = \mu(\partial u/\partial y)_{y=0}$. Here μ is the dynamic viscosity, u is the axial velocity (parallel to the plate) and the y the coordinate normal to the wall. Figure 6.12 present part of a curved wall with normal $\vec{n}_s$ and wall bounded cell with coordinate system (x',y',z'). There is not flux through the wall whereby the velocity components in z' direction is zero. If the velocity component in x' and y' direction are non-zero (they are zero at the wall though), the local wall shear stress vector $\vec{\tau}'_w$ reads,

$$\vec{\tau}'_w = [\partial u'/\partial z' \quad \partial v'/\partial z' \quad 0]^T = [\Delta u'/\Delta z' \quad \Delta v'/\Delta z' \quad 0]^T = [u'/d \quad v'/d \quad 0]^T. \tag{6.5}$$

To convert this to the global reference system, the dot product between the local wall shear stress vector and the normal of the surface is taken, i.e. $\vec{\tau}_w = \vec{\tau}'_w \cdot \vec{n}_s$.

The limiting stream lines for both sides of the wing are shown in Figure 6.13. For the SST simulation, the BL over the entire wing is turbulent and turbulent separation occurs just before the TE. All the transition simulations show a LSB on both sides over (part of) the span, decreasing the turbulence inflow quantities yields the bubble to become larger in streamwise and spanwise direction. Due to the presence of the LSB the BL is more resistant to flow separation near the TE of the wing on the suction side. From these global flow fields, it is evident that this set of inflow conditions mainly impacts the flow pattern over the suction side of the wing and that the inflow quantities in the 2D simulations are the right ones to test the hypothesis.

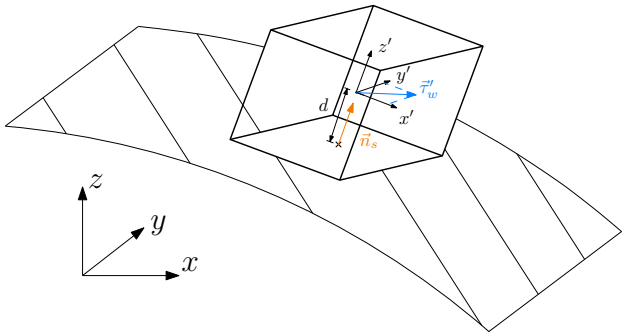

Figure 6.12: Schematic visualisation of the calculation of the wall shear stress vector in ReFRESCO.

To determine the effect on the actual BL thickness, two cross-sections along wingspan are considered. The first is at half-span (z/b=0.5, the location considered in the 2D calculations), the second at $z/b = 0.925$ as indicated by sections A-A and B-B in Figure 6.13. Figure 6.14 presents the corresponding BL characteristics along the chord for the two spanwise locations. The shape factors clearly indicate a turbulent BL for the SST simulation which results in the thickest BL. At half-span, the point of transition lies at $x_{LE}/c_0 \approx 0.7$ for all $\gamma - \tilde{Re}_{\theta_t}$ simulations except when the inflow conditions are set to $[I, \nu_t/\nu] = 4.0$. In that case the flow undergoes transition at $x_{LE}/c_0 \approx 0.2$. This is also reflected by $(\delta_s)_{[I,\nu_t/\nu]=4.0}$ which lies between the fully turbulent BL and the others. Near the tip ($z/b = 0.925$) all $\gamma - \tilde{Re}_{\theta_t}$ simulations undergo transition at 60-70% of the chord. This results in a constant BL of $\delta_s/c_0 \approx 0.4 \times 10^{-2}$ at $x_{LE}/c_0 = 0.8$. For both spanwise locations, the BL thickness of the $[I, \nu_t/\nu] = 0.5$ simulation is almost a factor three thinner compared to the SST result.

Note that the BL characteristics are monitored until $x_{LE}/c_0 = 0.99$, however not shown since turbulent separation for some cases results in large values for δ_s and H, making the graphs unreadable. The trend which is observed until $x_{LE}/c_0 = 0.8$ remains over the last part of the chord as well. The discretisation uncertainty is only determined for the shape factor at $x_{LE}/c_0 = 0.5$ as indicated by the error bars in the H graphs. They are all within 5%. The numerical uncertainties for the BL thickness are not displayed since the post-processing steps make this estimate unreliable. This is because the BL profiles are extracted from the CFD simulation by means of a 'nearest-cell' interpolation. The thickness can thus either be constant for two subsequent grid refinements, resulting in an uncertainty of zero, or be a step function, resulting a large uncertainty.

$\alpha = 9°$

For the higher AoA, the same set of plots is made. The visualisation of the limiting streamlines is not included here since (i) the limiting streamlines on the pressure side are similar to the $\alpha = 5°$ case shown in Figure 6.13, and (ii)

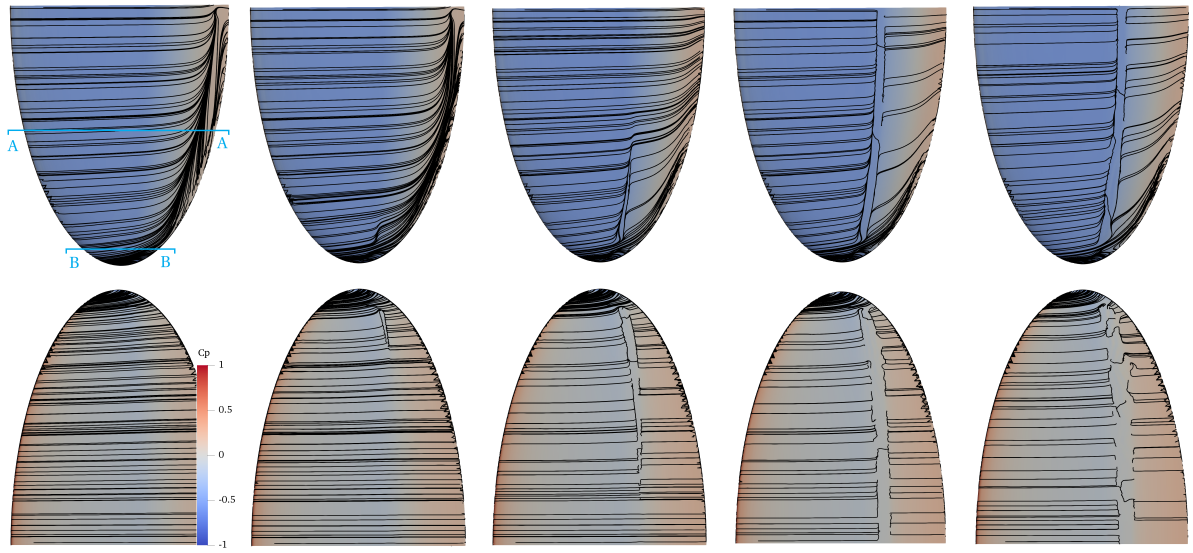

(a) SST (b) $[I, \nu_t/\nu] = 4.0$ (c) $[I, \nu_t/\nu] = 2.0$ (d) $[I, \nu_t/\nu] = 1.0$ (e) $[I, \nu_t/\nu] = 0.5$

Figure 6.13: Limiting streamlines over suction (top) and pressure (bottom) sides of the foil for different turbulent inflow conditions, wing coloured by the pressure coefficient. Top left figure indicates cross-sections A-A and B-B which are located at $z/b = 0.5$ and $z/b = 0.925$ respectively.

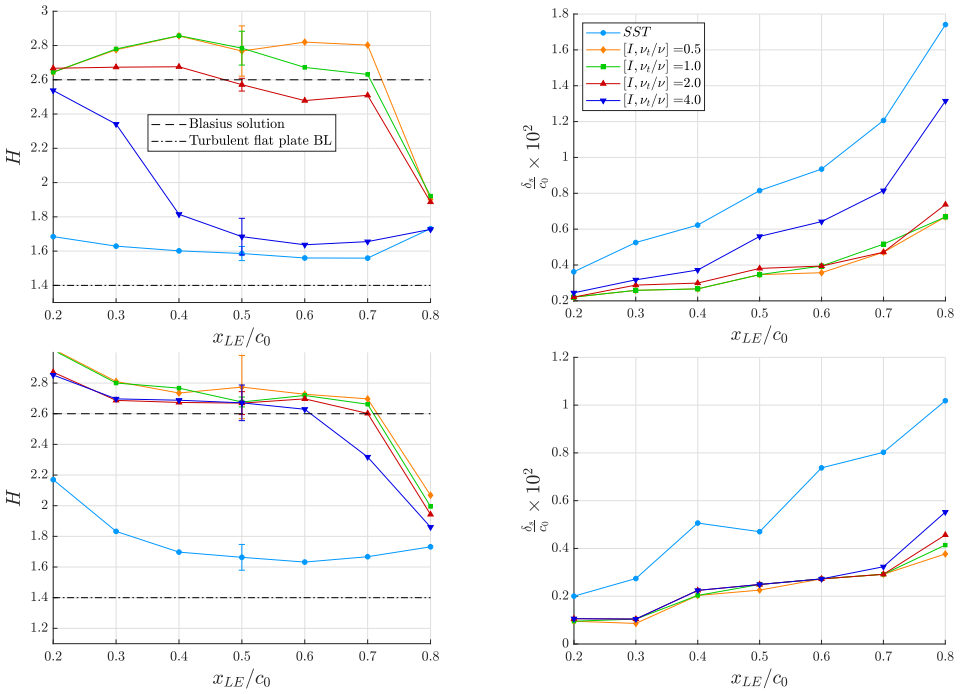

Figure 6.14: BL characteristics along the chord, shape factor (left) and BL thickness (right), for spanwise locations, $z/b = 0.5$ (top) and $z/b = 0.925$ (bottom). Wing at $\alpha = 5°$, grid $G^{3D}_{1,5}$ is used, and error bars indicate spatial discretisation uncertainty.

the limiting streamlines for the suction side all show that transition occurs just after the wing's LE and turbulent separation at about 90% of the chord. The only exception is the $[I, \nu_t/\nu] = 0.5$ case which has a small LSB on the suction side near the tip (at $0.8 \leq z/b \leq 1.0$).

Figure 6.15 presents the BL characteristics for both spanwise cross-sections. It can be observed that at $z/b = 0.5$ transition is triggered upstream of $x_{LE}/c_0 = 0.2$ regardless of the turbulent inflow conditions. This is also visible in the thickness of the BL which is much less sensitive to the turbulent inflow conditions. Due to the smaller chord length at $z/b = 0.925$ ($c_{z/b=0.925}/c_{z/b=0.5} = 46.9/109 \approx 0.32$), the absolute distance between these transition locations is relatively small whereby the BL thickness is not much affected. An additional point to make is the high value of the shape factor at $z/b = 0.925$, $x_{LE}/c_0 = 0.7$ for $[I, \nu_t/\nu] = 0.5$. This is because the LSB is located exactly at that location. This changes the BL profile and consequently the shape factor and BL thickness (at $x_{LE}/c_0 = 0.7$ the H and δ_s are overpredicted).

For both spanwise locations, the BL thickness on the suction side of the wing is less sensitive to the turbulent inflow conditions compared to the $\alpha = 5°$: for $\alpha = 5°$, δ_s is changed by a factor of three while for $\alpha = 9°$ the thickness is at maximum a factor 1.4 thinner compared to the fully turbulent BL. According to the hypothesis, the viscous core size and consequently the pressure in the vortex for the $\alpha = 5°$ case should be affected more than the $\alpha = 9°$ case if Γ_∞ is assumed to be constant. This is investigated next.

6.3.4. VORTEX CHARACTERISTICS

In this section the last part of the hypothesis is tested, i.e. $p(\eta = 0) \sim (\Gamma_0/\eta_v)^2 \sim (\Gamma_0/\delta_s)^2$. This is checked for both AoA. It is observed that the vortex trajectory is not much affected by applying the transition model and therefore these results are not presented.

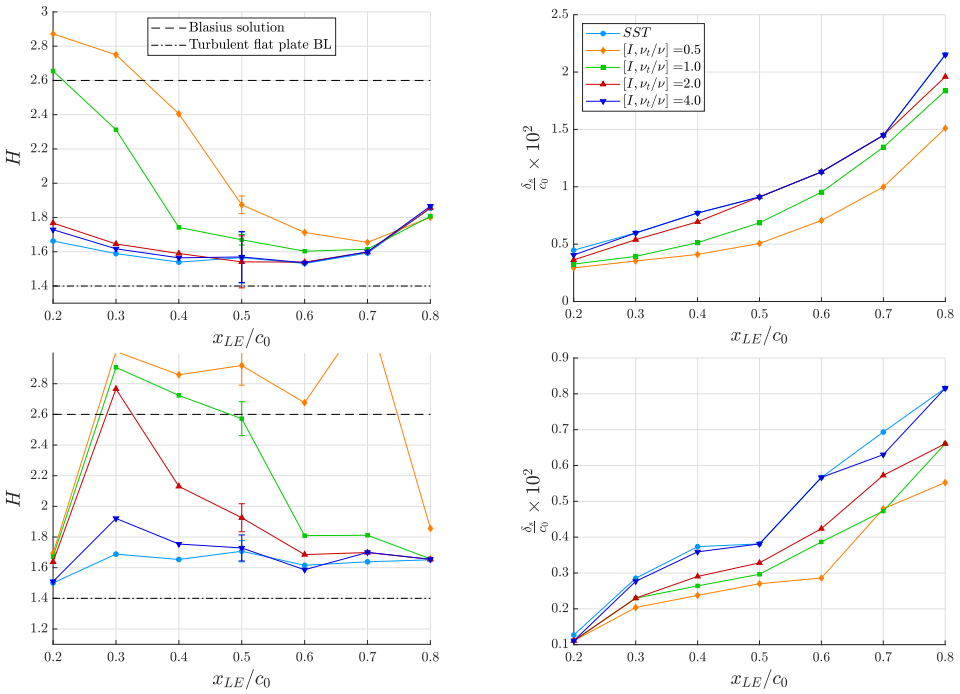

Figure 6.15: BL characteristics along the chord, shape factor (left) and BL thickness (right), for spanwise locations, $z/b = 0.5$ (top) and $z/b = 0.925$ (bottom). Wing at $\alpha = 9°$, grid $G^{3D}_{1,9}$ is used, and error bars indicate spatial discretisation uncertainty.

$\alpha = 5°$

In the previous section, it was concluded that the trailing BL for $\alpha = 5°$ is sensitive to the turbulent inflow conditions and can decrease by a factor of three when the $\gamma - \tilde{R}e_{\theta_t}$ model is applied. Figure 6.16 presents the two most important vortex parameters over the vortex trajectory to test the hypothesis: the viscous core size (η_v) and pressure coefficient in the vortex centre ($(C_p)_{\eta=0}$). It is observed that thinner boundary layers decrease the viscous core radius along the vortex trajectory. The circulation over the wing is observed to be relatively constant for

$\alpha = 5°$ which is because the increased LSB length on the pressure side which decreases the lift while less separated flow on the suction side increases the lift as the turbulent inflow conditions are lowered. The wing's circulation is directly obtained from the lift force according to Equation (2.12). The pressure in the centre of the vortex is consequently reduced. The thinnest BL ($[I, \nu_t/\nu] = 0.5$), decreases the pressure in the vortex at $x/c_0 = 0.35$ with more than 25%. It can be seen that the uncertainty increases as the pressure becomes lower. This is logical since numerical diffusion becomes more dominant for a stronger vortex and therefore affects the pressure in the core for the different grid refinements more. The uncertainties for the η_v are not shows since their values are not reliable due to the intermediate post-processing steps involved.

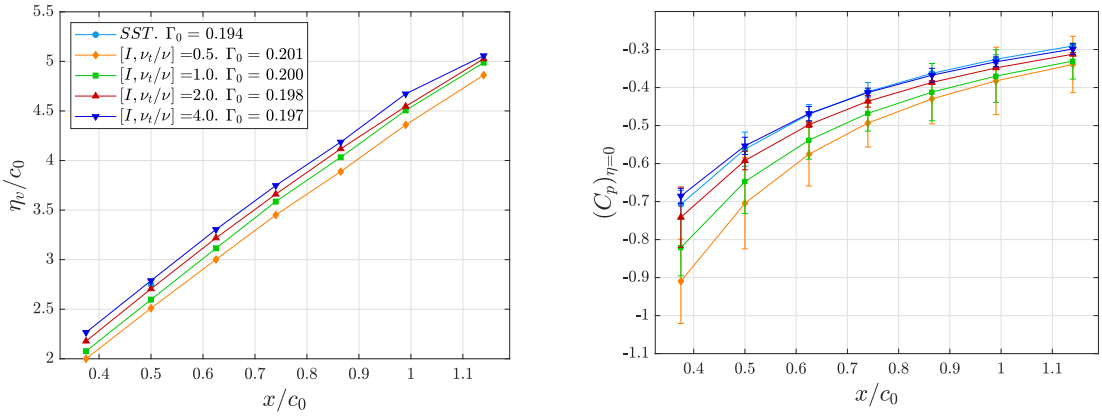

Figure 6.16: Vortex properties (η_v, left; $(C_p)_{\eta=0}$, right) along the trajectory. Results for SST and $\gamma - \tilde{R}e_{\theta_t}$ simulations on grid $G^{3D}_{1,5}$, $\alpha = 5°$. Error bars indicate spatial discretisation uncertainty.

Although a transitional BL appears to change the pressure in the vortex with more than 25% compared to a fully turbulent BL, it is not controlled in the experiments by i.a. Higuchi et al. (1987), Arndt et al. (1991), and Pennings et al. (2015b). The quality of the inflow, wall roughness, and nuclei could affect the transition location and if not controlled, change the vortex structure accordingly. No information concerning transition for the wing at 5 degrees AoA is available whereby the validation process of the vortex for this AoA by means of Stereographic-Particle Image Velocimetry (S-PIV) is less reliable. The measured integral quantities are useful though. The sensitivity analysis shows that the lift is insensitive to the inflow conditions, the force measurements are therefore considered to be valid since they are not affected by the transitional phenomena for $\alpha = 5°$.

The analytical expression by Bosschers (2015) states that the pressure in the vortex is not only proportional to the viscous core thickness, but also to the wing's circulation, i.e. $p(\eta = 0) \sim (1/\eta_v^2), \Gamma_0^2$. To test whether the results match this expression, all results are normalised with the same quantity obtained by the SST simulation and thus a fully turbulent BL. Figure 6.17 displays the results. In the left graph, the relative change of the viscous core radius and the relative change in total wing circulation are presented. Note that both quantities are written such that their units match with the expression of Bosschers (2015), i.e. $1/\eta_v^2$ and Γ_0^2. The pressure decrease along the trajectory is thus due to (i) the decrease in viscous core radius, and (ii) the increase in wing circulation. In the right graph of Figure 6.17, these relative changes are summed (assuming that they are uncorrelated) and compared to the actual relative decrease in pressure. It is clear that the general trend agrees quite well. At the start of the trajectory, the expected change in pressure (dashed line) is higher than the actual C_p; for $x/c_0 > 1.0$, it is a little lower. The vortex-roll up process is responsible for this. In Section 6.1, it was assumed that the freestream circulation of the vortex (Γ_∞) is directly proportional to the wing's circulation (Γ_0). However, this statement is not true if the roll-up process is not yet finished. This explains the overprediction in the first part of the trajectory since the full effect of the increased circulation is added while this is not plausible close to the wing tip. Schot (2014) estimated the roll-up process to end between $1 < x/c_0 < 2$ which explains why it matches better for $x/c_0 > 1$.

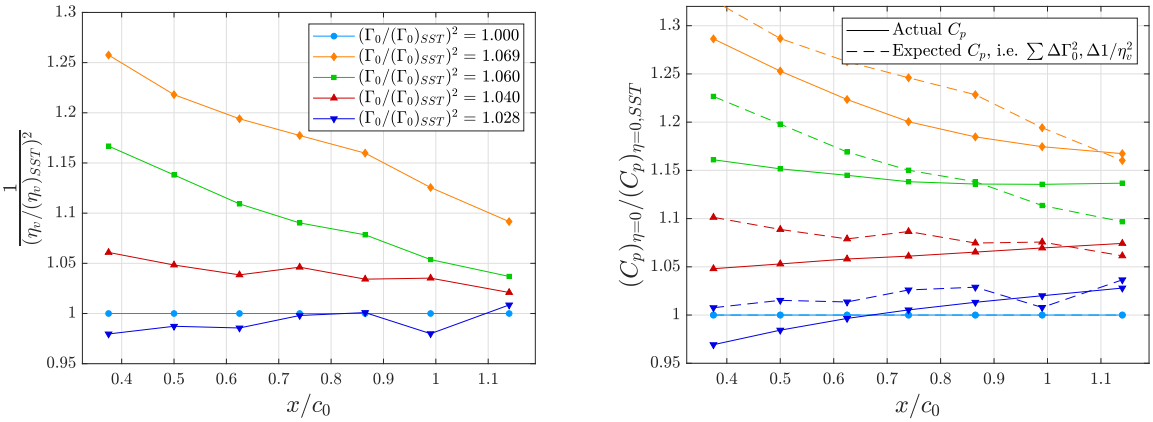

Figure 6.17: Normalised vortex properties (η_v, left; $(C_p)_{\eta=0}$, right) along the trajectory. Results normalised with the SST results, $\alpha = 5°$, and $G^{3D}_{1,5}$ is used.

$\alpha = 9°$

The left graph of Figure 6.18 shows that the insensitivity of the BL for the wing at 9 degrees AoA yields the viscous core radius to be similar for all simulations. The wing's circulation, however, is affected for $\alpha = 9°$. This is because the location where the flow separates is changed for the different inflow conditions as concluded in Section 6.3.3. Lowering the turbulence inflow quantities yields the flow to be attached over a longer distance along the chord which increases the lift and thus the circulation of the wing. The right graph of Figure 6.18 presents the pressure coefficient in the centre of the vortex along the trajectory. For 9 degrees AoA, transition on the suction side is

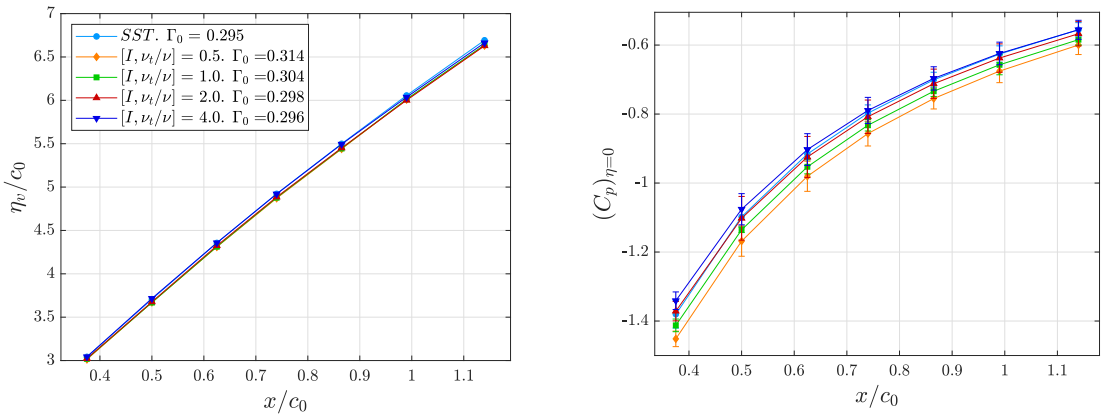

Figure 6.18: Vortex properties (η_v, left; $(C_p)_{\eta=0}$, right) along the trajectory. Results for SST and $\gamma - \tilde{R}e_{\theta_t}$ simulations on grid $G^{3D}_{1,9}$. Error bars indicate spatial discretisation uncertainty.

triggered just downstream of the LE regardless of the magnitude of the turbulent inflow conditions, whereby the BL thickness along the chord is insensitive towards the inflow conditions. This yields the pressure in the vortex to be less sensitive to the turbulent inflow conditions (note that it is slightly varying due to the increased circulation). As said, transition is not controlled in the S-PIV measurements by Pennings et al. (2015b). It was concluded that this could influence the pressure in the vortex more than 25% for $\alpha = 5°$. However, this is thus not true for the $\alpha = 9°$ case. However, at this AoA, the lift coefficient shows that the flow over the wing is much more sensitive to small perturbations in the inflow conditions (i.e. the change in inflow conditions shifts the separation location slightly, which decreases the lift). Since the turbulence intensity is not measured in the experiments, and there is no information about the separation location, one should interpret the measured lift force with care.

Again, the results are checked against the analytical expression by Bosschers (2015). Compared to the $\alpha = 5°$ case, the opposite is observed: a relatively constant η_v for the different inflow conditions but sensitive lift and thus circulation. Figure 6.19 presents η_v, Γ_0, and $(C_p)_{\eta=0}$ relative to the SST output. It can be seen that the viscous core radius differs 2% at most (this was more than 20% for $\alpha = 5°$). Furthermore, the wing's circulation is increased

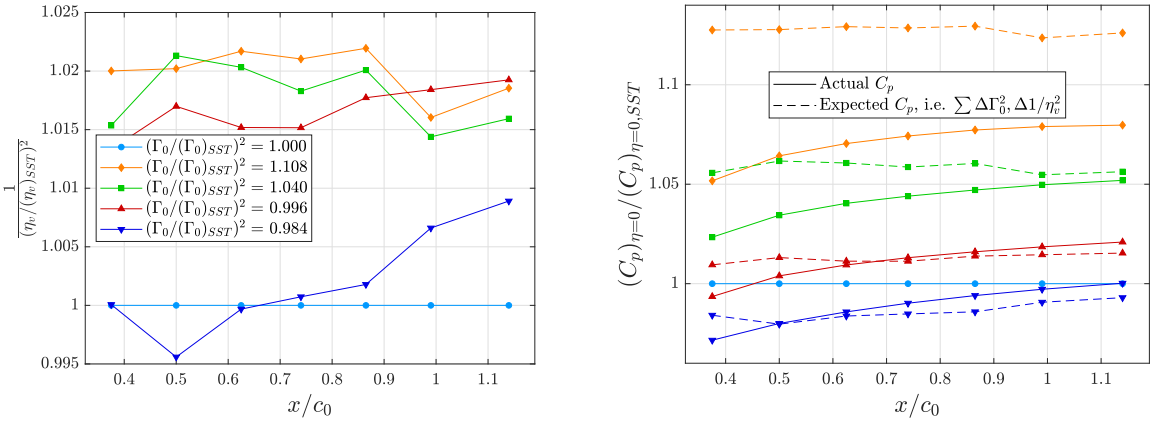

Figure 6.19: Normalised vortex properties (η_v, left; $(C_p)_{\eta=0}$, right) along the trajectory. Results normalised with the SST results, $\alpha = 9°$, and $G^{3D}_{1,9}$ is used.

by more than 6% (this was 3% for $\alpha = 5°$). Adding the two effects linearly results in the expected relative change of $(C_p)_{\eta=0}$ displayed by the dashed lines in the right graph of Figure 6.19. It is again observed to match well with the analytical relation. The expected value lies somewhat higher than the actual value of $(C_p)_{\eta=0}$ in the first part of the trajectory, afterwards it slightly underpredicts the value. This is again due to the roll-up process which is not incorporated in the expression. However, this is not true for the $[I, \nu_t/\nu] = 0.5$ case. It can be seen that the relative change in viscous core size is reasonable compared to the other cases. The circulation is increased with more than 6% though. This is because the flow field at the tip changes for that simulation. Instead of turbulent separation near the TE of the wing, a LSB appears for $0.8 < z/b < 1.0$. This LSB increases the lift coefficient directly due to the low pressure in the bubble but it also avoids turbulent separation which increases the circulation with respect to the other simulations even more.

6.3.5. VALIDATION

Finally, the CFD results are compared to the force and S-PIV measurements by Pennings et al. (2015b) for both AoA in the following paragraphs.

$\alpha = 5°$

Figure 6.20 presents the comparison of the integral quantities. Earlier, it was concluded that the lift coefficient is insensitive to the turbulent inflow conditions and the experimental value can therefore be interpreted as reliable. Figure 6.20 shows that the transition model increases the accuracy of the predicted lift coefficient, the results are found to match best for $[I, \nu_t/\nu] = 1.0$. The trend of the drag coefficient can be verified: the transition model decreases the drag coefficient as the BL remains laminar over a longer distance. Note that this is the case on both sides of the wing. If the turbulent inflow conditions are lowered, transition is delayed whereby the skin friction drag and thus the drag coefficient decrease (given a constant pressure drag).

Figure 6.21 displays the non-dimensional azimuthal and axial velocities, u_θ/U_∞ and u/U_∞ respectively, over the non-dimensional vortex radius (η/c_0) at two locations downstream of the tip, $x/c_0 = 0.50$ and $x/c_0 = 1.14$. The velocities are spatially averaged over sector I of the vortex, see Section 5.2.2. Although the transition location is not controlled in the experiments, which could affect the velocity measurements significantly for $\alpha = 5°$, the experimental values are still displayed in the figures. The main purpose of the figures is to determine the effect of transition modelling, not to validate the results.

The transition model increases the azimuthal velocity with 10% over almost the entire radius with respect to the SST result. This is because the viscous core radius (the location where u_θ/U_∞ is maximum) is decreased. The vortex clearly diffuses when the azimuthal velocity profiles at the different streamwise locations are compared: the viscous core radius is increased by turbulent and numerical diffusion which yields the maximum azimuthal velocity to be lower. The numerical uncertainty is also increased further downstream. This is because numerical diffusion is more present in that region since the structured multi-block grids coarsen further from the tip (see Figure 4.12).

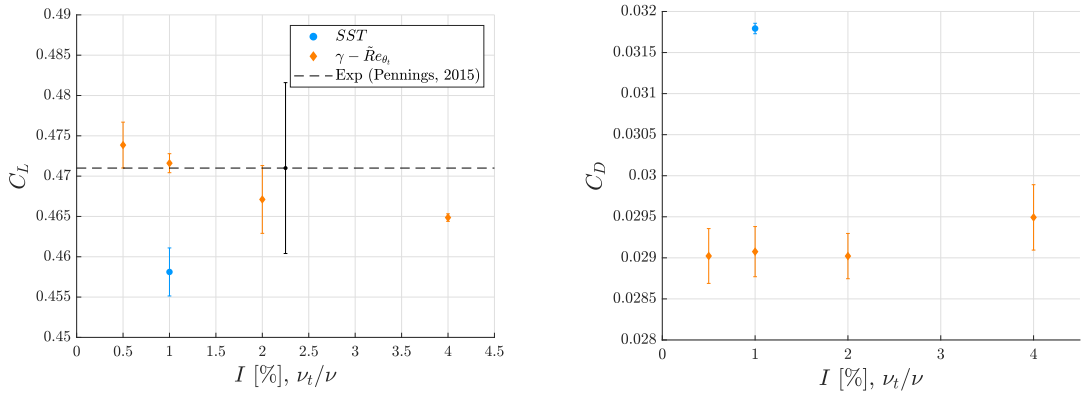

Figure 6.20: Comparison of lift coefficients with experimental value for $\alpha = 5°$, $Re = 8.95 \times 10^5$ in simulation. Measured value is for $Re = 9.20 \times 10^5$. Error bars indicate (i) experimental uncertainty for value by Pennings et al. (2015b), and (ii) spatial discretisation uncertainty for CFD results.

Furthermore, Figure 6.21 shows a remarkable result: while the flow in the viscous core is accelerated in the experiments, the simulations predict a deceleration. This is a well-known phenomenon for two-equation turbulence closures (see Schot (2014) and Asnaghi (2018)), and will be further elaborated on in the next chapter. Despite the discrepancy due to the turbulence model, moving away from a fully turbulent BL assumption clearly improves the results. The axial velocity in the vortex is improved by 5% and 4% at $x/c_0 = 0.50$ and $x/c_0 = 1.14$ respectively.

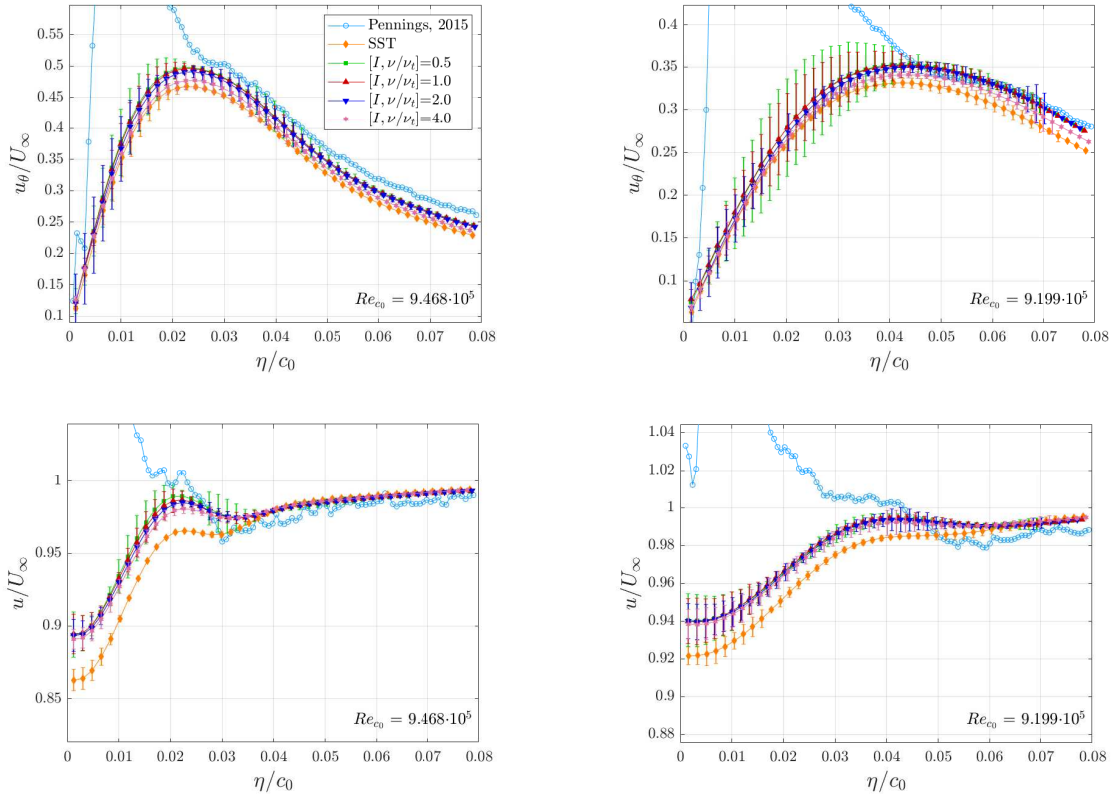

Figure 6.21: Azimuthal (top) and axial (bottom) velocity profiles averaged over sector I at $x/c_0 = 0.50$ (left) and $x/c_0 = 1.14$ (right) for $\alpha = 5°$. Bars indicate spatial discretisation uncertainty, Re_{c_0} during the experiment is presented. Reynolds number in simulation is 8.95×10^5.

Discrepancies between the experimental and numerical velocities in the far field arise from the set inflow velocity. In the CFD simulations, an exact value of $U_\infty = 7.1544$ can be set to acquire a Reynolds number of 8.95×10^5. However, in the experiments, the freestream velocity is typically set with fluctuation of ±0.5% (Pennings

et al., 2015b). This is indicated by the different Reynolds numbers as shown in the figure. The introduced input error is assumed to be in the order of 0.5% since U_∞ is used for non-dimensionalisation of the results.

Note however, that the temperature in the facility also varies, which affects the Reynolds number (the non-constant inflow velocity is also an contributor). The Reynolds number varies in the order of 5%. Arndt and Keller (1992) published the lift and drag curves (C_L and C_D versus α plots) for Reynolds numbers between 4.59×10^5 and 1.95×10^6. This increase in Reynolds number of almost 300% appears to affect the lift with about 6%. The 5% variation in Reynolds number is therefore not expected to affect the strength of the vortex. For this reason, the Reynolds number in the simulation is kept constant at 8.95×10^5 like it is done in other numerical investigations.

Table 6.3 presents an overview of the error of the normalised azimuthal and axial velocity at the viscous core radius of the vortex (designated peak velocities). The table shows that the error in the azimuthal peak velocity at both planes is higher than 40%, all errors in normal peak velocity exceed 25%. This shows the limitation of the turbulence models to capture the flow in the vortex core. The results obtained using the transition model are consistently better compared to the SST simulation with the case $[I, \nu_t/\nu] = 0.5$ matching best. It is interesting that the error in azimuthal peak velocity increases when $x/c_0 = 0.50$ and $x/c_0 = 1.14$ are compared while the error in axial peak velocity decreases. This implies that the azimuthal velocity is damped more than the axial velocity in the simulation compared to the experiment.

Table 6.3: Errors (in %) of normalised azimuthal and axial velocity at the viscous core radius. The vortex is considered at the two different streamwise locations downstream of the tip, the wing is at 5 degrees AoA.

$x/c_0 = 0.50$

	SST	$[I, \nu_t/\nu] = 0.5$	$[I, \nu_t/\nu] = 1.0$	$[I, \nu_t/\nu] = 2.0$	$[I, \nu_t/\nu] = 4.0$
$E((u_\theta/U_\infty)_v)$	43.85	40.00	40.21	40.90	42.59
$E((u/U_\infty)_v)$	32.76	31.85	31.84	31.83	31.80

$x/c_0 = 1.14$

	SST	$[I, \nu_t/\nu] = 0.5$	$[I, \nu_t/\nu] = 1.0$	$[I, \nu_t/\nu] = 2.0$	$[I, \nu_t/\nu] = 4.0$
$E((u_\theta/U_\infty)_v)$	55.81	52.72	52.84	53.23	54.42
$E((u/U_\infty)_v)$	26.27	25.41	25.42	25.49	25.62

$\alpha = 9°$

Figure 6.23 shows the integral quantities for the wing at 9 degrees AoA. In the previous section, it was concluded that the (experimentally) measured lift coefficient is sensitive to the turbulent inflow conditions due to the shifting separation location on the suction side of the wing. Since nothing is known about the inflow conditions, nor the location of separation, it is hard to judge whether the measured lift coefficient is reliable. The same trend as for the $\alpha = 5°$ case is observed, however the lift coefficient varies more for the reason given above. The trend in the

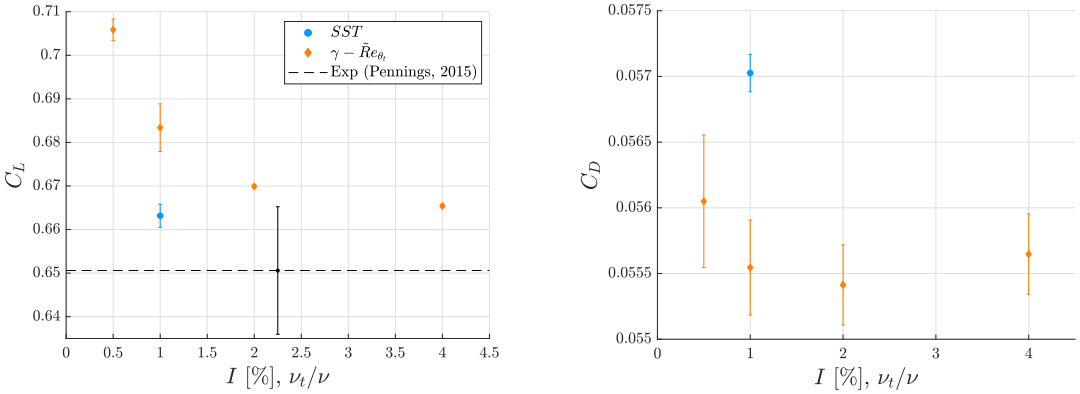

Figure 6.22: Comparison of lift coefficients with experimental value for $\alpha = 9°$, $Re = 8.95 \times 10^5$ in simulation. Measured value is for $Re = 8.91 \times 10^5$. Error bars indicate (i) experimental uncertainty for value by Pennings et al. (2015b), and (ii) spatial discretisation uncertainty for CFD results.

drag coefficient is also similar to the 5 degrees AoA case. The transition model yields the skin friction drag and therefore the total drag to be lower compared to the SST case. However, the sensitivity is much higher in this case,

because of the contribution of the pressure drag. By changing the turbulent inflow conditions, the separation location is slightly shifted whereby the pressure drag is also affected.

The velocity profiles in Figure 6.23 show the same behaviour as for the lower AoA and again imply the problem of the turbulence model. The results for this case are, like the pressure coefficient in the vortex (Figure 6.18), much less affected by the change in turbulent inflow conditions. This is because the BL on the suction side is not changed for the different inflow conditions, only the changing circulation is responsible for the change.

Table 6.4 displays the errors in peak velocities. Because the S-PIV measurements are less affected by the uncontrolled transition location in the experiments, the errors are generally smaller (although still dominated by the discrepancy by the turbulence model) compared to $\alpha = 5°$. At $\alpha = 9°$, the error in azimuthal peak velocity is about 3% lower compared to $\alpha = 5°$. It is advised to consider the wing at 9° to investigate the effect of turbulence modelling on the tip vortex in the nwext chapter.

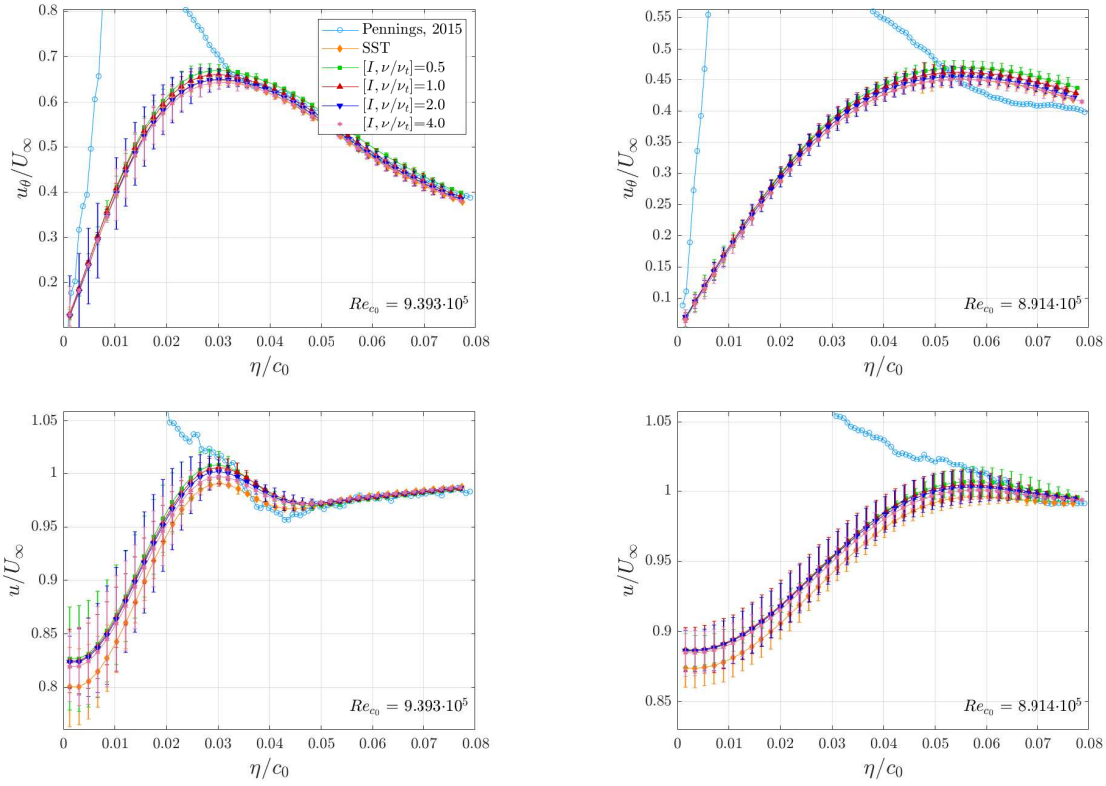

Figure 6.23: Azimuthal (top) and axial (bottom) velocity profiles averaged over sector I at $x/c_0 = 0.50$ (left) and $x/c_0 = 1.14$ (right) for $\alpha = 9°$, Re_{c_0} during the experiment is presented. Reynolds number in simulation is 8.95×10^5.

6.3.6. 3D CONCLUSIONS

In this section the set of inflow conditions obtained from the 2D calculations is used to test the effect of transition modelling on the structure of the vortex. Based on the outcome, arguments are made with regard to the reliability of the measurements by Pennings et al. (2015b) of the wing at 5 and 9 degrees AoA in which transition is not controlled.

The requirements for the grid resolution at the transition location (obtained from the converged 2D calculations) when a QUICK scheme for the discretisation of the convective fluxes for the transition variables are followed. No convergence is obtained, the grid at the transition location at both sides is refined in flow tangential and spanwise directions. This reduced the L_2 norm of the residual of the (dominant) variable (γ) by half an order of magnitude, however, still small stagnated regions of $(L_\infty)_\gamma = 1.5 \times 10^{-1}$ remain. These regions are located within the refined sections. It was decided to perform the sensitivity analysis *without* local grid refinement since the accuracy of the lift and skin friction drag only increases by 0.3% and 1.5% respectively while computational

costs increase by almost 200%.

The transition model reduces the BL thickness on the suction side of the wing with a factor of three for the $\alpha = 5°$ case, for the wing at $\alpha = 9°$ the BL is much less affected since transition is triggered just downstream of the LE regardless of the inflow conditions. This changed the viscous core radius for $\alpha = 5°$ with more than 25% compared to a fully turbulent BL, for $\alpha = 9°$ this was only 2%. This causes the pressure in the vortex to be also affected by almost the same amount. The circulation for $\alpha = 5°$ is insensitive to the inflow conditions; at $\alpha = 9°$ sensitivity of the (turbulent) separation location yields larger variations in the wing's circulation. In the light of

Table 6.4: Errors (in %) of normalised azimuthal and axial velocity at the viscous core radius. The vortex is considered at the two different streamwise locations downstream of the tip, the wing is at 9 degrees AoA.

$x/c_0 = 0.50$

	SST	$[I, \nu_t/\nu] = 0.5$	$[I, \nu_t/\nu] = 1.0$	$[I, \nu_t/\nu] = 2.0$	$[I, \nu_t/\nu] = 4.0$
$E((u_\theta/U_\infty)_v)$	39.41	37.44	38.31	39.31	39.90
$E((u/U_\infty)_v)$	29.47	28.23	28.39	28.67	29.00

$x/c_0 = 1.14$

	SST	$[I, \nu_t/\nu] = 0.5$	$[I, \nu_t/\nu] = 1.0$	$[I, \nu_t/\nu] = 2.0$	$[I, \nu_t/\nu] = 4.0$
$E((u_\theta/U_\infty)_v)$	54.16	52.25	53.01	53.72	54.14
$E((u/U_\infty)_v)$	25.5	24.72	24.87	25.01	25.16

this study, it is noted that the S-PIV measurements of the vortex can be affected by the uncontrolled transition location in the experiments $\alpha = 5°$. This results in a larger input uncertainty whereby it is not advised to consider the wing at 5 degrees AoA when different turbulence models are compared and validated in the next chapter. For the wing at $\alpha = 9°$ it is less likely that the transition affects the vortex measurements.

The hypothesis stated in the first section is based on the analytical expression by Bosschers (2015) which relates the pressure in the vortex centre to the viscous core size and the freestream circulation, i.e. $p(\eta = 0) \sim \Gamma_0^2/\eta_v^2$. This was tested for both AoA. At 5 degrees AoA, η_v varied and Γ_0 was almost constant. For 9 degrees AoA the opposite was found. For both AoA the proportionality was confirmed when the roll-up process is finished ($x/c_0 > 1.0$). Upstream of $x/c_0 = 1.0$, this relation overpredicts the pressure relative to a turbulent BL which is logical since the roll-up process is not finished yet, so that including the full contribution of Γ_0 is not valid.

7

TURBULENCE MODELLING RESULTS

In the previous chapter, the limitations of the Shear Stress Transport (SST) turbulence model in a vortical flow were exposed. The choice of this model was restricted since the $\gamma - \tilde{R}e_{\theta_t}$ transition model is the only transition model available in ReFRESCO and is only compatible with the SST model. This chapter aims to explore turbulence models which have not yet been extensively tested on the 'Arndt' wing and to study whether these models are able to capture the laminar flow (solid body rotation) within the vortex core and the anisotropic character of the turbulent structures around the viscous core radius.

7.1. INTRODUCTION AND HYPOTHESIS

The lift coefficient data in Figure 2.11 already showed the use of eight different turbulence models in literature. Schot (2014) concluded that the use of Reynolds Averaged Navier Stokes (RANS) in combination with one- and two-equation closures based on the Boussinesq hypothesis is not able to reproduce the anisotropic turbulence around in the vortex core, and overpredicts the eddy-viscosity in that region. This results in excessive diffusion in the vortex and therefore an underpredicted cavity size. Schot (2014) also employed Curvature Correction(s) (CC) for the RANS closures. CC reduced the turbulent viscosity in the core and consequently improved the results, however still not sufficiently (the error in lift coefficient was still 8.14% compared to the measurements by Pennings et al. (2015b)). Asnaghi et al. (2017a) drew the same conclusions regarding CC. The overpredicted eddy-viscosity is a consequence of the linear Boussinesq hypothesis which is insensitive to streamline curvature, already pointed out by Bradshaw (1973). Schot (2014) recommended the use of more comprehensive turbulence models, which are not based on the Boussinesq hypothesis.

Although the Explicit Algebraic Reynolds Stress Model(s) (EARSM) and the $k - \sqrt{k}L$ (KSKL) models are still based on the hypothesis, they theoretically should have some advantages over other RANS models and will therefore be tested in this chapter. The EARSM model is based on a non-linear constitutive relation and models the anisotropy tensor, while the KSKL model (in theory) should be able to dynamically adjust itself to some turbulent flow structures. The theory behind these statements was presented in Section 3.2.2.

Asnaghi (2018) and Paskin (2018) followed the recommendation by Schot et al. (2014) and continued simulating the flow around the same geometry using Scale Resolved Simulation(s) (SRS). Asnaghi (2018) performed Implicit Large Eddy Simulation(s) (ILES) and Localized Dynamic Kinematic subgrid stress Model (LDKM) simulations of the cavitating vortex. The comparison error of the integral quantities was below 5%, and the models prevent the early decay of the vortex. It is questionable whether all relevant physics are captured in the vortex since it is not certain that all velocity fluctuations in the Boundary Layer (BL) are properly developed whereby it is possible that the model predicts laminar flow in a too large region of the vortex (around the viscous core radius). Paskin (2018) performed Detached Eddy Simulation(s) (DES) for the 'Arndt' wing. Although the lift coefficient is not matching, the work showed the ability of the DES method to capture velocity fluctuations in the vortex. The discrepancy in lift coefficient is due to premature BL detachment. This is a well-known property of the model, Menter et al. (2003b) called it Grid Induced Separation (GIS) because the separation is not determined by flow physics but is grid dependent. GIS is the result of the sudden grid refinement at the RANS-Large Eddy Simu-

lation(s) (LES) boundary without balancing the reduction of eddy-viscosity by the resolved turbulence. Spalart et al. (2006) coined the term Modelled Stress Depletion (MSD) due to this unbalance in eddy-viscosity; GIS is thus a consequence of MSD.

This observation motivates to also test the Delayed Detached-Eddy Simulation(s) (DDES) and Improved Delayed Detached-Eddy Simulation(s) (IDDES) models. In theory, the lift and thus the circulation should be predicted more accurately.

7.2. RESULTS

This section presents the results for the different turbulence models. The first part concerns the numerical settings and error analysis. Then results are compared to the measurements by Pennings et al. (2015b).

7.2.1. NUMERICAL SETTINGS

In this chapter, the wing is only considered at 9 degrees Angle(s) of Attack (AoA) following the recommendations of Chapter 6. Numerical settings are kept the same for the different turbulence models (see Appendix D for further details). Note that the given explicit and implicit relaxation factors are an indication of what is used; they vary slightly for the different models to increase computation efficiency or avoid numerical instabilities.

The same grids as for the Three-Dimensional (3D) transition calculations are used (see Tables 4.2 and 4.3 for further details). As concluded in Section 4.3.4, the Courant-Friedrichs-Lewy (CFL) must not exceed one in the LES regions of the DDES and IDDES simulations. This resulted in a non-dimensional timestep of $\Delta t U_\infty / c_0 = 1.09 \times 10^{-2}$ for $G^{3D}_{1,9}$.

7.2.2. ERROR ANALYSIS

DISCRETISATION ERROR

To include both the spatial and temporal discretisation in the analysis, a total number of 16 simulations would be required (see Section 5.1.1). Considering the available computation resources, this would not be feasible. The method by Eça et al. (2010) fits a surface through the 16 data points to estimate the discretisation uncertainty. In this analysis, it is considered to be sufficient to perform the simulations for the grid and timestep combinations of the test-matrix in Table 7.1.

Table 7.1: Test matrix of grid and timestep combinations to assess the discretisation error.

	Δt_1	Δt_2	Δt_3	Δt_4
$G^{3D}_{1,9}$	✓	✓	✓	✓
$G^{3D}_{2,9}$	✓	✓		
$G^{3D}_{3,9}$	✓		✓	
$G^{3D}_{4,9}$	✓			✓

The timestep refinement ratios are set equal to the spatial ratios to keep the CFL number constant along the 'diagonal' (assuming that the flow field is grid independent). This results in the following values, $[\Delta t_1, \Delta t_2, \Delta t_3, \Delta t_4] \times U_\infty / c_0 = [1.09, 1.41, 1.75, 2.27] \times 10^{-2}$.

ITERATIVE ERROR

The convergence criterion for the outer loops is set by a trade-off between iterative accuracy and computational costs. To do so, SST and DDES simulations with different convergence criteria were performed. In ReFRESCO, an convergence criteria of $L_\infty = 10^{-5}$ for all variables was found to be sufficient for other problems (see Section 5.1.1). For this reason the considered convergence criteria are $L_\infty = [10^{-3}, 10^{-4}, 10^{-5}, 10^{-6}]$ for all variables. For these criteria, C_L and C_D are found to be within 0.05% compared to the $L_\infty = 10^{-6}$ solution. Another variable considered is the pressure coefficient in the vortex centre $(C_p)_c$. Figure 7.1 displays the normalised $(C_p)_c$ on the left axis and the normalised total number of iterations (so the number of timesteps times the number of outer loops per timestep) on the right axis for two different streamwise locations. For this case, an optimum is also reached at $L_\infty = 10^{-5}$. For all simulation, the normalised $(C_p)_c$ is within 0.02%. Increasing L_∞ to 10^{-4} would result in an error of at least 0.5% in the $(C_p)_c$ for DDES at $x/c_0 = 1.14$ which would be in the same order as the discretisation uncertainty and is therefore considered to be too large.

STATISTICAL ERROR

The statistical error and the required start-up time are assessed using the Transient Scanning Technique (TST) as presented in Section 5.1.1. To avoid any interpolation between the numerical and experiments results, the distances between the point in the plane monitors (dy_m and dz_m) are set such that they match the vector spacing

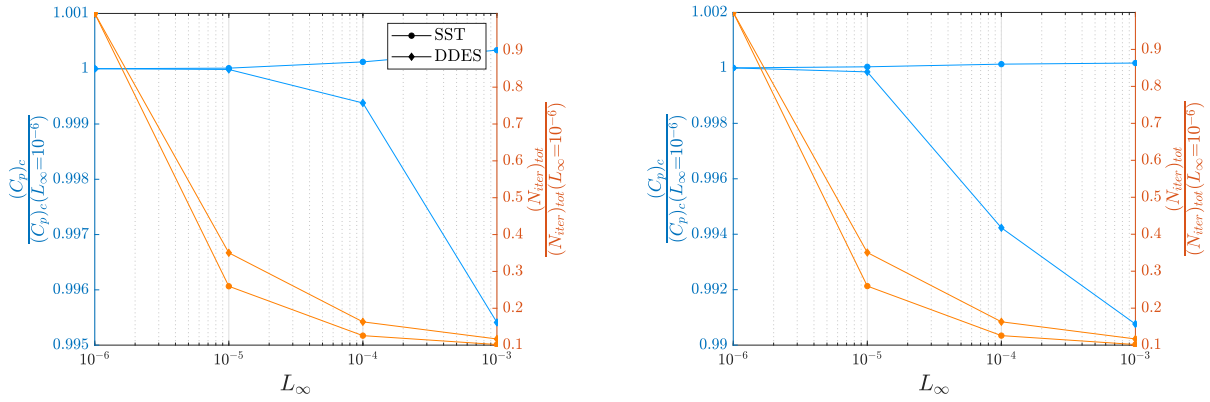

Figure 7.1: Iterative error analysis for $G^{3D}_{1,9}$ and Δt_1, showing the trade-off between numerical accuracy (left axis) and computational cost (right axis). Numerical accuracy is based on pressure coefficient in the vortex centre $(C_p)_c$ at $x/c_0 = 0.50$ (left) and $x/c_0 = 1.14$ (right).

as Pennings et al. (2015b) used (see Table 5.1) for all streamwise planes $x/c_0 = [0.50, 0.74, 1.14]$. All these planes consist of $\mathcal{O}(10^5)$ data-points, which makes it practically impossible to output them every timestep. To perform a proper averaging process over the stochastically stationary range, one should remove the start-up time. Since it is not possible to extract the data every timestep, the start-up time is determined priori and averaging of each variable is started after the start-up time. In this way, only the averaged values have to be extracted at the last timestep. Note that in this way vortex wandering (or meandering) is not taken into account. It is believed that this does not influence the comparison since vortex wandering in the measurements is predominantly due to the unsteadiness of the inflow in the test-facility according to Bosschers (2018). Furthermore, e.g. Heyes et al. (2004) mentioned that vortex wandering is barely observed for Computational Fluid Dynamics (CFD) computations of wings at moderate AoA.

The start-up time is a physical process where the flow field adjusts itself from the initial condition (uniform in this case) to a statistically converged vortex flow. It is therefore reasonable to say that the physical start-up time (in a time or length unit) is independent of the timestep. In order to check this, and to determine the start-up time, simulations on the coarsest grid with the finest (Δt_1) and coarsest (Δt_4) are performed. Figure 7.2 displays the analysis of the time signal of the pressure in the centre of the vortex at $x/c_0 = 0.50$. The dashed lines in the figures indicate the estimates of the start-up time, the same analysis was performed for Δt_4.

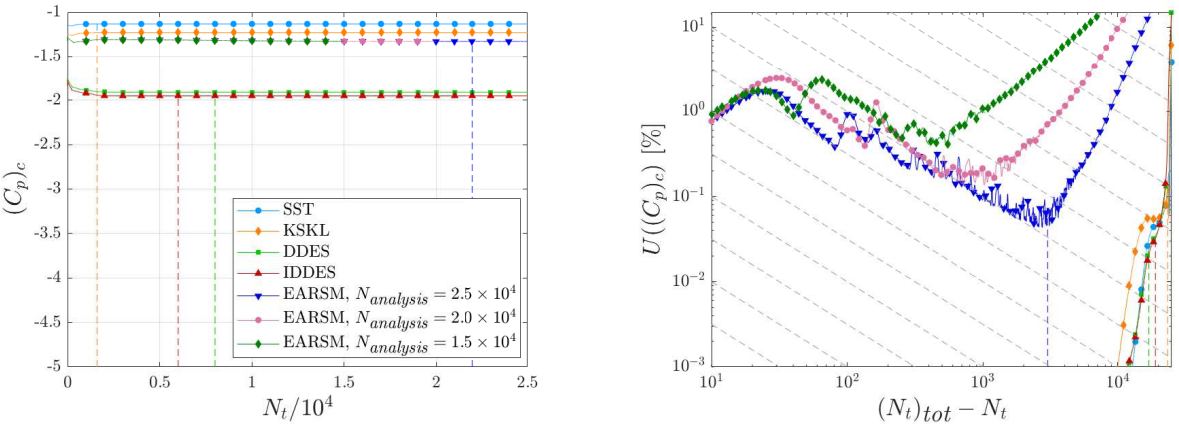

Figure 7.2: Time signal of the pressure coefficient in the centre of the vortex $(C_p)_c$ (left) and corresponding output of the TST (right), results for $G^{3D}_{4,9}$ and Δt_1. Dashed lines indicate the estimates of the start-up time.

The simulations for the two different timesteps appear to have the same behaviour. The SST and KSKL converge to a steady-state, after about 1000 timesteps. For the DES and IDDES simulations, the amount of start-up timesteps is somewhat higher, about 5000. The EARSM appears to be unsteady for much longer. Table 7.2 presents the estimates for the start-up time for both timesteps.

The start-up times for all closures for the two different timesteps appear to be very similar. For this reason, it

Table 7.2: Estimates of start-up time by means of the TST for Δt_1 (left) and Δt_4 (right) on $G^{3D}_{4,9}$ for different turbulence models. Here t_{start} denotes the start up time.

Closure	$N_{start}/10^3$	$\Delta t \times 10^5$ [s]	$t_{start} \times 10^1$ [s]
SST	1.6	1.93	0.31
KSKL	1.6	1.93	0.35
EARSM	22	1.93	4.25
DDES	8.0	1.93	1.54
IDDES	6.0	1.93	1.16

Closure	$N_{start}/10^3$	$\Delta t \times 10^5$ [s]	$t_{start} \times 10^1$ [s]
SST	1.0	4.00	0.4
KSKL	1.1	4.00	0.44
EARSM	10	4.00	4.00
DDES	5.0	4.00	2.00
IDDES	3.0	4.00	1.20

is assumed that the start-up time is indeed independent of the considered range of timesteps. In all simulations, the first N_{start} timesteps are excluded from the averaging process. Of course, this amount depends on the actual timestep, and the physical start-up time t_{start} which is considered constant for each turbulence model. In other words, $N_{start} = (t_{start})_{i^{th}\,model}/\Delta t_i$. The values of t_{start} at Δt_1 are used, a safety factor of 1.2 is applied to make sure that none of the start-up time is included in the averaging.

To make sure that the statistical error is at least one order of magnitude lower compared to the discretisation error, the signal of the most unsteady simulation (the EARSM simulation) is analysed for a different amount of timesteps ($N_{analysis}$). For $N_{analysis} < 22{,}000$, the signal appears not to be statistically converged yet. It can be seen that the statistical error drops from 1.0% to about 0.1% when comparing the $N_{analysis} = 2.5 \times 10^4$ and $N_{analysis} = 1.5 \times 10^4$ signals for EARSM. All other simulations are found to reach a statistically converged state earlier, and their statistical errors drop lower. To ensure that the statistical error for all simulations is at least 0.1% lower compared to the discretisation error, at least another 3,000 outer loops are run after the start-up timestep. All results presented in the following sections are the time averaged quantities over this last (statistically converged) part of the simulations.

7.2.3. VALIDATION

The following paragraphs compare the numerical results to the measurements by Pennings et al. (2015b). This is done according to the strategy presented in Section 5.2.2. All results which will be shown in this section are for grid $G^{3D}_{1,9}$ and Δt_1 (i.e. finest grid and timestep) unless indicated differently.

INTEGRAL QUANTITIES

Figure 7.3 presents the lift and drag coefficients for the different turbulence models compared to the experimental values. The results are shown graphically to compare the modelling error with the uncertainty levels. Readers interested in the numerical values are referred to Table 7.3. Before discussing the results, it should be emphasised that the models will not be labelled as valid only based on the lift measurements as argued for in Chapter 6.

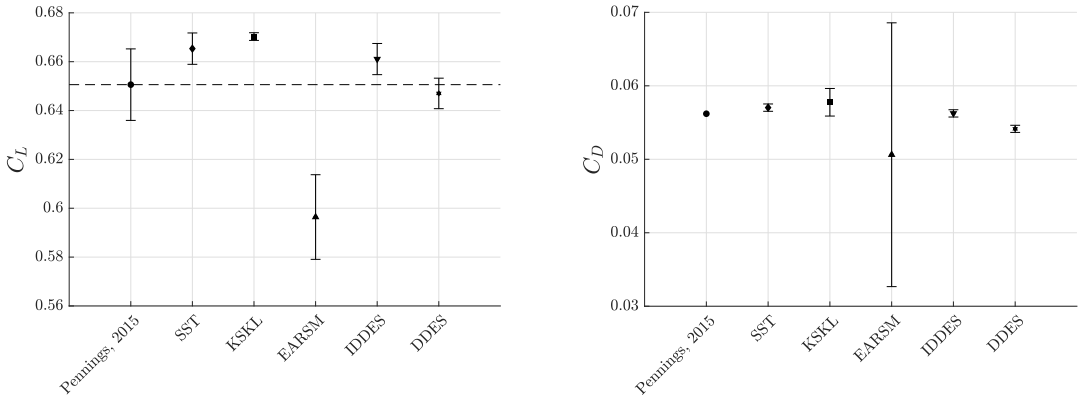

Figure 7.3: Validation of lift (left) and drag (right) coefficients for the different turbulence models. Error bars indicate discretisation plus statistical uncertainties.

In all upcoming graphs, the error bars indicate the (spatial and temporal) discretisation plus statistical uncertainty. The DDES and IDDES computations are assumed to have the same discretisation uncertainty as the SST. This is because the uncertainty of the DDES and IDDES simulation cannot be assessed by the procedure since the closure also depends on the grid size and therefore refining the grid would also change the model (i.e. error en-

tanglement violates some of the key assumptions made by Eça and Hoekstra (2014)). Since the DDES and IDDES simulations apply SST in the attached flow it is not expected that the uncertainties for the integral forces deviate a lot from the SST uncertainty. The effect of error entanglement in the vortex on the uncertainties of local flow variable is not known, this is a point for future research.

Table 7.3: Numerical values which are plotted in Figure 7.3. The table shows the non-dimensional values, numerical uncertainties, and error of lift and drag.

Closure	$\overline{C}_L \times 10^1$	$U(\overline{C}_L)$	$E(\overline{C}_L)$	$\overline{C}_D \times 10^2$	$U(\overline{C}_D)$	$E(\overline{C}_D)$
SST	6.653	1.930	2.265	5.703	0.150	1.477
KSKL	6.702	0.470	3.025	5.776	0.560	2.777
EARSM	5.964	5.810	-8.330	5.062	6.020	-9.925
DDES	6.611	1.930	1.610	5.624	0.150	0.0831
IDDES	6.470	1.930	-0.552	5.414	0.150	-3.659
Pennings, 2015	6.506	5	-	5.620	-	-

For both integral quantities, all simulations except the EARSM simulation point to similar values. The lift coefficient is predicted to be around 0.66, the drag coefficient about 0.057. The underprediction of the lift for the EARSM simulation is due to a larger region of Trailing Edge (TE) separation at the suction side of the wing. This also explains the discrepancy in the drag coefficient. Table 7.4 shows the pressure drag is reduced by 13% with respect to the SST simulation while the friction drag is almost the same. The larger region of separated flow also explains the higher uncertainty. By changing the grid density, the location of separation can be affected what largely influences the integral quantities for the different grids and thus the uncertainty.

Table 7.4: Different components of the drag force for the SST and EARSM turbulence models. Also results normalised by the SST result are shown.

Closure	$C_D \times 10^2$	$C_{D_f} \times 10^3$	$C_{D_p} \times 10^2$	$C_D/(C_D)_{SST}$	$C_{D_f}/(C_{D_f})_{SST}$	$C_{D_p}/(C_{D_p})_{SST}$
SST	5.70	9.52	4.75	1.00	1.00	1.00
EARSM	5.06	9.34	4.12	0.88	0.98	0.87

7

VORTEX TRAJECTORY

Figure 7.4 presents the trajectory of the vortex for the different turbulence models. Note that discretisation uncertainties were not determined for the y_c, z_c, and η_ν (see Figure 7.5) plots since these quantities are determined using a nearest-cell approach which results in step function between the different grids and thus either a relatively small or large uncertainty. The vortex is three times more deflected in the spanwise direction (z_c) compared to lift-wise direction (y_c). In other words, the vortex is drawn inwards in the plane of the wing. None of the simulations matches well with the experimental values. However, it has to be mentioned that the general trend for both y_c and z_c agrees well with the experiments. It is possible that the Stereographic-Particle Image Velocimetry (S-PIV) system was placed slightly off the centre line of the reference system what could explain the discrepancy in the magnitude. Furthermore, it is clear that all the different turbulence model result in similar values for both coordinates.

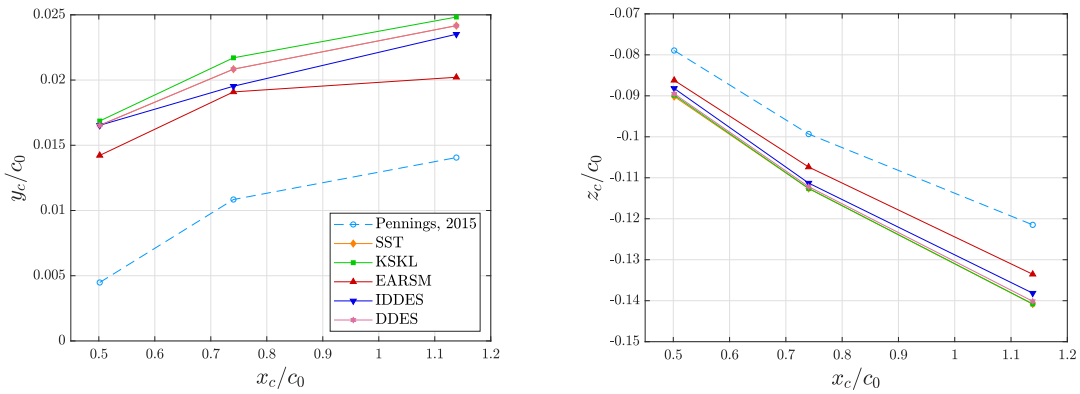

Figure 7.4: Lift normal (left) and spanwise (right) coordinates of the vortex centre along the trajectory for the different turbulence models compared to the experimental values.

More interesting are the viscous core radius and pressure in the vortex centre along the trajectory as also considered in Chapter 6. All turbulence models decreased the pressure in the vortex centre with reference to the SST simulation. DDES and IDDES clearly perform best and almost match the experimental value at $x/c_0 = 0.50$. Furthermore, the growth of the viscous core radius is observed to be almost linear for all turbulence models over the entire range. This linear growth in viscous core ratio yields a less negative pressure. According to the analytical expression by Bosschers (2015), as extensively elaborated on in Chapter 6, the trend in the pressure should vary quadratic along the trajectory which is more or less confirmed by the $(C_p)_c$ graph.

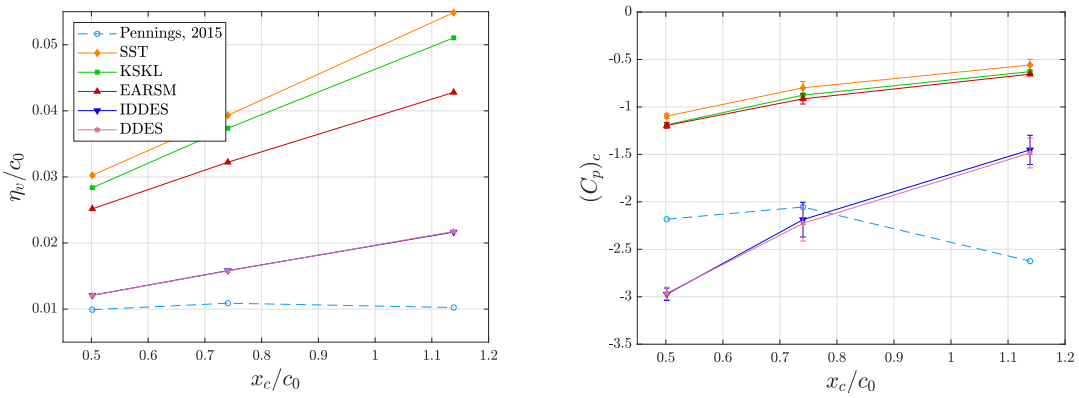

Figure 7.5: Viscous core size (left) and pressure in the centre of the vortex (right) along the trajectory for the different turbulence models compared to the experimental values. Error bars indicate numerical uncertainty.

The error of the pressure in the vortex centre at $x/c_0 = 0.74$ is within uncertainty bounds for DDES and IDDES simulations. However, the slope is the complete opposite. This is probably due to the roll-up process which is not captured accurately. In the experimental measurements, the roll-up process seems not to be finished still for $x/c_0 = 1.2$. The weaker effect of the roll-up in the simulations, in combination with turbulent and/or numerical diffusion of the vortex yields a different slope. This also explains why the simulation underpredicts the pressure (predicts a more negative value) at $x/c_0 = 0.50$. More BL fluid is already rolled-up in the simulation compared to the experiment whereby the pressure is already lower.

LOCAL VELOCITY PROFILES

Next are the local velocity profiles averaged over sector I of the vortex (the quarter of the vortex in positive lift direction, as indicated in Figure 5.8). Figure 7.6 compares the azimuthal and axial mean velocity profiles for the different turbulence models to the experimental values at two different streamwise locations.

From the azimuthal velocity distributions it is clear that the DDES and IDDES perform much better compared to the full RANS closures. At $x/c_0 = 0.50$, the location of the viscous core size aligns with the experimental value. However, at $x/c_0 = 1.14$ the vortex in the simulation is diffused much more than in the experiments. This is i.a. because the grid resolution in the vortex core does not match the requirement by Asnaghi et al. (2017b) any more for $x/c_0 > 1.0$ (see Section 4.4.2). Both hybrid models accelerate almost all the flow in the vortex core at $x/c_0 = 0.50$ as observed in the experiments. This is a big improvement over the other models which entirely decelerate the flow.

As was hypothesised in Section 7.1, the azimuthal and axial velocity profiles of the KSKL model are improved compared to the SST model. Still, this model is based on a linear constitutive relation for the eddy-viscosity whereby all velocities are diffused by the turbulent viscosity. This will be further elaborated on in Section 7.3. Against expectations, it is observed that the EARSM performs worst of all models despite its non-linear constitutive relation. However, this comparison is biased since the wing's circulation for the EARSM is more than 10% lower compared to the others. The lower circulation yields a weaker vortex and thus lower magnitude of all velocities in the vortex. To compare them more accurately, one should compare the velocity profiles for a constant lift force instead. Nevertheless, it can be observed that the viscous core radius of the EARSM is smaller (and thus better) compared to SST and KSKL models. Also, the slope of the azimuthal velocity ($\partial u_\theta/\eta$) for $\eta < \eta_v$ is better compared to these models. For the axial velocity however, the performance is far worse and cannot be explained by the underprediction of lift. The flow is decelerated about 40% more compared to the other RANS models.

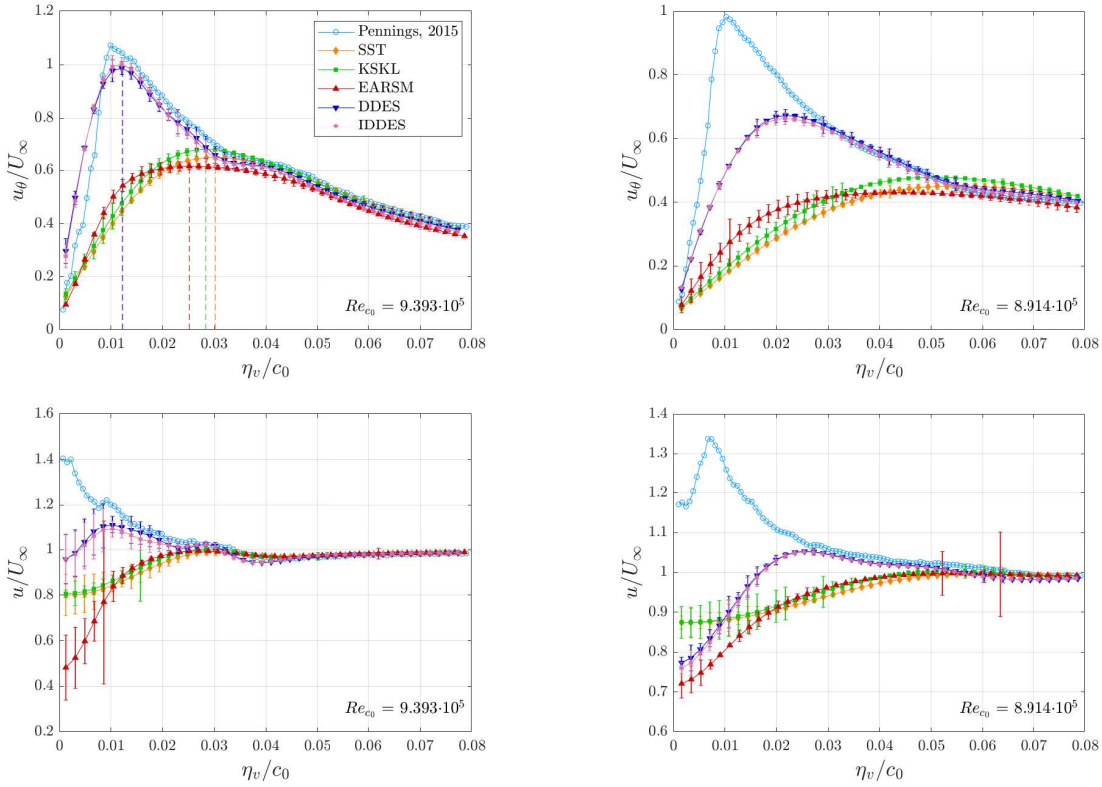

Figure 7.6: Azimuthal (top) and axial (bottom) velocity profiles averaged over sector I at $x/c_0 = 0.50$ (left) and $x/c_0 = 1.14$ (right), Re_{c_0} during the experiment is presented. Reynolds number in simulation is 8.95×10^5. Dashed lines in top left graph indicate the viscous core radii.

The results are compared quantitatively utilizing the multivariate metric r/r_{ref} as presented in Section 5.2.2. Table 7.5 presents the outcome. Note that the streamwise location $x/c_0 = 0.74$ is also analysed but not shown in Figure 7.6. The numbers in the table essentially confirm what is visualised in the local velocity profiles. The hybrid models perform best and are nearly valid over the entire range (which is the case when $r/r_{ref} \leq 1.0$). The validity decreases for the more downstream location due to numerical diffusion of u_θ and u. Of the pure RANS models, KSKL appears to perform best.

Note that from the velocity plots in Figure 7.6 it seems that the azimuthal velocity is predicted better than the axial velocity, however the multi-variant metrics imply the opposite. This is because the plots show the absolute non-dimensional velocity. The actual percentage error (on which the multi-variant metric is based) is much higher for the azimuthal velocity due to the lower magnitude what explains the lower values for r/r_{ref} for the axial velocity.

Table 7.5: Multivariate metrics (r/r_{ref}) of azimuthal (left) and axial (right) velocity profiles in sector I for different turbulence models as displayed in Figure 7.6.

Location	SST	KSKL	EARSM	DDES	IDDES
$x/c_0 = 0.50$	9.49	5.29	8.47	1.85	2.40
$x/c_0 = 0.74$	13.5	11.7	15.6	3.20	3.65
$x/c_0 = 1.14$	21.9	16.7	19.2	9.27	9.40

Location	SST	KSKL	EARSM	DDES	IDDES
$x/c_0 = 0.50$	3.29	3.65	3.91	1.71	1.87
$x/c_0 = 0.74$	3.72	5.38	4.97	2.02	1.96
$x/c_0 = 1.14$	9.27	14.0	11.1	4.35	4.50

The discretisation error appears to be dominated by the spatial discretisation. This is observed in two ways. First, the mean azimuthal and axial velocity distributions are visually checked for the effect of the grid and timestep sizes. Figure 7.7 presents the velocity distributions around the viscous core radius fir the KSKL and EARSM models. For both velocity components, it can be observed that the results on the finest grid are almost independent of the considered timesteps. Clearly, the spatial discretisation error is a few orders of magnitude higher compared to the temporal discretisation error. Secondly, the constants in the spatial and temporal power expansion, i.e. β_s

and β_t (see Equation (5.4)), are checked quantitatively. The discretisation uncertainty in Figure 7.6 is determined in N_d points for every local velocity profile. To quantify the relative influence of the spatial discretisation uncertainty with respect to the temporal discretisation, the vector $\vec{\beta}_s = [(\beta_s)_1, (\beta_s)_2, \ldots, (\beta_s)_{N_d}]^T$ is component wise divided by $\vec{\beta}_t$ and the Root Mean Square (RMS) value is determined. Table 7.6 shows that the temporal part is for all turbulence models and streamwise position, at least two orders of magnitude smaller compared to the spatial discretisation.

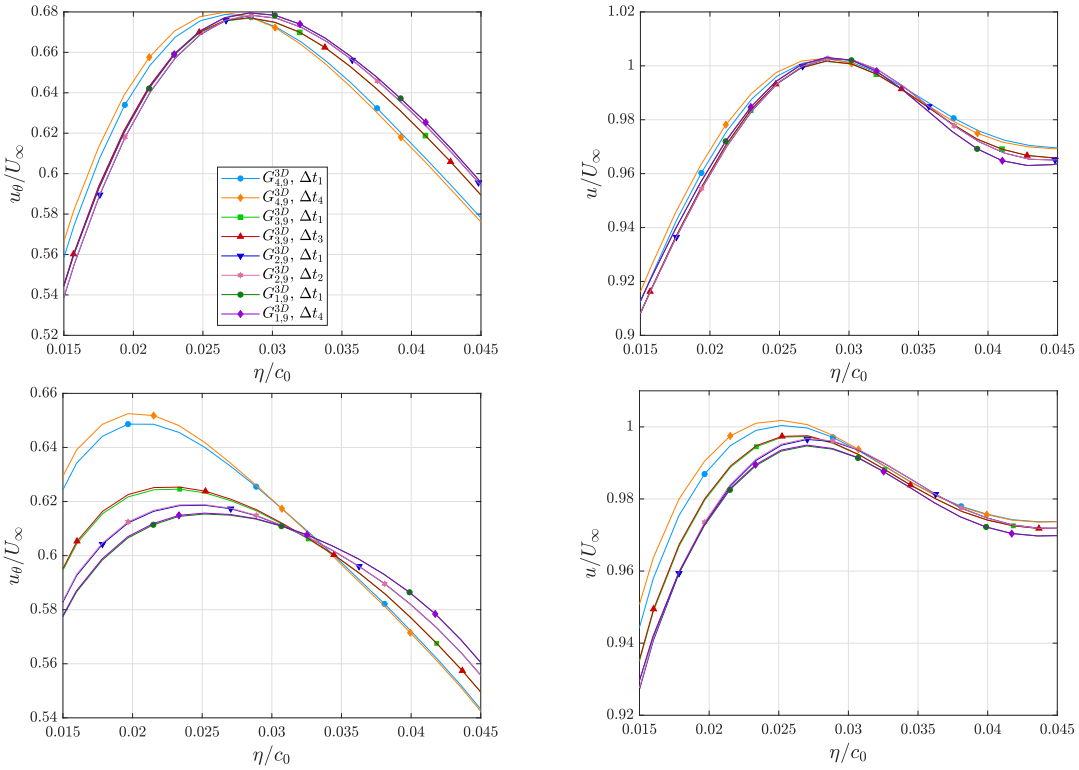

Figure 7.7: Zoom of azimuthal (left) and axial (right) velocity profiles averaged over sector I at $x/c_0 = 0.50$ for the KSKL (top) and EARSM (bottom). Plots include results for different grids and timesteps (for combinations see Table 7.1).

Table 7.6: RMS value of the vector $\vec{\beta}$ where $\vec{\beta} = [(\beta_s)_1/(\beta_t)_1, (\beta_s)_2/(\beta_t)_2, \ldots, (\beta_s)_{N_d}/(\beta_t)_{N_d}]^T$. Results for $\vec{\beta}(u_\theta/U_\infty)$ (left) and $\vec{\beta}(u/U_\infty)$ (right), all values are divided by 10^4.

Closure	SST	KSKL	EARSM
$x/c_0 = 0.50$	0.054	0.085	0.039
$x/c_0 = 0.74$	0.021	0.032	0.149
$x/c_0 = 1.14$	1.129	0.028	1.528

Closure	SST	KSKL	EARSM
$x/c_0 = 0.50$	0.223	0.100	0.039
$x/c_0 = 0.74$	0.678	0.134	0.747
$x/c_0 = 1.14$	0.004	0.1529	1.152

GLOBAL VELOCITY PROFILES

Spatially averaging over sector I, as was done in the previous section, filters out the possibility to recognise local flow phenomena. In this section, the full velocity fields in sector I are validated. Figure 7.8 shows the (temporal) mean azimuthal and axial velocities over sector I for the different turbulence models and the experimental measurements. Note that in all cases sector I is considered, however rotated by $\pi/2$ radians in the plotting routine. Also, the result for the SST simulation is present in both figures for comparison.

The azimuthal velocity fields for the RANS simulations are almost completely symmetric around the vortex centre and the velocity magnitudes are substantially underpredicted as already observed in the previous section. The contour lines of the DDES and IDDES simulations however, match the experimental measurements well. The asymmetry in sector I due to the roll-up process can be observed. The magnitude of the azimuthal velocity is higher in the right part of sector I which is because the roll-up process is counter-clockwise (negative around the

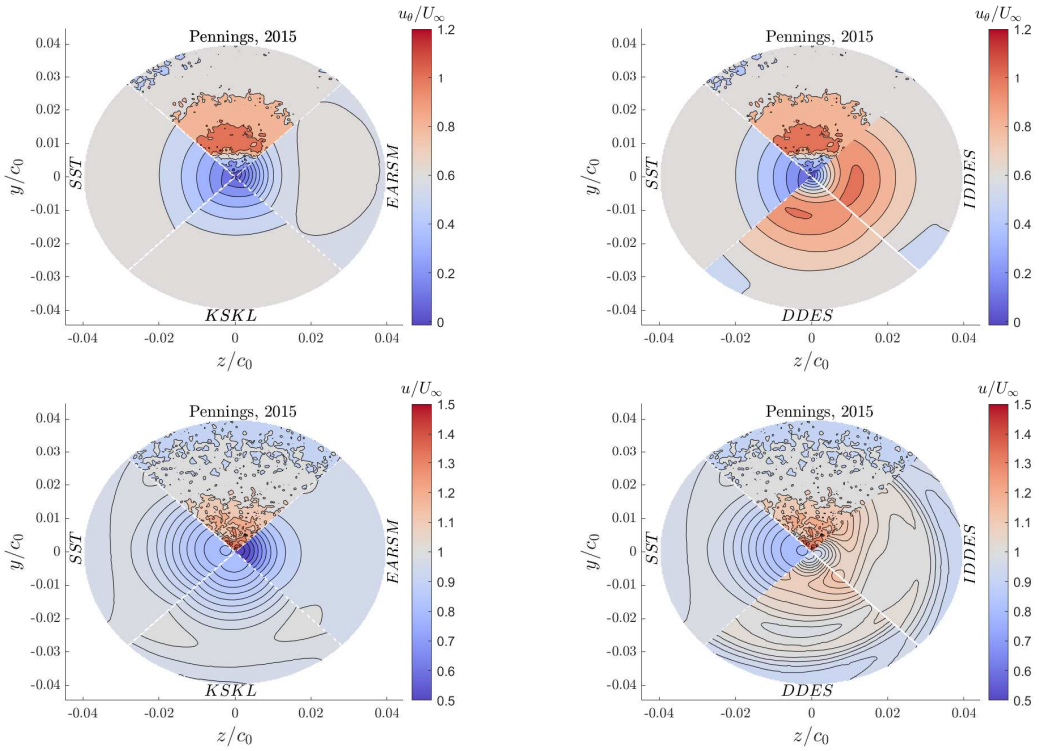

Figure 7.8: Azimuthal (top) and axial (bottom) velocity fields for SST, KSKL, and EARSM (left) and SST, DDES, and IDDES (right) turbulence models in sector I at $x/c_0 = 0.50$. The top sector shows the experimental results by Pennings et al. (2015b).

x-axis). The matching colours also indicate that the magnitude of the azimuthal velocity is similar, however the experimental measurement seems to have a slightly larger region of $u_\theta/U_\infty \approx 1.2$.

The axial velocity fields are also symmetric for all RANS models which implies that the RANS models encounter difficulties in predicting the roll-up process accurately. Here also the deceleration of the flow in all RANS models is observed while the flow is accelerated in the experiments. The hybrid models also show deceleration near the centre of the vortex but match the axial velocity quite well just outside the core. Again the asymmetry is present in the axial velocity fields of the DDES and IDDES simulations.

Figure 7.9 presents the magnitude of the error of the azimuthal and axial velocity fields for all turbulence models. The colour scheme is scaled such that red indicates an overprediction, blue an underprediction. The global trend for all turbulence closures is that the velocity is underpredicted. All RANS model underpredict the azimuthal and axial velocities in and around the viscous core. For the hybrid models, the azimuthal velocity near the viscous core is slightly overpredicted in some areas. For all models, an error in the freestream velocity is observed to be in the order of 0.01-0.1 $(\cdot)/U_\theta$. This is because the experimental freestream velocity is set with 0.5% accuracy (Pennings et al., 2015b).

In order to get a better insight into how large the modelling error is with respect to the validation uncertainty, the validation uncertainty is subtracted from the absolute error. By taking the absolute error, information regarding over/underprediction is lost, but this was already visualised in Figure 7.9. The validation uncertainty is determined according to the definition in Equation (5.15) where the experimental uncertainty is unknown and therefore set to be zero. This uncertainty is certainly larger than zero however there simply is no information regarding the magnitudes. The numerical error is composed of (i) the discretisation error in each point, and (ii) the statistical error (assumed to be maximum 0.1%) for every point as discussed in Section 5.1.1. To determine the discretisation uncertainty, the procedure as described in Section 5.1.1.3 is executed in each point. The process to determine the discretisation error composed of a spatial and temporal part is a factor $\mathcal{O}(10^3)$ more expensive in the most recent version of the uncertainty software compared to only considering the spatial discretisation error. The costs would be in the order of four days per turbulence model per streamwise plane on one processor. Parallelisation or optimising the computational efficiency of this process is not considered worthwhile since the

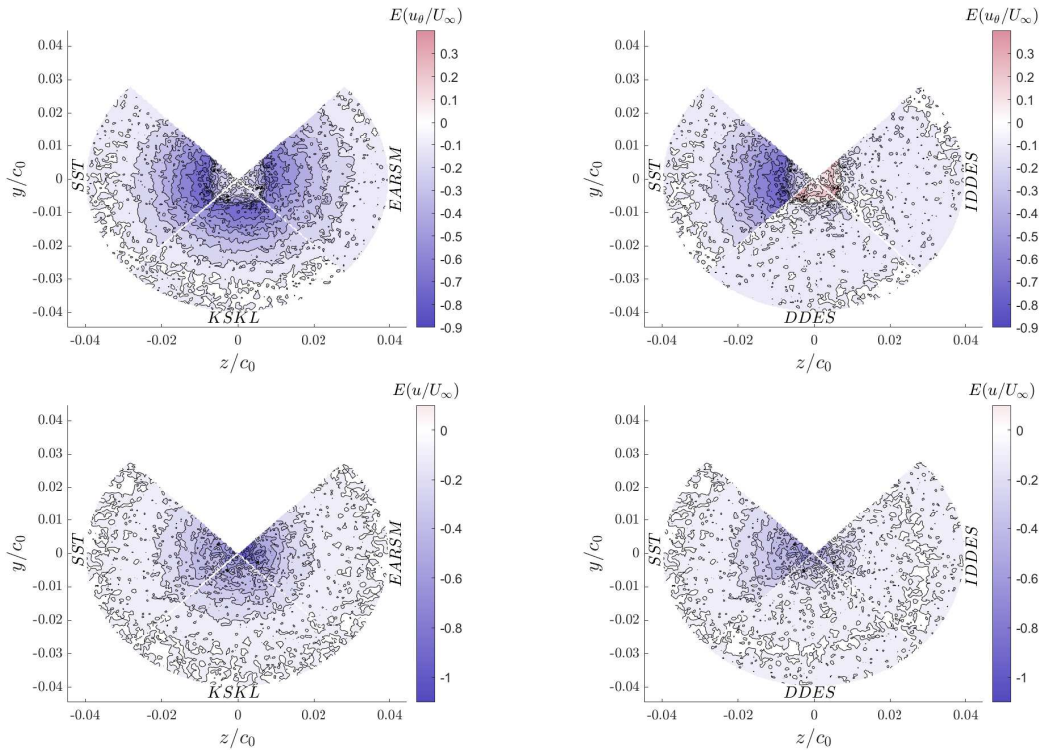

Figure 7.9: Errors of azimuthal (top) and axial (bottom) velocity fields for SST, KSKL, and EARSM (left) and SST, DDES, and IDDES (right) turbulence models in sector I at $x/c_0 = 0.50$.

solution was shown to be almost independent of the timesteps ($\Delta t_1 : \Delta t_4$) before. For this reason, only the spatial part of the discretisation error is considered in the analysis of the flow field.

Figure 7.10 shows the contours of $|E(\phi)| - U_v(\phi)$. The regions where this quantity is smaller than 0 are considered to be 'validated' with modelling error equal to $\pm(|E(\phi)| - U_v(\phi))$. Qualitatively it can be concluded that the hybrid models are validated over almost the entire sector for both velocity components. The azimuthal velocity is only just underpredicted in the right part of the viscous core; the axial velocity is underpredicted near the vortex centre. For all RANS models, the obvious conclusion is that the symmetry of the vortex and the underprediction of the velocity magnitudes yields the models to be invalid for the entire vortex.

To perform a quantitative comparison, again the multi-variant metric is determined but now for the entire flow field in sector I which consists of $\mathcal{O}(10^4)$ points. Table 7.7 presents the results for both velocity components. The numbers show a remarkable result. No distinction is made between the results for the different turbulence models any more, all r/r_{ref} values at each streamwise location are more or less identical. This observation is

Table 7.7: Multivariate metrics (r/r_{ref}) of azimuthal (left) and axial (right) velocity fields in sector I for different turbulence models as displayed in Figure 7.6.

Location	SST	KSKL	EARSM	DDES	IDDES
$x/c_0 = 0.50$	6.05	5.42	6.65	5.77	6.35
$x/c_0 = 0.74$	4.29	6.30	5.67	3.12	3.19
$x/c_0 = 1.14$	3.57	4.57	5.31	3.99	3.81

Location	SST	KSKL	EARSM	DDES	IDDES
$x/c_0 = 0.50$	4.03	3.32	2.83	2.98	3.05
$x/c_0 = 0.74$	4.70	2.78	5.09	3.48	3.47
$x/c_0 = 1.14$	3.52	5.30	2.85	1.54	1.58

found to be a limitation of a multi-variant metric when applied to vortical flow features. A uniform vector spacing is used in the measurements and thus also in the numerical results. Hereby the number of points within the vortex is in the order of 10% compared to the number of points in the freestream. In other words, when using the entire flow field, more 'weight' is given to the freestream measurements rather than the region of interest: the vortex. One could decrease the radius of sector I (η_{sI}, see Figure 5.8), but this choice would be arbitrary. Furthermore, the results would depend on this specified radius. Due to this uncontrolled factor (which would also be different for the different turbulence models due to the difference in diffusivity of the vortex) it was decided not to alter the

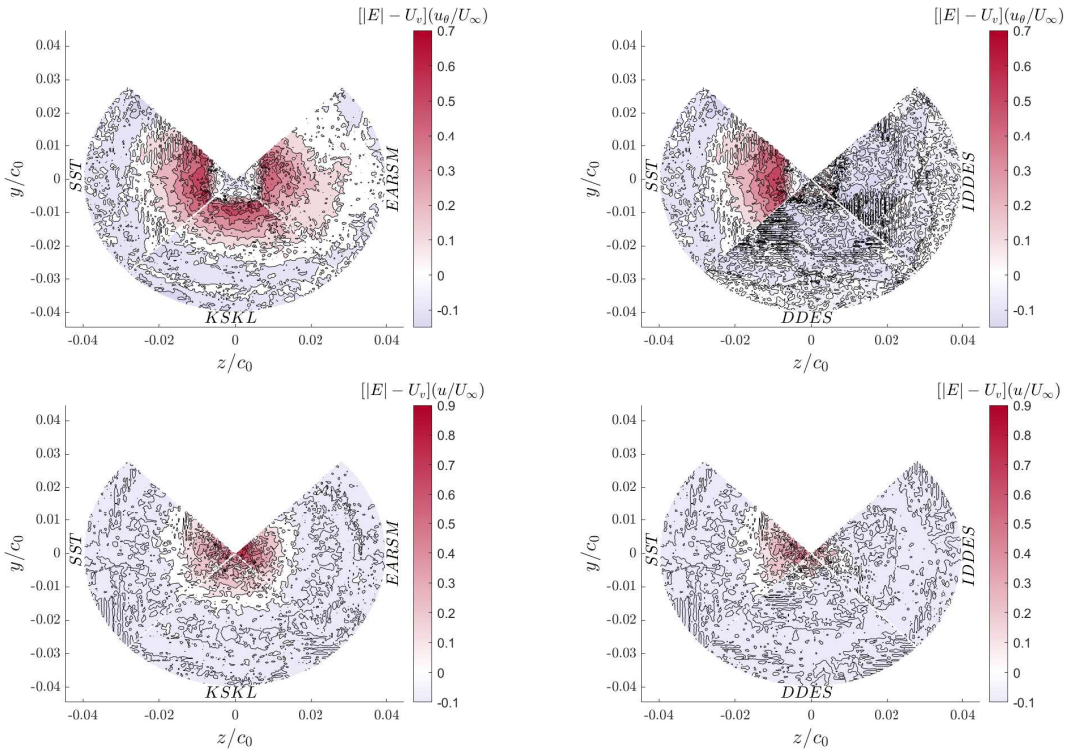

Figure 7.10: $|E(\phi)|-U_v(\phi)$ contours of azimuthal (top) and axial (bottom) velocity fields of the SST, KSKL, and EARSM (left) and SST, DDES, and IDDES (right) turbulence models in sector I at $x/c_0 = 0.50$.

'to-be-analysed radius' and consider the r/r_{ref} values of the local velocity profiles as leading (see Table 7.5). For further studies regarding vortices it is therefore advised to apply the multivariate metric on the spatially averaged velocity profiles rather than the full flow fields to emphasize the region of interest.

7.3. DISCUSSION OF RESULTS

In the previous section, the results were predominantly compared against experimental measurements. This section aims to expose the behaviour from a more theoretical perspective. First, the effect of turbulent diffusion is discussed. After that, Section 7.3.2 focusses on the characteristics of the turbulent flow in the vortex.

7.3.1. TURBULENT DIFFUSION

As introduced in Section 7.1, previous researchers encountered excessive turbulent diffusion of the vortex due to an overprediction of the eddy-viscosity which amplifies the diffusion term in the momentum equations. To understand what happens in the different turbulence models, this section aims to investigate the origin of this overprediction. Again, the spatially-averaged temporal mean quantities over sector I are considered in the $y-z$ plane at $x/c_0 = 0.50$. All results in this section are obtained using grid $G^{3D}_{1,9}$ with timestep Δt_1. Figure 7.11 presents the eddy-viscosity over the vortex radius for the different turbulence models. The dashed lines indicate the viscous core radii determined from Figure 7.6. The eddy-viscosity for the pure RANS models is more than an order of magnitude higher compared to the hybrid models. Remarkable is that the peak in eddy-viscosity for the SST and KSKL models is within the viscous core radius while for the EARSM it is clearly outside the viscous core.

For all are $k-\omega$ based models, the eddy-viscosity is a function of the ratio of k and ω, i.e. $\nu_t \sim k/\omega$, while for the KSKL model the eddy-viscosity is proportional to $\sqrt{k}L$ as defined in Equation (3.16). This proportionality can be slightly rewritten such that it matches the units in the numerator and denominator of k/ω, this yields $\nu_t \sim k/(\sqrt{k}/L)$. The overprediction of the eddy-viscosity can thus be due to either excessive production of turbulent kinetic energy or a low specific dissipation rate. Figure 7.13 shows the turbulent kinetic energy (numerator) and specific dissipation rate (denominator) where $\omega = \sqrt{k}/L$ for the KSKL model. The turbulent kinetic energy for the RANS models is more than a factor of five higher compared to the hybrid models. For the specific dissipation rate,

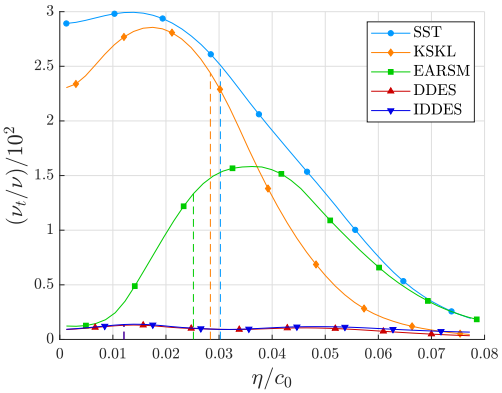

Figure 7.11: Eddy-viscosity ratio over sector I for the different turbulence models. Dashed lines indicate the viscous core radii as determined from Figure 7.6.

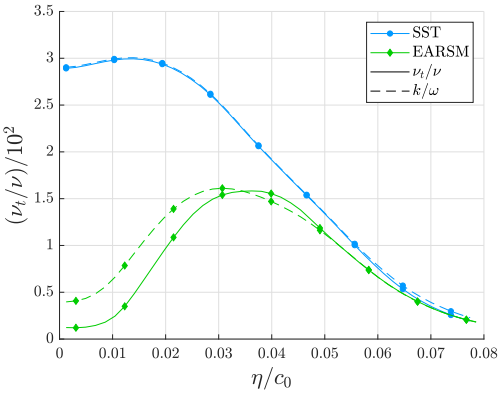

Figure 7.12: Quantification of the effect of the spatially varying C_μ on the eddy-viscosity of the EARSM model compared to the SST model.

the exact opposite holds which implies that excessive production of turbulent kinetic energy is responsible for the overprediction of eddy-viscosity.

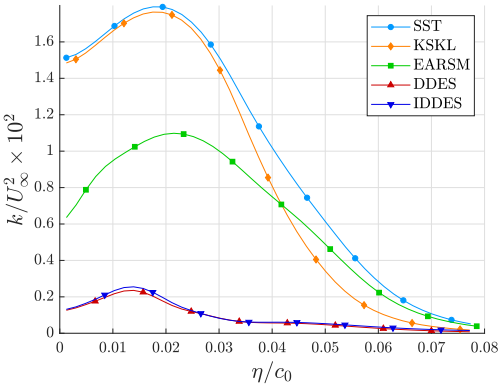

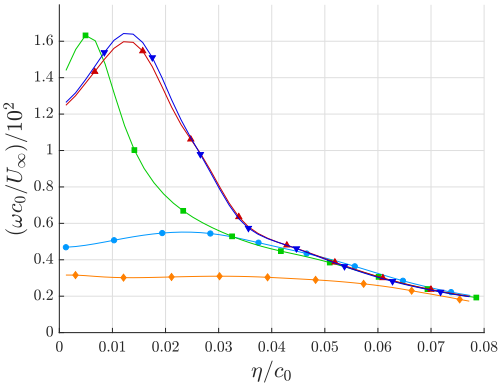

Figure 7.13: Turbulent kinetic energy (left) and specific dissipation rate (right) profiles averaged over sector I. Specific dissipation rate for the KSKL model is determined as $\sqrt{k}/L$.

Schot (2014) and Asnaghi (2018) also explained the axial velocity deficit (deceleration) by the high eddy-viscosity. It appears that the ν_t for the EARSM is in the same order as the hybrid models for $\eta_v/c_0 < 0.01$. However, Figure 7.6 clearly showed that the axial velocity of the EARSM model is even more than 40% lower compared to the SST and KSKL models in that region. The reasons why the eddy-viscosity drops near the centre of the vortex in the EARSM simulation are (i) the specific dissipation increases, and (ii) the eddy-viscosity in the EARSM is not only dependent on k and ω but also on C_μ, which is not a constant in this model (see Appendix B.2.2). In the EARSM, the C_μ varies in space dependent on $C_\mu \sim II_\omega \sim \Omega^*_{ij} \sim \tau \sim 1/\omega$. Through this relation, $\nu_t \sim 1/\omega^2$ whereby the effect of the increased specific dissipation rate is amplified. This is visualised in Figure 7.12 where the eddy-viscosity of the SST model is compared to the EARSM. The solid lines indicate the eddy-viscosity used in each model (direct export from ReFRESCO). The dashed lines are determined by dividing the turbulent kinetic energy by the specific dissipation rate. For the SST model, $\nu_t \sim k/\omega$ holds, for the EARSM model the effect of C_μ is clearly visible and indeed reduces the eddy-viscosity near the vortex centre. However, this still not explains the large deficit in axial velocity near the centre of the vortex in the EARSM simulation.

The deficit is due to the non-linear term in the definition of the Reynolds stress tensor, a_{ij} as defined in Equation (3.18). Figure 7.14 presents the normal and off-diagonal components of this tensor. All components appear to be highest in magnitude near the centre of the vortex. Especially the x-normal (a_{11}) and x-shear (a_{13}) are observed to be large which could be an explanation for the reduced axial velocity in the EARSM. This will be further discussed in Section 7.3.2.

By definition, the turbulent kinetic energy is determined by the trace of the Reynolds stress tensor, i.e.

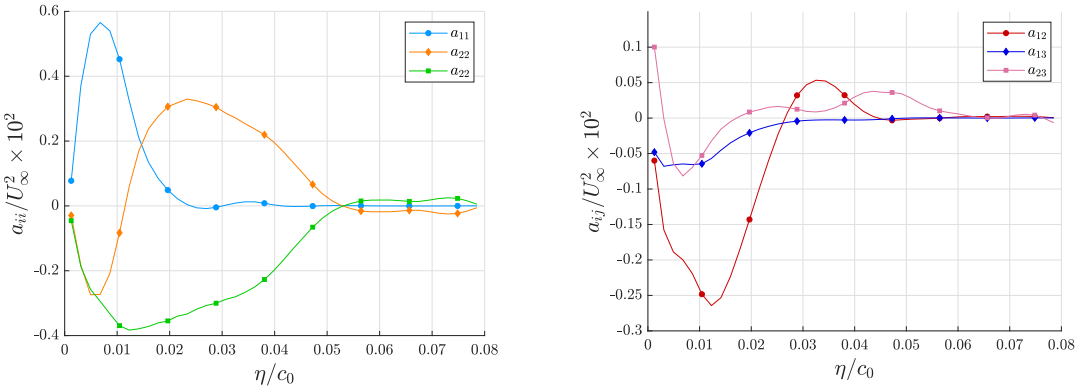

Figure 7.14: Normal (left) and shear (right) components of the anisotropy tensor of the EARSM simulation averaged over sector I.

$\left(k \equiv \overline{u_i' u_i'}/2\right)$. Figure 7.15 shows the three individual *unresolved* normal Reynolds stresses for the different turbulence models. For the SST, KSKL, DDES, and IDDES models, the normal components of the tensor are the same in magnitude which indicates the directional independence of the turbulent kinetic energy. This is not the case for the EARSM simulation where the x and y-normal components are dominant. Their distributions also vary strongly along the radius compared to one another.

The modelled velocity fluctuations in all directions for the hybrid models are more than five times lower compared to the other models. This is because the hybrid models apply LES in the refined vortex region and therefore resolve a part of the turbulence spectrum. To check to what extend LES is applied in the vortex, the turbulence length scales l_t^{DES} and l_t^{RANS} are determined for both models. The definition of the length scales for DDES and IDDES can be found in Sections B.2.3 and B.2.4. Figure 7.16 shows the different length scales for both closures. Clearly the LES length scales drop below the RANS scales within the vortex. Based on the length scales, about 70% the turbulent flow field within the vortex is determined based on to the LES framework, the rest is modelled by the RANS closure.

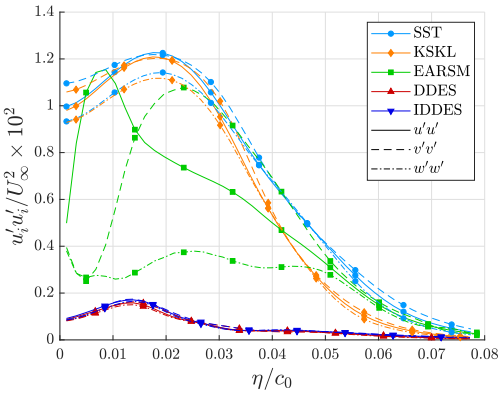

Figure 7.15: Normal components of the unresolved Reynolds stress tensor averaged over sector I for the different turbulence models.

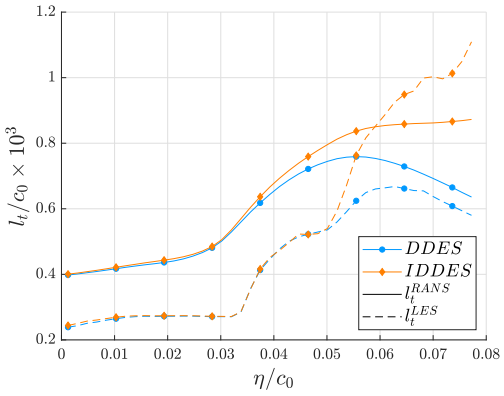

Figure 7.16: RANS (solid line) and DES (dashed line) length scales averaged over sector I for the DDES and IDDES turbulence models.

The transition between the RANS and LES region is critical for the quality of the results (i.e. one should avoid MSD by minimising commutation errors). At this interface, the model should transition from a fully statistical (unresolved) representation of turbulence to a region where part of the turbulence spectrum is resolved. In the vortex region, the Reynolds stress tensor (in hybrid simulations) is composed of resolved $(u_i' u_j')_r$ and unresolved $(u_i' u_j')_u$ components,

$$u_i' u_j' = (u_i' u_j')_r + (u_i' u_j')_u \,. \tag{7.1}$$

DES blends the RANS and LES frameworks by the destruction term $\sqrt{k^3}/l_t$ as presented in Equation (3.24).

When flow convects from the BL region, where pure RANS is applied, towards the vortex region where also LES is applied, the destruction term lowers the turbulent kinetic energy in the blending region. This should in principle destabilise the flow which allows flow disturbances (originating from e.g. unsteady effects, turbulent inflow, or the turbulent BL) in the LES region to develop. However, for the 'Arndt' wing, no large separation regions or other unsteady effects were observed whereby all turbulence is expected to be generated in the BL. Also, a steady inflow is specified whereby all velocity fluctuations in the vortex must originate from the BL and therefore rely on the quality of the interface. If the commutation error does not allow translation from an statistical representation of turbulence to actual resolved fluctuation, there are no disturbances in the flow which can develop into fluctuations whereby the turbulent activity in the LES region is expected to be underpredicted.

To check the impact of the commutation errors, Figure 7.17 shows the resolved versus the modelled Reynolds stresses in the vortex for the DDES and IDDES models. The resolved part of the Reynolds stress tensor was determined by subtracting the temporally averaged velocity field from the instantaneous quantities in the last 150 timesteps. It is clear that there are no resolved velocity fluctuations in the vortex, which also clarifies why the hybrid models converged to a steady as observed by the TST in Section 7.2.2.

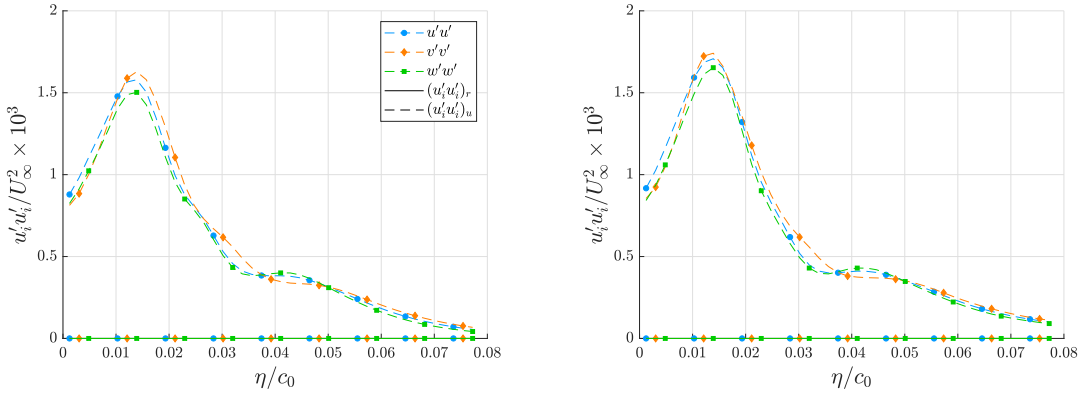

Figure 7.17: Resolved and unresolved normal components of the Reynolds stress tensor for DDES (left) and IDDES (right).

The reduction of turbulent kinetic energy in the vortex core for the hybrid models is thus because the resolved portion of the Reynolds stresses is in the order of 10^{-6}. This is, of course, unphysical and derives from the commutation errors what results in MSD.

Paskin (2018) applied DES on the 'Arndt' wing with an unsteady vortex region in which velocity fluctuations were resolved. He used the solver ISIS-CFD, details regarding the state of the inflow were not found. The problem of no resolved velocity fluctuations was also encountered by other researchers using ReFRESCO, e.g. Pereira and Vaz (2018). Researchers using other solvers also came across this problem which is extensively discussed by i.a. Tabor and Baba-Ahmadi (2010) and Mocket et al. (2018). According to these two references the two most common approaches to tackles this problem are (i) precursor simulation methods, and (ii) synthesised turbulence methods. In ReFRESCO, a synthetic turbulence generator which enables to specify time-varying stochastic velocity fluctuation in the inflow is currently being developed by Ir. M.D. Klapwijk (Klapwijk et al., TBD).

So although the hybrid models match the experimental data well, it is questionable whether all relevant physics are taken into account in the simulation. In other words, the LES region of the hybrid models results in a large amount of laminar flow in the vortex due to the absence of turbulent fluctuations. Within the solid body rotation of the vortex as described in Section 2.2.3 this would be plausible but for the region near the viscous core not.

7.3.2. TURBULENCE CHARACTERISTICS

In the previous section, the normal components of the Reynolds stress tensor were presented. Figure 7.18 presents the off-diagonal, or shear, components. The hybrid models again show much lower values for the Reynolds shear stresses compared to the RANS models for the same reasons given in the previous section. Note that the EARSM profiles are the linear minus the non-linear part. The $u'w'$ component for EARSM model is a factor three higher compared to the other two RANS models in the region $\eta/c_0 < 0.01$ which also contributes to the axial velocity deficit.

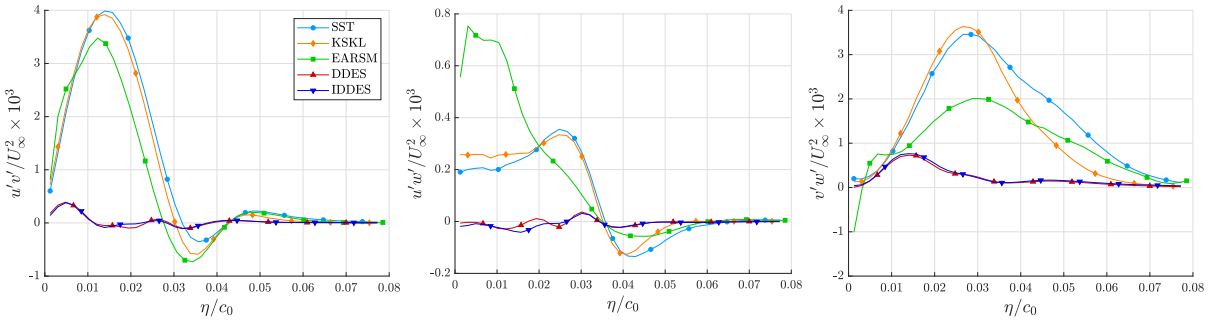

Figure 7.18: Reynolds shear stress tensor components $u'v'$ (left), $u'w'$ (middle), and $v'w'$ (right) averaged over sector I for the different turbulence models.

One of the most popular techniques in the CFD community to determine turbulence characteristics is the use of anisotropy invariant maps (Krogstad and Torbergsen, 2000). These maps are Two-Dimensional (2D) domains based on invariant properties of the Reynolds stress anisotropy tensor ($\tilde{\tau}_{ij}$) as originally proposed by Lumley and Newman (1977). The diagonalisation of $\tilde{\tau}_{ij}$ provides three eigenvalues, or magnitudes, λ_1, λ_2, and λ_3 and three eigenvectors, or directions, $\vec{v}_1$, $\vec{v}_2$, and $\vec{v}_3$ of the turbulence anisotropy. Most of the analysis techniques for CFD applications ignore the eigenvectors and therefore lose the directional information. Despite this shortcoming, these kind of maps have been used in numerical and experimental analyses of various fluid flows (Emory and Iaccarino, 2014).

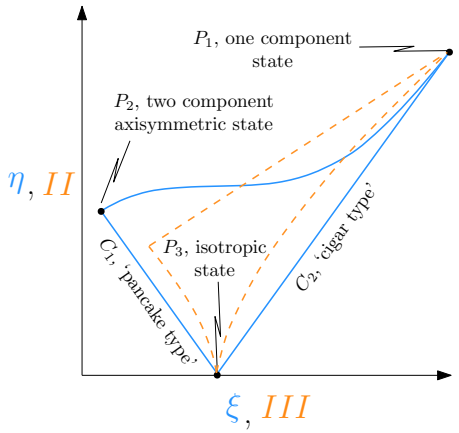

Figure 7.19: Illustation of turbulence (blue) and Lumley (orange) triangles with corresponding turbulent states.

In this work, the so-called turbulence triangle, as introduced by Choi and Lumley (2001), is used. This approach plots the invariants on a stretched version of the original Lumley triangle which makes it better applicable for isotropic turbulence (by definition the expected state of the turbulence for the SST model). The definition of the normalised Reynold stress anisotropy tensor reads,

$$\tilde{\tau}_{ij} = \frac{\tau_{ij}}{2k} - \frac{\delta_{ij}}{3}. \tag{7.2}$$

The eigenvalues of this matrix describe the relative strengths of the velocity fluctuations in each direction, i.e. the directionality of the turbulent flow field. By definition, all these eigenvalues are contained in the turbulence triangle as visualised in Figure 7.19. This figure also shows the original Lumley triangle by the dashed orange lines and the stretching near P_1 can be recognised. Three limiting states of the directionality, which define the boundaries of the turbulence triangle, exist:

I) *One-component turbulence (P_1)*, where turbulent fluctuations are only present in one direction which requires $\lambda_i = [2/3, -1/3, -1/3]^T$.

II) *Axisymmetric two-component turbulence (P_2)*, where turbulent fluctuations with equal magnitude are present along two directions which requires $\lambda_i = [1/6, 1/6, -1/3]^T$.

III) *Isotropic turbulence (P_3)*, where all eigenvalues are zero. This is easy to understand since if the turbulence is perfectly isotropic ($u'u' = v'v' = w'w'$), $k = 3u'u'/2 = 3v'v'/2 = 3w'w'/2$ whereby the diagonal of $\tau_{ij}/(2k)$ as shown in Equation (7.2) is [1/3 1/3 1/3]. This yields the diagonal components of the Reynolds stress anisotropy tensor and thus the eigenvalues of the tensor to be zero (provided that the off-diagonal components are negligible).

The connection of these states, or P_1, P_2, and P_3, creates the boundaries of the turbulence triangle but can also be interpreted physically. The curves C_1 and C_2 are axisymmetric states, the turbulence along C_1 has a 'pancake' form; the turbulence along C_2 is referred to as 'rod-like' or 'cigar-shaped' turbulence.

In the original proposal by Lumley and Newman (1977), the second and principle invariants were used to set-up the invariant maps,

$$II = \frac{1}{2}[\mathrm{tr}(\tilde{\tau}_{ij})^2 - \mathrm{tr}(\tilde{\tau}_{ij}^2)] = \lambda_1\lambda_2 + \lambda_1\lambda_3 + \lambda_2\lambda_3, \quad III = \det(\tilde{\tau}_{ij}) = \lambda_1\lambda_2\lambda_3\,. \tag{7.3}$$

In turbulence triangles these quantities are scaled such that $\xi = \sqrt[3]{III/2}$ and $\eta = \sqrt{II/3}$.

Figure 7.20 presents the turbulence triangles for the different turbulence models. For the turbulence triangles, again the velocity field (in Cartesian coordinates) in sector I at $x/c_0 = 0.50$ is considered. From Figures 7.15 and 7.18, it can be concluded that almost all components of the Reynolds stress tensor are negligible for $\eta/c_0 > 0.04$ compared to the values near the vortex centre. For this reason, only the points in the most inner part of the vortex ($\eta/c_0 < 0.4$) are considered in this analysis.

As expected, the models based on a isotropic turbulence assumption (i.e. the SST and KSKL models) end up near P_3 which verifies the isotropy. As already observed in the distributions of the Reynolds stress components, the EARSM is able to reproduce some of the anisotropy in the vortex structure. It is observed that the points close to the vortex centre are located closest to the C_2 boundary and therefore have a 'cigar' type of turbulence (i.e. 1D turbulence). This is in line with the Reynolds stress profiles as shown in Figures 7.15 and 7.18 where the fluctuations in streamwise (x) direction are observed to be dominant close to the vortex core. In the region around the viscous core size ($\eta/c_0 \approx 0.025$, see Figure 7.6), the points are located near C_1 and thus two-component or 'pancake' turbulence (i.e. 2D turbulence). Further outside the vortex, the different components become similar in magnitude whereby some of the turbulence in the considered region is isotropic.

The cloud of points in the turbulence triangle for the DDES and IDDES have similar shapes as the SST model. However, more points are located closer to the centre of the triangle. This is because of the almost laminar vortex for the hybrid models. The relative difference between the normal and shear components becomes less whereby the Reynolds stress tensor is less diagonally dominant. For this reason the off-diagonal components of τ_{ij} are higher compared to the SST case (since k is lower for DDES and IDDES). Hereby the eigenvalues of this matrix do not tend to zero as much as for the SST model even though the state of the turbulence is the same since the same turbulence model is used (in both cases the SST model since the LES contribution to the Reynolds stresses is zero as concluded in Section 7.3.1)

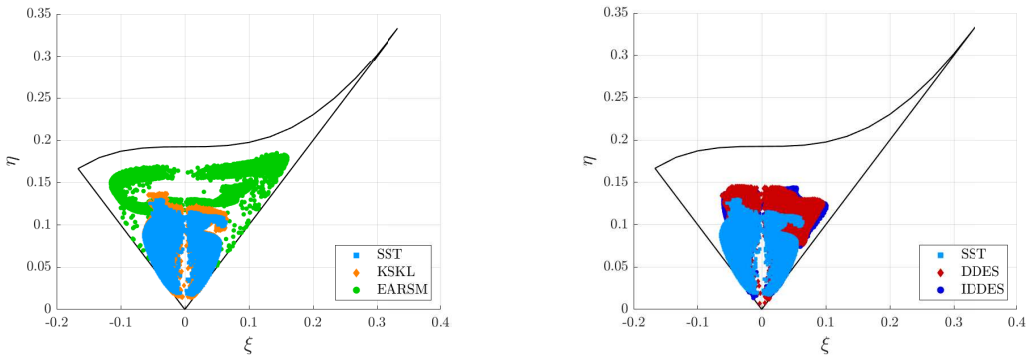

Figure 7.20: Turbulence triangles of the turbulence state in the vortex core for $\eta/c_0 < 0.04$ for different turbulence models: SST, KSKL, and EARSM (left) and SST, DDES, and IDDES (right).

7.4. CONCLUSIONS

In this chapter, the SST, KSKL, EARSM, DDES, and IDDES turbulence models have been assessed. These models are theoretically promising (see Chapter 3) for accurately predicting vortical flows, and were therefore applied on the 'Arndt' wing in this chapter. The numerical results are compared to experimental force and S-PIV measurements by Pennings et al. (2015b).

All models result in a lift coefficient of about 0.66 except the EARSM which underpredicts the lift due to a large separation region on the suction side. The viscous core radius and consequently the pressure in the vortex centre for the hybrid models (DDES and IDDES) match well with the experiments in the region one root-chord length

downstream of the tip. This is because these models predict the azimuthal and axial velocities profiles well in that region. Despite promising theory, the KSKL model still suffers from excessive production of turbulent kinetic energy and thus turbulent diffusion of the vortex. Although the velocity profiles of the EARSM simulation seem worse than the SST and KSKL models, the comparison is biased due to the lift (and thus vortex strength) which is underpredicted by 10%. It is advised to compare these models for a constant lift coefficient. Furthermore, it was observed that the location of the viscous core radius was better predicted by the EARSM model compared to the other RANS models.

Although the results of the hybrid models initially seem validated, the outcome is still judged to be have a large modelling error. The resolved Reynolds stresses are found to be negligible compared to the unresolved stresses. This is because all turbulence is developed in the wing's BL. Commutation errors result in damping of the fully statistical representation of turbulence to a resolved representation in the form of velocity fluctuations (i.e. modelled stress depletion). The destruction of turbulent kinetic energy in the area where RANS and LES are blended should decrease the stability of the flow whereby velocity fluctuations in the LES region could develop. However, it was observed that the absence of unsteady effects in the flowfield near the wing or in the freestream prevents this development which causes a too large region of laminar flow in the vortex.

The eddy-viscosity in the vortex centre of the EARSM simulation is found to be low compared to the other RANS models due to (i) an increased specific dissipation rate, and (ii) a spatially varying C_μ which amplifies the effect of the increased specific dissipation rate. This was expected to benefit the axial velocity at this location, but the opposite is observed (the axial velocity is underpredicted even more). By analysing the individual anisotropic normal and shear Reynolds stresses, it was observed that the Reynolds stresses in axial (x) direction are dominant near the vortex centre which explains the axial velocity deficit. The EARSM is the only model which is found able to reproduce some of the anisotropy of the turbulence in the viscous core. This encourages the belief that a full Reynolds stress model would perform well for this test case.

8

CAVITATION MODELLING RESULTS

The previous two chapters answered research questions II and III by means of wetted flow simulations. The aim of this chapter is to investigate whether the conclusions drawn in wetted flow conditions also apply to cavitating conditions. Section 8.2 presents the cavitating results in combination with the $\gamma - \tilde{R}e_{\theta_t}$ transition model (Chapter 6), Section 8.3 the cavitating results for the different turbulence models (Chapter 7). Furthermore, the effect of the presence of the cavity in the vortex core (i.e. the effect of the cavitation model) on other flow variables will be discussed by comparing the i.a. velocity, pressure, and eddy-viscosity profiles in the vortex for wetted and cavitating flow conditions.

8.1. INTRODUCTION AND HYPOTHESIS

In Section 2.1.2, it was found that cavitation can be triggered by flow features such as shock waves, shear layers, vibrations, and low pressure regions which makes inception hard to model. Cavitation models in modern Computational Fluid Dynamics (CFD) codes are predominantly related to the pressure since (i) low pressure regions are found to be the most dominant factor of inception (i.e. predominately hydrodynamic inception), and (ii) the other aspects are hard to incorporate in the models. Since the pressure is also considered in the previous two chapters, it is expected that the same conclusions regarding transition and turbulence modelling will be drawn in this chapter.

It is not known what the effect of the cavity in the vortex core on other variables is. As stated in Section 7.3.1, the liquid-vapour interface should act like a solid boundary which prevents turbulence momentum transfer in normal direction. For this reason, flow variables like velocity and shear stress profiles should be affected by the presence of the cavity. Unfortunately, this cannot be tested by comparing the numerical results to the Stereographic-Particle Image Velocimetry (S-PIV) measurements by Pennings et al. (2015b) because the expansion of the liquid pushes the measurement particles outside of the cavity and therefore the flow characteristics in this region are unknown.

Another interesting aspect is the movement away from pure Reynolds Averaged Navier Stokes (RANS) models which should introduce velocity and thus pressure fluctuations. As said, only hydrodynamic inception is considered in most CFD simulations. The effect of resolving pressure fluctuations instead of having an averaged pressure field on the behaviour of the cavitation model would be of interest. This is also recognised by Wang et al. (2017). In their outlook, they pose the question 'can the simplified mass transfer model deteriorate the high fidelity flow field obtained from Detached Eddy Simulation(s) (DES) and Large Eddy Simulation(s) (LES)?'. No resolved pressure fluctuations are present in the current simulations (see Section 7.3.1) and therefore the effect of the pressure fluctuations on the behaviour of the cavition model cannot be assessed in this work.

8.2. TRANSITION ANALYSIS

In this section, the transition simulations of Chapter 6 are performed in cavitating flow conditions. The results are again presented as follows: first the numerical settings are presented, then the iterative convergence is assessed, and finally the results are presented and discussed.

8.2.1. NUMERICAL SETTINGS

The same settings were used as for the earlier transition calculations (see Section 6.3.1 and Table D.2). The wing is only considered at $\alpha = 5°$ since it was concluded that for this Angle(s) of Attack (AoA) the vortex is most affected by transition modelling. Simulations are performed for a cavitation number σ of 1.7 to avoid sheet cavitation (Schot et al., 2014). The Schnerr-Sauer cavitation model as described in Section 3.3.2 is employed, detailed settings such as the bubble radius and the number of seeds can be found in Table D.4. These numbers were set based on the original publication by Schnerr and Sauer (2001), settings used by Schot et al. (2014), Hoekstra and Vaz (2009), and Van den Boogaard (TBD). The choice of these input parameters affects the mass transfer rates between both states. Physically this is intuitive since one can imagine that more or larger bubbles would for example affect the time scales in the process. However, this is considered to be out of the scope of this project and therefore the input parameters for the cavitation model are kept constant.

The grid used in this analysis is $G^{3D}_{1,5}$. The discretisation uncertainty is not assessed, it is expected to not deviate much compared to the results of Chapter 6. In the earlier chapters, the vortex was considered at three streamwise locations downstream of the tip, i.e. $x/c_0 = [0.50,\ 0.74,\ 1.14]$. However, due to the shortcoming of the SST model (even in combination with the $\gamma - \tilde{R}e_{\theta_t}$ transition model), the pressure is already too high at these locations to sustain the cavity. In the majority of the analysis presented next, the cavity is considered much closer to the wing tip ($x/c_0 = 0.1$). However, at this location the vortex trajectory is not parallel to the freestream. This means that monitor planes (in $y-z$) perpendicular to the freestream do not serve for an accurate analysis anymore. For this reason, the trajectory of the vortex was determined and the monitor planes were rotated such that the surface normals of the monitor planes align with the vector parallel to the vortex trajectory.

8.2.2. ITERATIVE CONVERGENCE

The simulations in general have the same convergence behaviour as was observed in Section 6.3.2, i.e. the iterative procedure (outer-loops for mass-momentum coupling, see Section 4.3.2) stagnates with the transition variables being at least 1.5 orders of magnitude higher compared to all others; all forces have converged; the maximum residuals are observed to be locally at the transition location on the pressure side of the wing.

To increase the robustness of solver, the simulations are started in wetted flow conditions after which the cavitation number is gradually decreased. To monitor the convergence of the cavitating regions, the source term for the vapour volume fraction (S_{ϕ_v}, see Equation (3.28)) and vapour volume in the entire domain are determined for each iteration. An additional requirement for the iterative convergence compared to wetted conditions is that the total vapour volume should become constant (i.e. the total source term should go to zero). Figure 8.1 shows the total source term and vapour volume in the entire domain for the range of turbulent inflow conditions. The source term converges to zero after about 2×10^3 outer loops whereby ϕ_v becomes constant for all simulations.

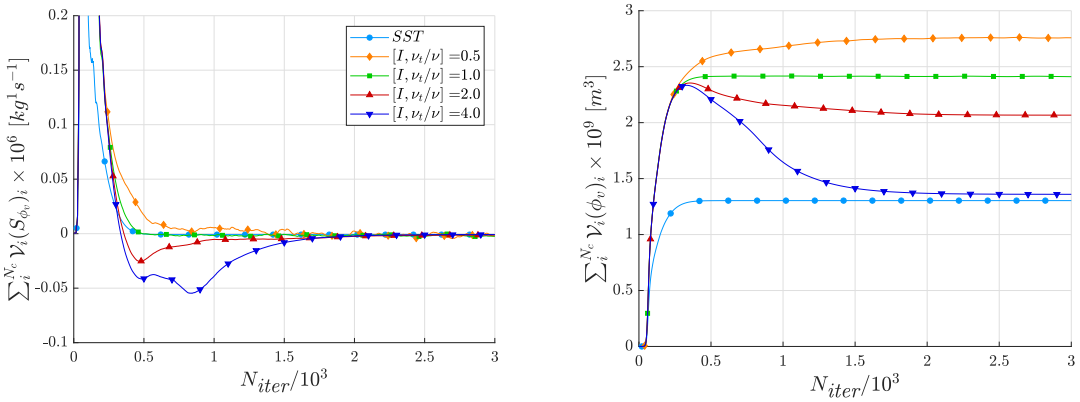

Figure 8.1: Total vapour source term (left) and total vapour volume (right) versus amount of outer loops for Shear Stress Transport (SST) and $\gamma - \tilde{R}e_{\theta_t}$ simulations for $\alpha = 5°$.

One of the conclusions of Chapter 6 was that the pressure in the vortex centre for $0.4 < x/c_0 < 1.1$ was reduced by 20% on averaged for the $\gamma - \tilde{R}e_{\theta_t}$ simulation with lowest turbulent inflow conditions compared to the SST simulation (see Figure 6.16). In other words, a thinner Boundary Layer (BL) results in a lower pressure in the vortex and should therefore result in a larger cavity. This is confirmed by the total vapour volume which is lowest for the

SST simulation and increases when decreasing the turbulent inflow conditions for the transition simulations.

Remarkable is the iterative behaviour of the total vapour volume of the $\gamma - \tilde{Re}_{\theta_t}$, $[I, \nu_t/\nu] = 4.0$ simulation as shown in Figure 8.1. Initially, the lines of all transition simulations collapse but after about 300 iterations they diverge from another. This is due to the initial condition of γ which is 1 in the freestream (indicating a turbulent flow) and 0 near walls (indicating a laminar flow) as described by Langtry (2006). The model therefore moves the transition location upstream for the $[I, \nu_t/\nu] = 4.0$ simulation until the Leading Edge (LE) of the wing and thus gradually increases the amount of turbulence in the BL. This is achieved by means diffusing $\tilde{Re}_{\theta_t}$ into the BL (for details concerning this process see Section 3.1) and therefore takes some iterations as visible in Figure 8.1. Eventually the BL becomes fully turbulent like for the SST simulation.

8.2.3. RESULTS

The main interest of this section is to investigate the effect of transition modelling, and thus the BL, on the size of the cavity. As done in many CFD publications concerning cavitation (e.g. by Watanabe et al. (2003) and Morgut (2012)), in this work the 'cavity' is considered as the region where $\phi_v \geq 0.1$. Figure 8.2 displays the source term and vapour volume fraction on the monitor plane $0.1c_0$ downstream of the tip. In the middle of the cavity, the source term is maximum which indicates maximal mass transfer from the liquid to the vapour state. Further outside the viscous core, regions of negative source term (condensation) are recognised. At this streamwise location, these regions are located north-east and south-west of the vortex core. These locations move clockwise around the vortex core further downstream (positive around the *local* x-axis which points into the paper in Figure 8.2) which yields the cavity in the vortex not to be axisymmetric around its axis of rotation. This can also be recognised in the contour plot of the vapour volume fraction. In the centre of the vortex, ϕ_v goes towards 1.0 which implies that the cells are almost completely filled with vapour.

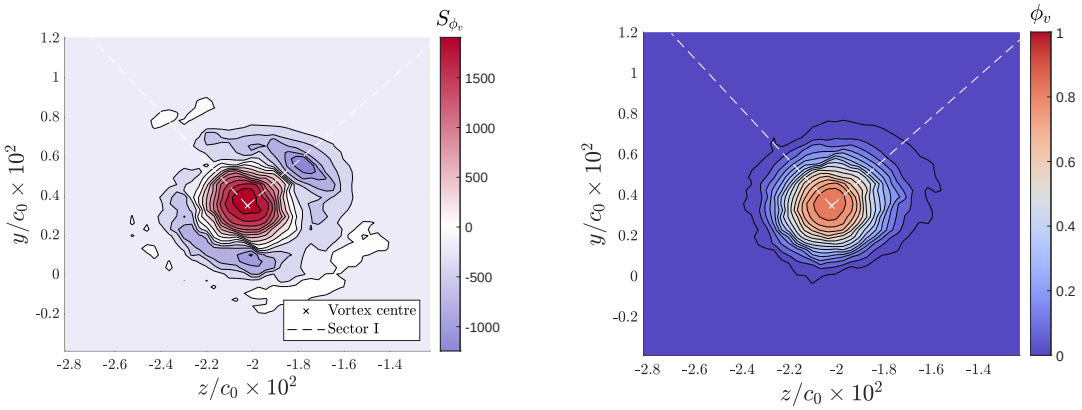

Figure 8.2: Contours of the vapour volume source term (left) and the vapour volume fraction (right) in the plane with normal parallel to the vortex trajectory. Results at $x/c_0 = 0.1$ for $[I, \nu_t/\nu] = 0.5$ simulation. Estimates for vortex centre and the region over which is averaged are indicated as well.

To further analyse the variables in and around the cavity, flow variables are again averaged over sector I as described in 5.8. Note that some spatial information is lost through this approach, however this will be accounted for by means of visualising flow fields like in Figures 8.2 and 8.4. In the wetted flow simulations, a minimum pressure criterion was used to determine the centre of the vortex. However, in cavitating conditions, this approach is not accurate since the pressure is found to become constant within the cavity (this will be further elaborated on in Section 8.3). The centre is determined by selecting all points within the cavity in the monitor plane (i.e. all points with $\phi_v \geq 0.1$ are selected) and average for both y and z direction.

The cavity radius was then determined like the viscous core radius in Figure 7.6, i.e. the point where $\phi_v = 0.1$ in the spatially averaged vapour volume fraction profile was determined. Figure 8.3 displays the S_{ϕ_v} and ϕ_v distributions of the SST simulation and $\gamma - \tilde{Re}_{\theta_t}$ simulations for varying inflow conditions. The cavity radii are displayed by the vertical lines in Figure 8.3. The S_{ϕ_v} graph shows that the the source term becomes negative already inside the cavity and is most negative near the cavity radius. The vapour volume fraction for the $[I, \nu_t/\nu] = 0.5$ simulation is clearly largest with $(\phi_v)_{max} = 0.82$. Although this number decreases for a more turbulent BL, the size of the region of constant ϕ_v in the centre of the cavity does not change while all simulations reach a fully

liquid state at $\eta/c_0 \approx 0.04$. In other words, the interphase region (interface between liquid and vapour state) for the most laminar BL is much 'sharper' ($\partial\phi_v/\partial\eta$ is larger) compared to the more turbulent BL states.

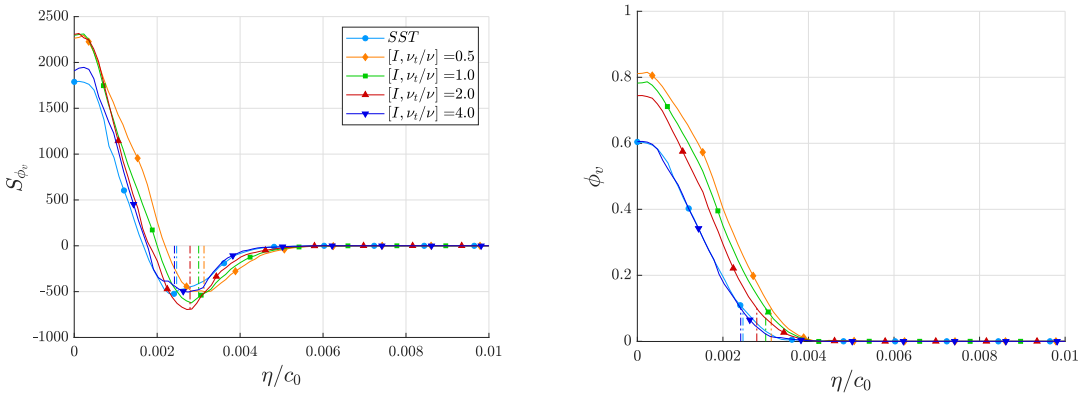

Figure 8.3: Vapour volume fraction source term (left) and vapour volume fraction (right) spatially averaged over sector I for the SST and $\gamma - \tilde{Re}_{\theta_t}$ simulations. Vertical lines indicate cavity radii.

Figure 8.4 displays the isocontours of the vapour volume fraction ($\phi_v = 0.1$) in the vortex region (note that this is the only region where cavitation occurs, none of the other types of cavitation mentioned in Section 2.2 were observed). In the left figure, the isocontours are clipped such that the lengths of the cavities can be compared. The cavity of the $\gamma - \tilde{Re}_{\theta_t}$,$[I,\nu_t/\nu] = 0.5$ simulation is clearly the longest, increasing the turbulence quantities decreases the cavity length due to the transition location which moves upstream. The simulation with highest turbulent inflow conditions results in a cavity length similar to the fully turbulent BL (SST simulation).

In the right figure, the isocontours are considered from another perspective. The isocontours are clipped such that one looks into the cavity in the negative streamwise direction. Lowering the turbulent inflow conditions also decreases the thickness (radius) of the cavity. Again, the SST and $\gamma - \tilde{Re}_{\theta_t}$, $[I,\nu_t/\nu] = 4.0$ simulations result in a thickness which is almost identical. The thickness of the cavity is particularly increased in positive y-direction, i.e. in the direction of the suction side of the wing. This is in line with the observation of Maines and Arndt (1997a) that the vortex mainly interacts with the BL on the suction side of the wing as stated in Section 6.1.

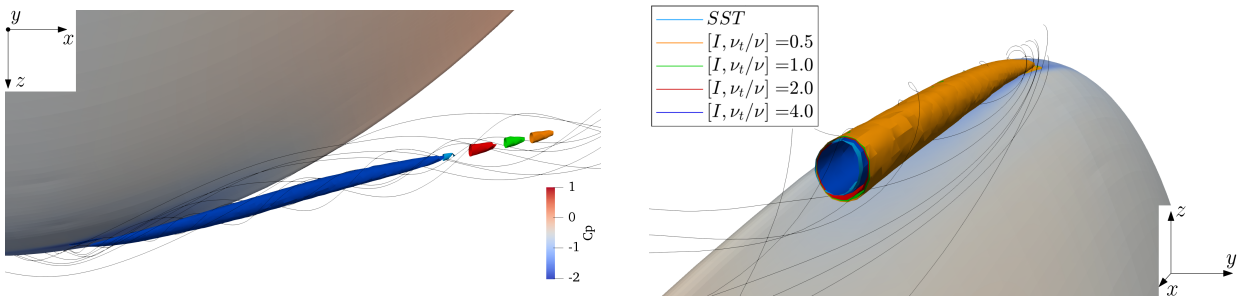

Figure 8.4: Vapour volume fraction isocontours ($\phi_v = 0.1$) for the SST and $\gamma - \tilde{Re}_{\theta_t}$ simulations. Colours indicate inflow conditions, black lines are streamlines and surface is coloured by the pressure distribution.

To quantify the change in length and thickness of the vortex, the isocontours are further analysed. Figure 8.5 presents the most downstream point of the cavity and the cavity radius over the trajectory for all simulations. What was visually observed in the isocontour plots is confirmed by the numbers; the end point of the cavity of the $\gamma - \tilde{Re}_{\theta_t}$, $[I,\nu_t/\nu]$=0.5 simulation lies 20% further downstream compared to the SST and $\gamma - \tilde{Re}_{\theta_t}$,$[I,\nu_t/\nu] = 4.0$ simulations. Also, there is a clear trend between the increase of turbulence intensity and the decrease of the cavity length. The vortex radius is not analysed for $x/c_0 < 0.04$ because the asymmetry of the vortex near the wing tip just above the BL which can be recognised in Figure 8.4. The cavity radius at $x/c_0 = 0.04$ is similar for all simulations. For all simulations, the maximum cavity radius is reached at $x/c_0 \approx 0.1$ with the $\gamma - \tilde{Re}_{\theta_t}$,$[I,\nu_t/\nu] = 0.5$ simulation resulting in the largest cavity. The growth rate of the cavity ($\partial\eta_c/\partial x$) increases when the turbulent inflow conditions are decreased since more high momentum (laminar) BL fluid enters the vortex. This decreases

the pressure as shown in Chapter 6. For $x/c_0 > 0.1$, the excessive turbulent diffusion resulting from the SST model (as elaborated on in Chapter 7) yields the vortex and thus the cavity to diffuse quickly. The diffusion rate is similar for all simulations.

The axisymmetry of the vortex can also be recognised in the cavity radius as shown Figure 8.5. The non-smoothness is due to the clockwise rotation of the regions where $S_{\phi_v} < 0$ around the local x-axis as shown in Figure 8.2. Since the cavity radius is determined in sector I, the maximum in each cycle will be reached when these regions are located north and south; minimum when located east and west. Each cycle takes about $\Delta x/c_0 = 0.01$ and is most apparent for the larger cavities ($[I, \nu_t/\nu] = 0.5,\ 1.0,\ 2.0$). This observation is consistent with the work by Pennings (2016) and Bosschers (2018). Downstream of $x/c_0 = 0.1$ the turbulent diffusion yields the cavity interface to be less sharp (i.e. more diffused). This yields a less accurate prediction of the vortex centre and therefore affects the calculation of the vortex radius whereby some peaks are observed in the plots.

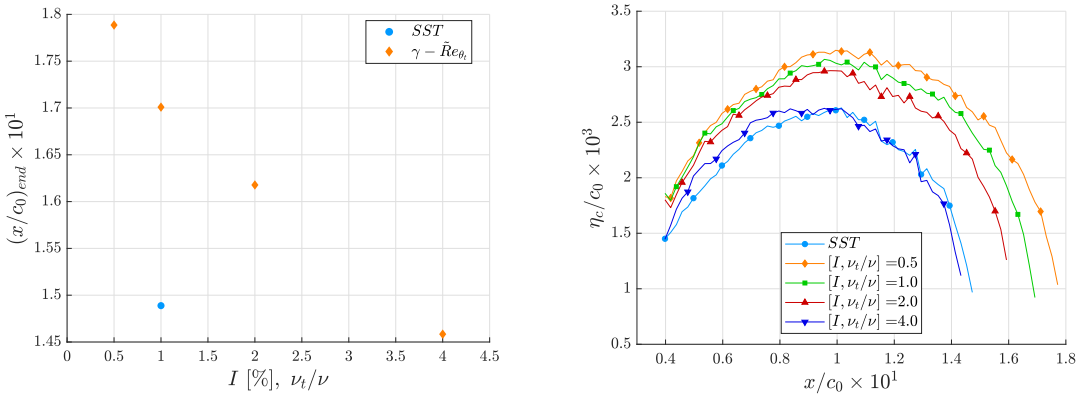

Figure 8.5: x-Coordinate of the most downstream point of the cavity (left) and cavity radius along the vortex trajectory (right) for the SST and $\gamma - \tilde{Re}_{\theta_t}$ simulations.

8

8.2.4. CONCLUSIONS

Convergence was checked by monitoring the total vapour volume and total source term in the domain. For all simulations, the mean of the source term went to zero and vapour volume was observed to become constant. For the rest of the variables, the same convergence behaviour as for the wetted flow conditions was observed.

The length of the cavity was found to be sensitive to the state of the BL. Similar numbers as for the sensitivity of the pressure in wetted flow conditions were observed, i.e. the cavity length and maximum cavity radius were increased by about 20% for the most laminar BL relative to a fully turbulent BL. Only growth of the cavity radius in positive lift direction is observed (at the suction side) which supports the observation by Maines and Arndt (1997a) that the vortex interacts with the BL on the suction side of the wing. Furthermore, the interface between liquid and vapour state for the most laminar BL is much 'sharper' ($\partial\phi_v/\partial\eta$ is larger) compared to the more turbulent BL states.

Regions with a negative source term were observed around the cavity radius. At 0.1 root-chord length downstream of the tip these regions are located north-east and south-west of the cavity centre and are observed to move clockwise around the local x-axis of the vortex. The cycle-distance (defined as the distance the freestream is convected in the time that the low source term regions are rotated by 2π radians around the vortex) of the process is about $0.01\Delta x/c_0$ and is observed to be similar for all turbulent inflow conditions. Due to the presence of these regions, the vortex is not axisymmetric around its local x-axis. This was observed for all flow settings but more apparent for the larger cavities which is consistent with the work by Pennings (2016) and Bosschers (2018).

8.3. TURBULENCE ANALYSIS

As done for the transition results, the effect of the turbulence models on the size and shape of the cavity is discussed in this section. However, the more important aspect of this section is the investigation of the effect of the cavity on the other flow variables. This will be assessed by comparing cavitating flow results against the wetted flow results of Chapter 7.

8.3.1. NUMERICAL SETTINGS

As done in Chapter 7, the wing is considered at 9 degrees AoA to remove the uncertainty of the transition location on the suction side of the wing. The finest grid and timestep are used, i.e. $G^{3D}_{1,9}$ and Δt_1. The rest of the numerical settings are the same as for the earlier calculations regarding turbulence as presented in Section 7.2.1 and Table D.3.

A cavitation number of 1.6 is used to be able to compare the results to the measurements by Pennings et al. (2015b). In Chapter 7 it was concluded that the SST and KSKL, as well as the DDES and IDDES turbulence models, yield similar results. For this reason only the SST, EARSM, and DDES turbulence models are considered in this section. The same start-up time is considered as presented in Table 7.2. The cavitation settings are the same as in the previous section, i.e. the Schnerr Sauer model is applied with the constants presented in Table D.4.

8.3.2. ITERATIVE CONVERGENCE

As done in the previous section, the total source term and vapour volume fraction in the domain are monitored. Figure 8.6 presents both quantities versus the number of time loops. For all simulations, the source term converges to the statistically converged state around zero. This is also visible in the total vapour volume which becomes (statistically) constant. Analogous to for the cavitating transition simulations, a relaxation procedure to decrease the cavitation number is used over the first 100 time loops. This significantly increases the vapour volume fraction over the first iterations. After that relaxation procedure the solution converges to a statistically converged solution. Clearly, the DDES simulation results in the largest amount of vapour volume in the domain. The convergence behaviour as well as the total vapour volume for the SST and EARSM simulations are almost identical. The vapour volume for the DDES simulation is a factor 2.3 higher compared to the other two.

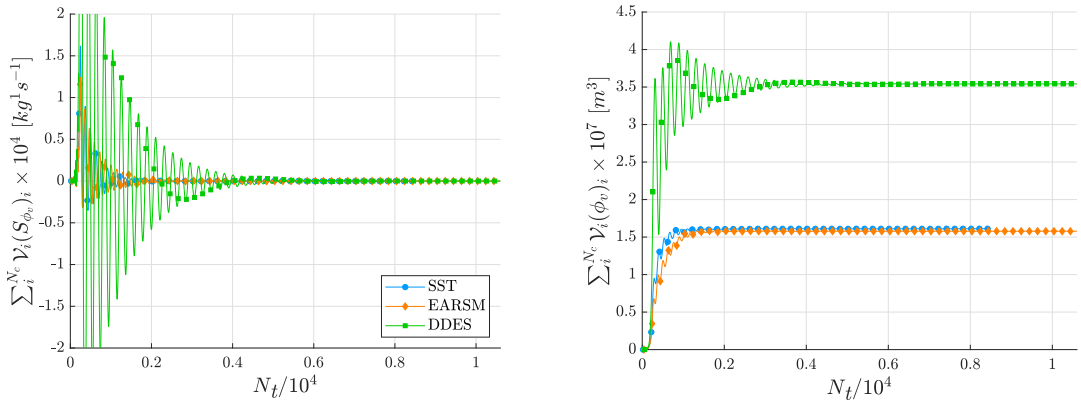

Figure 8.6: Total vapour source term (left) and vapour volume (right) versus amount of time loops (N_t) for the SST, EARSM, and DDES turbulence models for $\alpha = 9°$.

8.3.3. RESULTS

Figure 8.7 shows the contours of the source term and vapour volume fraction in the monitor plane at $x/c_0 = 0.25$. In the remainder of this section all results are for $x/c_0 = 0.25$ unless stated otherwise. This is because at this location the cavities for all turbulence models are fully developed and this is the point just before excessive diffusion of the vortex cavity starts (as will be shown by Figure 8.9). The contours already show a much sharper interface compared to the 5 degrees AoA. Also, the same behaviour of the source term is observed (more negative in certain regions around the vortex and these regions move clockwise around the local positive x-axis) which causes the vortex not to be axisymmetric.

In Chapter 6 it was concluded that the pressure over the trajectory of the hybrid simulations was a factor of two lower compared to the RANS simulations. The effect this has on the size of the cavity is qualitatively visualised in Figure 8.8. The DDES simulation results in a cavity which is about twice as large as the other models. The cavity in the EARSM simulation is slightly longer compared to the SST result, which is in line with the wetted flow results as shown in Figure 7.5. The same holds for the radius of the cavity as shown in the right graph. The cavity centres of the SST and DDES simulations almost coincide. It is observed that for this case the cavity is extended in both positive as well as negative lift direction which is because the BL for both simulations is fully turbulent

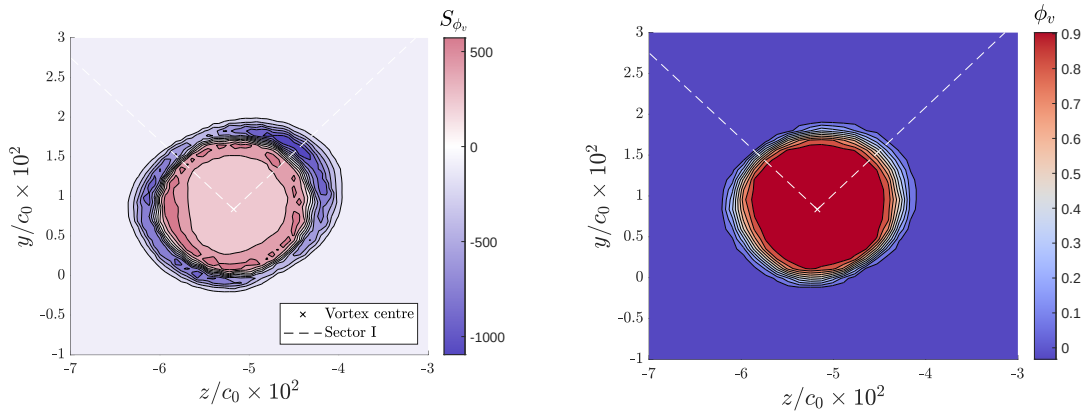

Figure 8.7: Contours of vapour volume source term (left) and vapour volume fraction (right) in the plane with normal parallel to the vortex trajectory. Results at $x/c_0 = 0.25$ for the SST simulation. Estimates for vortex centre and the region over which is averaged are indicated as well.

and therefore only the influence of the turbulence model is observed. The z-coordinates of the cavity trajectory of the EARSM model are similar to the cavities in the SST and DDES simulations however, the y-coordinates are not. The cavity in the EARSM simulation is less deflected in positive y-direction over its whole length.

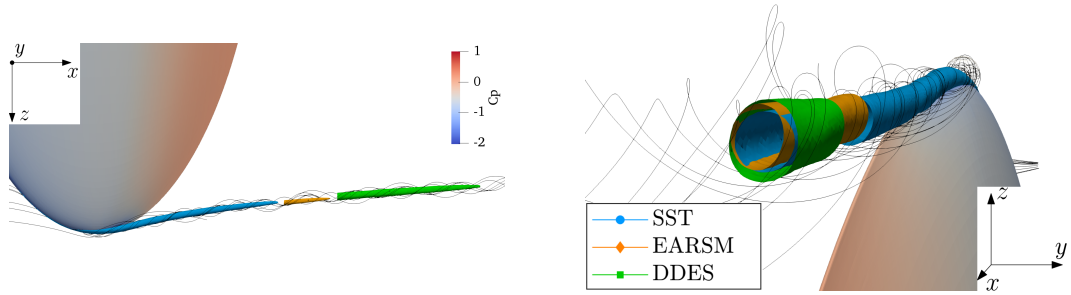

Figure 8.8: Vapour volume fraction isocontours ($\phi_v = 0.1$) for the SST, EARSM, and DDES turbulence models indicated by the colours. Black lines are streamlines and surface is coloured by the pressure distribution.

The cavity radius along the trajectory is determined in the same way as in the previous section. Figure 8.9 shows that the cavity radius in the DDES simulation is similar to the SST simulation near the tip. However, the diffusivity in the DDES simulation (due to the absence of resolved pressure fluctuations as found in Chapter 7) is much less which doubles the length of the cavity. The initial cavity radius for the EARSM simulation is about 10% less compared to the others which can be explained by the fact that the wing's circulation was also found to be about 10% less. Furthermore, the cavity in the EARSM simulation decays under a lower rate what is in line with the wetted velocity profiles as shown in Figure 7.6.

In literature, often isocontours of the vapour pressure are used to indicate the 'cavitation region' in wetted flow conditions (see e.g. Schot (2014) and Asnaghi (2018)). However, the effect of the cavity on other flow variables and therefore implicitly its own size is not found. Figure 8.10 compares the $\phi_v = 0.1$ isocontour from the cavitating SST simulation at a cavitation number of 1.6 with the isocontour of the vapour pressure ($p_v = -42{,}910\ Pa$, corresponding to a $\sigma = 1.6$ with $p_\infty = 0\ Pa$) from the wetted flow simulation. It appears that the end points $(x/c_0)_{end}$ of the cavities lie about 80% and 110% further downstream for the SST and EARSM simulations respectively compared to the 'cavities' in wetted flow conditions. For the DDES simulations, this effect is only 12.6% (see Table 8.1).

It is clear that the cavity affects other flow variables in the vortex. To further investigate the cause of this (large) discrepancy, flow variable such as pressure, velocities, and turbulence quantities in the vortex are considered next. To do so, the variables are again spatially averaged over sector I (note that these concern also temporally averaged values over the timesteps after the start-up time was finished, see Section 7.2.2). At first, the density along the vortex radius is considered. Figure 8.11 shows that the density in the freestream is equal to the liquid density and that the density within the cavity is a $\mathcal{O}(10^2)$ smaller. This is a direct consequence of the change in vapour volume fraction, since the density is determined according to the Volume of Fluid (VoF) framework as described in Equation (3.29). Although a change in density implies compressibility, this is not entirely true for this case and is often referred to as pseudo-(in)compressibility. This means that the density of the mixture is allowed to vary in space and time, however the densities of the individual phases are constant.

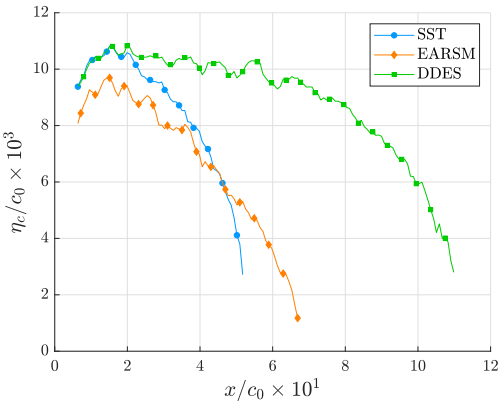

Figure 8.9: Cavity radius along the vortex trajectory for the SST, EARSM, and DDES turbulence models.

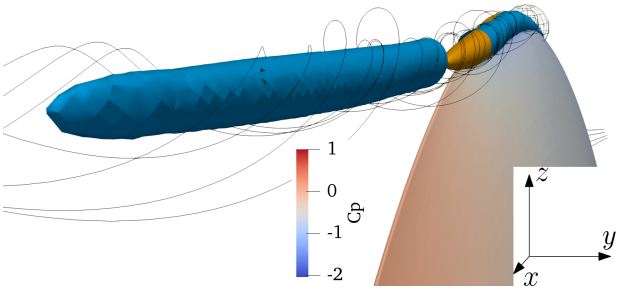

Figure 8.10: Comparison of 'cavity' in cavitating (blue) and wetted (orange) conditions for the SST turbulence model.

Table 8.1: Quantitaive comparison of 'cavity' in cavitating and wetted conditions for different turbulence models.

Closure	$(x/c_0)_{end,cav}$	$(x/c_0)_{end,wet}$	$\Delta(x/c_0)_{end}$ [%]
SST	0.523	0.289	81.2
EARSM	0.671	0.317	111.41
DDES	1.104	0.980	12.60

Figure 8.11 shows that the pressure coefficient in the cavity ends up slightly lower than the actual cavitation number of 1.6. This is because the source term which is modelled by the cavitation model is dependent on $\sqrt{p_v - p}$ whereby $p_v = p$ would result in no cavitation. The pressure in the cavity is observed to be constant. This is because the source yields the cavity to expand and therefore levels the pressure. In theory, the pressure could drop further when the mixture is only composed of vapour (i.e. $\phi_v = 1.0$) however this was not reached for these flow settings. Whether this is physical is hard to say. Pennings et al. (2015b) was not able to measure any flow quantity within the cavity due to the absence of measurement particles in the cavity. No other measurements of the flow in the cavity of a vortex are found, whether it would be feasible to measure within the cavity is also not know. Schot et al. (2014) observed the same behaviour using the OpenFOAM solver.

If the pressure in the vortex in cavitating conditions would have been the same as for wetted conditions, one would expect the axial velocities in cavitating conditions to be larger due to the lower dynamic viscosity of the vapour in the cavity. However, Figure 8.14 shows the exact opposite: the axial velocity profiles also level and are reduced in magnitude. To simplify the problem, the axial flow in the vortex can be considered as a straight duct flow in which the velocity is driven by an axial pressure gradient. This can mathematically be described by means of a Hagen-Poiseuille flow (see White and Corfield (2006) section 3.3.1.). In this formulation, the axial velocity profile is described as a function of the local duct radius (r) and the axial pressure gradient (dp/dx),

$$u = -\frac{dp}{dx}\frac{(r-R)^2}{4\mu}, \tag{8.1}$$

where R is the radius of the duct and μ the dynamic viscosity (here also the effect of the lower dynamic viscosity as stated at the beginning of the paragraph can be recognised). For a constant pressure gradient, this yields a

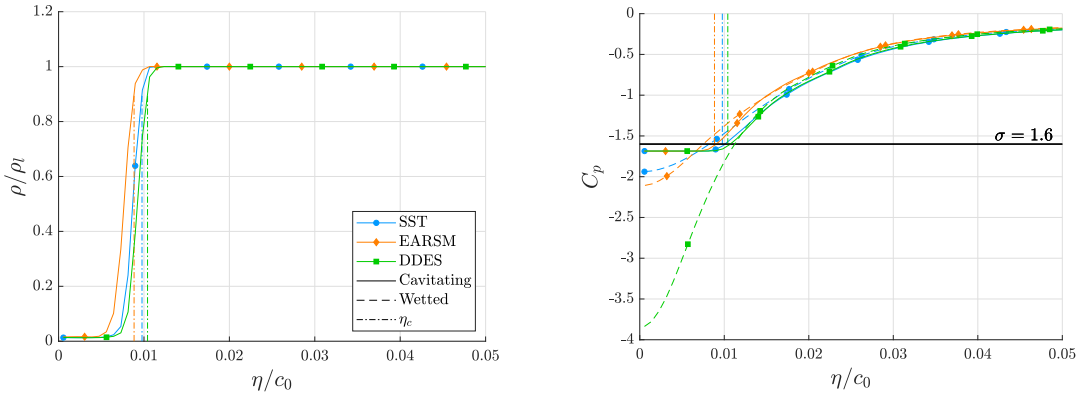

Figure 8.11: Density (left) and pressure (right) profiles averaged over sector I for the SST, EARSM, and DDES turbulence models. Solid lines are cavitating conditions, dashed lines wetted flow (not present for the density graph), and vertical lines indicate the cavity radii.

parabolic velocity profile as shown in Figure 8.12 (blue). The presence of the cavity yields the axial flow in the middle of the duct to deviate from this description. The pressure in the cavity is observed to become constant as shown in Figure 8.11, whereby there is no axial pressure gradient. This yields the axial velocity to be constant and equal in magnitude to the axial velocity just outside the cavity since the cavity is acting like a kind of slip wall as described in Section 3.2.1.

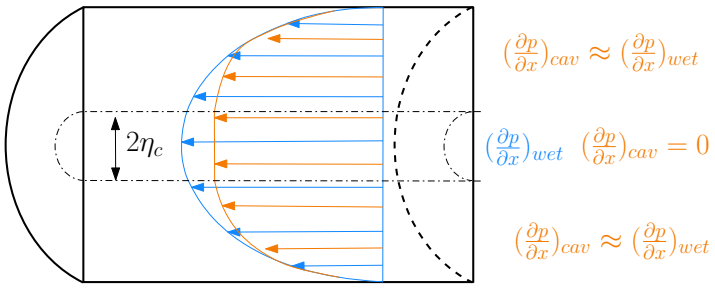

Figure 8.12: Simplified representation of the axial flow in the vortex according to the Hagen-Poiseuille formulation. Blue indicates wetted flow conditions, orange represents cavitating flow conditions.

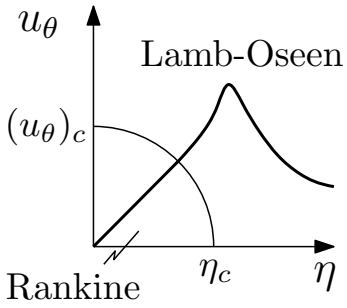

Figure 8.13: Schematic visualisation of what the azimthal velocity profile in a cavitating tip vortex most likely looks like.

Figure 8.14 also shows a similar kind of behaviour for the azimuthal velocity profiles. It can be seen that the magnitude throughout the entire cavity is almost constant and relatively small. For the SST and EARSM models, they drop on average by a factor of five compared to the wetted flow simulations, for the DDES this is even more. For all cavitating simulations, the peak azimuthal velocity is almost equal to the freestream velocity (i.e. $u_\theta/U_\infty = 1.0$) and is located just outside the cavity radius.

Within the cavity, the azimuthal velocity drops to $u_\theta/U_\infty \approx 0.1$ and stays at this level over the entire cavity radius. For sheet cavitation, detailed measurements of the vapour volume fraction and velocities within the cavity were performed by Stutz and Reboud (1997) and Stutz and Reboud (2000) respectively, however no such measurements for vortex cavitation were found. Most likely, the azimuthal velocity profile within the cavity has a linear profile as in a solid body rotation (J. Bosschers, personal communication, June 20, 2019), like a Rankine vortex. Figure 8.13 presents a schematic visualisation of what the azimuthal velocity profile should look like in theory. It thus seems that this is a limitation of the cavitation model. The cavitation model does (in these flow conditions) not allow for any pressure gradients in the cavity which forces a constant azimuthal velocity in the solution which is almost zero.

To further elaborate on the rotation in the vortex centre in wetted and cavitating conditions, Figure 8.15 shows the contours of the local x-components of the vorticity vector (the other components are negligible compared to the axial component). In wetted flow conditions, ω_x is of course largest in the centre of the vortex and decreases more outwards. In cavitating conditions though, (almost) no vorticity is present within the cavity. The

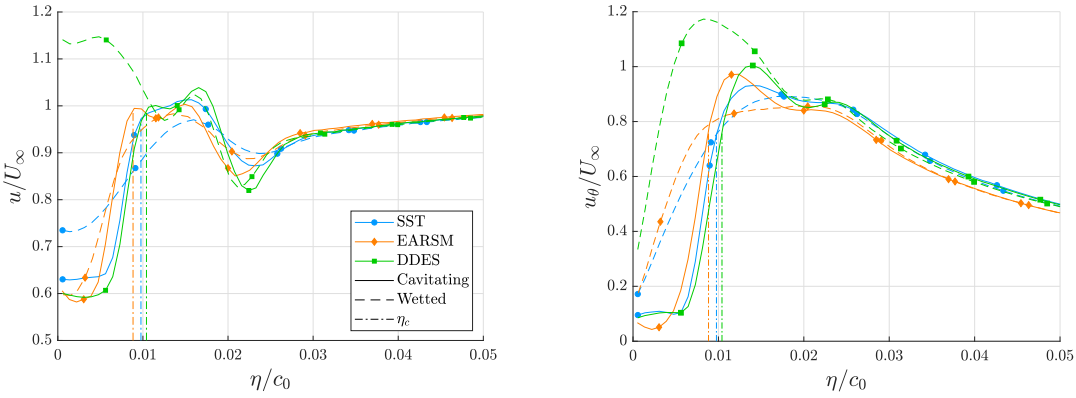

Figure 8.14: Axial (left) and azimuthal (right) velocity profiles averaged over sector I for the SST, EARSM, and DDES turbulence models. Solid lines are cavitating conditions, dashed lines wetted flow, and vertical lines indicate the cavity radii.

cavity forces the region of minimum vorticity to expand and be largest in magnitude just outside the cavity. The magnitude however, is increased with respect to the wetted flow conditions what explains the higher azimuthal velocities just outside the cavity compared to the wetted flow conditions for the SST and EARSM simulations. Furthermore, regions of positive vorticity are present in Figure 8.15 which means that part of the vapour flow in the cavity rotates in opposite direction with respect to the liquid outside the cavity. Within the cavity, the flow can thus be assumed to be (i) irrotational, (ii) incompressible, and (iii) inviscid (this will be elaborated on next) which are the characteristics of a potential flow. As said, this is probably due to the lack of physics taken into account by the cavitation model and would likely not be the case in reality.

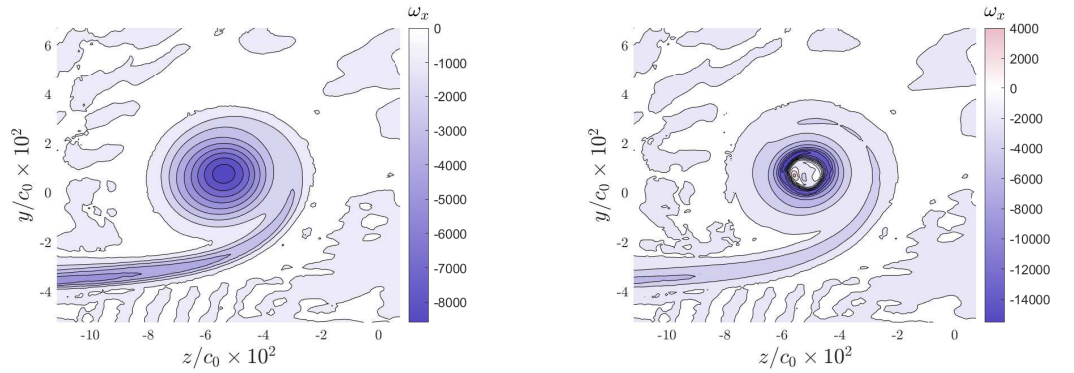

Figure 8.15: Contours of local x-component of the vorticity vector in the monitor plane which normal is parallel to the vortex trajectory. Results for wetted flow (left) and cavitating flow (right), colour scheme is centred around 0.

As done in Chapter 7, the turbulence quantities within the vortex are considered. Figure 8.16 shows the eddy-viscosity ratio (note that the eddy-viscosity is normalised by the viscosity of the pure liquid rather than the local viscosity which varies according to Equation (3.29)). The figure shows that the eddy-viscosity ratio within the cavity becomes almost zero. Furthermore, the eddy-viscosity in cavitating conditions is in general lower over the entire radius with respect to the wetted flow conditions. As already mentioned in Chapter 7, the eddy-viscosity ratio is proportional to k/ω (and for the EARSM model k/ω^2 due to the spatially varying C_μ, see Section 7.3.1). Figure 8.17 shows both turbulence transport variables. The graphs show that the turbulent kinetic energy is decreased in the cavitating simulations

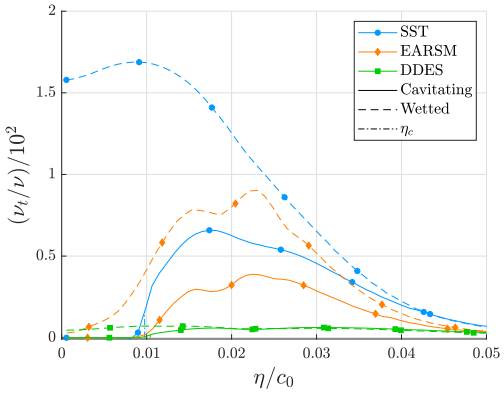

Figure 8.16: Eddy-viscosity over the vortex radius averaged over sector I for the SST, EARSM, and DDES turbulence models.

compared to the wetted flow simulations. The opposite holds for the specific dissipation rate which is larger in cavitating flow conditions. This increase of specific dissipation rate is an implicit effect of the drop in turbulent kinetic energy since ω is inversely proportional to k.

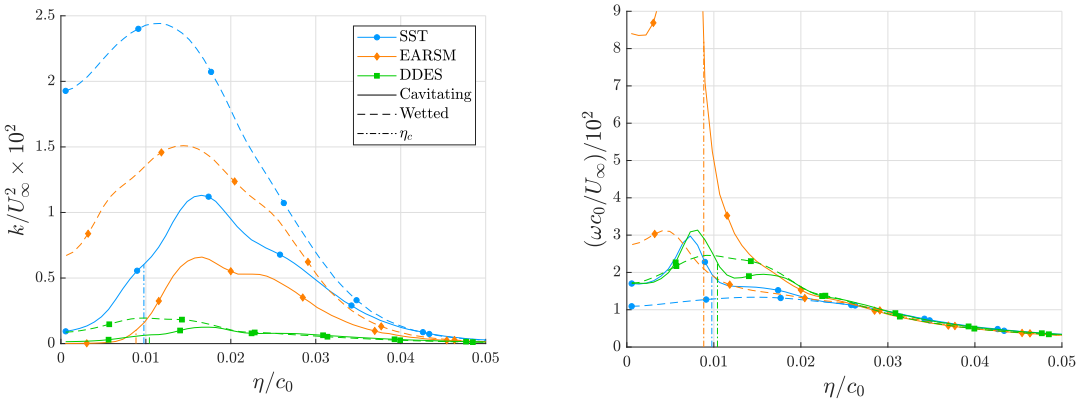

Figure 8.17: Turbulent flow variables, i.e. turbulent kinetic energy (left), and specific dissipation rate (right), over the vortex radius averaged over sector I for SST, Explicit Algebraic Reynolds Stress Model(s) (EARSM), and Delayed Detached-Eddy Simulation(s) (DDES) turbulence models.

The decrease of the turbulent kinetic energy originates from the lack of velocity gradients in the cavity. The lack of velocity gradients (and thus strain-rate) disturbs the balance between the production and destruction of turbulent kinetic energy. This is because the production (P_k) is dependent on the velocity gradients, but the destruction (D_k) is not,

$$P_k = 2\nu_t |S_{ij}|, \quad \text{and} \quad D_k = -\beta^* \rho \omega k, \tag{8.2}$$

where $|S_{ij}| = \sqrt{2S_{ij}S_{ij}}$. Vortical flow (with high k) suddenly cavitates and forms a region with low-velocity gradients and thus low production of turbulent kinetic energy. However, the turbulent kinetic energy and specific dissipation rate remain relatively constant over this short time period. This yields the destruction term to remain similar in magnitude whereby all turbulent kinetic energy is destroyed. Figure 8.18 displays the production and destruction term profiles in the vortex for both cavitating as well as wetted flow conditions. While the production of turbulent kinetic energy remains the same in the region of the 'cavity' in wetted flow conditions, it indeed entirely vanishes for cavitating conditions. The trend of the destruction term in cavitating flow however, is similar as in the wetted flow. It does decrease slightly due to the decrease of turbulent kinetic energy in that region. It is likely that the vapour flow in the cavity is much less turbulent relative to the liquid around the cavity. However, it is not likely that it becomes fully laminar within the entire cavity in the author's opinion. This limitation again comes down to the cavitation model which causes the pressure in the entire cavity to become constant.

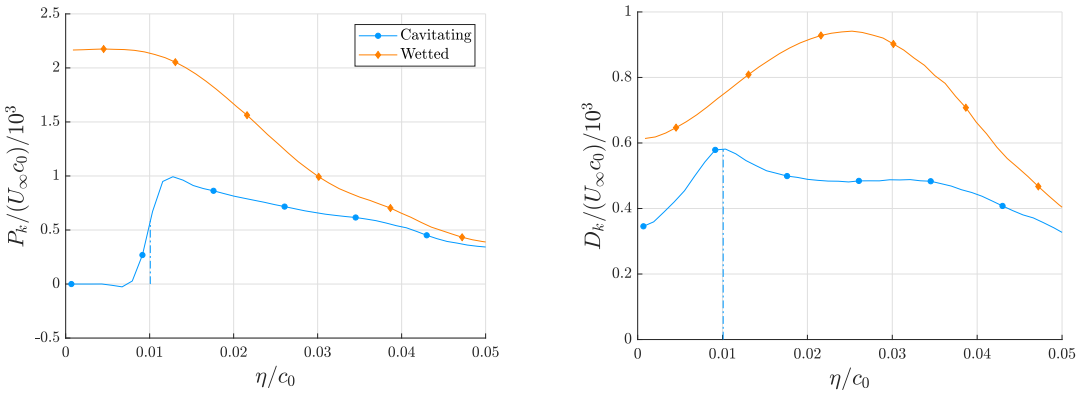

Figure 8.18: Production (left) and destruction (right) terms of the turbulent kinetic energy transport equation of the SST model averaged over sector I for cavitating and wetted conditions.

Figure 8.19 displays the effect this has on the unresolved normal components of the Reynolds stress tensor.

In general, it is observed that the Reynolds stresses decrease in cavitating conditions compared to the wetted flow. The unresolved Reynolds stress tensor is determined as $\tau_{ij} = 2\nu_t S_{ij} - 2/3k\delta_{ij}$ (for further details see Equation (3.8)). The absence of turbulent kinetic energy in the cavity means that the normal components of this tensor are only dependent on the strain-rate. However, in the previous paragraph it was also observed that, due to the absence of any velocity gradients in the cavity, the strain-rate tensor is also almost zero. This explains why all normal components of the Reynolds stress tensor are also going towards zero for the cavitating simulations. In Section 3.2.1 it was argued that the liquid-vapour interface should restrict the turbulent momentum transfer perpendicular to the cavity. As Figure 8.19 shows results for Sector I (positive y-direction), physically it would be required that the $v'v'$ component of the unresolved Reynolds stress tensor goes towards zero at η_c. This is clearly not the case for any of the simulations as $v'v'$ is a continuous line at the location of the interface. In Section 7.3 the isotropic character of the turbulence in the SST, KSKL, and DDES simulations was observed (i.e. the magnitudes of the unresolved normal Reynolds stresses $u_i'u_i'$ were found to be the same for all three components over the radius of the vortex). However, Figure 8.19 shows that this is not true for this streamwise location (the results in Section 7.3 were for $x/c_0 = 0.50$, these results are for $x/c_0 = 0.25$). The eddy-viscosity and turbulent kinetic energy in the Boussinesq hypothesis are scalars whereby all directionality (in the SST, KSKL, and in the RANS region of the DDES simulations) originates from the strain-rate tensor. This implies that the proportion of the normal components of this tensor (i.e. $\partial u/\partial x$, $\partial v/\partial y$, and $\partial w/\partial z$) change when comparing these two streamwise locations. However, in cavitating conditions, it is observed that the lines for the three different normal Reynolds stresses collapse again. This implies that the presence of the cavity enhances the isotropic character of the turbulence in and outside the vapour region.

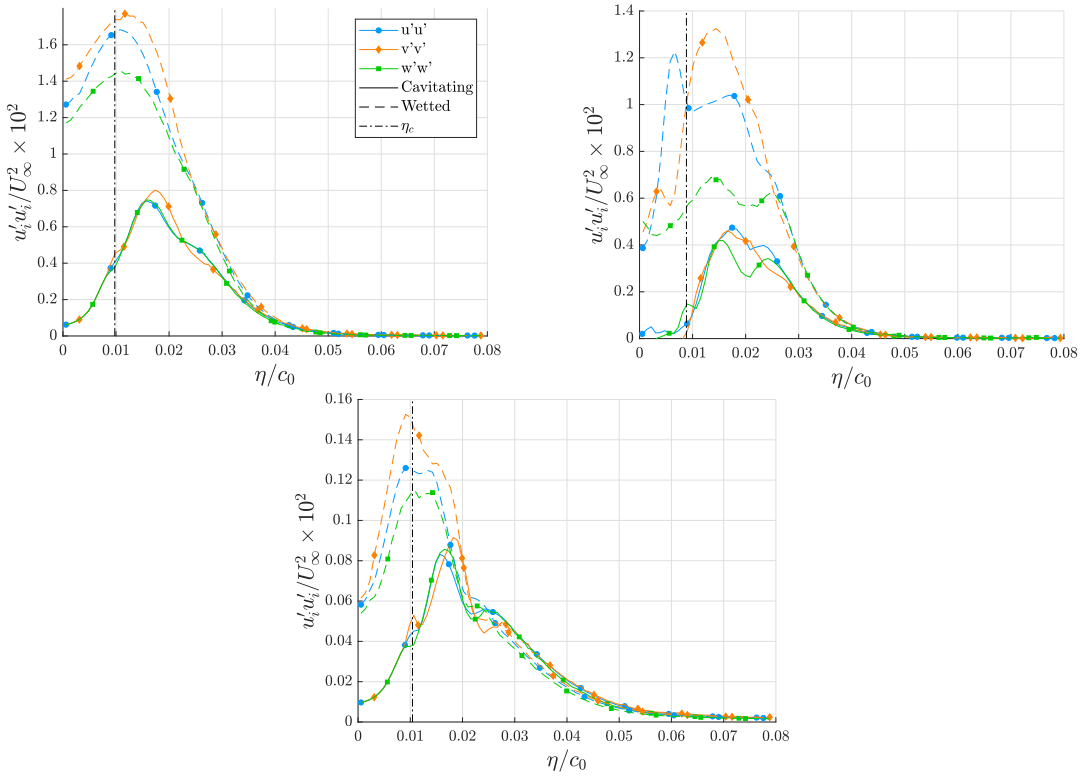

Figure 8.19: Normal components of the unresolved Reynolds stress tensor averaged over sector I for the SST (top-left), EARSM (top-right), and DDES (bottom) turbulence models.

Validation of the flow around the cavity was not possible since Pennings et al. (2015b) only measured at $x/c_0 = 1.14$ in cavitating conditions (for all turbulence models the cavity has decayed before that location). For this reason, it was decided to compare the wetted and cavitating azimuthal velocity profiles with the analytical expression of the wetted and cavitating Lamb-Oseen vortex as defined in Section 2.3.2. Note that the expression of the cavitating Lamb-Oseen vortex was compared against the measurements by Pennings et al. (2015b) and it was found that 'the applied boundary condition (jump relations) at the interface is realistic' based on the azimuthal

velocity profiles. Furthermore, it was found that in cavitating conditions, the viscous core size should be corrected to obtain a good fit. The correction was found by a non-linear fitting procedure of the azimuthal velocity distribution (the viscous core radius was tuned such that it matches the experimental data for the wing at 5, 7, and 9 degrees AoA best) and reads,

$$(\eta_v)_{corr} = \eta_v f(\eta_c/\eta_v) = \eta_v \sqrt{1+2.214(\eta_c/\eta_v)^2}\,. \tag{8.3}$$

The only dependent variables in the analytical expression of the (wetted) Lamb-Oseen vortex are (i) the freestream circulation Γ_∞ which is determined by integrating the local x-component of the vorticity vector in the local $y-z$ plane of the vortex (see Figure 8.15 and note that the other two components of the vorticity are negligible), and (ii) the viscous core radius η_v (which is determined as in Figure 7.6). For the cavitating Lamb-Oseen vortex, there is one additional dependent variable namely the cavity radius η_c (which is determined as in Figure 8.4). Table 8.2 presents the details of the dependent variables in wetted and cavitating conditions.

Table 8.2: Numerical values (freestream circulation Γ_∞, viscous core radius η_v, and cavity radius η_c) given as inputs for the analytical expression for the (non)-cavitating Lamb-Oseen vortex.

Closure	$\Gamma_\infty \times 10^2$ $[m^2 s^{-1}]$	$\eta_v/c_0 \times 10^2$
SST	-8.87	1.68
EARSM	-9.66	1.95
DDES	-12.4	0.82

Closure	$\Gamma_\infty \times 10^2$ $[m^2 s^{-1}]$	$\eta_c/c_0 \times 10^2$	$\eta_v/c_0 \times 10^2$	$(\eta_v/c_0)_{corr} \times 10^2$
SST	-7.18	0.98	1.40	2.01
EARSM	-6.80	0.88	1.24	1.81
DDES	-6.99	1.04	1.40	2.09

Figure 8.20 compares the azimuthal velocity profiles of the CFD simulations to the analytical expressions for the (non)-cavitating Lamb-Oseen vortex with as input parameters Γ_∞, η_v, and η_c as shown in Table 8.2. For the pure RANS models, the analytical formulation yields lower azimuthal velocities compared to the CFD results. This is because the freestream circulation is much lower compared to the DDES simulation due to turbulent diffusion as can be observed in the table. Furthermore, the cavity in the SST and EARSM models is already diffused quite extensively at $x/c_0 = 0.25$ as shown by Figure 8.9. This yields the cavity radius to decrease and the vortex core radius to increase. This results in a decrease of the ratio of both radii, i.e. η_c/η_v, whereby the azimuthal velocity for the cavitating case is overpredicted (see Figure 2.10). It seems that the analytical expression for the (corrected) cavitating conditions matches quite well for the SST and EARSM simulations, but it is expected that this is due to error cancellation since the underpredicted Γ_∞ drives the azimuthal velocity down and the overpredicted ratio of η_c and η_v drives the velocity up.

In Chapter 7 it was found that the DDES simulation overpredicts the amount of laminar flow within the vortex which prevents excessive turbulent diffusion. For this reason, the found Γ_∞ in the wetted flow is about 30% higher compared to the SST and EARSM models. This is reflected by the analytical expression which matches the azimuthal velocity in the region $\eta/c_0 > 0.025$ much better. However, the peak azimuthal velocity of the non-cavitating Lamb Oseen vortex is 50% larger compared to the CFD result. For the cavitating conditions, the azimuthal velocity profile is predicted quite well. Correcting the viscous core radius also improves the results for this situation.

8.3.4. CONCLUSIONS

The size of the cavities of the SST and EARSM simulations are found to be about half of the size of the cavity in the DDES simulation what is in line with the conclusions drawn regarding the pressure in wetted flow conditions (see Figure 7.5). The length of the actual cavity was compared to the 'cavity' in wetted conditions (isocontour plots of the vapour pressure) and it was found that for the SST and EARSM simulations the actual cavity extends 81% and 110% further downstream. For the DDES simulation, this number was much smaller, 12.6%. This is because the excessive turbulent diffusion in the SST and EARSM models is reduced by the vapour region within the vortex.

While the pressure in the vortex in wetted flow conditions is minimum in the vortex centre, the formulation of the cavitation model yields the pressure to become constant (slightly below the vapour pressure) in the entire cavity. For this reason, there are no pressure and velocity gradients in any direction. The absence of velocity gradients yields (i) constant axial and azimuthal velocities in the cavity (the magnitude of the axial component of the vorticity vector is also almost zero which makes the flow irrotational), (ii) almost no eddy-viscosity since the production terms of k vanishes while the destruction term remains, and (iii) much lower Reynolds normal stresses in the cavity due to the Boussinesq hypothesis (the Reynolds stresses are dependent on the strain-rate tensor which is low due to the absence of flow gradients). This yields the vapour flow in the cavity to have the

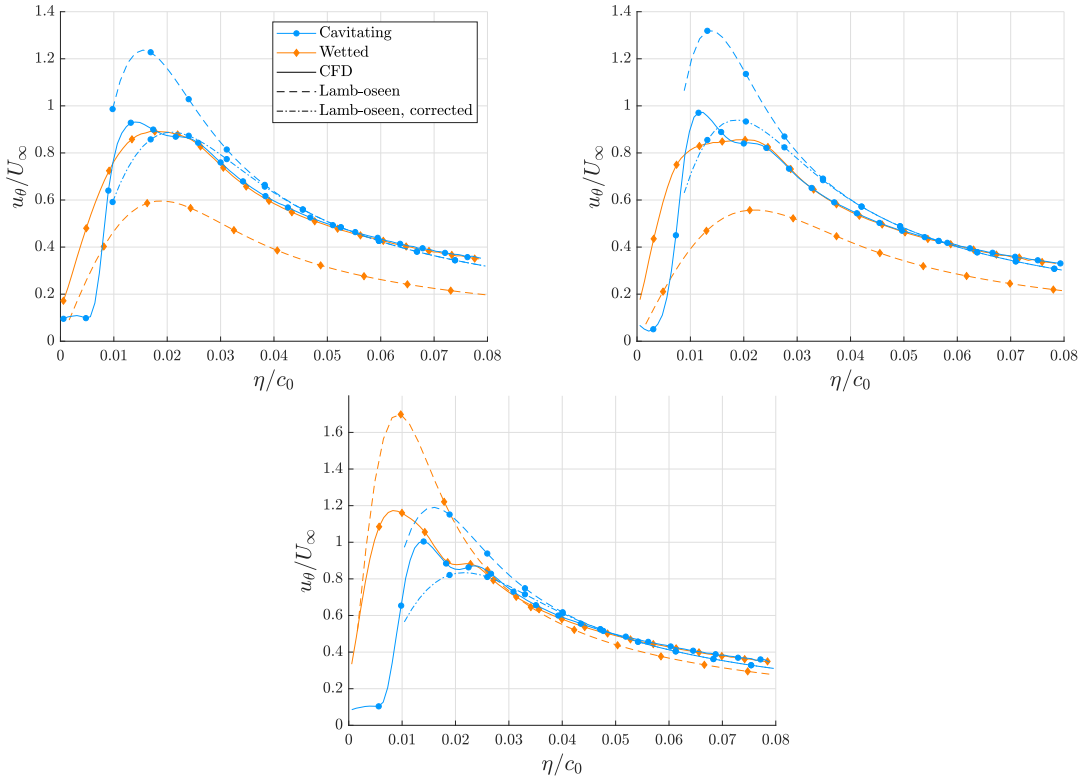

Figure 8.20: Comparison of analytical wetted and cavitating Lamb Oseen vortex to CFD results for the SST (top-left), EARSM (top-right), and DDES (bottom) turbulence models.

same characteristics as a potential flow. Whether it is physically plausible that the cavitation model result in a constant pressure in the cavity is questionable however no pressure (not velocity) measurements of the flow within a cavity in a tip vortex were found in the literature (it is also not known whether it would be possible to accurately measure in that region). Furthermore, it is observed that the Reynolds stresses normal to the liquid-vapour interface are non zero which implies that there exists turbulent momentum transfer through the interface. This is not unexpected since the VoF method inherently removes the sharp interface. However, in reality there should be no turbulent momentum transfer according to the literature.

The closest downstream location at which Pennings et al. (2015b) measured was $x/c_0 = 1.14$ whereby validation of the cavity radius and velocity profiles in cavitating conditions was not possible. For this reason, the simulations were compared to the analytical expressions for the (non)-cavitating Lamb-Oseen vortex. For the cavitating conditions the analytical expression for the cavitating vortex matched the SST and EARSM simulations well, however this is probably due to error cancellation. For the DDES simulation, the analytical expressions matched well. Correcting the viscous core radius as proposed by Bosschers (2018) was found to benefit the results.

User specified number of seeds and bubble radius in the cavitation model are expected to affect the mass transfer rates between the two phases. In this research these parameters were kept constant because this would result in a too large test matrix. Furthermore, the question what the effect of resolving pressure fluctuations instead of having an averaged pressure field on the behaviour of the cavitation model remains unanswered. This was not assessed due to the absence of the resolved Reynolds stresses.

9

CONCLUDING REMARKS

An extensive verification and validation study in the context of transition and turbulence modelling of an elliptical planform with NACA66_2-415 cross-section (known as the 'Arndt' wing) was carried out. A literature study showed that cavitation models only depend on the pressure difference between the vapour and hydrodynamic pressure, while in reality cavitation inception is also triggered by other aspects such as e.g. nuclei content, surface roughness, and shear flow. For this reason, both transition and turbulence models were first assessed in wetted flow conditions with as primary parameter of interest the pressure in the vortex. The literature showed that the pressure is inherently coupled to other parameters such as the viscous core radius, boundary layer thickness and the wing's circulation. Subsequently it was checked whether the conclusions drawn also apply to cavitating flow conditions, while the effect of the cavity in the vortex core on other flow variables in the vortex was investigated.

9.1. CONCLUSIONS

The following paragraphs present the answers the four research questions as presented in Chapter 1. For more elaborate conclusions one is referred to the concluding sections of Chapters 5, 6, 7, and 8.

VERIFICATION AND VALIDATION

Solution verification is performed for the majority of the results, the following conclusions were drawn for the different components of the numerical error. Firstly, the spatial discretisation error is the dominant numerical error source. Secondly, for both steady and unsteady calculations, a convergence criterion for the maximum residual of at least 10^{-5} for all variables is required to ensure that the iterative error is at least one order lower compared to the discretisation error. Thirdly, it was not possible to assess the input uncertainty resulting from the unknown turbulent inflow conditions due to the correlation of eddy-viscosity and turbulence intensity. Its potential effect was investigated by a sensitivity analysis which showed that the uncertainty can introduce an input error of 20% in the pressure of the vortex at a half root-chord length downstream of the tip. To assess the exact magnitude of this error, measurements of the inflow turbulence are required.

It was found that the multivariate metric is only a suitable tool for validation of vortical flows if it is applied to spatially averaged velocity profiles. When analysing global flow fields, this technique emphasizes the errors in the freestream whereby it results in distorted conclusions.

It was analytically shown that the difference in vapour and actual inception pressure is positively correlated with the gas content and negatively with the surface tension of the nuclei. In the majority of the modern Computational Fluid Dynamics (CFD) simulations, an Eulerian volume of fluid approach is employed which does not take bubble trajectories nor bubble expansion or contraction into account. For this reason it was concluded that one should use measurements with low nuclei content for validation purposes.

TRANSITIONAL FLOW

Previous experimental results showed that the vortex mainly interacts with the Boundary Layer (BL) on the suction side of the wing through the vortex roll-up process. While prior researchers explained early decay of vorticity and therefore an underpredicted cavity size by (i) numerical diffusion, and (ii) overprediction of eddy-viscosity,

it was argued that the assumption of a fully turbulent BL in CFD simulations also contributes. This argument was substantiated by combining the 'McCormick' hypothesis with an analytical expression for a cavitating Lamb-Oseen vortex.

This was tested by combining the Shear Stress Transport (SST) turbulence model with the $\gamma - \tilde{R}e_{\theta_t}$ transition model which is known to be sensitive to the inflow conditions for the turbulence quantities. By means of changing these inflow conditions, the state, and thus the thickness of the BL was controlled and the effect on the vortex was assessed.

Prior to performing 3D calculations, suitable inflow conditions to control the BL thickness were obtained by means of a 2D sensitivity analysis in which both the turbulence intensity and eddy-viscosity ratio were varied. When both quantities are tripled, the transition location on the suction side of the wing moves 0.15 chords upstream for the wing at 5 degrees Angle(s) of Attack (AoA). For 9 degrees AoA, transition is triggered just downstream of the leading edge regardless of the specified turbulent inflow conditions. To obtain this sensitivity it was necessary to control the decay of turbulence intensity by (i) solve the transport equations for the turbulence quantities without destruction terms until 0.1 root-chords upstream of the wing, and (ii) simultaneously change eddy-viscosity and turbulence intensity.

In the 3D calculations, the BL thickness was decreased by a factor of three for an almost laminar BL relative to a fully turbulent BL for the wing at 5 degrees AoA. It was concluded that transitional modelling decreased the viscous core radius and consequently the pressure in the vortex by 20%. The vortex at 9 degrees AoA was not affected by the state of the BL. Because transition was not controlled (nor measured) in the experiments by Pennings et al. (2015b), only the measurements for 9 degrees AoA could be used for validation purposes.

The analytical expression for the pressure in a cavitating Lamb-Oseen vortex states that the pressure in the vortex is proportional to (i) the viscous core radius, and (ii) the wing's circulation. This relationship was tested against the numerical results where the viscous core radius was found to be relatively constant for the wing at 9 degrees AoA and the circulation of the wing was almost constant for 5 degrees AoA. For both cases, the analytical relationship appears to overpredict the pressure in the region until one root-chord downstream of the wing tip because the roll-up process is not finished yet. At about one root-chord downstream of the tip the numerical results are found to match the relationship quite well. The results are not compared further downstream because it is expected that numerical diffusion of the vortex does not allow for a proper comparison.

Furthermore, a well-known property of the $\gamma - \tilde{R}e_{\theta_t}$ model, namely stagnation of the iterative solution procedure, was addressed. It was argued and mathematically substantiated that local grid refinement in streamwise direction at the transition location should avoid stagnation of the calculations. For the 2D calculations, this was shown to be true. However, the 3D calculations do not reach iterative convergence, even though these calculations use the same grid resolution (both in streamwise as well as spanwise direction) as used in the 2D calculations. Further refining the grid theoretically should overcome this but at excessive computational costs. The stagnation is not expected to impact the previously presented conclusions since the forces were well converged and the problem was observed to be localised at the pressure side of the wing with one of the transition variables as the maximum residual (other variables were at least 1.5 orders of magnitude lower).

TURBULENT FLOW

Previous research has shown that overprediction of eddy-viscosity yields excessive turbulent diffusion of the vortex. theoretically, the KSKL, EARSM, DDES, and IDDES models should suffer less from turbulent diffusion, or be able to capture the anisotropic character of the turbulent structures in the vortex. The main conclusions drawn regarding each model are summed next.

The lift coefficient predicted by all models is within the uncertainty bounds of the experimental results except for the EARSM simulation, which underpredicts the lift due to early flow separation. Although the velocity profiles of the EARSM simulation seem worse compared to all other models, the comparison is biased due to the lift (and thus vortex strength) which is underpredicted by 10%. It is advised to compare these models for a constant lift coefficient. It was shown that the EARSM model is able to predict the location of the viscous core radius better than the KSKL model. The eddy-viscosity near the vortex centre of the EARSM simulation is found to be low compared to the other RANS models due to (i) an increased specific dissipation rate, and (ii) a spatially varying C_μ which amplifies the effect of the increased specific dissipation rate. This was expected to benefit the axial velocity in the vortex, but the opposite is observed. By analysing the individual anisotropic normal and shear Reynolds stresses, it was observed that the Reynolds stresses in axial direction are dominant near the vortex centre which explains the axial velocity deficit. The EARSM model is the only model that was able to reproduce some of the

anisotropy of the turbulence near the viscous core radius.

Even though promising theory, the KSKL model still suffers from excessive production of turbulent kinetic energy and thus turbulent diffusion of the vortex. Despite the well matching lift coefficient, this still yields large modelling errors of the flow quantities in the vortex region.

The viscous core radius and consequently the pressure in the vortex centre for the hybrid models (DDES and IDDES) matches well with the experiments in the region one root-chord length downstream of the tip, because the axial and azimuthal velocity profiles are well predicted. Although the results of the hybrid models initially seem validated, the outcome still contains a large modelling error. The resolved Reynolds stress components are found to be negligible compared to the unresolved stresses. This is because all turbulence is developed in the wing's BL. Commutation errors result in damping of the fully statistical representation of turbulence to a resolved representation in the form of velocity fluctuations (i.e. modelled stress depletion). When the flow convects from a RANS region into a region where predominantly LES is applied, the destruction of turbulence kinetic should decrease the stability of the flow whereby velocity fluctuations in the LES region could develop. However, it was observed that the absence of unsteady effects in the flowfield near the wing and in the freestream prevents this development which causes a too large region of laminar flow in the vortex.

In all, although the integral quantities for most models matched well, all models showed discrepancies in the vortex region with respect to the measurements. These limitations were analysed in detail and led to some of the recommendations in Section 9.2.

CAVITATING FLOW

The length of the cavity was found to be sensitive to the state of the BL. Similar numbers as for the sensitivity of the pressure in wetted conditions were observed, i.e. the cavity length and maximum cavity radius were increased by about 20% for the most laminar BL relative to a fully turbulent BL. Only growth of the cavity radius in positive lift direction is found (at the suction side), which supports the observation by Maines and Arndt (1997a) that the vortex interacts with the BL on the suction side of the wing. Furthermore, the interface between liquid and vapour state for the most laminar BL is found to be much 'sharper' compared to the more turbulent BL states.

The length of the actual cavity for the different turbulence models was compared to the 'cavity' in wetted conditions (isocontours of the vapour pressure). It was found that for the SST and EARSM simulations, the actual cavity extends 81% and 111% further downstream because the excessive turbulent diffusion is reduced by the vapour region within the vortex.

The formulation of the cavitation model yields a constant pressure in the entire cavity. For this reason, there are no pressure and velocity gradients in any direction. The absence of velocity gradients yields (i) constant axial and azimuthal velocities in the cavity (the magnitude of the azimuthal velocity is almost zero and it was found that the flow is more or less irrotational), (ii) almost no eddy-viscosity since the production term of k vanishes while the destruction term remains, and (iii) much lower Reynolds normal stresses in the cavity due to the Boussinesq hypothesis (linear dependency between the Reynolds stresses and the strain-rate tensor). This yields the vapour flow in the cavity to have the same characteristics as a potential flow. Whether the constant pressure is physically plausible is questionable, but hard to judge because no pressure (nor velocity) measurements of the flow within a cavity in a tip vortex were found in literature.

9.2. RECOMMENDATIONS

The $\gamma - \tilde{R}e_{\theta_t}$ transition model could only be used in combination with the SST turbulence model in ReFRESCO. Despite the previously reported shortcomings of the SST model in vortical flows, a large effect of transition modelling on the vortex was shown for the wing at 5 degrees AoA. It is therefore proposed to use the $\gamma - \tilde{R}e_{\theta_t}$ model with other $k-\omega$ based hybrid models or Reynolds stress models. To what extent the model is compatible with other turbulence models, and whether recalibration is required, has to be addressed.

For validation purposes, the ideal situation would be to control or measure the transition location during the measurements. However, if this is not done, it is advised to consider the wing at 9 degrees AoA when comparing CFD results to experiments to minimise the input uncertainty resulting from the transition location. However, one has to take flow separation into account for an AoA of 9 degrees, which also introduces additional uncertainty. The effect of a varying separation location was not assessed in this work.

For the results obtained using the $\gamma - \tilde{R}e_{\theta_t}$ model, the modelling error of the flow around the wing should still be assessed. Furthermore, the input uncertainty resulting from the turbulence intensity should still be determined. It is therefore recommended to perform Stereographic-Particle Image Velocimetry (S-PIV) around the

wing and locate the measurement plane such that the wall-bounded flow and the turbulent inflow can be measured simultaneously.

To tackle the problem concerning the absence of resolved Reynolds stresses in hybrid simulations, a synthetic turbulence inflow generator is currently being implemented in ReFRESCO. In theory, time-varying stochastic velocity fluctuations in the freestream should allow the development of turbulent structures in the regions of decreased modelled turbulent kinetic energy (in the LES region relative to the RANS region) and thus the development of resolved turbulence in the viscous core region of the vortex. Since DDES and IDDES predicted the wing circulation more accurately compared to DES, which was a problem encountered by prior research regarding hybrid models on the 'Arndt' wing, it is recommended to redo calculations with the these models including resolved turbulent inflow conditions. In that case the effect of resolving pressure fluctuations instead of having an averaged pressure field on the behaviour of the cavitation model can also be assessed.

The ability of the EARSM model to capture anisotropy in the vortex encouraged the belief that a full Reynolds stress model is suitable for cavitating tip vortex application. Since it was not available in ReFRESCO yet, it is recommended to apply such a model on the 'Arndt' wing.

User specified number of seeds and bubble radius in the Schnerr-Sauer cavitation model are expected to affect mass transfer rates between the two phases. Further research in this topic in the context of cavitating tip vortices is advised.

To account for the overprediction of the pressure by the analytical expression for the Lamb-Oseen vortex in the region where the roll-up is not finished yet, it is recommended to adapt this expression such that the freestream circulation downstream of the tip is related to the total circulation of the wing.

BIBLIOGRAPHY

Abbott, I. H. and Von Doenhoff, A. E. (1959). *Theory of wing sections, including a summary of airfoil data*. Courier Corporation.

Ahmad, N. N. (2013). Numerical simulation of the aircraft wake vortex flowfield. In *5th AIAA Atmospheric and Space Environments Conference*, page 2552.

Ahuja, V., Hosangadi, A., and Arunajatesan, S. (2001). Simulations of cavitating flows using hybrid unstructured meshes. *Journal of Fluids Engineering*, 123(2):331–340.

Akhatov, I., Lindau, O., Topolnikov, A., Mettin, R., Vakhitova, N., and Lauterborn, W. (2001). Collapse and rebound of a laser-induced cavitation bubble. *Physics of Fluids*, 13(10):2805–2819.

Alfonsi, G. (2009). Reynolds-Averaged Navier-Stokes equations for turbulence modeling. *Applied Mechanics Reviews*, 62(4):040802.

Anderson Jr, J. D. (2010). *Fundamentals of aerodynamics*. Tata McGraw-Hill Education.

Apfel, R. (1982). Acoustic cavitation: a possible consequence of biomedical uses of ultrasound. *The British journal of cancer. Supplement*, 5:140.

Arakeri, V. H. (1975). Viscous effects on the position of cavitation separation from smooth bodies. *Journal of Fluid Mechanics*, 68(4):779–799.

Arndt, R., Arakeri, V., and Higuchi, H. (1991). Some observations of tip-vortex cavitation. *Journal of fluid mechanics*, 229:269–289.

Arndt, R. E. (2012). Some remarks on hydrofoil cavitation. *Journal of Hydrodynamics*, 24(3):305–314.

Arndt, R. E. and Keller, A. P. (1992). Water quality effects on cavitation inception in a trailing vortex. *Journal of fluids engineering*, 114(3):430–438.

ASME (2009). Standard for verification and validation in computational fluid dynamics and heat transfer. *ASME V&V 20-2009*.

Asnaghi, A. (2018). *Computational modelling for cavitation and tip vortex flows*. PhD thesis, Sweden: Chalmers University of Technology.

Asnaghi, A., Bensow, R., and Svennberg, U. (2017a). Comparative analysis of tip vortex flow using RANS and LES. In *VII International Conference on Computational Methods in Marine Engineering*.

Asnaghi, A., Bensow, R. E., and Svennberg, U. (2017b). Implicit large eddy simulation of tip vortex on an elliptical foil. In *Fifth International Symposium on Marine Propulsion, SMP*.

Asnaghi, A., Feymark, A., and Bensow, R. (2015). Numerical analysis of tip vortex flow. In *Proceedings of the 19th Numerical Towing Tank Symposium (NuTTS'16), Oléron, French*.

Baltazar, J., Rijpkema, D., and de Campos, J. F. (2018). On the use of the $\gamma-\mathrm{Re}_{\theta_t}$ transition model for the prediction of the propeller performance at model-scale. *Ocean Engineering*, 170:6–19.

Bark, G., Berchiche, N., and Grekula, M. (2004). Application of principles for observation and analysis of eroding cavitation-the erocav observation handbook. *EROCAV Report, Dept. of Naval Architecture, Chalmers University of Technology, Göteborg, Sweden*.

Baudin, E. and Mumm, H. (2015). Guidelines for regulation on uw noise from commercial vessels. *Technical report, AQUO and SONIC EU FP7 projects, Bureau Veristas, DNV-GL*.

Bendat, J. S. and Piersol, A. G. (2011). *Random data: analysis and measurement procedures*, volume 729. John Wiley & Sons.

Billet, M. L. (1985). Cavitation nuclei measurements-a review. In *Cavitation and multiphase flow forum-1985*.

Bosch, G. and Rodi, W. (1998). Simulation of vortex shedding past a square cylinder with different turbulence models. *International journal for numerical methods in fluids*, 28(4):601–616.

Bosschers, J. (2009). Modeling and analysis of a cavitating vortex in 2D unsteady viscous flow. In *7th International Symposium on Cavitation*.

Bosschers, J. (2015). An analytical solution for the viscous flow around a 2D cavitating vortex. *Trans. ASME J. Fluids Engng (submitted)*.

Bosschers, J. (2017). A semi-empirical method to predict broadband hull pressure fluctuations and underwater radiated noise due to cavitating tip vortices. In *Fifth International Symposium on Marine Propulsors*. SMP.

Bosschers, J. (2018). *Propeller tip-vortex cavitation and its broadband noise*. PhD thesis, The Netherlands: University of Twente.

Boussinesq, J. (1877). Theorie de l'ecoulement tourbillant. *Mem. Acad. Sci.*, 23:46.

Bradshaw, P. (1973). Effects of streamline curvature on turbulent flow. Technical report, Advisory group for aerospace research and development Paris (France).

Brennen, C. (1969). A numerical solution of axisymmetric cavity flows. *Journal of Fluid Mechanics*, 37(4):671–688.

Brennen, C. E. (2005). *Fundamentals of multiphase flow*. Cambridge university press.

Brennen, C. E. (2015). Cavitation in medicine. *Interface focus*, 5(5):20150022.

Brouwer, J., Tukker, J., and Van Rijsbergen, M. (2015). Uncertainty analysis and stationarity test of finite length time series signals. In *The 4th International Conference on Advanced Model Measurement Technology for the Maritime Industry (AMT'15), Istanbul, Turkey*.

Carlton, J. (2018). *Marine propellers and propulsion*. Butterworth-Heinemann.

Ceccio, S. L. and Brennen, C. E. (1991). Observations of the dynamics and acoustics of travelling bubble cavitation. *Journal of Fluid Mechanics*, 233:633–660.

Celik, I. and Hu, G. (2004). Single grid error estimation using error transport equation. *Journal of Fluids Engineering*, 126(5):778–790.

Celik, I. and Rodi, W. (1988). Modeling suspended sediment transport in nonequilibrium situations. *Journal of Hydraulic Engineering*, 114(10):1157–1191.

Celik, I. B., Ghia, U., Roache, P. J., et al. (2008). Procedure for estimation and reporting of uncertainty due to discretization in CFD applications. *Journal of fluids Engineering-Transactions of the ASME*, 130(7).

Chaves, H., Knapp, M., Kubitzek, A., Obermeier, F., and Schneider, T. (1995). Experimental study of cavitation in the nozzle hole of diesel injectors using transparent nozzles. *SAE transactions*, pages 645–657.

Choi, K.-S. and Lumley, J. L. (2001). The return to isotropy of homogeneous turbulence. *Journal of Fluid Mechanics*, 436:59–84.

Chou, P. Y. (1945). On velocity correlations and the solutions of the equations of turbulent fluctuation. *Quarterly of Applied Mathematics*, 3(1):38–54.

Coder, J. (2017). A perspective on transition modeling in computational fluid dynamics. Presented at the NASA Ames Research Center AMS Seminar Series.

Coleman, H. W. and Stern, F. (1997). Uncertainties in CFD code validation. *ASME J. Fluids Engineering*, 119:795–803.

Dacles-Mariani, J., Zilliac, G. G., Chow, J. S., and Bradshaw, P. (1995). Numerical/experimental study of a wingtip vortex in the near field. *AIAA journal*, 33(9):1561–1568.

De Lorenzo, F. and Biot, M. (2006). Noise and vibration: comfort standards evolving in the wrong direction? *NAVAL ARCHITECT*, pages 36–39.

Dekking, F. M., Kraaikamp, C., Lopuhaä, H. P., and Meester, L. E. (2005). *A Modern Introduction to Probability and Statistics: Understanding why and how*. Springer Science & Business Media.

Devenport, W. J., Rife, M. C., Liapis, S. I., and Follin, G. J. (1996). The structure and development of a wing-tip vortex. *Journal of Fluid Mechanics*, 312:67–106.

Dol, H., Kok, J., and Oskam, B. (2002). Turbulence modelling for leading-edge vortex flows. In *40th AIAA Aerospace Sciences Meeting & Exhibit*, page 843.

Drela, M. and Giles, M. B. (1987). Viscous-inviscid analysis of transonic and low reynolds number airfoils. *AIAA journal*, 25(10):1347–1355.

Dreyer, M., Decaix, J., Münch-Alligné, C., and Farhat, M. (2014). Mind the gap: a new insight into the tip leakage vortex using stereo-PIV. *Experiments in fluids*, 55(11):1849.

Eça, L. and Hoekstra, M. (2006). On the influence of the iterative error in the numerical uncertainty of ship viscous flow calculations. In *26th Symposium on Naval Hydrodynamics*, pages 17–22.

Eça, L. and Hoekstra, M. (2014). A procedure for the estimation of the numerical uncertainty of CFD calculations based on grid refinement studies. *Journal of Computational Physics*, 262:104–130.

Eça, L., Vaz, G., and Hoekstra, M. (2014). Code verification of ReFRESCO with a statistically periodic manufactured solution. In *ASME 2014 33rd International Conference on Ocean, Offshore and Arctic Engineering*, pages V002T08A015–V002T08A015. American Society of Mechanical Engineers.

Eça, L., Vaz, G., and Hoekstra, M. (2010). Code verification, solution verification and validation in RANS solvers.

Emory, M. and Iaccarino, G. (2014). Visualizing turbulence anisotropy in the spatial domain with componentality contours. *Cent. Turbul. Res. Annu. Res. Briefs*, pages 123–138.

Feder, D.-F., Dhone, M., Kornev, N., and Abdel-Maksoud, M. (2018). Comparison of different approaches tracking a wing-tip vortex. *Ocean engineering*, 147:659–675.

Ferziger, J. H. and Peric, M. (2012). *Computational methods for fluid dynamics*. Springer Science & Business Media.

Foeth, E.-J. (2008). *The structure of three-dimensional sheet cavitation*. PhD thesis, The Netherlands: Delft University of Technology.

Franc, J.-P. and Michel, J.-M. (2006). *Fundamentals of cavitation*, volume 76. Springer science & Business media.

Frank, T., Lifante, C., Jebauer, S., Kuntz, M., and Rieck, K. (2007). CFD simulation of cloud and tip vortex cavitation on hydrofoils. In *Proceedings of the International Conference on Multiphase Flow*.

Frisk, G. V. (2012). Noiseonomics: The relationship between ambient noise levels in the sea and global economic trends. *Scientific Reports*, 2:437.

Germano, M. (1992). Turbulence: the filtering approach. *Journal of Fluid Mechanics*, 238:325–336.

Geurts, B. J. and Holm, D. D. (2006). Commutator errors in large-eddy simulation. *Journal of physics A: mathematical and general*, 39(9):2213.

Goldstein, S. et al. (1938). Modern developments in fluid dynamics, vol. 1. *Clarendon Press, London, Eng-land*, 309:310.

Green, S. (2012). *Fluid vortices*, volume 30. Springer Science & Business Media.

Gritskevich, M. S., Garbaruk, A. V., Schütze, J., and Menter, F. R. (2012). Development of DDES and IDDES formulations for the k-ω shear stress transport model. *Flow, turbulence and combustion*, 88(3):431–449.

Han, X., Sagaut, P., and Lucor, D. (2012). On sensitivity of RANS simulations to uncertain turbulent inflow conditions. *Computers & Fluids*, 61:2–5.

Hellsten, A. K. (2005). New advanced $k-\omega$ turbulence model for high-lift aerodynamics. *AIAA journal*, 43(9):1857–1869.

Helmholtz, H. (1858). Über integrale der hydrodynamischen gleichungen, welche den wirbelbewegungen entsprechen. *Journal für Mathematik Bd. LV. Heft*, 1:4.

Heyes, A., Jones, R., and Smith, D. (2004). Wandering of wing-tip vortices. In *Proceedings of the 12th International Symposium on Applications of Laser Techniques to Fluid Mechanics*, pages 35–3.

Hickel, S. and Hulshoff, S. (2017). *Lecture notes AE4137 - Large Eddy Simulations*. Delft University of Technology.

Higuchi, H., Arndt, R., and Rogers, M. (1989). Characteristics of tip vortex cavitation noise. *Journal of fluids engineering*, 111(4):495–501.

Higuchi, H., Quadrelli, J. C., and Farell, C. (1987). Vortex roll-up from an elliptic wing at moderately low reynolds numbers. *AIAA journal*, 25(12):1537–1542.

Hildebrand, J. A. (2009). Anthropogenic and natural sources of ambient noise in the ocean. *Marine Ecology Progress Series*, 395:5–20.

Hills, R. G. (2006). Model validation: model parameter and measurement uncertainty. *Journal of Heat Transfer*, 128(4):339–351.

Hirt, C. W. and Nichols, B. D. (1981). Volume of Fluid (VoF) method for the dynamics of free boundaries. *Journal of computational physics*, 39(1):201–225.

Hoekstra, M. and Vaz, G. (2009). The partial cavity on a 2D foil revisited. In *7th International Symposium on Cavitation*.

Hunt, J. C., Wray, A. A., and Moin, P. (1988). Eddies, streams, and convergence zones in turbulent flows.

Jeong, J. and Hussain, F. (1995). On the identification of a vortex. *Journal of fluid mechanics*, 285:69–94.

Kaden, H. (1931). Aufwicklung einer unstabilen unstetigkeitsfläche. *Archive of Applied Mechanics*, 2(2):140–168.

Karplus, H. (1958). The velocity of sound in a liquid containing gas bubbles, armour research foundation; project no. a-097. *Atomic Energy Commission Contract No. AF (11-1)-528, United States Atomic Energy Commission*.

Kato, H., Konno, A., Maeda, M., and Yamaguchi, H. (1996). Possibility of quantitative prediction of cavitation erosion without model test. *Journal of fluids engineering*, 118(3):582–588.

Katz, J. and Plotkin, A. (2001). *Low-speed aerodynamics*, volume 13. Cambridge university press.

Klapwijk, M. (2018). Elliptical planform foil with a NACA66_2-415 cross section: an overview. MARIN, internal document.

Klapwijk, M., Llyod, T., and Vaz, G. (TBD). Evaluation of scale-resolving simulations for a turbulent channel flow at $Re_\tau = 395$.

Knapp, R. T. (1955). Recent investigations of the mechanics of cavitation and cavitation damage. *Transactions of the ASME*, 77:1045–1054.

Knapp, R. T. (1970). Cavitation. *McGraw-Hill, Inc.*, 6.

Krogstad, P. and Torbergsen, L. E. (2000). Invariant analysis of turbulent pipe flow. *Flow, turbulence and combustion*, 64(3):161–181.

Kuiper, G. (1997). Cavitation research and ship propeller design. *Applied scientific research*, 58(1-4):33–50.

Kunz, R. F., Boger, D. A., Stinebring, D. R., Chyczewski, T. S., Lindau, J. W., Gibeling, H. J., Venkateswaran, S., and Govindan, T. (2000). A preconditioned Navier-Stokes method for two-phase flows with application to cavitation prediction. *Computers & Fluids*, 29(8):849–875.

Lamb, H. (1932). Hydrodynamics (6th edn). *Cambridge UniverSity PrCSS*.

Lance, M. and Bataille, J. (1991). Turbulence in the liquid phase of a uniform bubbly air–water flow. *Journal of fluid mechanics*, 222:95–118.

Langtry, R. and Menter, F. (2005). Transition modeling for general CFD applications in aeronautics. In *43rd AIAA aerospace sciences meeting and exhibit*, page 522.

Langtry, R. B. (2006). *A correlation-based transition model using local variables for unstructured parallelized CFD codes*. PhD thesis, Germany: Universität Stuttgart.

Langtry, R. B. and Menter, F. R. (2009). Correlation-based transition modeling for unstructured parallelized computational fluid dynamics codes. *AIAA journal*, 47(12):2894–2906.

Launder, B. E. and Spalding, D. B. (1972). *Mathematical models of turbulence*. Number BOOK. Academic press.

Li, Z. (2012). *Assessment of cavitation erosion with a multiphase Reynolds-Averaged Navier-Stokes method*. PhD thesis, The Netherlands: Delft University of Technology.

Liebrand, R., Klapwijk, M., Lloyd, T., Vaz, G., and Lopes, R. (2019). A sensitivity analysis of CFD transition modelling in the context of vortex roll-up prediction. In *Proceedings of VIII International Conference on Computational Methods in Marine Engineering, Gothenburg, Sweden*.

Ligtelijn, J. T. (2010). The pay-off between cavitation and efficiency. *Proc. of IMarEST Ship*.

Lin, W., Oortmessen, G., Davies, M., Faltisen, O., Haimov, A., Hocquet, P., and Della Logia, B. (1990). Report of the panel on validation procedures. In *Proceedings of the 18th ITTC*, pages 577–605.

Lopes, R., Eça, L., and Vaz, G. (2018). Assessment of RANS transition models. In *Proceedings of the 21th Numerical Towing Tank Symposium (NuTTS'18), Cortina, Italy*.

Lumley, J. L. and Newman, G. R. (1977). The return to isotropy of homogeneous turbulence. *Journal of Fluid Mechanics*, 82(1):161–178.

Mack, L. M. (1984). Boundary-layer linear stability theory. Technical report, California intitute of technology Pasadena jet propulsion lab.

Maines, B. and Arndt, R. E. (1997a). The case of the singing vortex. *Journal of fluids engineering*, 119(2):271–276.

Maines, B. H. and Arndt, R. (1997b). Tip vortex formation and cavitation. *Journal of fluids engineering*, 119(2):413–419.

Mazzitelli, I. M., Lohse, D., and Toschi, F. (2003). The effect of microbubbles on developed turbulence. *Physics of fluids*, 15(1):L5–L8.

McCormick, B. (1962). On cavitation produced by a vortex trailing from a lifting surface. *Journal of Basic Engineering*, 84(3):369–378.

Menter, F. and Egorov, Y. (2006). Revisiting the turbulent scale equation. In *IUTAM Symposium on One Hundred Years of Boundary Layer Research*, pages 279–290. Springer.

Menter, F., Esch, T., and Kubacki, S. (2002). Transition modelling based on local variables. In *Engineering Turbulence Modelling and Experiments 5*, pages 555–564. Elsevier.

Menter, F., Garbaruk, A., and Egorov, Y. (2012). Explicit algebraic reynolds stress models for anisotropic wall-bounded flows. *Progress in Flight Physics*, 3:89–104.

Menter, F., Kuntz, M., and Bender, R. (2003a). A scale-adaptive simulation model for turbulent flow predictions. In *41st aerospace sciences meeting and exhibit*, page 767.

Menter, F. R. (1994). Two-equation eddy-viscosity turbulence models for engineering applications. *AIAA journal*, 32(8):1598–1605.

Menter, F. R., Egorov, Y., and Rusch, D. (2006). Steady and unsteady flow modelling using the k-$\sqrt{k}$l model. In *Ichmt Digital Library Online*. Begel House Inc.

Menter, F. R., Kuntz, M., and Langtry, R. (2003b). Ten years of industrial experience with the SST turbulence model. *Turbulence, heat and mass transfer*, 4(1):625–632.

Merkle, C. L. (1998). Computational modelling of the dynamics of sheet cavitation. In *Proc. of the 3rd Int. Symp. on Cavitation, Grenoble, France, 1998*.

Mocket, C., Haase, W., and Schwamborn, D. (2018). *Go4Hybrid: Grey Area Mitigation for Hybrid RANS-LES Methods*, volume 134. Springer.

Molloy, S. (2006). *Uncertainty analysis of ship powering prediction methods using Monte Carlo simulation*. PhD thesis, Canada: Memorial University of Newfoundland.

Moore, D. (1974). A numerical study of the roll-up of a finite vortex sheet. *Journal of Fluid Mechanics*, 63(2):225–235.

Moore, R. and Ruggeri, R. (1969). Method for prediction of pump cavitation performance for various liquids, liquid temperatures, and rotative speeds.

Morgut, M. (2012). *Predictions of non-cavitating and cavitating flow on hydrofoils and marine propellers by CFD and advanced model calibration*. PhD thesis, Italy: Università degli Studi di Udine.

Morkovin, M. V. (1969). On the many faces of transition. In *Viscous drag reduction*, pages 1–31. Springer.

Ortega, J. M. and Rheinboldt, W. C. (1970). *Iterative solution of nonlinear equations in several variables*, volume 30. Siam.

Osterman, A., Dular, M., Hočevar, M., and Širok, B. (2010). Infrared thermography of cavitation thermal effects in water. *Strojniški vestnik-Journal of Mechanical Engineering*, 56(9):527–534.

Paskin, L. (2018). A numerical assessment of turbulence modeling in tip vortex flows at cavitating conditions. Master's thesis, France: Ecole Centrale de Nantes.

Patankar, S. V. and Spalding, D. B. (1983). A calculation procedure for heat, mass and momentum transfer in three-dimensional parabolic flows. In *Numerical Prediction of Flow, Heat Transfer, Turbulence and Combustion*, pages 54–73. Elsevier.

Patek, S., Korff, W., and Caldwell, R. (2004). Biomechanics: deadly strike mechanism of a mantis shrimp. *Nature*, 428(6985):819.

Pennings, P. (2016). *Dynamics of vortex cavitation*. PhD thesis, The Netherlands: Delft University of Technology.

Pennings, P., Bosschers, J., Westerweel, J., and Van Terwisga, T. (2015a). Dynamics of isolated vortex cavitation. *Journal of Fluid Mechanics*, 778:288–313.

Pennings, P., Westerweel, J., and Van Terwisga, T. (2015b). Flow field measurement around vortex cavitation. *Experiments in Fluids*, 56(11):206.

Pereira, F. (2018). *Towards predictive scale-resolving simulations of turbulent external Flows*. PhD thesis, Portugal: universidade de liboa intituto superior technico.

Pereira, F. S., Eça, L., Vaz, G., and Girimaji, S. S. (2018). Challenges in scale-resolving simulations of turbulent wake flows with coherent structures. *Journal of Computational Physics*, 363:98–115.

Pereira, F. S. and Vaz, G. (2018). Simulation of a wingtip vortex flow with RANS and SRS methods.

Pereira, F. S., Vaz, G., and Eça, L. (2015). On the numerical requirements of rans and hybrid turbulence models. In *VI International Conference on Computational Methods in Marine Engineering (MARINE2015)*.

Phillips, T. and Roy, C. (2011). Residual methods for discretization error estimation. In *20th AIAA Computational Fluid Dynamics Conference*, page 3870.

Phillips, W. (1981). The turbulent trailing vortex during roll-up. *Journal of Fluid Mechanics*, 105:451–467.

Plesset, M. S. (1949). The dynamics of cavitation bubbles. *Journal of applied mechanics*, 16:277–282.

Pope, S. B. (2000). *Turbulent flows*. Cambridge university press.

Rayleigh, L. (1917). VIII. On the pressure developed in a liquid during the collapse of a spherical cavity. *The London, Edinburgh, and Dublin Philosophical Magazine and Journal of Science*, 34(200):94–98.

ReFRESCO (2017). *ReFRESCO Theory Manual*. Available at `www.refresco.org`.

Reverberi, A., Lloyd, T., and Vaz, G. (2016). Towards cavitation modelling accounting for transition effects.

Reynolds, O. (1873). The causes of the racing of the engines of screw steamers investigated theoretically and by experiment. *Trans. Inst. Naval Arch*, 14:56–67.

Reynolds, O. (1895). On the dynamical theory of incompressible viscous fluids and the determination of the criterion. *Philosophical Transactions of the Royal Society of London. A*, 186:123–164.

Rijpkema, D. and Vaz, G. (2011). Viscous flow computations on propulsors: verification, validation and scale effects. *Proceedings of the Developments in Marine CFD*.

Rijsbergen, M. (2016). A review of sheet cavitation inception mechanisms. *Proceedings of ISROMAC2016*, (356).

Roache, P. J. (1997). Quantification of uncertainty in computational fluid dynamics. *Annual review of fluid Mechanics*, 29(1):123–160.

Roache, P. J. (2009). *Fundamentals of verification and validation*. Hermosa publ.

Rodi, W. (1976). A new algebraic relation for calculating the reynolds stresses. In *Gesellschaft Angewandte Mathematik und Mechanik Workshop Paris France*, volume 56.

Rotta, J. (1951). Statistische theorie nichthomogener turbulenz. *Zeitschrift für Physik*, 129(6):547–572.

Rumsey, C. L. (2007). Apparent transition behavior of widely-used turbulence models. *International Journal of Heat and Fluid Flow*, 28(6):1460–1471.

Rumsey, C. L. and Spalart, P. R. (2009). Turbulence model behavior in low reynolds number regions of aerodynamic flowfields. *AIAA journal*, 47(4):982–993.

Saffman, P. G. (1992). *Vortex dynamics*. Cambridge university press.

Salahudeen, A. and Baeder, J. D. (2018). Uncertainty quantification for free stream turbulence intensity effects on airfoil characteristics. In *2018 AIAA Aerospace Sciences Meeting*, page 0033.

Sampson, R. (2010). *Lecture notes Resistance & Propulsion (I)*. School of Marine Science and Technology. Newcastle University.

Schlichting, H. and Gersten, K. (2016). *Boundary-layer theory*. Springer.

Schnerr, G. H. and Sauer, J. (2001). Physical and numerical modeling of unsteady cavitation dynamics. In *Fourth International Conference on Multiphase Flow*, volume 1. ICMF New Orleans.

Schot, J. (2014). Numerical study of vortex cavitation on the elliptical Arndt foil. Master's thesis, The Netherlands: Delft University of Technology.

Schot, J. J., Pennings, P. C., Pourquie, M., and Van Terwisga, T. J. (2014). Modelling of tip vortex cavitation for engineering applications in OpenFOAM. In *Proceedings-WCCM XI: 11th World Congress on Computational Mechanics; ECCM V: 5th European Conference on Computational Mechanics; ECFD VI: 6th European Conference on Computational Fluid Dynamics, Barcelona, Spain, 20-25 July 2014*. CIMNE.

Senocak, I. and Shyy, W. (2002). Evaluations of cavitation models for Navier-Stokes computations. In *ASME 2002 Joint US-European Fluids Engineering Division Conference*, pages 395–401. American Society of Mechanical Engineers.

Shur, M. L., Spalart, P. R., Strelets, M. K., and Travin, A. K. (2008). A hybrid RANS-LES approach with delayed-DES and wall-modelled LES capabilities. *International Journal of Heat and Fluid Flow*, 29(6):1638–1649.

Singhal, A. K., Athavale, M. M., Li, H., and Jiang, Y. (2002). Mathematical basis and validation of the full cavitation model. *Journal of fluids engineering*, 124(3):617–624.

Smagorinsky, J. (1963). General circulation experiments with the primitive equations: I. the basic experiment. *Monthly weather review*, 91(3):99–164.

Song, C. and Qin, Q. (2001). Numerical simulation of unsteady cavitation flows. *http://resolver. caltech. edu/cav2001: sessionB5. 004*.

Sozer, E., Brehm, C., and Kiris, C. C. (2014). Gradient calculation methods on arbitrary polyhedral unstructured meshes for cell-centered cfd solvers. In *52nd Aerospace Sciences Meeting*, page 1440.

Spalart, P. R. (1997). Comments on the feasibility of LES for wings, and on a hybrid RANS/LES approach. In *Proceedings of first AFOSR international conference on DNS/LES*. Greyden Press.

Spalart, P. R., Deck, S., Shur, M. L., Squires, K. D., Strelets, M. K., and Travin, A. (2006). A new version of detached-eddy simulation, resistant to ambiguous grid densities. *Theoretical and computational fluid dynamics*, 20(3):181.

Spalart, P. R. and Rumsey, C. L. (2007). Effective inflow conditions for turbulence models in aerodynamic calculations. *AIAA journal*, 45(10):2544–2553.

Staufenbiel, R. W. (1984). Structure of lift-generated rolled-up vortices. *Journal of aircraft*, 21(10):737–744.

Steinhoff, J., Yonghu, W., Mersch, T., and Senge, H. (1992). Computational vorticity capturing-application to helicopter rotor flows. In *30th Aerospace Sciences Meeting and Exhibit*, page 56.

Stern, F., Wilson, R., and Shao, J. (2006). Quantitative V&V of CFD simulations and certification of CFD codes. *International journal for numerical methods in fluids*, 50(11):1335–1355.

Stutz, B. and Reboud, J.-L. (1997). Two-phase flow structure of sheet cavitation. *Physics of fluids*, 9(12):3678–3686.

Stutz, B. and Reboud, J.-L. (2000). Measurements within unsteady cavitation. *Experiments in fluids*, 29(6):545–552.

Süli, E. and Mayers, D. F. (2003). *An introduction to numerical analysis*. Cambridge university press.

Sussman, M., Smereka, P., and Osher, S. (1994). A level set approach for computing solutions to incompressible two-phase flow. *Journal of Computational physics*, 114(1):146–159.

Tabor, G. R. and Baba-Ahmadi, M. (2010). Inlet conditions for large eddy simulation: A review. *Computers & Fluids*, 39(4):553–567.

Thiruvengadam, A. (1974). Handbook of cavitation erosion. Technical report, Hydronautis inc Larel MD.

van Buuren, R. (1999). *Time integration methods for compressible flow*. PhD thesis, The Netherlands: Twente University.

Van den Boogaard, M. (TBD). Numerical investigation of the dynamics of a cavitating line vortex in a converging-diverging nozzle. Master's thesis, The Netherlands: Delft University of Technology.

Van Ingen, J. (1956). *A suggested semi-empirical method for the calculation of the boundary layer transition region*. Delft University of Technology.

Van Terwisga, T., Kuiper, G., and Van Rijsbergen, M. (1999). On experimental techniques for the determination of tip vortex cavitation on ship propellers. In *Proc. of 1999 ASME/JSME Fluids Engineering Division Summer Meeting, San Francisco, CA, 18–23 July*.

van Wijngaarden, E., Bosschers, J., and Kuiper, G. (2005). Aspects of the cavitating propeller tip vortex as a source of inboard noise and vibration. In *ASME 2005 Fluids Engineering Division Summer Meeting*, pages 539–544. American Society of Mechanical Engineers.

Van Wijngaarden, H. C. J. (2011). *Prediction of propeller-induced hull-pressure fluctuations*. PhD thesis, The Netherlands: Twente University.

Veritas, D. N. (2003). Comfort class. *DNV Rules*, (Part 5).

Vuik, C. and Lahaye, D. (2015). *Lecture notes Scientific Computing (WI4201)* . Delft University of Technology.

Walker, G. (1992). The role of laminar-turbulent transition in gas turbine engines: a discussion. In *International Gas Turbine and Aeroengine Congress and Exposition 1992*. American Society of Mechanical Engineers.

Wallin, S. and Johansson, A. V. (2000). An explicit algebraic Reynolds stress model for incompressible and compressible turbulent flows. *Journal of Fluid Mechanics*, 403:89–132.

Walters, D. K. and Cokljat, D. (2008). A three-equation eddy-viscosity model for Reynolds-Averaged Navier-Stokes simulations of transitional flow. *Journal of fluids engineering*, 130(12):121401.

Wang, B.-l., Liu, Z.-h., Li, H.-y., Wang, Y.-y., Liu, D.-c., and Zhang, L.-x. (2017). On the numerical simulations of vortical cavitating flows around various hydrofoils. *Journal of Hydrodynamics*, 29(6):926–938.

Wang, Y.-C. and Brennen, C. E. (1995). The noise generated by the collapse of a cloud of cavitation bubbles. In *ASME*, number 226, pages 17–29. American Society of Mechanical Engineers.

Watanabe, T., Kawamura, T., Takekoshi, Y., Maeda, M., and Rhee, S. H. (2003). Simulation of steady and unsteady cavitation on a marine propeller using a RANS CFD code. In *Proceedings of The Fifth International Symposium on Cavitation (Cav*. Citeseer.

Waterson, N. P. and Deconinck, H. (2007). Design principles for bounded higher-order convection schemes–a unified approach. *Journal of Computational Physics*, 224(1):182–207.

White, F. M. and Corfield, I. (2006). *Viscous fluid flow*, volume 3. McGraw-Hill New York.

Wilcox, D. C. et al. (1998). *Turbulence modeling for CFD*, volume 2. DCW industries La Canada, CA.

Zheng, Q., Durben, D., Wolf, G., and Angell, C. (1991). Liquids at large negative pressures: water at the homogeneous nucleation limit. *Science*, 254(5033):829–832.

Zheng, W., Yan, C., Liu, H., and Luo, D. (2016). Comparative assessment of SAS and DES turbulence modeling for massively separated flows. *Acta Mechanica Sinica*, 32(1):12–21.

Zwart, P. J., Gerber, A. G., and Belamri, T. (2004). A two-phase flow model for predicting cavitation dynamics. In *Fifth international conference on multiphase flow, Yokohama, Japan*, volume 152.

A

PROJECT DETAILS

A.1. INITIAL PROJECT DESCRIPTION

For MARIN Academy we are looking for a student for the following MSc internship/assignment:

"Numerical modelling of cavitating vortex for an elliptical wing"

Tip vortex cavitation on marine propellers generate hull pressure fluctuations and underwater radiated noise. These phenomena are typically undesirable as they contribute to reduced comfort onboard and increased environmental impact respectively. Studying the behaviour of cavitating tip vortices remains challenging, due to the strong dynamics involved and the broadband nature of the resulting noise sources. These originate from both the oscillations as well as the collapse/bursting of the cavitating vortex. Previous work has focussed on developing semi-analytical models for predicting cavitating tip vortex dynamics and noise generation (Pennings et al., 2015b), which have also subsequently been validated using experimental measurement data (Pennings et al., 2015b). An often studied testcase is the cavitating tip vortex of the elliptical wing used by (Arndt et al., 1991; Pennings et al., 2015b) This test case leads to a strong tip vortex without any rotation making experiments and simulations easier. The test case has been evaluated experimentally and numerically, but for a limited number of conditions and numerical settings. Also there are a number of uncertainties involved in the precise geometry of the foil. This project will further existing knowledge on the simulation of the elliptical foil test case by performing extensive numerical sensitivity studies with the aim of examining the effect on the prediction of the vortex and its dynamics, and the effect of the precise geometry. The project consists out of two parts, out of which the project should deliver the first part, if time allows the second part can be performed. Alternatively the second part will potentially be performed in a second internship. The following primary tasks are envisaged in the first part:

- A literature review on the simulation of this particular test case;
- A comparison between results obtained on structured and unstructured grids;
- Examination of the effect of trailing edge and tip geometry on the integral quantities (lift, drag, etc.), local flow quantities and vortex dynamics. Both for wetted flow and cavitating flow conditions;
- A grid and timestep refinement (verification) study based on the available elliptical wing geometry, and comparison with experiments (validation);
- Investigation into the use of local/adaptive grid refinement to capture the vortex.

The following tasks are envisaged in the second part:

- Examination of the effect of turbulence modelling on the flow prediction for both non-cavitating and cavitating conditions;
- Investigation of the effect of cavitation and Reynolds number on the cavitating vortex;
- Simulation of vortex dynamics expected to lead to significant noise generation, such as vortex collapsing or bursting;
- All CFD work in the project will be performed with the code ReFRESCO. For the first part the simulations are restricted to RANS methods.

A

A.2. TECHNICAL DRAWING 'ARNDT' WING

Figure A.1 displays the technical drawing of the 'Arndt' wing.

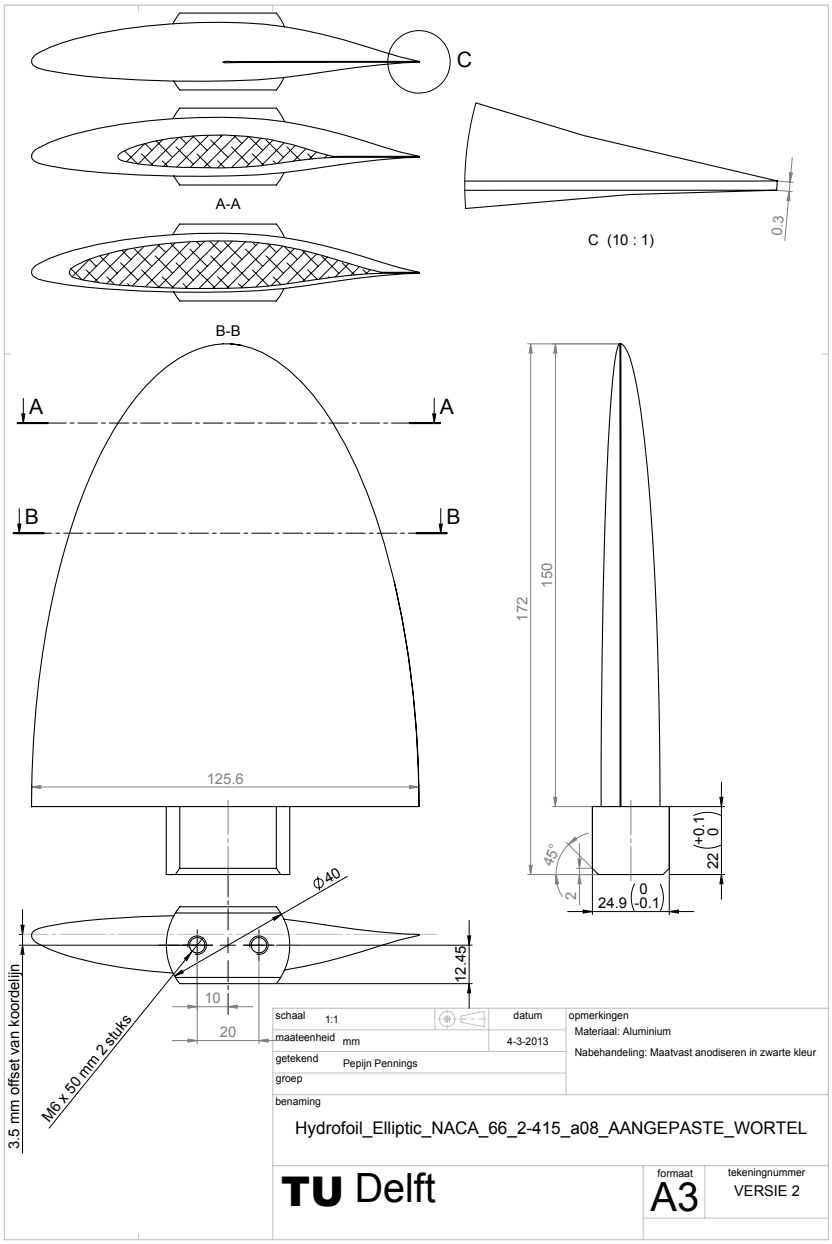

Figure A.1: Technical drawing of the 'Arndt' wing (Pennings et al., 2015b). Note measurement unit is mm.

B

MATHEMATICAL DETAILS OF PHYSICAL MODELS

This appendix serves as the mathematical support for the physical models of Chapter 3. Some of the models are totally described in that chapter, for others some additional information is presented in this appendix.

B.1. $\gamma - \tilde{Re}_{\theta_t}$ TRANSITION MODEL

All the coefficients of the model are shown in Table B.1. The details of the two transport equations are given next.

Table B.1: Coefficients of the $\gamma - \tilde{Re}_{\theta_t}$ transition model.

c_{e1}	c_{e2}	c_{a1}	c_{a2}	c_{θ_t}	σ_f	σ_{θ_t}	s_1
1.0	50	2.0	0.06	0.03	1.0	2.0	2.0

B.1.1. INTERMITTENCY TRANSPORT EQUATION

PRODUCTION TERM (P_γ)

The additional equation for the onset criterion in the production term is shown in Equation (B.1). Furthermore, the intensity of transition is determined by the equations shown in Equation (B.2). Lastly, the equations accounting for separation induced transition are given in Equation (B.3).

$$F_{onset} = \max\left(F_i - F_{onset3}, 0\right), \tag{B.1a}$$

$$F_{onset2} = \min\left(\max\left(F_{onset1}, F_{onset1}^4\right), 2.0\right), \tag{B.1b}$$

$$F_{onset1} = \frac{Re_V}{2.193 Re_{\theta c}}, \tag{B.1c}$$

$$Re_{\theta c} = \begin{cases} -396.035\times10^{-2} + 1.012\times10^{-8}\tilde{Re}_{\theta t} - 868.230\times10^{-6} \\ Re_{\theta t}^2 + 696.506\times10^{-9}\tilde{Re}_{\theta t}^3 - 174.105\times10^{-12}\tilde{Re}_{\theta t}^4, & \tilde{Re}_{\theta t} \le 1870; \\ \tilde{Re}_{\theta t} - \left(593.11 + 0.482\left(\tilde{Re}_{\theta t} - 1870.0\right)\right), & 1870 < \tilde{Re}_{\theta t}, \end{cases} \tag{B.1d}$$

$$F_{onset3} = \max\left[1 - \left(\frac{R_T}{2.5}\right)^3, 0\right], \tag{B.1e}$$

$$R_T = \frac{\rho k}{\mu\omega}. \tag{B.1f}$$

$$F_{length} = F_{length,1}\left(1 - F_{sublayer}\right) + 40.0 F_{sublayer}, \tag{B.2a}$$

$$F_{length,1} = \begin{cases} 39.8189 + (-119.270\times10^{-4})\tilde{R}e_{\theta t} + (-132.567\times10^{-6})\tilde{R}e_{\theta t}^2, & \tilde{R}e_{\theta t} < 400; \\ 263.40 - 123.93\times10^{-2}\tilde{R}e_{\theta t} + 194.54\times10^{-5}\tilde{R}e_{\theta t}^2 - 101.69\times10^{-8}\tilde{R}e_{\theta t}^3, & 400 \le \tilde{R}e_{\theta t} < 596; \\ 0.5 - (3.0\times10^{-4})(\tilde{R}e_{\theta t} - 596.0), & 596 \le \tilde{R}e_{\theta t} < 1200; \\ 0.3188, & 1200 \le \tilde{R}e_{\theta t} \end{cases} \tag{B.2b}$$

$$F_{sublayer} = exp\left[-\left(\frac{Re_\omega}{200}\right)^2\right], \tag{B.2c}$$

$$Re_\omega = \frac{\rho\omega d^2}{\mu}. \tag{B.2d}$$

$$\gamma_{sep} = \min\left(s_1 \max\left[0, \left(\frac{Re_V}{3.235Re_{\theta c}}\right) - 1\right] F_{reattach}, 2\right) F_{\theta t}, \tag{B.3a}$$

$$F_{reattach} = \exp\left[-\left(\frac{R_T}{20}\right)^4\right]. \tag{B.3b}$$

RELAMINARISATION TERM (E_γ)

$$E_\gamma = c_{a2}\rho|\Omega_{ij}|\gamma F_{turb}\left(c_{e2}\gamma - 1\right), \tag{B.4a}$$

$$F_{turb} = \exp\left[-\left(\frac{R_T}{4}\right)^4\right]. \tag{B.4b}$$

Here $|\Omega_{ij}|$ is the magnitude of the vorticity tensor, i.e. $|\Omega_{ij}| = \sqrt{2\Omega_{ij}\Omega_{ij}}$.

B.1.2. TRANSPORT EQUATION FOR TRANSITION MOMENTUM THICKNESS

PRODUCTION TERM (P_{θ_t})

$$J = \frac{500\mu}{\rho U_\infty^2}, \tag{B.5a}$$

$$F_{\theta t} = \min\left[\max\left(F_{wake}\exp\left(-\left(\frac{d}{\delta}\right)^4\right), 1.0 - \left(\frac{c_{e2}\gamma - 1}{c_{e2} - 1}\right)^2\right), 1.0\right], \tag{B.5b}$$

$$\delta = \frac{375|\Omega_{ij}|\mu\tilde{R}e_{\theta t}d}{\rho U_\infty^2}, \tag{B.5c}$$

$$F_{wake} = exp\left[-\left(\frac{Re_\omega}{1\times10^5}\right)^2\right]. \tag{B.5d}$$

EMPIRICAL RELATIONS FOR Re_{θ_t}

$$Re_{\theta t} = \begin{cases} \left(1173.51 - 589.428I + 0.2196I^{-2}\right) F(\lambda_\theta), & I \le 1.3; \\ 331.50\,(I - 0.5658)^{-0.671}\, F(\lambda_\theta), & I > 1.3, \end{cases} \tag{B.6a}$$

$$F(\lambda_\theta) = \begin{cases} 1 + \left[12.986\lambda_\theta + 123.66\lambda_\theta^2 + 405.689\lambda_\theta^3\right]\exp\left(-\left(\frac{I}{1.5}\right)^{1.5}\right), & \lambda_\theta \le 0; \\ 1 + 0.275\left[1 - \exp\left(-35.0\lambda_\theta\right)\right]\exp\left(-\frac{I}{0.5}\right), & \lambda_\theta > 0. \end{cases} \tag{B.6b}$$

In these equations, $I = 100\frac{\sqrt{2k/3}}{U_\infty}$ and $\lambda_\theta = \frac{\theta^2}{\nu}\frac{dU|}{ds}$. In the latter, θ_t denotes the momentum thickness at the transition location and s the coordinate parallel to the local velocity vector with magnitude U.

B.2. TURBULENCE MODELS

This section presents the mathematical details of the KSKL, EARSM, DDES, and IDDES turbulence models which were introduced in Section 3.2.

B.2.1. $k\sqrt{k}L$ (KSKL) MODEL

The newly formulated transport equation by Rotta (1951) is shown in Equation (B.7). The individual terms are written out in the original published form,

$$\frac{\partial kL}{\partial t} + C_{kL} = -P_{kL} + E_{kL} - D_{kL}, \tag{B.7a}$$

$$C_{kL} = u_j \frac{\partial kL}{\partial x_j} + \frac{3}{16}\int_{-\infty}^{\infty}\left[\frac{\partial u(\vec{x}+s_y)}{\partial x} - \frac{\partial u(\vec{x})}{\partial x}\right] R_{ii}\, ds_y, \tag{B.7b}$$

$$P_{kL} = \frac{3}{16}\left(\frac{\partial u(\vec{x})}{\partial y}\int_{-\infty}^{\infty} R_{12}\, ds_y + \int_{-\infty}^{\infty}\frac{\partial u(\vec{x}+s_y)}{\partial y} R_{12}\, ds_y\right), \tag{B.7c}$$

$$E_{kL} = \frac{3}{16}\left(\int_{-\infty}^{\infty}\frac{\partial}{\partial r_k}[R_{(ik)i} - R_{i(ik)}]\, ds_y + 2\nu\int_{-\infty}^{\infty}\frac{\partial^2 R_{ii}}{\partial r_k \partial r_k}\, ds_y\right), \tag{B.7d}$$

$$D_{kL} = \frac{\partial}{\partial y}\left(\frac{3}{16}\int_{-\infty}^{\infty}\left[R_{(ik)i} + \frac{1}{\rho}(\overline{p'v'} + \overline{v'p'})\right] ds_y - \nu\frac{\partial kL}{\partial y}\right). \tag{B.7e}$$

Here R_{ij} represents the correlation matrix, s_y the y-distance between two correlation points. The main term of interest is the production term, which can be rewritten using a Taylor expansion,

$$\frac{\partial u(\vec{x}+s_y)}{\partial y} = \frac{\partial u(\vec{x})}{\partial y} + \frac{\partial^2 u(\vec{x})}{\partial y^2} s_y + \frac{1}{2}\frac{\partial^3 u(\vec{x})}{\partial y^3} s_y^2 + \dots, \tag{B.8a}$$

$$\int_{-\infty}^{\infty}\frac{\partial u(\vec{x}+s_y)}{\partial y} R_{12}\, ds_y = \frac{\partial u(\vec{x})}{\partial y}\int_{-\infty}^{\infty} R_{12}\, ds_y + \frac{\partial^2 u(\vec{x})}{\partial y^2}\int_{-\infty}^{\infty} R_{12} s_y\, ds_y + \frac{1}{2}\frac{\partial^3 u(\vec{x})}{\partial y^3}\int_{-\infty}^{\infty} R_{12} s_y^2\, ds_y + \dots \tag{B.8b}$$

Rotta (1951) assumed homogeneous turbulence in his work, this yields the term dependent on the second derivative to vanish because R_{12} is symmetric and s_y anti-symmetric whereby the integral is zero. Equation (B.9) presents the remaining integral terms. Furthermore, the only term modelled based on dimensionality arguments in the destruction term, see Equation (B.9),

$$L_{12,1} = \frac{3}{16\overline{u_1' u_2'}}\int_{-\infty}^{\infty}(R_{12} + R_{21})\, ds_y \quad \text{modelled as} \quad L_{12,1} = c_{kL,1} L, \tag{B.9a}$$

$$L_{12,n} = \left[\frac{3}{16(n-1)!\overline{u_1' u_2'}}\int_{-\infty}^{\infty} R_{12} s_y^{n-1}\, ds_y\right]^{1/n} \quad \text{modelled as} \quad L_{12,3} = c_{kL,2} L^3, \tag{B.9b}$$

$$-\frac{3}{16}\int_{-\infty}^{\infty}\frac{\partial}{\partial r_k}(R_{(ik)i} - R_{i(ik)})\, ds_y = c_{kL,3} k^{3/2}. \tag{B.10}$$

The final formulation of the model, including the model constants, is shown in Equation (B.11). The constant term in the definition of the eddy viscosity is chosen such that it yields $L = \kappa y$ in the logarithmic part of the near-wall BL.

$$\frac{\partial k}{\partial t} + u_j\frac{\partial k}{\partial x_j} = P_k - c_\mu^{3/4}\frac{k^{3/2}}{L} + \frac{\partial}{\partial x_j}\left(\frac{\nu_t}{\sigma_k}\frac{\partial k}{\partial x_j}\right) \quad \text{with} \quad \nu_t = c_\mu^{1/4}\frac{kL}{\sqrt{k}}, \tag{B.11a}$$

$$\frac{\partial kL}{\partial t} + u_j\frac{\partial kL}{\partial x_j} = -\overline{u'v'}\left(c_{kL,1} L\frac{\partial u_j}{\partial x_j} + c_{kL,2} L^3\frac{\partial^3 u_j}{\partial x_j^3}\right) - c_{kL,3} k^{3/2} + \frac{\partial}{\partial x_j}\left[\frac{\nu_t}{\sigma_{kL}}\frac{\partial kL}{\partial x_j}\right]. \tag{B.11b}$$

Table B.2: Coefficients of the KSKL turbulence model.

$c_{kL,1}$	$c_{kL,2}$	$c_{kL,3}$	c_μ	σ_k	σ_{kL}
0.09	0.8	1.47	0.0288	2/3	2/3

B.2.2. EXPLICIT ALGEBRAIC REYNOLDS STRESS MODEL (EARSM)

The definition of all further closures (β-constants) required to calculate the explicit formulation of the Reynolds-stress anisotropy tensor in the EARSM model as defined in Equation (3.18) read,

$$\beta_3 = -\frac{12 II_{\overline{S}\,\overline{\Omega}}}{NQ}, \quad \beta_4 = -\frac{2(N^2 - 2II_{\overline{\Omega}})}{Q}, \quad \beta_6 = -\frac{6N}{Q}, \quad \beta_9 = \frac{6}{Q}, \tag{B.12a}$$

$$Q = \frac{5}{6}(N^2 - 2II_{\overline{\Omega}})(2N^2 - II_{\overline{\Omega}}), \tag{B.12b}$$

where N is obtained from the solution of a cubic equation as shown in Equation (B.13). Note that for Three-Dimensional (3D) cases this is an sixth order polynomial for which no explicit solution can be found. The Two-Dimensional (2D) solution is used in this model.

$$N = \begin{cases} \frac{A_3'}{3} + \left(P_1 + \sqrt{P_2}\right)^{1/3} + \text{sign}\left(P_1 - \sqrt{P_2}\right)\left|P_1 - \sqrt{P_2}\right|^{1/3}, & P_2 \geq 0; \\ \frac{A_3'}{3} + 2\left(P_1^2 - P_2\right)^{1/6} \cos\left[\frac{1}{3}\cos^{-1}\left(P_1/\sqrt{P_1^2 - P_2}\right)\right], & P_2 < 0, \end{cases} \tag{B.13}$$

where,

$$P_1 = \left[\frac{A_3'^2}{27} + \left(\frac{9}{20}\right) II_{\overline{S}} - \frac{2}{3} II_{\overline{\Omega}}\right] A_3', \quad P_2 = P_1^2 - \left[\frac{A_3'^2}{9} + \left(\frac{9}{10}\right) II_{\overline{S}} + \frac{2}{3} II_{\overline{\Omega}}\right]^3. \tag{B.14}$$

The only variable missing still is A_3',

$$A_3' = \frac{9}{5} + \frac{9}{4} C_{diff}\left[\max\left(1 + \beta_1^{(eq)} II_{\overline{S}}, 0\right)\right], \quad \text{with} \quad \beta_1^{(eq)} = -\frac{6}{5}\left[\frac{N^{(eq)}}{\left(N^{(eq)}\right)^2 - 2II_{\overline{\Omega}}}\right]. \tag{B.15}$$

Table B.3 presents all coefficients.

Table B.3: Coefficients of the EARSM turbulence model.

γ_1	γ_2	β_1	β_2	σ_{k1}	σ_{k2}	$\sigma_{\omega 1}$	$\sigma_{\omega 2}$	σ_{d1}	σ_{d2}	β^*	$N^{(eq)}$	C_{diff}
0.518	0.44	0 0747	0.0828	1.1	1.1	0.53	1.0	1.0	0.4	0.09	80/20	2.2

B.2.3. DELAYED DETACHED EDDY SIMULATIONS (DDES)

The Delayed Detached-Eddy Simulation(s) (DDES) length scale is determine according,

$$l_t^{DDES} = l^{RANS} - \tilde{f}_d \max(0, l_{RANS} - l_{LES}), \tag{B.16}$$

where the individual length scales can be determined according,

$$l_t^{RANS} = \frac{\sqrt{k}}{C_\mu \omega}, \tag{B.17a}$$

$$l_t^{LES} = C_{DES}\Delta_c, \quad \text{with} \quad C_{DES} = C_{DES1}F_1 + C_{DES2}(1 - F_1), \tag{B.17b}$$

in which F_1 is one of the blending functions of the SST model as presented in Equation (3.11). The blending reads,

$$\tilde{f}_d = 1 - \tanh\left[(C_{d1} r_d)^{C_d 2}\right], \tag{B.18a}$$

$$r_{dl} = \frac{\nu}{\kappa^2 d_w^2 \sqrt{0.5(|S_{ij}|^2 + |\Omega_{ij}|^2)}}, \tag{B.18b}$$

where $|S_{ij}|$ and $|\Omega_{ij}|$ are magnitudes of the strain-rate and vorticity tensors respectively, and d_w denotes the distance to the closest wall. All model constants can be found in Table B.4.

Table B.4: Coefficients of the DDES turbulence model.

C_μ	κ	C_{DES1}	C_{DES2}	a_1	C_{d1}	C_{d2}
0.09	0.41	0.78	0.61	0.31	20	3

B.2.4. IMPROVED DELAYED DETACHED EDDY SIMULATIONS (IDDES)

The blending of the Reynolds Averaged Navier Stokes (RANS) and Large Eddy Simulation(s) (LES) formmulations starts in the definition of the turbulent length scale,

$$l_t^{IDDES} = \tilde{f}_d(1+f_e)l_t^{RANS} + (1-\tilde{f}_d)l_t^{LES}. \tag{B.19}$$

The length scales have the same definition as for the Detached Eddy Simulation(s) (DES) model. The remianing part in Equation (B.19) are the blending and elevating fuctions, $\tilde{f}_d$ and f_e respectively. The blending function is defined as,

$$\tilde{f}_d = \max[1-f_{dt}, f_b], \tag{B.20a}$$

$$f_{dt} = 1-\tanh\left[(C_{dt1}r_{dt})^{C_{dt2}}\right], \text{ with } r_{dt} = \frac{\nu_t}{\kappa^2 d_w^2\sqrt{0.5(|S_{ij}|^2+|\Omega_{ij}|^2)}}, \tag{B.20b}$$

$$f_b = \min[2e^{-9\alpha^2}, 1.0], \text{ with } \alpha = 0.25 - d_w\Delta_c. \tag{B.20c}$$

The elevating function reads,

$$f_e = f_{e2}\max[f_{e1}-1.0, 0.0], \tag{B.21a}$$

$$f_{e1} = \begin{cases} 2e^{-11.09\alpha^2}, & \alpha \geq 0; \\ 2e^{-9.0\alpha^2}, & \alpha < 0, \end{cases} \tag{B.21b}$$

$$f_{e2} = 1.0 - \max(f_t, f_l), \quad \text{with } f_t = \tanh\left[(C_t^2 r_{dt})^3\right];\ f_l = \tanh\left[(C_l^2 r_{dt})^{10}\right], \tag{B.21c}$$

$$r_{dl} = \frac{\nu}{\kappa^2 d_w^2\sqrt{0.5(|S_{ij}|^2+|\Omega_{ij}|^2)}}. \tag{B.21d}$$

The empirical coefficients can be found in Table B.5.

Table B.5: Coefficients of the IDDES turbulence model.

C_μ	κ	C_{DES1}	C_{DES2}	C_{dt1}	C_{dt2}	C_l	C_t
0.09	0.41	0.78	0.61	20	3	5.0	1.87

B.3. CAVITATION MODELS

The source term (S_{i_p}) in the continuity equation for vapour/liquid phase, as shown in Equation (3.28), can for all models be written in the form $S_{i_p} = C^{\pm} f(\phi_v) f(p)$. When cavitating C^+ is active in the continuity equation for the vapor phase and is matched by C^- in the continuity equation for the liquid phase. The following tables show the different terms for the different models. Table B.7 is concerning the family of models based on the Rayleigh-Plesset (R-P) equation and Table B.8 about the models finding their origin in the equation of state.

Table B.6: Coefficients of the different cavitation models.

$C_{e,Si}$	$C_{c,Si}$	$C_{e,Zw}$	$C_{c,Zw}$	$C_{e,Ku}$	$C_{c,Ku}$	$C_{e,Ah}$	$C_{c,Ah}$
0.02	0.01	50	0.01	9×10^5	3×10^4	0.001	0.001

Table B.7: Overview of the cavitation models based on the R-P equation.

Model	Physical basis	Notes	C	$f(\phi_v)$	$f(p)$
(Schnerr and Sauer, 2001)	Cavitation is based on bubble growth and collapse originating from nuclei, relating ϕ_v directly to R_B. Production term is related to the increase of number of bubbles in the cell and corresponding bubble growth.	Note that Cavitating is equal to minus condensation in this formulation. A limiter is build into the code for switching.	$C^+ = 4\frac{\rho_l\rho_v}{\bar{\rho}}\pi R_B^2 n_b$ $C^- = -4\frac{\rho_l\rho_v}{\bar{\rho}}\pi R_B^2 n_b$	$(1-\phi_v)$ ϕ_v	$\sqrt{\frac{2}{3}\frac{p_v-p}{\rho_l}}$ $\sqrt{\frac{2}{3}\frac{p-p_v}{\rho_l}}$
(Singhal et al., 2002)	Correlation from the nuclear industry is used where the bubble radius is found to be, $R_B = \frac{0.061We\sigma}{2\rho_l V_{rel}^2}$. The effect of turbulence in taken into account by representing one of the velocity terms by $\sqrt{k}$	V_{ch} should be quadratic according to dim-analysis, however is in most practical cases found to be linear. Originally proposed non-condensable gas correction is *not* implemented.	$C^+ = C_{e,Si}\frac{\rho_l\rho_v}{\bar{\rho}}\frac{\sqrt{k}}{\sigma}$ $C^- = -C_{c,Si}\frac{\rho_l\rho_v}{\bar{\rho}}\frac{\sqrt{k}}{\sigma}$	$(1-\phi_v)$ ϕ_v	$\sqrt{\frac{2}{3}\frac{p_v-p}{\rho_l}}$ $\sqrt{\frac{2}{3}\frac{p-p_v}{\rho_l}}$
(Zwart et al., 2004)	The model works well for condensation. It is physically incorrect (and numerically unstable) if applied to cavitation. One of the key assumptions in its derivation is that the cavitation bubbles do not interact with each other. Therefore ϕ_v is replaced by $\phi_{nuc}(1-\phi_v)$ during cavitation.	Zwart's model is (most) similar to the original formulation. However, ReFRESCO (2017) reports relatively larger condensation/vaporisation rates.	$C^+ = C_{e,Zw}\frac{3\phi_{v,nuc}\rho_v}{R_B}$ $C^- = C_{c,Zw}\frac{3\rho_v}{R_B}$	$(1-\phi_v)$ ϕ_v	$\sqrt{\frac{2}{3}\frac{p-p_v}{\rho_l}}$ $\sqrt{\frac{2}{3}\frac{p-p_v}{\rho_l}}$

Table B.8: Overview of the cavitation models based on the equation of state.

Model	Physical basis	Notes	C	$f(\phi_v)$	$f(p)$
(Kunz et al., 2000)	Sources terms are specified in the form described by Merkle (1998). By solving separate continuity equations for liquid and gas phase fields, one can account for and model the separate dynamics and thermodynamics on the liquid, condensable vapor, and non-condensable gas fields.	Source terms are proportional to the liquid volume fraction and the amount by which the pressure is below the vapour pressure. A mixture volume continuity equation is employed rather than mass (better for non-linear performance of segregated pressure based algorithms)	$C^+ = \frac{C_{e,Ku}\rho_v}{0.5\rho_l U_\infty^2 t_\infty}$	$(1-\phi_v)$	$(p_v - p)$
			$C^- = \frac{C_{c,Ku}\rho_v}{t_\infty}$	$(1-\phi_v)^2\phi_v$	1
(Ahuja et al., 2001)	Reducing the compressible system of equations to an acoustically accurate system taking the mixture into account. Therefore the model should perform better in the incompressible regime.	Isothermal relation $c = \partial P/\partial\rho$ is used to incorporate compressibility. A mixture sound speed c_m is specified to ensure an accurate propagation of the waves though the interface where the acoustic speed and density vary very rapidly.	$C^+ = \frac{1}{C_{e,Ah}}\frac{\rho_l}{0.5L_\infty\rho_\infty U_\infty}$	$(1-\phi_v)$	$(p_v - p)$
			$C^- = -\frac{1}{C_{c,Ah}}\frac{\rho_v}{0.5L_\infty\rho_\infty U_\infty}$	ϕ_v	$(p - p_v)$

C

MATHEMATICAL DETAILS OF UNCERTAINTY ANALYSIS

This appendix provides mathematical support for the uncertainty analysis presented in Section 5.1. The first section presents the least-squares fitting procedure for the discretisation error, the second section derives the theoretical expression for the standard deviation as required to assess the statistical uncertainty.

C.1. LEAST-SQUARES FITTING

Instead of directly determining the errors from the fit as presented in Equation (5.4), the procedure by Eça and Hoekstra (2014) employs least squares fitting to increase robustness. The spatial discretisation error is determined by calculating the minimum of the function S_d,

$$S_d(\phi_0, \beta_s, p_s) = \sqrt{\sum_{i=1}^{N_g} w_i(\phi_i - (\phi_0 + \beta_s \Delta h_i^{p_s}))^2}, \tag{C.1}$$

where N_g is the number of grids used in the analysis, w_i the weights, and the rest of the variables were already defined in Section 5.1.1.3. The weights are determined according,

$$w_i = \frac{1/\Delta h_i}{\sum_{i=1}^{N_g} 1/\Delta h_i}, \quad \text{guaranteeing that} \quad \sum_{i=1}^{N_g} w_i = 1. \tag{C.2}$$

For the different convergence rates (p_s) and and power series expansions, the determination of the error and standard deviation are shown below.

First-order single term expansion

For a monotonic convergence behaviour with $p_s = 1$, the to-be-minimised function reads,

$$S_1(\phi_0, \beta_s) = \sqrt{\sum_{i=1}^{N_g} w_i(\phi_i - (\phi_0 + \beta_s \Delta h_i))}, \tag{C.3}$$

which is minimised by setting $\partial S_1/\partial \phi_0 = 0$ and $\partial S_1/\partial \beta_s = 0$. This results in the system of linear equations,

$$\begin{bmatrix} 1 & \sum_{i=1}^{N_g} w_i \Delta h_i \\ \sum_{i=1}^{N_g} w_i \Delta h_i & \sum_{i=1}^{N_g} w_i \Delta h_i^2 \end{bmatrix} \begin{bmatrix} \phi_0 \\ \beta_s \end{bmatrix} = \begin{bmatrix} \sum_{i=1}^{N_g} w_i \phi_i \\ \sum_{i=1}^{N_g} w_i \phi_i \Delta h_i \end{bmatrix}, \tag{C.4}$$

with standard deviation,

$$\sigma_1 = \sqrt{\frac{\sum_{i=1}^{N_g} N_g w_i (\phi_i - (\phi_0 + \beta_s \Delta h_i))^2}{N_g - 2}}. \tag{C.5}$$

Second-order single term expansion

For a monotonic convergence behaviour with $p_s = 2$, the to-be-minimised function reads,

$$S_2(\phi_0, \beta_s) = \sqrt{\sum_{i=1}^{N_g} w_i(\phi_i - (\phi_0 + \beta_s \Delta h_i))^2}, \tag{C.6}$$

which is minimised by setting $\partial S_2/\partial\phi_0 = 0$ and $\partial S_2/\partial\beta_s = 0$. This results in the system of linear equations,

$$\begin{bmatrix} 1 & \sum_{i=1}^{N_g} w_i \Delta h_i^2 \\ \sum_{i=1}^{N_g} w_i \Delta h_i^2 & \sum_{i=1}^{N_g} w_i \Delta h_i^4 \end{bmatrix} \begin{bmatrix} \phi_0 \\ \beta_s \end{bmatrix} = \begin{bmatrix} \sum_{i=1}^{N_g} w_i \phi_i \\ \sum_{i=1}^{N_g} w_i \phi_i \Delta h_i^2 \end{bmatrix}, \tag{C.7}$$

with standard deviation,

$$\sigma_2 = \sqrt{\frac{\sum_{i=1}^{N_g} N_g w_i (\phi_i - (\phi_0 + \beta_s \Delta h_i^2))^2}{N_g - 2}}. \tag{C.8}$$

Unknown-order single term expansion

For a monotonic convergence behaviour with convergence rate p_s, the to-be-minimised function reads,

$$S_d(\phi_0, \beta_s, p_s) = \sqrt{\sum_{i=1}^{N_g} w_i (\phi_i - (\phi_0 + \beta_s \Delta h_i^{p_s}))}, \tag{C.9}$$

which is minimised by setting $\partial S_d/\partial\phi_0 = 0$, $\partial S_d/\partial\beta_s = 0$, and $\partial S_d/\partial p_s = 0$. This results in the system of non-linear equations,

$$\phi_0 = \sum_{i=1}^{N_g} w_i \phi_i - \beta_s \sum_{i=1}^{N_g} w_i \Delta h_i^{p_s}, \tag{C.10a}$$

$$\beta_s = \frac{\sum_{i=1}^{N_g} w_i \phi_i \Delta h_i^{p_s} - \left(\sum_{i=1}^{N_g} w_i \phi_i\right)\left(\sum_{i=1}^{N_g} w_i \Delta h_i^{p_s}\right)}{\sum_{i=1}^{N_g} w_i \phi_i \Delta h_i^{2p_s} - \left(\sum_{i=1}^{N_g} w_i \Delta h_i^{p_s}\right)\left(\sum_{i=1}^{N_g} w_i \Delta h_i^{p_s}\right)}, \tag{C.10b}$$

$$\sum_{i=1}^{N_g} w_i \phi_i \Delta h_i^{p_s} \log(\Delta h_i) - \phi_0 \sum_{i=1}^{N_g} w_i \Delta h_i^{p_s} \log(\Delta h_i) - \beta_s \sum_{i=1}^{N_g} w_i \Delta h_i^{2p_s} \log(\Delta h_i) = 0, \tag{C.10c}$$

with standard deviation,

$$\sigma_d = \sqrt{\frac{\sum_{i=1}^{N_g} N_g w_i (\phi_i - (\phi_0 + \beta_s \Delta h_i^{p_s}))^2}{N_g - 3}}. \tag{C.11}$$

First- and second-order two term expansion

For a non-monotonic convergence behaviour, the to-be-minimised function reads,

$$S_{12}(\phi_0, \beta_{s1}, \beta_{s2}) = \sqrt{\sum_{i=1}^{N_g} w_i (\phi_i - (\phi_0 + \beta_{s1} \Delta h_i + \beta_{s2} \Delta h_i^2))^2}, \tag{C.12}$$

which is minimised by setting $\partial S_{12}/\partial\phi_0 = 0$, $\partial S_{12}/\partial\beta_{s1} = 0$, and $\partial S_{12}/\partial\beta_{s1} = 0$. This results in the system of linear equations,

$$\begin{bmatrix} 1 & \sum_{i=1}^{N_g} w_i \Delta h_i & \sum_{i=1}^{N_g} w_i \Delta h_i^2 \\ \sum_{i=1}^{N_g} w_i \Delta h_i & \sum_{i=1}^{N_g} w_i \Delta h_i^2 & \sum_{i=1}^{N_g} w_i \Delta h_i^3 \\ \sum_{i=1}^{N_g} w_i \Delta h_i^2 & \sum_{i=1}^{N_g} w_i \Delta h_i^3 & \sum_{i=1}^{N_g} w_i \Delta h_i^4 \end{bmatrix} \begin{bmatrix} \phi_0 \\ \beta_{s1} \\ \beta_{s2} \end{bmatrix} = \begin{bmatrix} \sum_{i=1}^{N_g} w_i \phi_i \\ \sum_{i=1}^{N_g} w_i \phi_i \Delta h_i \\ \sum_{i=1}^{N_g} w_i \phi_i \Delta h_i^2 \end{bmatrix}, \tag{C.13}$$

with standard deviation,

$$\sigma_{12} = \sqrt{\frac{\sum_{i=1}^{N_g} N_g w_i (\phi_i - (\phi_0 + \beta_{s1} \Delta h_i + \beta_{s2} \Delta h_i^2))^2}{N_g - 3}}. \tag{C.14}$$

C.2. THEORETICAL EXPRESSION OF STANDARD DEVIATION

To determine the statistical uncertainty, the standard deviation of the signal is compared to the theoretical expression for the standard deviation. This section derives this theoretical expression. The time averaged mean ($\overline{\phi}$) and sample standard deviation (σ_i) of the time signal of quantity ϕ are defined as (Dekking et al., 2005),

$$\overline{\phi} = \frac{1}{T}\int_0^T \phi_i(t)\mathrm{d}t, \quad \text{and} \quad \sigma_i^2 = \frac{1}{T}\int_0^T (\phi_i(t)-\overline{\phi})^2\mathrm{d}t, \tag{C.15}$$

where i indicates the measurement at the i^{th} timestep, and T the measurement (simulation) time. Since the time signal will always be finite, $\overline{\phi}$ will deviate from the exact mean μ_ϕ. In theory, the expected value of the standard deviation of the mean can thus be written as,

$$\sigma_{\overline{\phi}}^2 = \mathbb{E}[(\overline{\phi}-\mu_\phi)^2]. \tag{C.16}$$

Substituting the expression for $\overline{\phi}$ yields,

$$\sigma_{\overline{\phi}}^2 = \mathbb{E}\left[\left(\frac{1}{T}\int_0^T \phi_i(t)\mathrm{d}t - \mu_\phi\right)^2\right], \tag{C.17a}$$

$$\sigma_{\overline{\phi}}^2 = \mathbb{E}\left[\frac{1}{T^2}\left(\int_0^T \phi_i(t)\mathrm{d}t\right)^2 - 2\frac{\mu_\phi}{T}\int_0^T \phi_i(t)\mathrm{d}t + \mu_\phi^2\right], \tag{C.17b}$$

$$\sigma_{\overline{\phi}}^2 = \mathbb{E}\left[\frac{1}{T^2}\left(\int_0^T \phi_i(t)\mathrm{d}t\right)^2\right] - 2\mathbb{E}\left[\frac{\mu_\phi}{T}\int_0^T \phi_i(t)\mathrm{d}t\right] + \mathbb{E}[\mu_\phi^2], \tag{C.17c}$$

$$\sigma_{\overline{\phi}}^2 = \mathbb{E}\left[\frac{1}{T^2}\left(\int_0^T \phi_i(t)\mathrm{d}t\right)^2\right] - 2\mu_\phi^2 + \mu_\phi^2, \tag{C.17d}$$

$$\sigma_{\overline{\phi}}^2 = \frac{1}{T^2}\int_0^T\int_0^T \mathbb{E}[\phi_i(t_1)\phi_i(t_2)]\mathrm{d}t_1\mathrm{d}t_2 - \mu_\phi^2. \tag{C.17e}$$

The autocovariance function ($C_{\phi\phi}(dt)$) presented in Bendat and Piersol (2011) reads,

$$C_{\phi\phi}(t_1,t_2) = \mathbb{E}[(X_{t_1}-\mu_{t_1})(X_{t_2}-\mu_{t_2})] = \mathbb{E}[X_{t_1}X_{t_2}] - \mu_{t_1}\mu_{t_2}. \tag{C.18}$$

For a statistical stationary process, it holds that $\mu_{t_1} = \mu_{t_2} = \mu_t$ and $C_{\phi\phi}(t_1,t_2) = C_{\phi\phi}(t_1-t_2) = C_{\phi\phi}(dt)$ with $dt = t_2 - t_1$. This yields the theoretical expression for $\sigma_{\overline{\phi}}$,

$$C_{\phi\phi}(dt) = \frac{1}{T}\int_0^T \phi_i(t)\phi_i(t+dt)\mathrm{d}t - \mu_\phi^2 \quad \rightarrow \quad \sigma_{\overline{\phi}}^2 = \frac{1}{T}\int_0^T \left(1-\frac{dt}{T}\right)C_{\phi\phi}(dt)\mathrm{d}(dt). \tag{C.19}$$

The autocovariance function is not directly calculated but a one sided Fourier transform is used for computational efficiency reasons,

$$C_{\phi\phi}(dt) = \int_0^\infty S_{\phi\phi}(f)\cos(2\pi f\, dt)\mathrm{d}f, \tag{C.20}$$

where f is the frequency, and $S_{\phi\phi}$ the power spectral density function which is calculated as the Fourier transform of the time signal. Mathematically described as,

$$S_{\phi\phi}(f) = \frac{2}{T}|X(f)|^2, \quad \text{with} \quad X(f) = \int_0^T (\phi_i(t) - \overline{\phi}e^{-j2\pi f})\mathrm{d}t, \tag{C.21}$$

with j being the imaginary unit.

D

NUMERICAL SETTINGS

D.1. TRANSITION SIMULATIONS

Table D.1: Numerical settings of 2D transition simulations.

Family	Aspect	Settings
General	Inflow vel. $[m^1 s^{-1}]$	0.8986
	Root chord $[m^1]$	1
	Eddy viscosity ratio [-]	[1, 2, 3]
	Turbulence int. [%]	[1, 2, 3]
	Reynolds number [-]	$8.95 \cdot 10^5$
Material	Water density $[kg^1 m^{-3}]$	998
	Water kin. visc. $[m^2 s^{-1}]$	$1.002 \cdot 10^{-3}$
Time-loop	Steady-state	
Outerloop	Conv. tolerance	10^{-5}
	Maximum terations	2,400
Solver	Mass mom. solver	FRESCO
Momentum	Solver	GMRES
	Preconditioner	Jacobi
	Conv. tolerance	10^{-2}
	Max iterations	200
	Implicit relaxation	0.925
	Explicit relaxation	0.25
	Flux discretatisation	QUICK
Pressure	Solver	CG
	Preconditioner	BJACOBI
	Conv. tolerance	10^{-2}
	Max iterations	1,000
	Explicit relaxation	0.15
Turbulence	Solver	GMRES
	Preconditioner	BJACOBI
	Conv. tolerance	10^{-2}
	Max iterations	1,000
	Implicit relaxation	0.925
	Explicit relaxation	0.1
	Flux discretatisation	UPWIND
Transition	Solver	GMRES
	Preconditioner	BJACOBI
	Conv. tolerance	10^{-2}
	Max iterations	200
	Implicit relaxation	0.925
	Explicit relaxation	0.3
	Flux discretatisation	UPWIND

Table D.2: Numerical settings of 3D transition simulations.

Family	Aspect	Settings
General	Inflow vel. $[m^1 s^{-1}]$	7.1544
	Root chord $[m^1]$	0.1256
	Eddy viscosity ratio [-]	[0.5,1, 2, 4]
	Turbulence int. [%]	[0.5, 1, 2, 4]
	Reynolds number [-]	$8.95 \cdot 10^5$
Material	Water density $[kg^1 m^{-3}]$	998
	Water kin. visc. $[m^2 s^{-1}]$	$1.002 \cdot 10^{-3}$
Time-loop	Steady-state	
Outerloop	Conv. tolerance	10^{-5}
	Maximum terations	30,000
Solver	Mass mom. solver	FRESCO
Momentum	Solver	GMRES
	Preconditioner	Jacobi
	Conv. tolerance	10^{-2}
	Max iterations	200
	Implicit relaxation	0.925
	Explicit relaxation	0.25
	Flux discretatisation	QUICK
Pressure	Solver	CG
	Preconditioner	BJACOBI
	Conv. tolerance	10^{-2}
	Max iterations	500
	Explicit relaxation	0.15
Turbulence	Solver	GMRES
	Preconditioner	BJACOBI
	Conv. tolerance	10^{-2}
	Max iterations	200
	Implicit relaxation	0.925
	Explicit relaxation	0.1
	Flux discretatisation	UPWIND
Transition	Solver	GMRES
	Preconditioner	BJACOBI
	Conv. tolerance	10^{-2}
	Max iterations	200
	Implicit relaxation	0.925
	Explicit relaxation	0.3
	Flux discretatisation	UPWIND

D.2. TURBULENCE SIMULATIONS

Table D.3: Numerical settings of turbulence simulations.

Family	Aspect	Settings
General	Inflow vel. $[m^1 s^{-1}]$	7.1544
	Root chord $[m^1]$	0.1256
	Eddy viscosity ratio [-]	1
	Turbulence int. [%]	1
	Reynolds number [-]	$8.95 \cdot 10^5$
Material	Water density $[kg^1 m^{-3}]$	998
	Water kin. visc. $[m^2 s^{-1}]$	$1.002 \cdot 10^{-3}$
Time-loop	Time-steps	Case dep.
	Δt	Grid dep.
	Discretization scheme	Implicit three time level
Outerloop	Conv. tolerance	10^{-5}
	Maximum terations	100
Solver	Mass mom. solver	FRESCO
Momentum	Solver	GMRES
	Preconditioner	Jacobi
	Conv. tolerance	10^{-2}
	Max iterations	200
	Implicit relaxation	0.925
	Explicit relaxation	0.45
	Flux discretatisation	QUICK
Pressure	Solver	CG
	Preconditioner	BJACOBI
	Conv. tolerance	10^{-2}
	Max iterations	200
	Explicit relaxation	0.2
Turbulence	Solver	GMRES
	Preconditioner	BJACOBI
	Conv. tolerance	10^{-2}
	Max iterations	200
	Implicit relaxation	0.925
	Explicit relaxation	0.3
	Flux discretatisation	UPWIND
Transition	Solver	GMRES
	Preconditioner	BJACOBI
	Conv. tolerance	10^{-2}
	Max iterations	200
	Implicit relaxation	0.925
	Explicit relaxation	0.2
	Flux discretatisation	UPWIND

D.3. CAVITATION SIMULATIONS

Table D.4: Numerical settings of cavitation simulations.

Family	Aspect	Settings
Material	Vapour density $[kg^1 m^{-3}]$	0.024
	Vapour kin. visc. $[m^2 s^{-1}]$	$1.002 \cdot 10^{-5}$
Cavitation	Solver	GMRES
	Preconditioner	BJacobi
	Conv. tolerance	10^{-2}
	Max iterations	200
	Implicit relaxation	0.975
Cavitation	Explicit relaxation	0.25
	Flux discretatisation	QUICK
	Model	Schnerr-Sauer
	noOfSeeds	1×10^9
	BubbleRadius $[m^1]$	3×10^{-5}
	maxBubbleRadius $[m^1]$	1×10^{-2}
	Vapour pressure	Case dep.

Faculty of Aerospace Engineering
Kluyverweg 1
2629 HS Delft

Maritime Research Institute Netherlands
Haagsteeg 2
6708 PM Wageningen